



HAL
open science

Développement d'une méthode in situ pour mesurer les champs de déformation élastique et totale à l'échelle du grain

Wang Chow

► **To cite this version:**

Wang Chow. Développement d'une méthode in situ pour mesurer les champs de déformation élastique et totale à l'échelle du grain. Autre. Université Paris Saclay (COMUE), 2017. Français. NNT : 2017SACLC003 . tel-01502333

HAL Id: tel-01502333

<https://theses.hal.science/tel-01502333v1>

Submitted on 5 Apr 2017

HAL is a multi-disciplinary open access archive for the deposit and dissemination of scientific research documents, whether they are published or not. The documents may come from teaching and research institutions in France or abroad, or from public or private research centers.

L'archive ouverte pluridisciplinaire **HAL**, est destinée au dépôt et à la diffusion de documents scientifiques de niveau recherche, publiés ou non, émanant des établissements d'enseignement et de recherche français ou étrangers, des laboratoires publics ou privés.

NNT : 2017SACL003

THESE DE DOCTORAT
DE
L'UNIVERSITE PARIS-SACLAY
PREPAREE A
CENTRALESUPELEC

ECOLE DOCTORALE N° 579
Sciences mécaniques et énergétiques, matériaux et géosciences

Spécialité de doctorat : Mécanique des Matériaux

Par

Mme. Chow, Wang

Développement d'une méthode in situ pour mesurer les champs de déformation élastique et totale à l'échelle du grain

Thèse présentée et soutenue à Châtenay-Malabry le 1 Février 2017:

Composition du Jury :

M. Hubert, Olivier	Professeur, ENS Paris-Saclay	Président du jury
M. Saintier, Nicolas	Professeur, Ecole Nationale Supérieure d'Arts et Métiers	Rapporteur
M. Castelnau, Olivier	Directeur de recherche CNRS	Rapporteur
M. Mareau, Charles	Maître de conférences, Ecole Nationale Supérieure d'Arts et Métiers	Examineur
M. Solas, Denis	Maître de conférences, Université Paris-Sud	Encadrant de thèse
M. Puel, Guillaume	Professeur, CentraleSupélec	Encadrant de thèse
Mme. Aubin, Véronique	Professeur, CentraleSupélec	Directrice de thèse

Contents

General introduction	v
1 Literature review	1
1.1 Research background	1
1.2 Microstructure-based mechanical behaviour	2
1.2.1 Face-centered cubic crystal structure	2
1.2.2 Elasticity	3
1.2.3 Plasticity	5
1.3 Polycrystalline aggregates Modelling	9
1.3.1 Crystal plasticity constitutive equation	9
1.3.2 Establishment of a polycrystalline model linking the macroscopic response with the microscopic behaviour	11
1.4 Local mechanical measurement	13
1.4.1 Total strain field measuring methods	13
1.4.2 Elastic strain field measuring methods in a single crystal	15
1.4.3 Energy or heat dissipation measuring method	21
1.4.4 Choice of the local mechanical informations	22
1.4.5 Choice of the measuring methods	22
1.5 Identification procedure	23
1.5.1 Type of variables	23
1.5.2 Identification strategies	23
1.5.3 Complexity of the model to be identified	26
1.6 Conclusion	27
2 Material and sample preparation	29
2.1 Materials	29
2.1.1 Choice of material	29
2.1.2 Chemical composition	32
2.2 Sample Preparation	32
2.2.1 Design of the specimen shape	32
2.2.2 Sample production	34
2.3 Studied samples and their initial microstructure	35
2.3.1 Grain geometry	36
2.3.2 Euler angles	37
2.3.3 Schmid factor	39
2.3.4 Initial microstructure for Sample No.2	40
2.4 Conclusion	42

3	Elastic strain field measurement using X-ray diffraction	43
3.1	Application of XRD in ε^e field measurement	43
3.2	Experimental apparatus: Diffractometer	44
3.3	General principle in ε^e full-field measurement	45
3.4	ε^e measurement using XRD in single crystal	46
3.4.1	The $\sin^2\psi$ method and its limits	46
3.4.2	Recall of the principle of X-ray Diffraction and the Bragg's law	46
3.4.3	Difference between XRD measurement in an aggregate and a single crystal	49
3.4.4	Transformation between the sample and the crystal frames .	50
3.4.5	Positioning of the normal of $\{hkl\}$ planes for XRD	51
3.4.6	Definition of crystal frame in direct and reciprocal lattice and calculation of lattice parameter a_o of Al-alloy(5052)	53
3.4.7	ε^e measuring method in monocrystal: First Ortner Method [Ortner (1986a,b)]	57
3.5	Development of an experimental methodology for diffraction peak measurement	60
3.5.1	Understanding the relationship between the diffraction signal and XRD scanning in ϕ , ψ and 2θ space	61
3.5.2	Focusing the diffracted signal during (ϕ, ψ) measurement: prevent beam divergence using Soller's slits	61
3.5.3	Relocating peak position: iteration process	62
3.5.4	Handling of Mosaicity : Refinement of beam size, choice of scanning step size and acquisition time	64
3.5.5	Determination of the final peak position: Peak simulation . .	66
3.5.6	Assumption of XRD in single crystal at deformed state . . .	68
3.6	Uncertainty estimation of the elastic strain tensor σ_{ε^e}	68
3.6.1	Uncertainty of peak position σ_{θ}	68
3.6.2	Uncertainty of the elastic strain tensor σ_{ε^e}	71
3.7	Discussion	76
3.7.1	Penetration of X-ray beam during ε^e measurement - Why is it considered as a surface measurement in this experiment? .	76
3.7.2	Influence of the change of sample thickness towards the diffrac- tion area during deformation.	76
3.8	Conclusion	78
4	Development of an in situ method for measuring elastic and total strain fields.	79
4.1	Total strain field measurement using digital image correlation (DIC)	79
4.1.1	Application of DIC	79
4.1.2	General principle	79
4.1.3	Speckle paint	80
4.1.4	Texture analysis of speckle painting and selection of DIC spa- tial resolution	82
4.2	Implementation	85

4.2.1	Micro-tensile test	85
4.2.2	Camera	87
4.2.3	Experimental set-up	88
4.3	Experimental protocol	90
4.3.1	Principle of in situ full-field measurements	90
4.3.2	Experimental procedure	90
4.4	Discussion	93
4.4.1	Size of X-ray beam spot on the specimen	93
4.4.2	Movement of the grip system during a tensile test	93
4.4.3	Relaxation	94
4.5	Conclusion	95
5	Experimental Results	97
5.1	Experimental results of sample 1	97
5.1.1	Zone of XRD and DIC measurement	97
5.1.2	Tensile test	98
5.1.3	Total strain field measurement ε^t	99
5.1.4	Elastic strain field measurement ε^e	101
5.1.5	Stress field calculation σ^e	103
5.1.6	Discussion	106
5.2	Experimental results of sample 2	112
5.2.1	Zone of XRD and DIC measurement	112
5.2.2	Tensile tests	113
5.2.3	Total strain field measurement ε^t	113
5.2.4	Elastic strain field measurement ε^e	116
5.2.5	Stress field σ^e calculation	118
5.2.6	Discussion	121
5.3	Conclusion	127
	General Conclusion and Perspective	129
	Bibliography	133
	Drawing of the micro-tensile machine	147
	Drawing of the sample	151
	Full path of X-ray diffraction	153
	Uncertainty estimation of the elastic strain tensor σ_{ε^e} - Monte Carlo Method	155
	Drawing of the supplementary elements for experimental setup as- sembly	159

Experimental Potocol - complementary information	163
.1 Position of the sample center in goniometer	163
.2 Position of the sample on the goniometer during DIC	163
.3 Restriction of the movement of goniometer during in-situ measurement	164
.4 In-situ measuring procedure of XRD and DIC	164
Résumé substantiel en français	167

General introduction

Background

Crystal plasticity models are applied to describe the mechanical behaviour and the microstructure evolution (e.g. disorientation of grains, phase transformation, pile-ups of dislocation, etc.) of a crystalline material which allows to forecast its local behaviour. Thanks to the strain-causing based physical mechanisms, these constitutive equations enable us to deduce the microstructure change under complex loading conditions [Saai (2008); Saai et al. (2010); Badulescu et al. (2011); Evrard et al. (2010b)]. It can predict, for example, the local disorientations due to hot forming [De Jaeger et al. (2012)] or the location of the plastic deformation which leads to crack initiation in fatigue [Schwartz (2011); Li et al. (2012)].

However, the mechanisms that they describe (e.g. evolution of dislocation density, strain hardening, pile-ups at grain boundaries, changes in dislocation microstructures, etc.) are at a small scale and the associated quantification can be very complicated. For this reason, the parameters of these models are difficult to identify and plenty of existing works performed identification using macroscopic data [Evrard et al. (2010a); Guilhem et al. (2013)]. Since the range of heterogeneities at the grain scale cannot be taken into account, sometimes even minimization of a cost function between simulations and experiments let local minima appear, and the identified parameters may not necessarily have physical meaning.

In this way, methodologies has been sought to access experimental data at the grain scale to increase the robustness of the parameter identification [Avril et al. (2008a); Grédiac and Hild (2013)].

Objective

Our research objective is to develop an experimental method and then validate the experimental protocol to obtain two distinct mechanical measurements simultaneously during a tensile test. During the experimental stage, the total (ε^t) and elastic (ε^e) strain fields of a specimen with around 12 grains are measured at the same time. The test is stopped at increasing levels of strain, and ε^t and ε^e measured in the useful part of the specimen. The ε^t are determined by the Digital Image Correlation technique (DIC) [Hild and Roux (2008)] while the ε^e are calculated from the X-ray diffraction (XRD) measurements [Zhou (1994); Huang (2007); Eberl (2000)] (Fig.1).

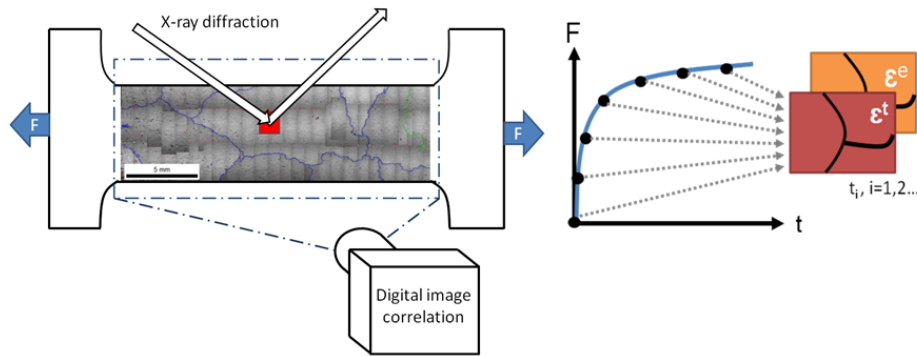


Figure 1: Principle of simultaneous kinematic full-fields measurements

Research design

For the sample, a material with simple microstructure and mechanical properties favouring the local strain field measurement is preferred. Recrystallisation procedure is performed to obtain large grains (about 5 mm) so that the measurements of strain gradient inside the grains can be accessible.

In order to achieve our research goals, an experimental apparatus is designed to perform Digital Image Correlation (DIC), X-ray Diffraction (XRD) and tensile tests in situ in an X-ray diffractometer. Full-field measurements of both elastic and total strains are applied on sample surface and the fineness of the grid measurement is defined according to the grain size. There are approximately 10 points of XRD measurement in a grain. The spatial resolution for DIC is much finer than for XRD.

Meanwhile, certain experimental difficulties had to be overcome in order to achieve the measurements. For example, the appearance of mosaicity in crystal during plasticity may complicate the ϵ^e calculation, etc.

Scope of the study

Throughout the experiments, the samples are deformed every 0.1% until ϵ^t about 0.4%. Small deformation step is defined to ensure the traceability of DIC speckle pattern as well as XRD signal on heterogeneous deformed sample surface during plasticity. The direct measurements on the sample surface conducted at the beginning of the tensile curve can already give us a first sight of the actual location of heterogeneity of the samples for ϵ^t and ϵ^e .

Significance of the study

The study provided the experimental results that allows ones to carry out an identification of material parameters later.

Organization of the manuscript

This dissertation is divided into five chapters.

The first chapter is a synthesis of the latest research interest in modelling crystal plasticity and its corresponding difficulties/challenges to overcome. The microstructure-based mechanical behaviour is recalled. The polycrystalline aggregate modelling method and existing constitutive parameter identification procedure are synthesised. The methodologies to answer our research questions are chosen according to their accuracy and feasibility in actual practice.

The second chapter describes the material selection and the sample preparation for our research use. Two samples in aluminium alloy are prepared and their initial microstructures are also presented.

The third chapter discusses the methodologies to conduct X-ray diffraction (XRD) for ε^e measurement. The X-ray diffractometer is introduced. Then, the ε^e measurement in a single crystal using XRD is given. Followed by, the methodologies developed to achieve local ε^e field measurement as well as the corresponding uncertainties quantification on a oligo-crystal sample are described.

The fourth chapter focuses on in-situ experimental measurement. The method developed for measuring ε^t and ε^e at the grain scale is presented. It introduces the device specifically developed, presents the measurement concept and describes testing procedure, analysis method as well as the precautions taken to minimise experimental errors.

The last chapter is devoted to results obtained through our in situ experiments. Besides results and analysis, the corresponding uncertainties during each measurement were quantified as well.

A general conclusion summarizes the tasks that we have accomplished and achieved. It closes the manuscript with suggestions of future work in this domain.

Literature review

In this chapter, the current research interest in modelling crystal plasticity is firstly introduced. Then, a recall on the microstructure-based mechanical behaviour is made. Afterwards, the polycrystalline aggregate modelling method and existing constitutive parameters identification procedure are synthesised. The choice of methodologies to answer our research questions are explained followed by a review of the state of the art concerning experimental measurements of local identification approaches and mechanical response. A conclusion is given to summarize this chapter.

1.1 Research background

Constitutive equations describe the deformation of a material under the action of mechanical stress. To identify these models, it is necessary to carry out an experimental campaign composed of tests representative of the variety of in-service loadings (in terms of amplitudes, loading paths, strain rate, temperature, etc.). Parameters of the constitutive law can then be identified on this experimental basis. It has been observed that to have a model valid of a large variety of loadings, the identification database had to be sufficiently large [Calloch (1997); Portier (1999); Aubin et al. (2003)]; otherwise, the predictions non-covered by this identification database are generally very poor. One of the drawbacks of these macroscopic models is the robustness of the parameter calibration. Moreover, if the chemical composition or the fabrication process changes, all the experimental procedure has to be repeated once again — these models suffer a lack of physical meaning. To overcome these drawbacks, micromechanical models have been proposed, whose variables are based on physical mechanisms such as dislocation density.

Experimental characterizations have been carried out on single crystals [Franciosi and Zaoui (1982); Mughrabi (1978)]. Constitutive laws have been proposed to link the hardening to the applied strain [Sidoroff (1982)] and the evolution of the dislocation microstructure [Zerilli (2004)]. However, there are still open questions, for instance:

1. Can a same behaviour law describe both the small strain responses and large strain responses accurately? How can we express a kinematic hardening in the framework of dislocation densities?
2. Several ways of expressing the interactions of slip systems have been proposed, obtained from mechanical experiments [Franciosi and Zaoui (1982)] and from

dislocation dynamic simulations [Devincre and Condat (1992)]. But the hardening matrices proposed in these two methods are contradictory [Schwartz et al. (2010); Schwartz (2011)]. Is there any way to figure out which method is correct?

In order to work on and answer these questions, local responses are needed and an experimental set-up is proposed to allow these local measurements to be obtained.

1.2 Microstructure-based mechanical behaviour

During our research, aluminium alloy (5052) was chosen for fabricating samples and the material selection will be presented in the next chapter. In order to measure local responses, it is important to understand what microstructure-based information we are interested in. At the beginning of this section, the crystal structure of aluminium (Face-centered cubic FCC) as well as the definition of a grain/crystal are recalled. Then, the elasticity and plasticity in a single crystal are presented. Later, we will talk about the phenomenon of heterogeneous elastic and plastic strain in polycrystalline sample under mechanical loading.

1.2.1 Face-centered cubic crystal structure

Aluminium has a face-centered cubic FCC crystalline lattice (Fig.1.1). Crystal lattice is the unique and regularly repeated arrangement of atoms in a material (Fig.1.2). The face-centered cubic (FCC) unit cell is a cube (all sides of the same length and every face perpendicular to each other) with an atom at each corner of the unit cell and an atom situated in the middle of each face of the unit cell.

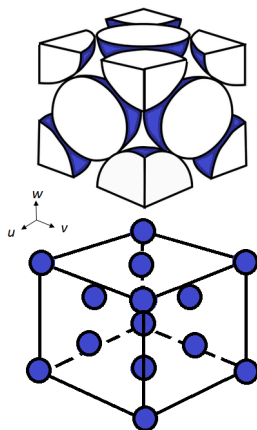


Figure 1.1: Presentation of FCC unit cell in two different ways.

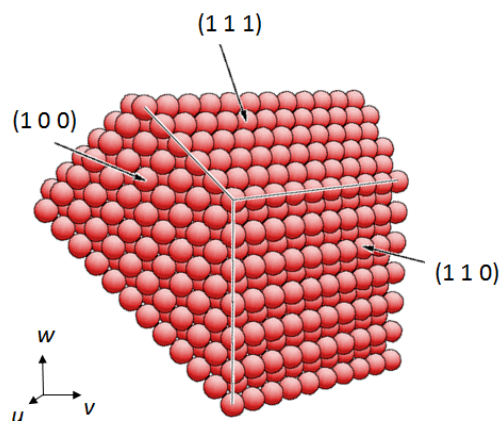


Figure 1.2: Schema of FCC crystal structure. (Source: <http://www.fhi-berlin.mpg.de/~hermann/Balsac/pictures.html>)

A crystal is the zone where the atomic arrangement shares the same orientation in three dimensions on a lattice. Therefore, for two crystals with different orientations of atom arrangement, there is an interface with misalignment of atoms defined as grain boundary. Once we have these basic concepts of microstructure, we can start to understand the elasticity and plasticity inside a single crystal under loading.

1.2.2 Elasticity

When a sufficient load is applied to a crystal, each unit cell is distorted and thus the crystal deforms. This change in shape is called deformation. In the case of elastic deformation, once the stress is removed, the unit cells return to their original position and the crystal returns to its original shape and size.

1.2.2.1 Mechanism

In fact, this elastic response arises from interatomic forces $F(r)$ and this temporary shape change can be explained from fundamental physics. In the metallic bond, the attraction between the electrons and the atom core is balanced by the repulsion between atom cores. This interaction separates two atoms by a distance r . Interatomic spacing r_0 , which is the equilibrium distance between atoms, occurs when the total energy of the pair of atoms is at a minimum or when external force is absent. The interatomic potential energy $U(r)$ of this interaction can be expressed using Lennard-Jones potential:

$$U(r) \propto r^2 \quad (1.1)$$

and, so, the interatomic forces $F(r)$ can be derived as:

$$F(r) \propto \frac{\partial U(r)}{\partial r} \quad (1.2)$$

$$\propto r$$

Stress and strain can be calculated from $F(r)$ and r respectively and their linear relationship explains the reversible mechanical property in elasticity. Also, the steepness of the slope, the Young's modulus \mathbf{E} , implies the stiffness of a material. A stiff material requires more stress to be deformed at a given strain.

1.2.2.2 Isotropic and anisotropic elasticity

Within a crystal, atoms are arranged differently in $\{hkl\}$ planes and $\langle hkl \rangle$ directions. Thus, the mechanical properties can vary with different loading directions. This crystal anisotropic elastic behaviour can be described using a 4th-order stiffness tensor C^e with 81 elastic coefficients representing the properties in the different directions. i.e. the stress σ^e and the strain tensors ε^e can be written as:

$$\sigma^e = C^e : \varepsilon^e \quad (1.3)$$

or

$$\sigma_{ij}^e = C_{ijkl}^e : \varepsilon_{kl}^e \quad (1.4)$$

As σ^e , ε^e and C^e are symmetric, the number of independent elastic coefficients can be reduced to 21. Thanks to the cubic symmetry of FCC, the elasticity is orthotropic and needs only 3 independent elastic constants, i.e. C_{11}^e , C_{12}^e and C_{44}^e . It can be represented using the Voigt notation in crystal coordinates (R_c) as Eq.1.5:

$$\begin{pmatrix} \sigma_{11}^e \\ \sigma_{22}^e \\ \sigma_{33}^e \\ \sigma_{23}^e \\ \sigma_{31}^e \\ \sigma_{12}^e \end{pmatrix} = \begin{pmatrix} C_{11}^e & C_{12}^e & C_{12}^e & 0 & 0 & 0 \\ C_{12}^e & C_{11}^e & C_{12}^e & 0 & 0 & 0 \\ C_{12}^e & C_{12}^e & C_{11}^e & 0 & 0 & 0 \\ 0 & 0 & 0 & C_{44}^e & 0 & 0 \\ 0 & 0 & 0 & 0 & C_{44}^e & 0 \\ 0 & 0 & 0 & 0 & 0 & C_{44}^e \end{pmatrix} \begin{pmatrix} \varepsilon_{11}^e \\ \varepsilon_{22}^e \\ \varepsilon_{33}^e \\ 2\varepsilon_{23}^e \\ 2\varepsilon_{31}^e \\ 2\varepsilon_{12}^e \end{pmatrix} \quad (1.5)$$

The anisotropy of a given material is characterized by the anisotropy coefficient, $\alpha_{anisotropy}$:

$$\alpha_{anisotropy} = \frac{2 \times C_{44}^e}{C_{11}^e - C_{12}^e} \quad (1.6)$$

An isotropic elastic material has $\alpha_{anisotropy} = 1$. However, in reality, real materials are never perfectly isotropic. A material can be said rather elastic isotropic or anisotropic by comparison of its anisotropy coefficient to the isotropic case. Several common FCC metals are given as examples in Table 1.1. γ -iron and copper are highly anisotropic ($\alpha_{anisotropy} = 3.3$ or $3.4 \gg 1$) while aluminium has small anisotropy ($\alpha_{anisotropy} = 0.8$ which is very close to 1).

FCC Metal	C_{11}^e (GPa)	C_{12}^e (GPa)	C_{44}^e (GPa)	$\alpha_{anisotropy}$
Aluminium	107	60.8	28.3	1.2
α -iron (Ferrite)	247.7	144.6	118	2.3
Copper	170	124	75	3.3
γ -iron (Austenite)	197.5	125	122	3.4

Table 1.1: Elastic constants and anisotropy coefficients of several common FCC metals [Huntington (1958)]

Figure 1.3 indicated that this elastic anisotropy results in an inhomogeneous stress distribution from grain to grain in a polycrystalline sample under tensile loading. For aluminium, thanks to its $\alpha_{anisotropy}$ being close to isotropic case, this inhomogeneity of stress distribution is small and most of the crystals will be subjected to similar stress levels. Therefore, the elasticity of aluminium can be assumed to be isotropic in our studies.

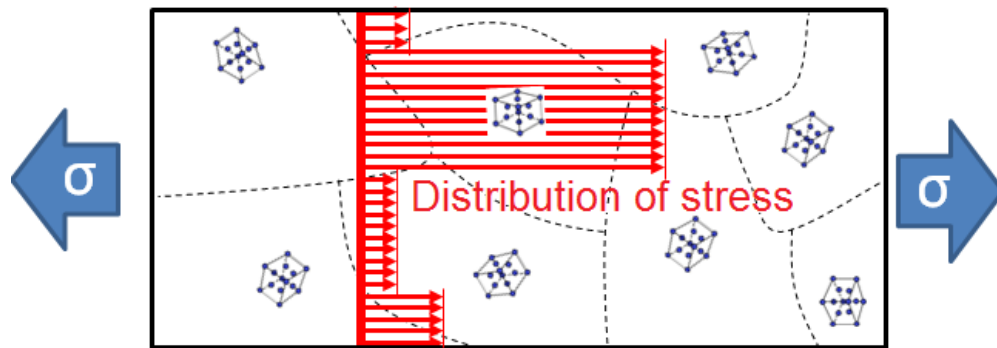


Figure 1.3: Schematic diagram of polycrystalline sample made of anisotropic material: An inhomogeneous distribution of stress due to anisotropic elastic behaviour in crystals.

1.2.3 Plasticity

If the force on the crystal structure is increased sufficiently, the crystal is permanently deformed after stress is removed. This non-reversible change of shape is called plastic deformation and can be explained using several basic mechanisms: dislocation, slip gliding and strain hardening.

1.2.3.1 Concept of dislocation

The concept of crystal dislocation was firstly introduced and used to explain the origin of plastic deformation in three independent papers by Orowan (1934), Polanyi (1934) and Taylor (1934). It has been experimentally proved that imperfections exist within the ordered atomic arrangement in real crystalline networks. These irregularities may appear in form of point defects (e.g. vacancies, interstitials or a precipitates), line defects (e.g. dislocations), or planar defects (e.g. twinings, grain boundaries) (Fig.1.4).

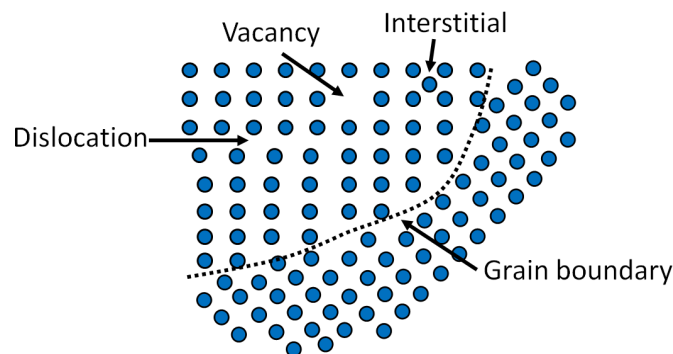


Figure 1.4: Schematic diagram of defects in crystalline networks

A dislocation is a line defect in a perfect lattice around which atoms are misaligned. As disclosed in some publications (e.g. Friedel (1964); Jaoul (1965); Hull

and Bacon (2001)), according to the experimental observation through Transmission electron microscopy (TEM), plastic deformation starts when the dislocation movement occurs. In fact, the dislocation moves by the breaking of atomic bonds and shifting of the atoms through interatomic distances (Fig.1.5). In other words, plastic deformation of a single crystal takes place only when a sufficiently large strain is applied to initiate this dislocation motion, which is also called a slip.

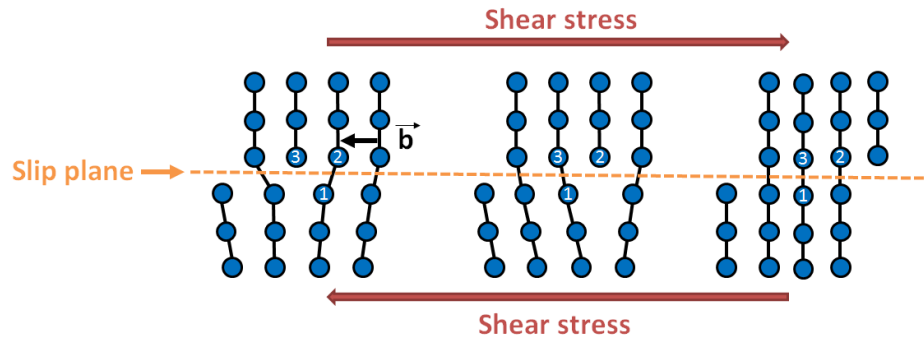


Figure 1.5: Schematic diagram of slip

1.2.3.2 Slip system and introduction of Schmid law

Schmid law postulates that a slip system is activated only when its resolved shear stress τ^s applied on the slip system reaches its critical shear stress τ_c^s .

In order for the dislocations to move along their slip system, a shear stress should be applied to overcome the resistance to dislocation motion. For a FCC metal, slip occurs along the close packed planes containing the greatest number of atoms per area, and in close-packed directions, containing most atoms per length (Fig.1.6). There are 4 close-packed $\{111\}$ planes and 3 close-packed directions of the form $\langle 110 \rangle$ within each plane, giving a total of 12 slip-systems (Tab.1.2).

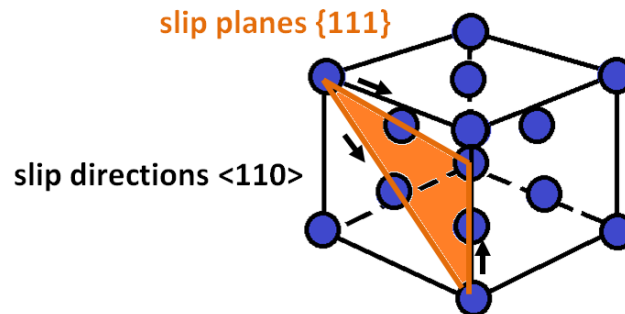


Figure 1.6: Schematic diagram of slip system in a FCC crystal.

Schmid factor (SF) is a tool to describe the critical resolved shear stress τ^s acting in the slip direction of a crystal. Suppose a unidirectional stress is applied to

Slip planes {h k l}	Slip directions <h k l>	Slip planes {h k l}	Slip directions <h k l>
1 1 1	-1 0 1	-1 1 1	0 -1 1
1 1 1	0 -1 1	-1 1 1	1 1 0
1 1 1	-1 1 0	-1 1 1	1 0 1
1 -1 1	-1 0 1	1 1 -1	-1 1 0
1 -1 1	0 1 1	1 1 -1	1 0 1
1 -1 1	1 1 0	1 1 -1	0 1 1

Table 1.2: 12 slip-systems in a FCC structure: 4 close-packed {111} planes and 3 close-packed directions of the form $\langle 110 \rangle$ within each plane.

a single crystal as shown in Fig.1.7, the slip plane $\{hkl\}$ and slip direction hkl to loading axis can be oriented by defining angles λ and Ψ . λ is the angle between the slip direction and the loading axis, and Ψ is the angle between the normal to the slip plane and the loading axis. So that the critical resolved shear stress τ_c^s acting in the slip direction of a crystal can be described by a Schmid factor ($SF = \cos\Psi\cos\lambda \in [0., 0.5]$) (Fig.1.7) and it can be calculated using formula (1.7). The first activated slip system of each crystal will be the system with the greatest Schmid factor. The resolved shear stress in different directions of a crystal may become favourable to activate the slip system if it is close to 0.5.

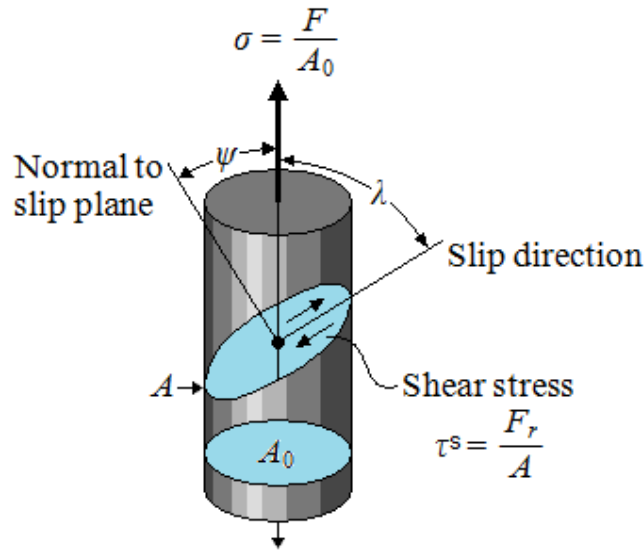


Figure 1.7: Schematic diagram of a resolved shear stress τ_r produced on a slip system. (Source: <http://www.engineeringarchives.com>)

$$\begin{aligned}\tau_c^s &= \sigma \cos\Psi \cos\lambda \\ &= \sigma \times SF\end{aligned}\tag{1.7}$$

1.2.3.3 Strain hardening

In addition, the value of τ_c^s may increase because extra stress is required to overcome different barriers which restrict the dislocation motions, e.g. Peierls-Nabarro stress required to move a dislocation within a plane of atoms in the unit cell (Fig.1.5), interaction of dislocations when mobile dislocations encounter non-mobile ones (forest of dislocations) (Fig.1.8), precipitates, grain boundaries, etc.

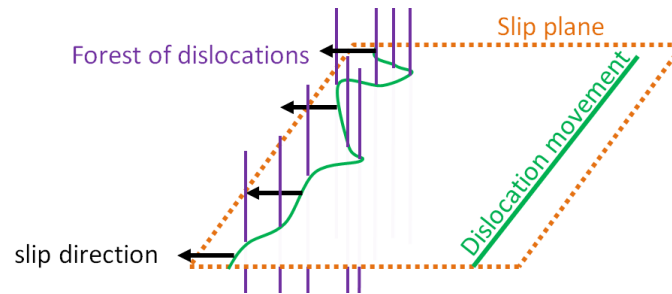


Figure 1.8: Schematic diagram of interaction between mobile dislocations and forest of dislocations.

In FCC structure, forest of dislocations is the pre-barrier restricting the movement of dislocations. One of the predominant mechanisms of the formation of the dislocation forest, using the expression by Frank and Read, is the production of dislocations when a sufficiently significant plastic deformation of a crystal takes place (Fig.1.9). A section of the dislocation is first blocked by any barrier (e.g. precipitates, non-mobile dislocations, grain boundaries, etc.) pinned at two points within a crystal lattice. The section is then bent under the influence of the external force and successively grows until the closed dislocation loop is formed and separated. The section is regenerated again at its initial position (two pinned points). This progressive increase of the number of non-mobile dislocations in crystal can be presented using the evolution of the dislocation densities ρ^s . The cumulation of this effect results in an increase of the value of τ_c^s and such evolution is perceived as strain hardening (Fig.1.10).

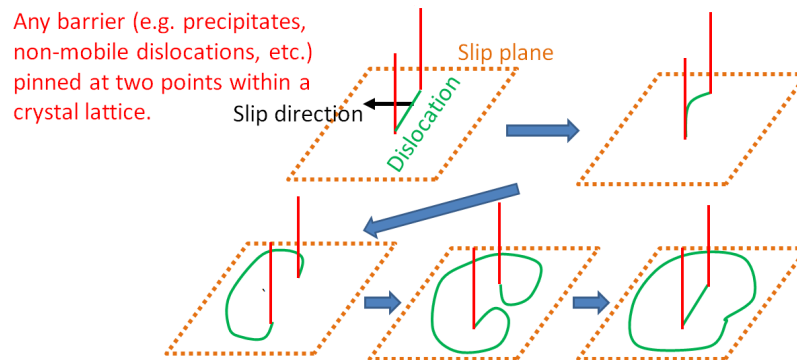


Figure 1.9: Schematic diagram of a Frank-Read dislocation source.

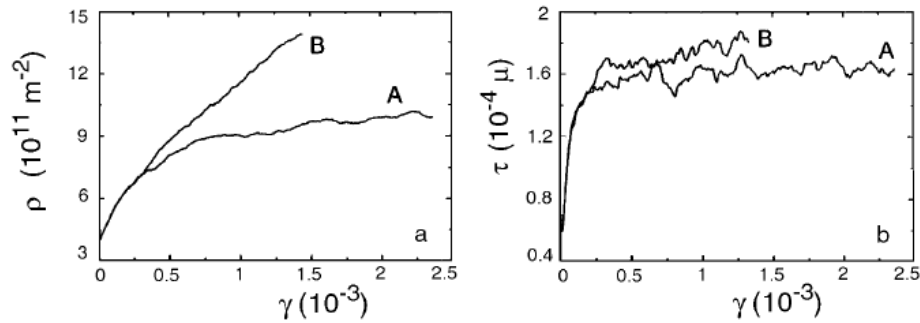


Figure 1.10: Numerical simulation of strain hardening during deformation of an aluminium crystal by taking into account the interaction between dislocations: a. dislocation density vs. shear strain and b. shear stress vs. shear strain. A and B represent the curves obtained by considering with and without cross-slip respectively. [Kubin and Devincere (1999)]

1.2.3.4 Heterogeneity of a polycrystalline sample during plastic deformation

When loading is applied to a polycrystalline sample, the grains having a crystallographic orientation favourable to activate slip system along the loading direction deform earlier than others. These different instants of plastic deformation give heterogeneous plastic strain in an aggregate under the same loading level.

Moreover, although SF gives an indication of the grains which may be more/less intensively deformed during loading, it is not sufficient to predict an exact value of stress locally. In fact, the heterogeneous behaviour of an aggregate or inside a crystal depends mostly on the neighbouring grain texture (crystallographic orientation). If we consider a grain with a high SF value but the surrounding grains are less likely to deform, a heterogeneous stress distribution within the grain can be obtained. For instance, we can get a gradient of strain with high strain concentration in the grain center but low strain level at the grain boundary.

Last but not least, this heterogeneity of strain changes throughout the plastic deformation because of the strain hardening.

1.3 Polycrystalline aggregates Modelling

Now, if we want to answer the question risen in section 1.1, a polycrystalline aggregates model linking the macroscopic response with the microscopic behaviour fits our research need very well.

1.3.1 Crystal plasticity constitutive equation

Based on the physical mechanisms of materials in previous section, crystal plasticity constitutive equations were developed. The presented crystal plasticity behaviour

law model in this section was used in several theses (Schwartz et al. (2010); Mu (2011); De Jaeger et al. (2012)). This model is based on the hypothesis of small elastic deformation and large rotations of the crystal lattice formulated by Peirce et al. (1983), Tabourot (1992) and Teodosiu et al. (1992). It is not the only example for crystal plasticity constitutive equation but a consensus developed for this type of behaviour law based on dislocation density.

1.3.1.1 Elastic behaviour

The elastic behaviour of aluminium is assumed to be isotropic thanks to its small anisotropy ($\alpha_{anisotropy} = 0.8 \approx 1$). There are only two parameters, Young's modulus \mathbf{E} and Poisson's ratio ν , to describe the elasticity, so C_{11}^e , C_{12}^e and C_{44}^e can be directly written as:

$$\begin{cases} C_{11}^e = \frac{E(1-\nu)}{(1+\nu)(1-2\nu)} \\ C_{12}^e = \frac{E\nu}{(1+\nu)(1-2\nu)} \\ C_{44}^e = \frac{E}{2(1+\nu)} \end{cases} \quad (1.8)$$

1.3.1.2 Viscoplastic behavior

Work hardening is due to interactions between dislocations moving within the general condition given by Schmid law. There is a plastic flow if the resolved shear stress τ^s applied on the slipping system \mathbf{s} is equal to its critical shear stress τ_c^s :

$$|\tau^s| - \tau_c^s = 0 \quad (1.9)$$

where τ^s can be calculated using the macroscopic stress $\bar{\sigma}$ applied on the slipping system with the normal of the slipping plan n^s and the collinear unit Burgers vector \vec{b} :

$$\tau^s = (\bar{\sigma} \vec{n}^s) \cdot \vec{m}^s \quad (1.10)$$

The evolution of the τ_c^s associated with every \mathbf{s} involves the dislocation densities ρ^u corresponding to each system \mathbf{s} , and the interaction matrices α^{su} of the FCC or BCC materials proposed by Franciosi (1984). Expressed together with the coefficient of isotropic shear strain μ and the norm of Burgers vector b , τ_c^s is written as:

$$\tau_c^s = \tau_0 + \mu \times b \sqrt{\sum_u \alpha^{su} \rho^u} \quad (1.11)$$

and the flow rule becomes:

$$\begin{cases} \dot{\gamma}^s = \dot{\gamma}_0^s \left(\frac{\tau^s}{\tau_c^s} \right)^n, & \text{if } |\tau^s| \geq \tau_c^s \\ \dot{\gamma}^s = 0, & \text{if } |\tau^s| < \tau_c^s \end{cases} \quad (1.12)$$

$\dot{\gamma}_0^s$ is the initial slip rate of each \mathbf{s} while n is the coefficient of stress sensitivity. Finally, the evolution of the dislocation densities ρ^s associated with each \mathbf{s} can be expressed together with the parameters related to the production of dislocations K and the annihilation distance y_c :

$$\dot{\rho}^u = \frac{\dot{\gamma}^s}{b} \left(\frac{\sum_u \rho^u}{K} - 2y_c \rho^s \right) \quad (1.13)$$

1.3.2 Establishment of a polycrystalline model linking the macroscopic response with the microscopic behaviour

The crystal plasticity constitutive equations allow one to predict the changes of microstructure (e.g. disorientation of grains, phase transformation, pile-ups of dislocation, etc) of a crystalline material under thermomechanical loading. As a result, the origin of strain and stress heterogeneities would be likely figured out [Saai (2008); Saai et al. (2010); Badulescu et al. (2011); Evrard et al. (2010b)]. In other words, the local mechanical behaviour of that material can be predicted such as the local disorientations due to forming [De Jaeger et al. (2012)] or the localisation of the plastic deformation which leads to crack initiation in fatigue (Fig. 1.11) [Schwartz et al. (2010); Li et al. (2012)].

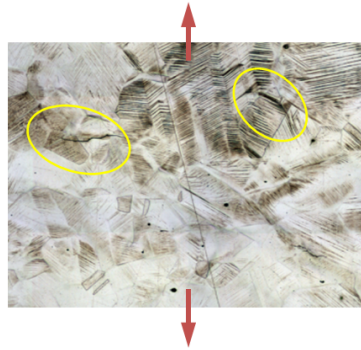


Figure 1.11: Crack initiation in fatigue due to the localisation of the plastic deformation [Li et al. (2012)].

Meanwhile, the identification of their parameters is generally performed by comparison of the mean behaviour (behaviour of the volume element) to the macroscopic experimental one. However, the distribution of local stresses and strains can be very different from the experimental ones, and this method does not allow us to control it. Moreover, the parameters of these models are difficult to identify, because the mechanisms they describe are at a small scale and are thus complicated to measure

directly (e.g. evolution of dislocation density, strain hardening, pile-ups at grain boundaries, changes in dislocation microstructures, etc.). Identification of the parameters of these models is usually performed by inverse method from macroscopic tests curves [Evrard et al. (2010a); Guilhem et al. (2013)]. In order to establish a polycrystalline model linking both the macroscopic response measurement and the microscopic behaviour prediction, there are two feasible approaches.

The first approach uses the self-consistent method based on [Eshelby (1957)] and [Kroner (1958)] works — the mechanical behaviour is described using a micromechanical model, where grains are considered as inclusions embedded in the homogeneous equivalent medium [Lebensohn and Canova (1997); Molinari et al. (1997); Abdul-Latif et al. (1998); Evrard et al. (2008)]. In this approach, texture and elongation ratio of grains can be taken into account. Yet, neither a specific shape of the grains nor specific grain boundary misorientation is dealt with. One of the advantages of this approach is, as stresses and strains are considered homogeneous per grain, the calculations are fast. This approach allows one for simulations over long periods of time (fatigue, creep), to have a detailed description of the texture of the material (i.e. thousands of crystal orientations can be used to describe the experimental texture). This moderate-cost calculation also allows one to use this approach to define a local law of behaviour at each point of Gauss of a finite element calculation. However, this approach does not allow one to take specific local configurations into account, such as a specific form of grain, the various grain sizes or the groups of neighbouring grains with particular orientation/disorientation. This approach is indicated particularly for considering only the average behaviour of a material, but not the response of either a particular crystalline aggregate nor a observed variance on the particular set of configurations.

Another approach consists in modelling representative 3D polycrystalline aggregates, which can be obtained experimentally by FIB-SEM serial-sectioning or by tomography [Cédât et al. (2012); Ludwig et al. (2009)] or by Voronoi tessellation (CVT) [Barbe et al. (2001a,b); Brahme et al. (2006); St-Pierre et al. (2008)]. In order to account for the mean behaviour of the material, it is necessary to meet a sufficient number of configurations (e.g. grain orientations and positions, grain neighbourings and shapes). These configurations can be met in a unique aggregate if it is sufficiently large (the Representative Volume Element, RVE) or in several smaller aggregates. The mean behaviour of these small aggregates, if not too small, converges to the behaviour of the RVE [Kanit et al. (2003)]. This method, although the calculations are more time-consuming, allows to take specific characteristics of the microstructure (realistic shape of the grains, specific neighbouring misorientation, percolation of one or several phases, etc.) into consideration.

These two methods allow to simulate the macroscopic stress-strain response and to perform the parameter identification by comparison with experimental measurements.

1.4 Local mechanical measurement

However, minimising a cost function (the difference between experimental and calculated data) based on macroscopic measurements may lead to local minima, and not to a global one. The validity of such an identification is thus generally limited to the experimental tests used during the identification stage. In order to increase the robustness of the identification, it is necessary to give a physical meaning to the parameters. To accomplish this, local experimental data at the grain scale can be used. The richness of the data provided by the experimental fields measured on the surface of the specimen should allow one to constrain the values of the parameters to be identified.

In order to yield an experimental database sufficient for parameter identification, the best way is to develop a procedure to access the coupling nature quantities, e.g. stress-strain (σ - ε), strain-energy (ε - \mathbf{Q}) or even stress-energy (σ - \mathbf{Q}), at different points of the monocrystal. Thus, the questions about the possibility of accessing these quantities as completely as possible and the corresponding practical measurement method should be thought thoroughly. The thesis research highlights principally in this particular objective and the methods of accessing these quantities are going to be described in this section.

1.4.1 Total strain field measuring methods

Digital correlation image method (DIC), Moiré fringe method and grid method provide full-field displacement/strain measurement between several successive states.

1. Digital image correlation

The digital image correlation DIC is a $2D$ or $3D$ method for measuring the displacement field between two images of the same region of the sample successively taken by a camera [Sutton et al. (2000)]. For this, a speckle pattern painting has to be applied on the sample surface excepted for samples with natural contrast. During the mechanical test, images of the deformed sample surface are taken regularly. The movement of the grey value pattern in the deformed image is tracked in small local neighbourhood facets and the displacement field can be calculated (Fig.1.12). Hence, a total strain field could be derived. DIC enables the total strain field measurement far into the range of plastic deformation (Fig.1.13) and a large number of applications can be found in literature in this context [Lucas and Kanade (1981); Sutton et al. (1983); Chu et al. (1985); Kahn-Jetter and Chu (1990); Allais et al. (1994); Luo et al. (1994); Helm et al. (1996); Mazza et al. (1996); Mitchell et al. (1999); Doumalin (2000); Tatschl and Kolednik (2003); Sutton et al. (2006, 2007a); Saai (2008); Bourcier (2012); Guery (2014)].

2. Moiré fringe method

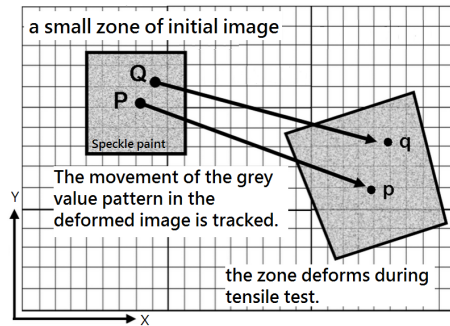


Figure 1.12: Scheme of digital image correlation method (DIC) for total strain field measurement. The movement of speckle pattern painting in the small local neighbourhood facets is tracked [Sutton et al. (2007b)].

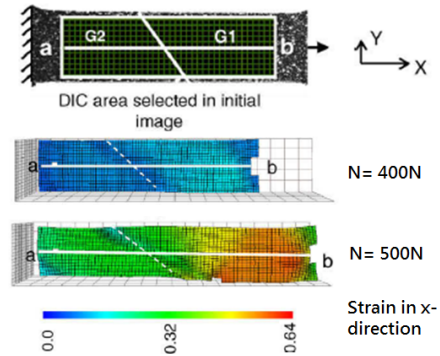


Figure 1.13: Total strain field measurement of a bi-crystal (G1 & G2) sample under a tensile loading of 400N and 500N using DIC method [Saai et al. (2010)].

This method makes use of Moiré effect to measure surface strain. Moiré effect is the optical interference of light by superimposing a fringe pattern or grating which varies in line spacing or rotation (Fig.1.14). The pattern of broad dark lines, Moiré pattern, can be used as a gauging signal to perform accurate displacement measurement [Post (1968)]. In practice, an active grating is attached on the surface of the sample. The grating deforms together with the test sample and when an undeformed (reference) grating superimposes onto it, a Moiré pattern depicting the nature and the magnitude of the deformation field is obtained. Since the Moiré pattern is a full field representation of the relative displacement between the gratings (Fig.1.15), it is an excellent tool for observing and quantifying the gradients in local deformation, e.g. Tang et al. (2012).

3. Grid method

Grid method makes use of grid markings, either applied as a fine regular array of dots or lines (Fig.1.16), on the sample surface as strain gauge to measure local displacement before and after deformation. Images of the grid-lines after deformation are captured at each loading level to reveal the total strain field [Dally and Riley (1978); Dürr (1991)]. Comparing with fringe method and DIC method, grid method allows an accurate and direct strain measurement under large deformation [Goldrein et al. (1995)].

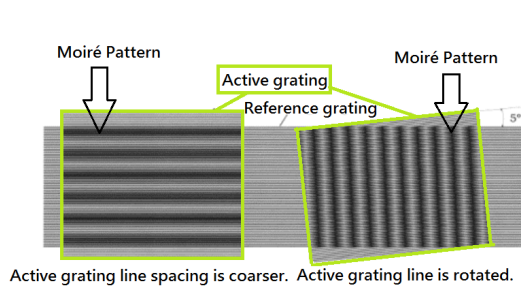


Figure 1.14: Scheme of Moiré effect. A Moiré pattern is formed by superimposing two sets of parallel lines. The pattern of broad dark lines is used as a gauging signal to measure displacement (Source: [Gungor (n.d.)], The Open University of UK).

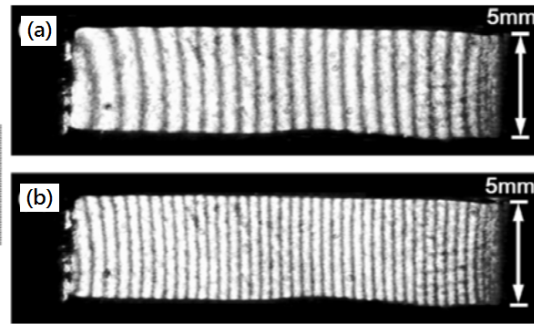


Figure 1.15: Moiré fringes of an aluminum sample under a Moiré interferometer in loading experiment (in horizontal direction). Displacement fields are indicated by the Moiré fringes under load of (a) 180 N and (b) 300 N. Each Moiré pattern represents a equal distance of 833 nm [Tang et al. (2012)].

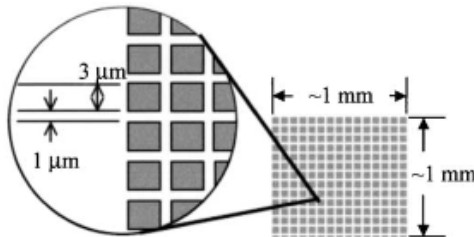


Figure 1.16: Example of grid [Schroeter and McDowell (2003)].

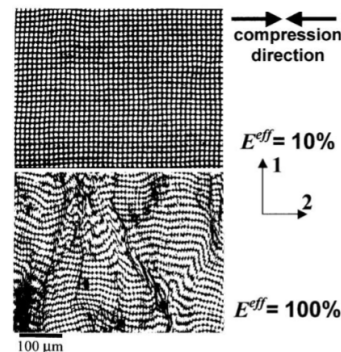


Figure 1.17: A sample is subjected to compression at different effective strain E_{eff} levels. The movement of the grids show a strong heterogeneity of deformation [Schroeter and McDowell (2003)].

1.4.2 Elastic strain field measuring methods in a single crystal

Several methods allow local elastic strain assessment in a single crystal, e.g. X-ray diffraction (XRD) [Eberl (2000)], Kossel microdiffraction [Bouscaud et al. (2014b)], Laue microdiffraction [Robach et al. (2011); Petit et al. (2012)] or hole-drilling method [Baldi (2014)]. Since there are three methods making use of diffraction to determine the elastic strain, the application of Bragg's law is firstly presented. Then, the measuring principles of Kossel microdiffraction and Laue microdiffraction

tion method are introduced afterward. Followed by, the hole-drilling method is presented. At the same time, the advantages, disadvantages and limitations of these methods are mentioned. Later, an explanation of our choice of methods is made to conclude this subsection.

1. X-ray diffraction

When X-ray is sent to a crystalline material, the signal received by the captors allows to know the distance between atomic planes. Since the atomic planes in unstrained solids are spaced at a distance that corresponds to a minimum energy, when the material is deformed elastically, this distance changes and energy increases, producing a restoring force. The interaction is often modelled as the Lennard-Jones potential assuming the distance variation between atom is linear to the applied force (recall §1.2.2.1). Thus, the distance variation between atoms (or the interreticular plane distance d_{hkl}) can be used as a gauge to measure the local elastic strain ε^e applied on the crystal (Fig.1.18). The Bragg's law (Eq.1.14) shows the relationship between X-ray wavelength λ , inter-reticular distance d_{hkl} and diffraction angle θ_{hkl} :

$$d_{hkl} = \frac{\lambda}{2\sin(\theta_{hkl})} \quad (1.14)$$

where θ is the diffraction angle and λ is the wavelength of the X-ray source.

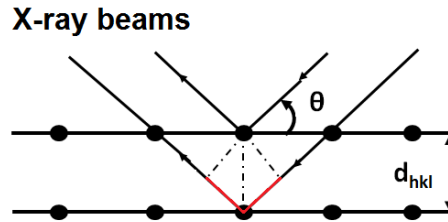


Figure 1.18: Relationship between X-ray wavelength λ , inter-reticular distance d_{hkl} (distance between atoms) and diffraction angles θ .

For d_{hkl} measurement by X-ray diffraction, the single crystal is mounted on a wafer holder in a goniometer and rotated according to its crystallographic directions, normal to a monochromatic X-ray beam ($\lambda = \text{constant}$ and in the range of 0.01 to 10 nm). To make the correct θ_{hkl} for reflection of the monochromatic incident beam, the crystal and a 1D punctual detector move until the diffracted signal is received at its maximum intensity (Fig.1.19).

Differentiating Eq.(1.14) by using the product rule, we get:

$$\varepsilon_{hkl} = \frac{\delta d_{hkl}}{d_{hkl}} = -\cot\theta_{hkl} \cdot \delta\theta_{hkl} \quad (1.15)$$

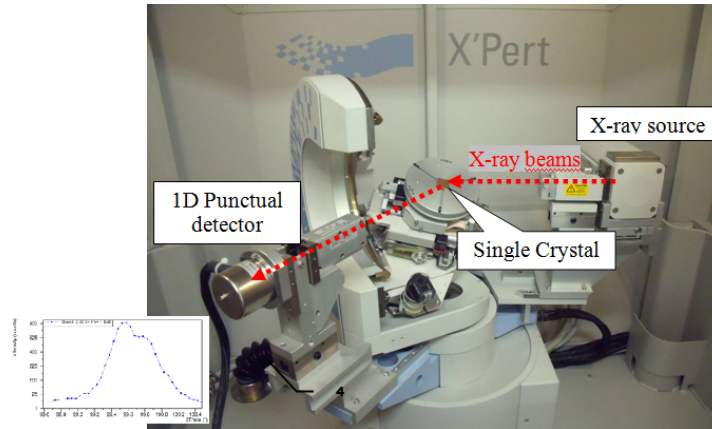


Figure 1.19: Principle of X-ray Diffractometer

Therefore, if d_{hkl} increases (which corresponds to a tension state, $\varepsilon_{hkl} > 0$), $2\theta_{hkl}$ of the peak decreases with respect to its initial position (Fig.1.21), and vice versa.

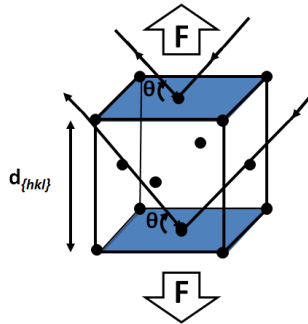
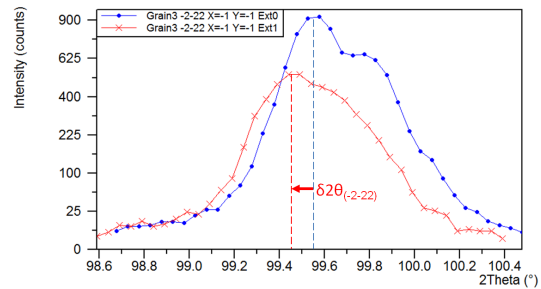


Figure 1.20: Scheme of X-ray diffraction method.

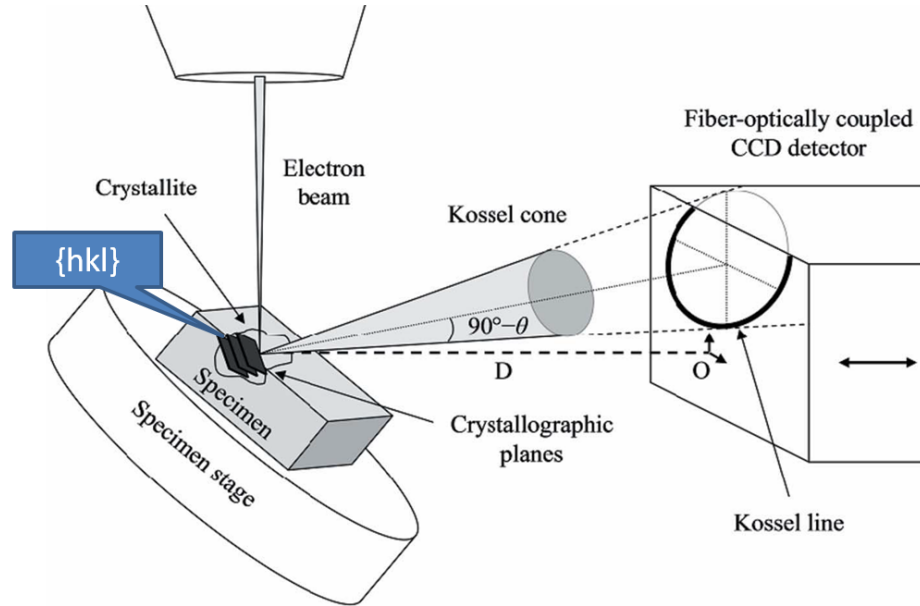
Figure 1.21: $2\theta_{(-2-22)}$ of Grain3 ($X=-1, Y=-1$) in its initial state (blue) and at $\bar{\varepsilon}_{xx}^t = 7.4 \times 10^{-3}$ (red).

The signal intensity obtained has always a high signal to noise ratio (e.g. ≥ 60) which increases the accuracy of d_{hkl} measurement. However, since the accessibility of θ_{hkl} by a standard goniometer is $10^\circ \leq \theta_{hkl} \leq 80^\circ$, a limited number of $\{hkl\}$ planes can be taken into account when calculating elastic strain. For instance, the measurable $\{hkl\}$ planes for a FCC crystal are $\{111\}$, $\{200\}$, $\{220\}$, $\{311\}$, $\{222\}$, $\{400\}$, $\{331\}$, $\{420\}$, $\{422\}$ and $\{511\}$. It is also known as a large angle X-ray scattering method.

2. Kossel microdiffraction

For d_{hkl} measurement by Kossel microdiffraction, the single crystal is placed in a scanning electron microscope (SEM) with emission of monochromatic X-ray source ($\lambda = \text{constant}$ in the range of 1 to 10 nm) and a 2D charge coupled

detector (CCD). The X-ray diffracted by a stack of crystallographic planes with hkl spacing is captured by a planar detector, a conic pattern (Kossel line) can be recorded (Fig.1.22) [Bouscaud et al. (2014b)].



D: Specimen-to-detector distance

O: Pattern center

SEM chamber

Figure 1.22: Principle of Kossel microdiffraction [Bouscaud et al. (2014b)]

Since the dimension of the Kossel cone is a function of diffracting angle θ_{hkl} (Fig.1.23), the variation of its diameter can indicate the δd_{hkl} during deformation (See again Eq.1.15).

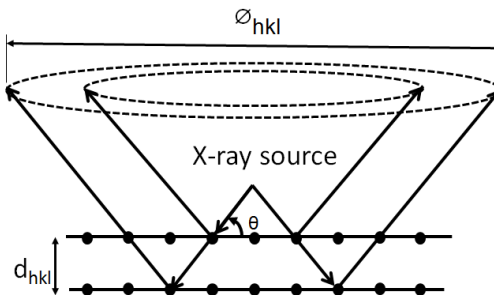


Figure 1.23: Illusion of the diffracted X-ray signal captured by a 2D detector. The signal forms a conic pattern (Kossel line) with the diameter indicating the distance between diffracting planes.

Kossel microdiffraction is also known as a small angle X-ray scattering method because the diffracting angles of hkl are $1^\circ \leq \theta_{hkl} \leq 2^\circ$ using SEM. As soon

as there are $\{hkl\}$ planes diffracted, elastic strain tensor can be calculated. Therefore, a large variety of $\{hkl\}$ planes can be taken into account and it enhances the sensibility to elastic strain level. For instance, only 11 Kossel cones are needed to reach the precision of strain measurement up to 2×10^{-4} [Bouscaud et al. (2014a,b)]. Moreover, Kossel microdiffraction allows to access the local information of crystal with dimension from $1\mu\text{m}$ to several mm. It allows to map the strains/stresses and orientation of crystallites simultaneously. On the downside, the signal intensity obtained has a weak signal to noise ratio [Bauch et al. (1999)]. To obtain a clearer Kossel signal, a superposition of 5-20 frames (with an acquisition time of 10-30s per frame) is required for each measurement to obtain sufficient image contrast. In addition, due to the existing resolution of EBSD camera and the artefact of the captured image, Kossel line positions can hardly be determined precisely. The strain tensor calculated using this method is based on three assumptions — the shifts of Kossel patterns are assumed to be caused only by strain but not by the presence of mosaicity, there are only small orientation change between initial and deformed states, and the change of pattern center and pattern-to-detector distance is negligible [Morawiec (2014)].

3. "Rainbow" method using laue microdiffraction [Robach et al. (2011)]

For d_{hkl} measurement by "Rainbow" method using Laue microdiffraction, a microbeam of white radiation (polychromatic X-ray with energy spectrum varying from 5 to 22keV) is sent to sample surface and the diffracted signal captured by a 2D charge coupled detector (CCD), so that the spot (photon) energy (E) of the diffracted signal and the Laue pattern can be recorded simultaneously for strain tensor calculation (Fig.1.24).

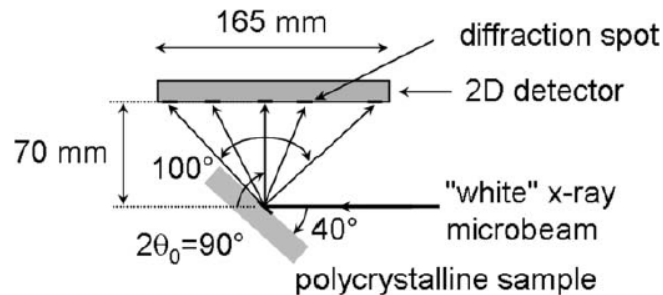


Figure 1.24: Experimental geometry of "Rainbow" method using Laue microdiffraction for elastic strain measurement [Robach et al. (2011)].

During deformation, d_{hkl} changes and the λ and θ_{hkl} of the diffracted x-ray beam varies. The relation between wavelength ($\lambda \neq \text{constant}$) and energy is described as follows:

$$E = \frac{hc}{\lambda} \quad (1.16)$$

where h is Planck's constant and c is the speed of light. Differentiating Eq.1.14 and Eq.1.16 by using the product rule, we have

$$\varepsilon_{hkl} = -\cot\theta_{hkl} \cdot \delta\theta_{hkl} - \frac{\delta E}{E} \quad (1.17)$$

Since the accuracy of elastic strain depends more on the term of the change of energy ($\frac{\delta E}{E} \approx \times 10^{-4}$) rather than the term of change of diffracting angles ($-\cot\theta_{hkl} \cdot \delta\theta_{hkl} \approx \times 10^{-5}$) [Robach et al. (2011)], Eq.1.17 can be simplified as

$$\varepsilon_{hkl} = -\frac{\delta E}{E} \quad (1.18)$$

This is an indirect method using the change of energy during deformation to calculate elastic strain. The entire measuring time of Laue microdiffraction takes only 5s and a significant signal-to-photon-noise ratio of about 600 at saturation can be achieved. However, limited by existing experimental set-up nowadays, the maximum range of white beam the energy spectrum can only vary from 1 to 22keV and the best achieved accuracy of the elastic strain using this method $\approx \times 10^{-4}$ [Petit et al. (2012)].

4. Hole-drilling method

Hole-drilling method is a mechanical strain relaxation (MSR) technique. A small blind hole (in μm) is made in the surface area of interest and the locked-in stress is released. Then, the in-plane (longitudinal) and out-of-plane (axial) elastic strain can be obtained using either strain-gauge [Rendler and Vigness (1966)] or digital image correlation [Baldi (2014)] (Fig. 1.25-1.26).

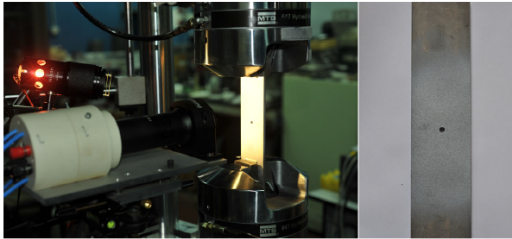


Figure 1.25: Experimental setup for residual stress measurement using hole drilling and integrated digital image correlation techniques [Baldi (2014)].

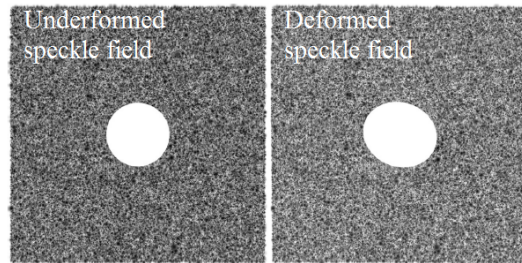


Figure 1.26: Illusion of speckle field around the drilled hole before and after stress relaxation [Baldi (2014)].

However, this is a semi-destructive method on the surface for elastic strain measurement. Also one drilled hole is used for every loading level and it cannot be reused to provide a continuous local response for other loading levels. Therefore, this method is not considered in our study. Moreover, its application in an anisotropic monocrystal is still not guaranteed [Glacet (2015)]. The strain tensor is calculated using an inverse method based on finite element simulations of the drilling. A converged result can only be achieved for isotropic materials but not for anisotropic one.

1.4.3 Energy or heat dissipation measuring method

The dissipated energy Q can also be quantified during the mechanical loading, by measuring the amount of heat emitted locally with a 2D-infra-red camera and then using the local results to identify behaviour law [Chrysochoos (1987); Chrysochoos and Louche (2000); Bodelot (2008); Chrysochoos et al. (2008); Saai (2008)]. However, difficulties under several experimental conditions have to be first overcome to succeed the measurement. Measurements have to be carried out in real time during experiments, which is, for the moment, not compatible with ε^e measurements with crystal diffraction. However, the access to a local heat measurement is still a challenge [Bodelot (2008)]. There are three types of difficulties for applying this measuring method:

1. Difficulty related to measuring time
Heat dissipation in metallic material is a quite rapid homogenisation process as the variation of temperature during cold deformation is small (within one degree) (Refer to the two examples in Saai (2008)) and instantaneous. Also, during the heat measurement, the speckle pattern applied on the sample surface should be compatible with both DIC and IR measurement [Bodelot (2008)]. All these make the measurement at grain scale even more difficult.
2. Difficulty related to experimental background and data accessibility
The quantity of intrinsic heat of our sample throughout the deformation is sought and measured. However, this quantity is even smaller than the heat radiated by its experimental background. As a result, the experimental environment should be perfectly isolated [Chrysochoos and Louche (2000); Chrysochoos et al. (2008)]. Moreover, several elements have to be taken into account when we want to conduct several measurements simultaneously. For example, if ε^t - Q fields are measured at the same time, the optical and infra-red cameras should be positioned differently (with an angle shift) without bothering the measurement of each another, so that the diffracted beams of each measurement could be separately captured. In this case, the zone(s) of interested are distorted and the accessed data should be amended before usage.
3. Difficulty related to the infra-red (IR) camera calibration
When measuring temperature by IR thermal imaging, the emissivity of the sample surface has to be constant to guarantee the quality of the captured heat

[Saai (2008)]. However, this ideal situation is very difficult to achieve. The emissivity depends on the surface roughness, material or coating nature of the analysed sample but these parameters may change during the experimental test, e.g. surface roughness of aluminium alloy sample change remarkably along the mechanical loading because of the anisotropic behaviour of grains.

1.4.4 Choice of the local mechanical informations

For the quantities that we may access nowadays, the kinematic quantities can be achieved by measuring the displacement or total strain field of a material under loading. In the existing literature, we see that measuring the ε^t field is very widespread. For the stress quantities, however, it is impossible to measure them directly. As a result, we "fall-back" to measure ε^e . From ε^e , it will be possible to reconstruct σ , knowing the Hooke's law. Another possibility is to quantify the energy dissipated Q during the loading. We observe that the technical skill for measuring Q locally are still incompatible with those of the ε^e measurement. For example, the measurement cannot be conducted at several loading levels. It is because the measurement of the change of heat energy can only be recorded in a continuous loading whereas ε^e measurement has to be done at successive loading levels and takes a long time to each level. Moreover, measuring various quantities on the same specimen under loading means different device around the specimen to impose the loading and measure every quantity. It was not possible to position a CCD camera, an IR camera and a diffraction device around the specimen. Only two of them could be selected. Therefore, we have chosen to focus on ε^t and ε^e full-field measuring method which allows a direct measurement of the behaviour law.

Meanwhile, these information should be obtained through either surface or volume measurement. Since 3D representative polycrystalline aggregates modelling would be used for microstructural calculation to identify the behaviour laws, mastering the strain fields of the grain in form of 3D is indispensable. Until now, a 3D local micromechanic response mapping using large infrastructure to validate crystalline plasticity model is still absent. So, by knowing these local answers on grains surface and extruded throughout a thickness is the solution we worked for.

1.4.5 Choice of the measuring methods

During our research, the studied total deformation is smaller than 5% ($\varepsilon_{xx}^t = 3.56\%$ in the experiment of sample 1 and 4.23% of sample2). Digital image correlation is sufficiently sensitive (up to $\pm 4 \times 10^{-4}$) to small total strain. Moreover, from a practical point of view, depositing a speckle is much easier than a grid or fringe pattern. The required apparatus is relatively simple to be integrated with elastic strain measurement comparing with the two other options — only a camera installed perpendicularly in front of the sample surface is needed.

X-ray diffraction method is a direct, non-destructive and effective way to measure the evolution of d_{hkl} , it avoids the complexity of signal calibration and inaccuracy generated by distorted image or indirect energy converting method. Also,

when sample is deformed plastically, XRD still enables the measurement under the rotation of grain.

The accessibility of measurements by these two techniques are the most appropriated options to achieve our experimental needs.

1.5 Identification procedure

Upon the determination of the crystalline plasticity model, the establishment of a polycrystalline model and collection of experimental data, methods of comparing the simulated results with experimental measurements are needed. In addition to the local measurement of variables $\sigma - \varepsilon$, this research is intended as a contribution to allow identification of a crystalline constitutive equation.

1.5.1 Type of variables

Observable variables, internal variables and material parameters are essential elements for constitutive equation identification.

The observable variables are the experimental data. They are usually prescribed and can be the macroscopic or microscopic response of a material during mechanical test. For example, during a uniaxial/multiaxial loading, the variables of macroscopic response are the average stress ($\bar{\sigma}$) applied on the material under the control of average strain ($\bar{\varepsilon}$). At the same time, there are several microscopic responses of the material which can be measured, such as the rotation of the crystal texture, the evolution of temperature and the local strain ($\varepsilon_{11}, \varepsilon_{12}, \varepsilon_{22}$) obtained on the sample surface as well as the local strain ($\varepsilon_{ij}, i=1,2,3, j=1,2,3$) supposed could be soon accessed by tomography in the sample volume.

The material parameters can then be identified using the observable variables and the chosen constitutive equation. These values allow to reach back certain internal variables afterwards. In the case of the involvement of strain-hardening, the internal variables, like the position shift of the yield surface for kinematic hardening or the size changes of the yield surface for isotropic hardening, can be quantified. These quantified internal variables will contribute to the experimental database.

1.5.2 Identification strategies

In many situations, some of the input data (e.g. parameters of the behaviour law, boundary conditions, etc.) of the model cannot be measured directly and they have to be sought depending on the response of the model. Therefore, an identification procedure is performed by fitting the simulation results to the experimental data of kinematic fields, namely inverse method. A cost function $\mathcal{F}(\zeta_{num}, \zeta_{exp})$ is introduced to define a norm of the difference between numerical ζ_{num} and experimental quantities ζ_{exp} . These two quantities can be compared at the scale of the grain [Héripré (2006)] either point by point using displacement/strain fields or, by the strain field averaged per grain, or by the strain distribution. The identification makes use of

all of the experimental data. The resulting cost function \mathcal{J}_{res} is a weighted sum of all these terms $\mathcal{F}_k(\zeta_{num}, \zeta_{exp})$ which are the discrepancies ω_k of the synchronised measuring points/zones at different moment of all the experiments (Eq.1.19).

$$\mathcal{J}_{res} = \sum_k \omega_k \mathcal{F}_k(\zeta_{num}, \zeta_{exp}) \quad (1.19)$$

The publications of Avril et al. (2008a) and Grédiac and Hild (2013) overview the recently developed strategies for constitutive parameter identification based on kinematic full-field measurements.

1. Finite element model updating method (FEMU)

The finite element model updating method (FEMU) is based on the minimization of the discrepancy between an actual measurement (either known and predicted forces, or measured and predicted displacement fields) and a finite element simulation (Fig. 1.27). The simulations are performed iteratively until the computed results match the measured ones, then the parameters are identified. It has been applied for microstructural characterization coupling with the experimental data obtained via SEM [Hoc et al. (2003); Guery (2014)] or in front of a camera with a microscopic lens [Kajberg and Lindkvist (2004); Kajberg and Wikman (2007)], etc.

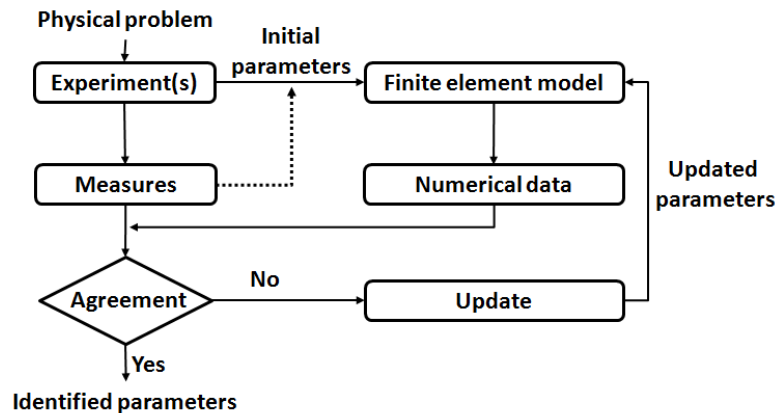


Figure 1.27: Schematic diagram of FEMU identification. [Grédiac and Hild (2013)]

This method owns a high flexibility and capacity to handle a variety of situations and data [Genovese et al. (2006)]. Yet, the accuracy of the method can be seriously affected by incorrect selection of model for the studied material, experimental errors and the non-linear problems of the numerical simulation [Meuwissen et al. (1998); Molimard et al. (2005); Hendricks (1991); Oomens et al. (1993); Van Ratingen (1994); Forestier et al. (2002); Kajberg and Lindkvist (2004); Kajberg and Wikman (2007); Giton et al. (2006)].

2. Constitutive equation gap method (CEGM)

The constitutive equation gap method (CEGM) estimates the errors in the finite element method [Ladeveze and Leguillon (1983)] during model updating. Its principle is minimizing the distance between an given admissible stress and an other stress field computed from experimental displacement field. CEGM has been used for identification of elastic properties [Constantinescu (1995); Calloch et al. (2002); Geymonat et al. (2002); Geymonat and Pagano (2003)] as well as heterogeneous elastoplastic properties and strain energy densities using kinematic field measurements [Chrysochoos et al. (2008); Latourte (2007); Latourte et al. (2008)]. Thanks to the strong and clear physical meaning represented by CEG functionals and their additive character with respect to the structure, the error associated with the identified parameters can be quantified locally.

3. Virtual fields method (VFM)

The virtual fields method (VFM) is based on the principle of virtual work (PVW) applied with correctly selected virtual fields [Grédiac (1989)]. The experimental strain field and the loading conditions are assumed to be known. Once the constitutive model is chosen and virtual fields are selected, a set of scalar equations can be generated by introducing each virtual field into a PVW equation. The solutions obtained in the least square sense are the identified constitutive parameters. VFM has already been applied to identify parameters in the case of elastoplasticity with either numerical [Grédiac and Pierron (2006)] or experimental data [Pannier et al. (2006); Avril et al. (2007); Pierron et al. (2010)] and in the case of viscoplasticity [Avril et al. (2008b)]. However, the error on the stress increment may become larger because of the small associated strains subjected to experimental noise [Pierron et al. (2010)].

In fact, the loading distribution involved in the virtual work identification is difficult to be quantified experimentally [Grédiac et al. (2002)]. Thus, only the measured resultant forces are defined in the virtual fields and the virtual displacement is prescribed as a constant boundary condition along the resultant forces direction. Moreover, the microstructure calculation of aggregates is 3-Dimensional computation and the strain field within the solid has to be known. Thus, in practise, the strain fields are quantified from beam- or plate-like sample surface then they are assumed to be constant or linear through this thickness.

4. Equilibrium gap method (EGM)

The equilibrium gap method (EGM) is based on the discretization of the equilibrium equations. The EGM functional is developed similarly to the one

of VFM except non-zero displacement data on a regular grid resolution is assumed to be available. Therefore, they share the same limitations in terms of experimental strain field. This method can be applied in identification of damage field [Claire et al. (2002, 2004)] because it can only allow to identify relative variation of parameters.

5. Reciprocity gap method (RGM)

The reciprocity gap method (RGM) is based on the Maxwell-Betti reciprocity theorem and it is applicable when mechanical field measurements are available on the whole boundary. The principle of this method is to analyse the difference in reciprocity between the real experimental field and a fictitious solution field without the unknown entities (e.g. cracks, inclusions, etc.). These entities are defined as a set of parameters. They are first calculated from PVW and the RGM functional is defined by applying them in both experimental state and fictitious state. This method is useful in crack identification [Andrieux et al. (1997); Ben Abda et al. (1999); Bui et al. (2004)]. Although this method is simple for identification of constitutive properties, there is still a challenge to conduct a complete kinematic field measurement on the outer boundary of the studied body.

As we use a polycrystalline aggregates model linking the macroscopic response with the microscopic behaviour, FEMU and CEGM are the most appropriate approaches to identify the parameters of crystalline plasticity law using the local mechanical measurements (which will be presented in next section).

1.5.3 Complexity of the model to be identified

The complexity of the model to be identified is also worth discussing. The identification using macroscopic response in a linear or a simple non-linear model is relatively easy and simple, so it has been performed in many works for a long time. However, for complicated non-linear models, it is still a topic of development due to its highly non-linear nature and involvement of many constitutive parameters [Andrade-Campos et al. (2007); Evrard et al. (2008, 2010b,a); Schwartz et al. (2010); Mu (2011)].

For the identification using field measurements in linear models, it has been applied in anisotropic models [Grédiac and Pierron (2006); Pannier et al. (2006); Avril et al. (2008b); Pierron et al. (2010)]. In the case of simple non-linear models (e.g. describing an elasto-plastic behaviour with bilinear approach Latourte (2007)), only few constitutive parameters have to be identified. Until now, there are only two attempts using field measurements to identify parameters in non-linear models [Tran (2013); Guery (2014)]. With these field measurements on the representative volume element, some very complicated models with various phenomena can be identified, e.g. elasto-plasticity, cyclic hardening/softening, aspect of multi-axial/non-proportionality, anisotropy, etc. Yet, sufficient tests are needed to yield

the experimental database for characterising these phenomena. Also, the choice of identification strategy is also a challenge because we have to be thoughtful enough to decide which parameters should be identified in which order or if we can directly measure certain parameters [Pierron et al. (2010); Schwartz et al. (2010)].

In addition, one of the perspective of the research is making use of local full-field measurements of mechanical response to identify these models. Yet, the calculations is not realised in the present work.

1.6 Conclusion

We have presented in this chapter a literature review on crystal plasticity model with microstructure-based mechanical predictions. We have seen the interest of local mechanical responses of a material and the accessibility of these quantities at present. The total and elastic strain fields have been finally chosen thanks to a widespread literature and well-developed technique for their measurements. After comparing the performance and the set-up of several measuring methods, the total strain fields were determined by digital image correlation. For this, a speckle-painting was applied on the sample surface which was tracked to derive the total deformation of the specimen surface under loading. The local elastic strains were calculated from X-ray diffraction measurements. This research is placed in the perspective to allow identification of a crystalline constitutive equation based on the experimental results provided by this study and the necessary conditions were recalled to fulfill this objective.

Material and sample preparation

Chapter 2 is divided into three parts: Material and specimen shape selection (Section 2.1), sample preparation (Section 2.2) and studied samples and their initial microstructures (Section 2.3). The first part presents how a comprehensive consideration of the material selection is conducted so as to obtain the desired mechanical responses and take into account the loading and elongation limits of the micro-tensile machine. The design of sample shape and its specific dimensions are also discussed. In the second part, it is shown how the sample is recrystallised. A further completed initial microstructure of the studied samples and their determining methods are described in the last section.

2.1 Materials

An in-situ experiment is designed specifically to obtain both the total and elastic strain fields simultaneously inside the grains of the sample during a tensile test. Therefore, obtaining the desired experimental results accurately is the main consideration when choosing a studied material as well as the specimen shape. The chosen material and its chemical composition are shown afterwards.

2.1.1 Choice of material

The material is chosen following several criteria.

1. The material should have a simple microstructure.

As we have mentioned in chapter 1, only total and elastic strain fields of a sample are measured. In order to avoid any complicated or particular mechanical responses (e.g. phase transformation due to non-equilibrium conditions in martensite) during the experiment under mechanical loading, a material with single-phase microstructure is preferred. So that the deformation mechanism is principally caused by the movement of dislocations inside crystals (rather than other mechanisms, e.g. twinning). Also, a single-phase material is wanted to avoid the involvement of more than one crystalline plasticity law in our studies. Otherwise, a set of crystalline plasticity behaviour laws will be required in a multiple-phase material [Libert (2007); Libert et al. (2011); Cédât et al. (2012)] and the situation will be more complicated.

Moreover, crystallographic system during sample deformation is no more orthogonal. Hence, materials with cubic lattice is preferable, e.g. FCC and BCC rather than HCP or Triclinic, because it facilitates the transformation of lattice planes from an incalculable direct network to a calculable reciprocal network during follow-up analytical procedure

2. The microstructure of the material should be accessible by XRD - The grain size is optimised.

X-ray diffraction (XRD) is chosen to measure the elastic strain field of each grain on the sample surface. As we want to measure the intragranular gradients of elastic strain, the grain size of the sample should be large enough to enable the X-ray beam to conduct several measurements per grain. Since the minimum size of the X-ray beam emitted by the X-ray diffractometer in our laboratory is in $0.02 \times 0.02 \text{ mm}^2$, it implies the grain size on our sample surface should be at least 1 mm^2 .

In addition, larger grain contain more measuring points and result in a richer intragranular information. Meanwhile, a sample containing 10-50 grains gives not only intragranular information but also an intergranular information as the mechanical answer of a grain is not only affected by its own crystalline orientation [Schmid and Boas (1951)] but also by the surrounding grains with different crystal orientations [Martin et al. (2013)]. So, the chosen material should be capable to produce oligocrystal samples, e.g. Nickel [Eberl (2000)], Copper [Huang (2007)], Aluminium [Saai (2008); Tran (2013)], etc.

3. A Small Young's modulus facilitates the achievement of the desired measurement.

A higher Young's modulus implies a smaller elastic strain field ε^e during the total deformation ε^t (Fig.2.1). In other words, a material with a small Young's modulus shows a larger ε^e and this facilitates the XRD measurement for a given uncertainty. The principle of ε^e measurement and its uncertainty will be further presented in Chapter 3.

The maximum loading capacity of our micro-tensile machine is 1kN. The tensile strength σ_f of the material and the section of the specimen should be selected to respect this limit.

According to the grip system of the micro-machine (see 58), the thickness of the sample should be 0.5-2 mm while the width should be 6-13 mm. The range of the sample section can be varied from $0.5 \times 6 \text{ mm}^2$ to $2 \times 13 \text{ mm}^2$. Therefore, the operating stress σ_f of the material should be between 40-330 MPa. Moreover, a material with an observable yield strength σ_y and having at least 2 objective loading stresses $\sigma_{obj_i, i=1,2,\dots}$ (measuring points) in plastic zone are preferred (Fig.2.2). Referring to the plot of Young's Modulus of various materials in Fig.2.3, Al-alloys, Mg-alloys, Ti-alloys and Lead-alloys are

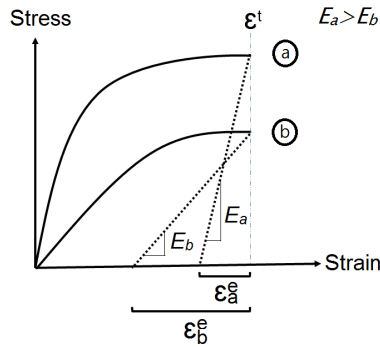


Figure 2.1: Comparison of ϵ^e obtained in two materials have different Young's modulus: the one with smaller Young's modulus shows a larger elastic strain field ϵ^e for an identical total deformation ϵ^t .

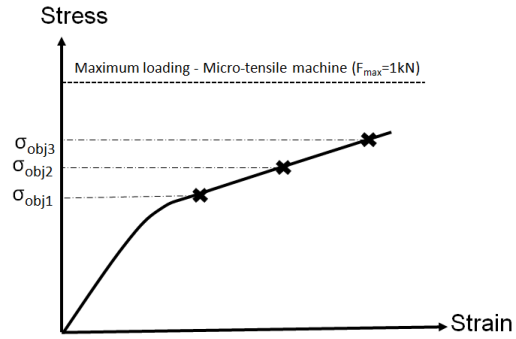


Figure 2.2: Schematic diagram of the objective test: Observable the yield stress and 2 objective loading stresses in plastic zones

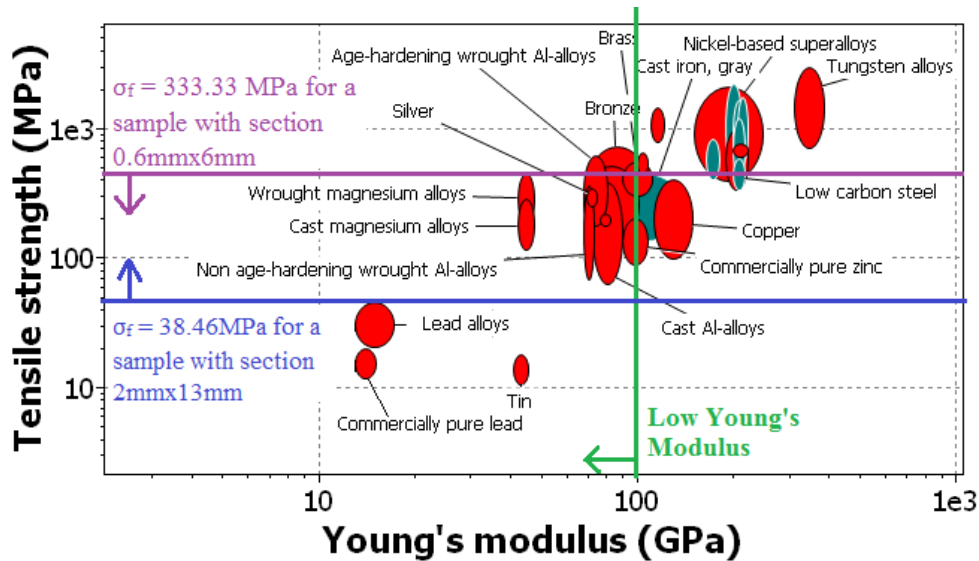


Figure 2.3: Plot of tensile strength-Young's Modulus. Al-alloys show a weak Young's modulus ($<100\text{GPa}$) but higher yield strength within the operating limit of the machine ($40\text{ MPa} \leq \sigma_f \leq 330\text{ MPa}$).

materials with Young's modulus below 100 GPa. Furthermore, Al-alloys show a relatively higher yield strength within the operating limit of the machine with reference to the Ashby plot of strength of different materials. For Al-alloy with 3% of Mg (5052), Young's Modulus is around 70 GPa and the elastic limit can be up to 280 MPa, so that the observed zone could be large enough for having several grains in a sample width about 8 mm and thickness of 0.5

mm.

So we chose Al-alloys as our material. A verification of its behaviour under relaxation was made on a representative polycrystalline Al-alloy (5052) (with around 3% of Mg) specimen to confirm the material selection. It is because X-Ray measurements take a very long time (about 2 weeks) and relaxation of materials becomes inevitable. We observed that the relaxation of the chosen material was slow and stable enough to not affect the ε^e measurement. The details of this relaxation test will be presented in Chapter 4 §4.4.3.

2.1.2 Chemical composition

The chemical composition of Al alloy (5052) is given in Table 2.1.

Si	Fe	Cu	Mn	Mg	Cr	Zn	Al
0.45	0.45	0.10	0.10	2.2-2.8	0.15-0.35	0.10	Balance

Table 2.1: Chemical composition (in Wt%) of the aluminium alloy used (5052)

It was laminated to 0.79 mm thick and wasn't annealed in its initial state.

2.2 Sample Preparation

For the sample preparation, the specimen shape was first designed to fulfill our experimental needs. It was obtained through laminating and machining. Later, the process of recrystallisation was conducted to obtain large crystals in the samples as for facilitating the strain measurements inside the grains.

2.2.1 Design of the specimen shape

The microstructure of the entire sample should be known for a representative 3D polycrystalline modelling. For this, the applied force and stress on the aggregate should be known. So, when designing our sample shape, all the mechanical responses on the active zone of the sample should be traceable and observable by our experimental apparatus (e.g. Camera and X-ray diffractometer) during mechanical loading. Next, the local behaviour in a grain is widely affected by the geometry of the microstructure below the surface [Zeghadi et al. (2007)]. Thus, we need to know our studied aggregate thoroughly, if possible, in a non-destructive way. The specimen shape is designed based on 2 conditions:

1. As the maximum length of sample accessible by XRD is 14.5mm (see 59), in order to have more observable local information during our tensile test, a relatively homogeneous distribution of stress in this active zone is preferred and the sample should not break in the grip system. Therefore, a dog bone

sample is used.

The maximum active zone was identified using numerical simulation. The boundary condition was set as actual gripping system in the micro-machine: two ends was clipped and reinforced using two metal rods. Samples were modelled with various fillet radius as well as various widths of gauge section. The acceptability the dimensions were verified using the homogeneity of the stresses in the gauge section as one of the criteria. In Fig. 2.5, the active zone is the area with relatively homogeneous distribution of stress (in MPa) in the gauge section. The numerical estimation showed that the largest active zone of 8 mm x 18 mm can be achieved with the fillet radius of 4 mm or 6 mm. In this case, a larger radius is preferred to lower strain concentration at the transaction between fillets and the gauge section. Therefore, a sample shape with the width of gauge section of 8 mm and fillet radius of 6 mm was chosen (Fig. 2.4).

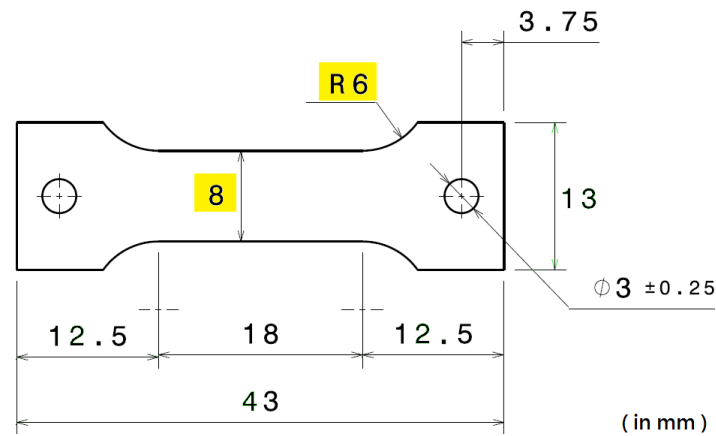


Figure 2.4: Drawing of the sample.

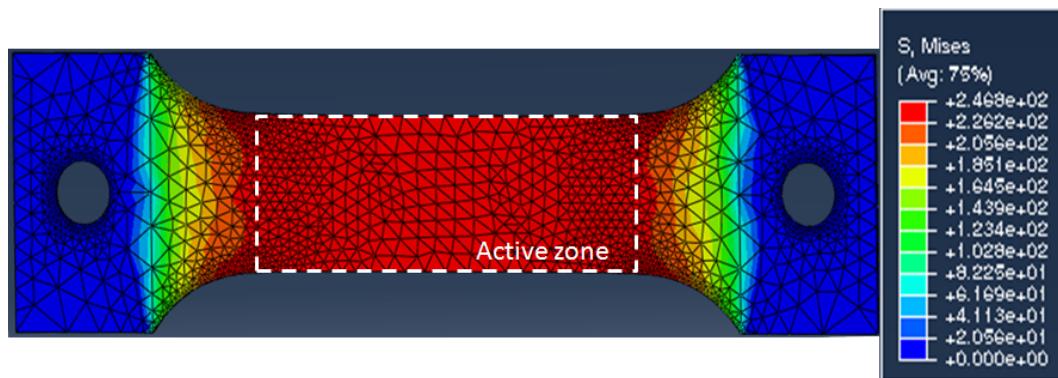


Figure 2.5: The maximum active zone was identified using numerical simulation.

2. All the grain shapes and orientations in the sample should be known. Limiting the number of grains in sample thickness from 1 to 2 ensures the geometry and the initial microstructure of each grain could be measured.

2.2.2 Sample production

The as-rolled Al-alloy (5052) metal sheet with 0.79 mm thick and without annealing was received as initial state. Then, it was laminated to a thickness of 0.55 mm. After, the specimens were machined from this thin metal sheet according to the designed sample shape. The exterior specimen dimensions were $13 \times 43 \text{ mm}^2$ with a thickness of 0.55 mm. The gauge zone was $8 \times 18 \text{ mm}^2$ and the fillet radius was 6 mm (See 60).

In order to facilitate the measurements of strain gradients inside the grains, samples with very large grains was prepared referencing to the recrystallization work of Saai (2008) and Tran (2013). The recrystallization procedure [Philibert et al. (1998)] was stated below as well as their corresponding parameters. These parameters influence the size of the final grains.

1. Recovery annealing.

Specimens were first submitted to a recovery annealing to restore the microstructure and remove the residual stresses resulting from rolling and machining. The time and temperature of the recovery annealing are lower than those of recrystallization treatment. This additional thermal energy allows the dislocations to move (Fig.2.6-2.7).

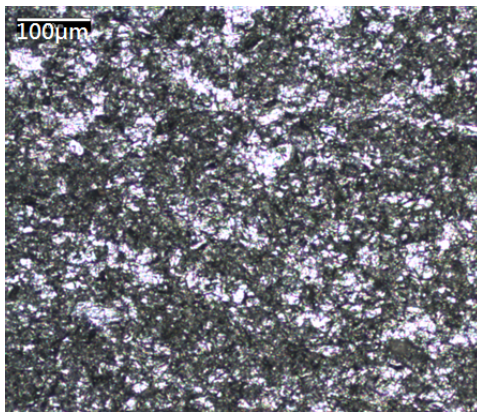


Figure 2.6: Initial grain size of Al-alloy (5052) sample without Recovery annealing.

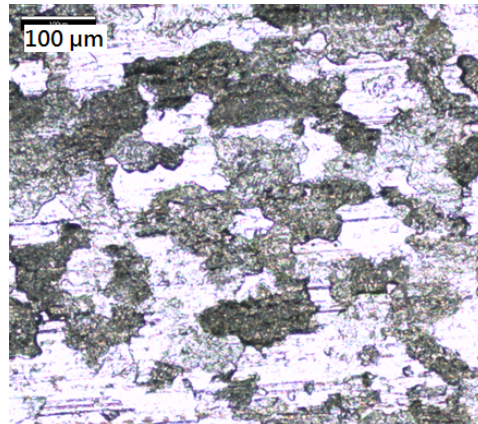


Figure 2.7: Initial grain size of Al-alloy (5052) sample with Recovery annealing at 450 °C for 1 hour.

If the initial material has undergone a higher strain rate, more energy is preferred. So, our samples were first subjected to an annealing at 450 °C for

two hours to release internal residual stresses.

2. Imposed strains - critical work hardening.

Followed by the recovery annealing, a small deformation was imposed on these samples to create dislocation accumulation. These accumulations will be the nuclei of recrystallisation during the last stage.

3. Recrystallization annealing.

Lastly, an annealing at higher temperature was performed, the nuclei grew to form new crystals. In fact, these nuclei are small quasi-perfect crystallites. They grow under the effect of temperature and the presence of favourable grain orientations around their neighbours.

The temperature and the time of recrystallization annealing were searched so as to obtain a fully recrystallized active zone. Non-recrystallized areas can be avoided by increasing the annealing temperature and/or increasing the annealing time (Fig.2.8). In the case of aluminum, it is limited by the melting temperature (600 °C). As a result, to ensure a complete recrystallization of the sample, we increased the annealing time.

Also, the imposed deformation affects the grain size. As shown on Fig.2.8, the crystallographic structure retains its initial status unless the imposed deformation exceeds the critical value, called critical work hardening, to start recrystallization. Beyond this value, new structures appear and the number of nuclei increases along the augmentation of the deformation level. Each nucleus grows until it meet up with others.

For our sample, the critical work hardening at 4.7% strain was found and our recrystallisation annealing was performed at 540 °C for two days to obtain grain sizes of about 5 mm (Fig.2.9).

The final sample contained about 12 grains on each side and 2 grains through the thickness. The grain boundaries between the two layers are at mid-thickness (Fig. 2.10).

2.3 Studied samples and their initial microstructure

There are 2 samples prepared and their initial microstructures will be described in the following pages. Knowing the initial microstructure of each grain in the sample is essential for X-ray diffraction. An accurate initial crystalline orientation is needed for positioning the sample with respect to the X-ray beam during elastic strain characterisation process. Moreover, the grain geometry and the crystal orientations of the active zone can be used during a representative 3D polycrystalline modelling. This information was obtained as follows.

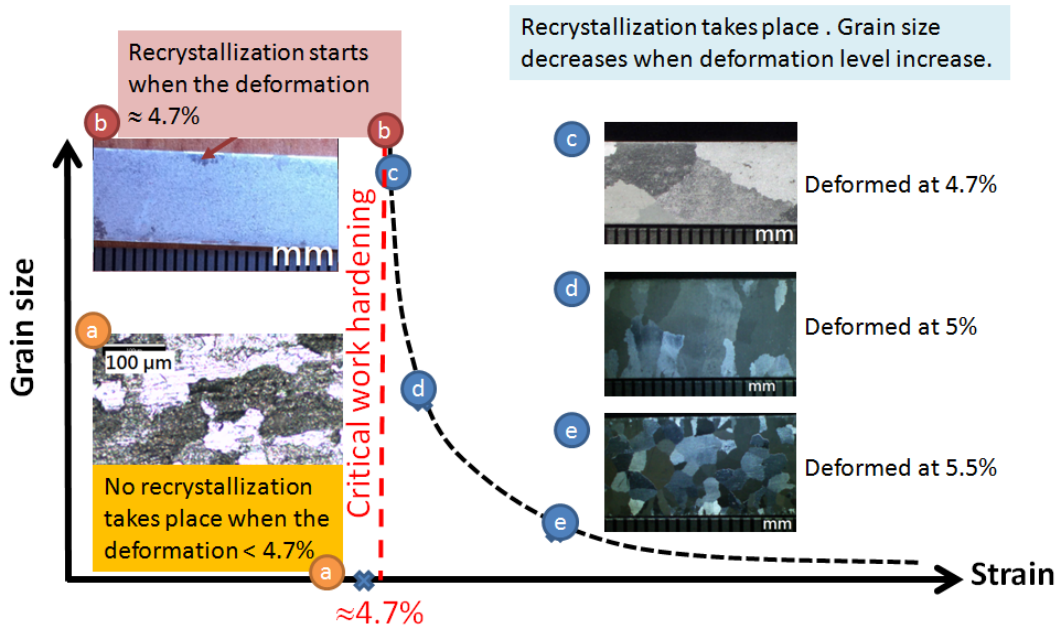


Figure 2.8: Grain size obtained during recrystallization depends on the level of work hardening applied on the sample.

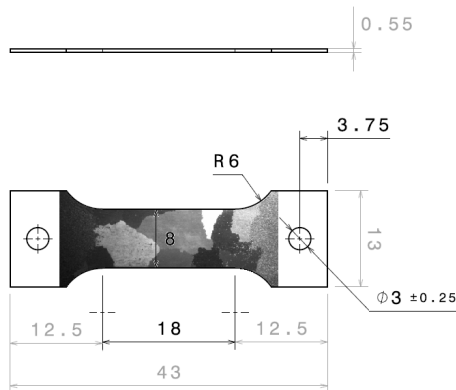


Figure 2.9: Sketch of the sample used with its large grains (in mm).

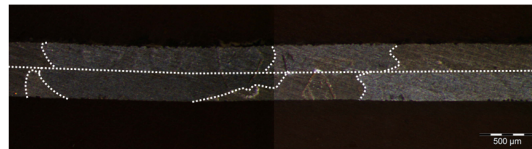


Figure 2.10: View in sample thickness. Grain boundaries (in dashed lines) between the two layers are at mid-thickness.

2.3.1 Grain geometry

Each grain shape and position in the sample was measured using optical microscope (e.g. sample No.1 is shown in Fig.2.11-2.12). To better distinguish and outline the grain boundaries, photos of the sample at the same position were captured with different lighting directions. With an accurate grain cartography, it facilitated the XRD scanning programming as well as the model setting up in later finite element simulations.

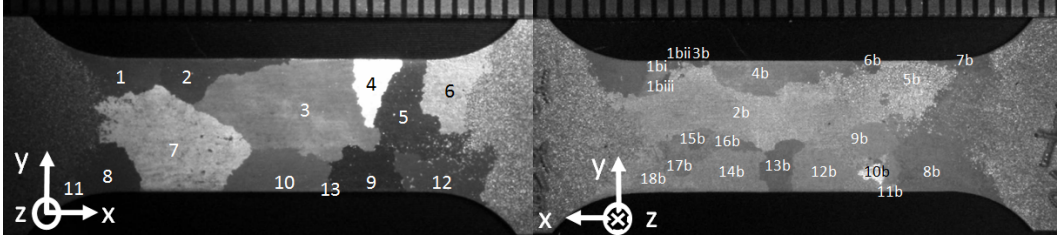


Figure 2.11: Front view of sample No.1 with its grains numbered.

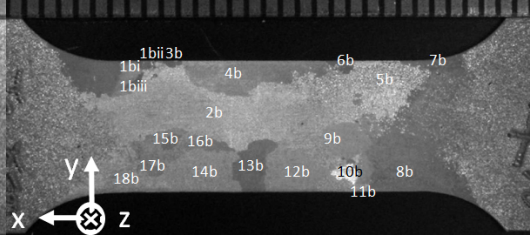


Figure 2.12: Back view of sample No.1 with its grains numbered.

2.3.2 Euler angles

The crystal orientations are represented by three Euler angles ($\varphi_1, \Phi, \varphi_2$) and they are achieved by composing three elemental rotations about axes z - x' - z'' starting from the sample x - y - z coordinate system. The crystal orientation of each grain on the two surfaces is firstly characterised by X-ray diffraction.

1. characterisation of crystal orientations using XRD method

First, a complete texture scan was performed on each single crystal on the sample in its initial state. The peak positions $(\phi, \psi)_{\{hkl\}}$ in the pole figure of $\{220\}_{grain}$ and $\{222\}_{grain}$ inter-reticular planes were recorded. After, Euler angle triplets were generated every 30° and the corresponding $(\phi, \psi)_{\{220\}}$ and $(\phi, \psi)_{\{222\}}$ were calculated. The triplet giving the closest pole figure was selected and a procedure of optimisation was then carried out by minimising the difference between calculated and measured (ϕ, ψ) values in order to determine Euler angles of the grain. Once the crystal orientation is identified, all the resting $(\phi, \psi)_{\{hkl\}}$ can be therefore calculated (e.g. 311 pole figure shown in Fig.2.13). Euler angles of each grain were obtained by this inverse method (Fig.2.14).

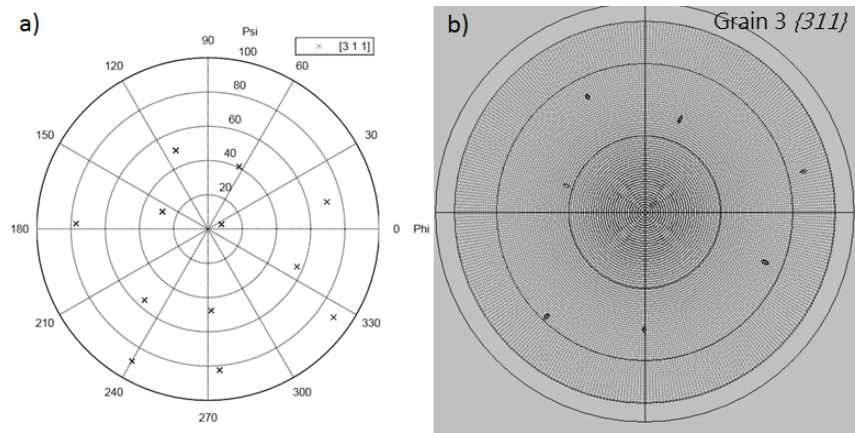


Figure 2.13: (a) Calculated and (b) measured pole figure of $\{311\}$ in Grain 3.

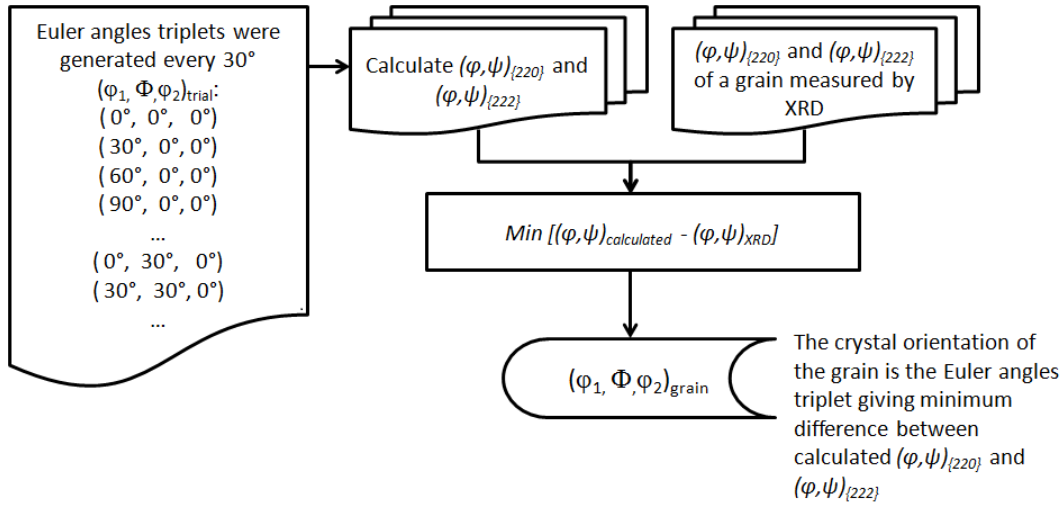


Figure 2.14: Logic diagram for finding Euler angles of a given grain which matches the results measured by XRD.

The coordinate system of the sample was defined as in Fig. 2.11. When measuring the Euler angles of the grains on the back side $(\varphi_1', \Phi', \varphi_2')_{\text{grain}}$ of the sample, the sample is rotated 180° along y-axis (Fig. 2.12). Therefore, the actual grain orientations $(\varphi_1, \Phi, \varphi_2)_{\text{grain}}$ on this side need to take the rotation of 180° along y-axis, Ry , into account. There are two options for this transformation,

$$\varphi_1 = \pi - \varphi_1'; \Phi = \pi + \Phi'; \varphi_2 = \varphi_2' \quad (2.1)$$

$$\varphi_1 = -\varphi_1'; \Phi = \pi - \Phi'; \varphi_2 = \pi + \varphi_2' \quad (2.2)$$

The crystal orientations of both sides of the sample No.1 are shown in Tab.2.2.

2. Why XRD but not EBSD?

We have conducted the measurement using XRD because XRD enables one to determine the materials texture with a 'gross' surface. Unlike EBSD scanning, XRD does not require a high quality of polishing of the sample surface, so that the risk of bending the thin sample during polishing can be avoided. Moreover, the EBSD scanning is limited to a relatively small region $2 \times 3 \text{ mm}^2$, whereas active zones of samples were $8 \times 18 \text{ mm}^2$. If we aim to obtain a full picture of the texture in the active zone, this scanning has to be conducted several times (zone by zone) and then the results are put together into a complete one. Yet, the angle of incidence of the beam on the periphery of the area of interest creates artifacts. Also, overlapping around twenty EBSD diagrams cumulates errors. Therefore, EBSD is not used during texture determination.

Besides, there is one more convenience of giving up EBSD at this stage. If the sample is put back in the XRD goniometer for an in-situ experiment after the

a. Front side				b. Back side			
Grain	ϕ_1	Φ	ϕ_2	Grain	ϕ_1	Φ	ϕ_2
1	251.44	37.20	212.35	1bi	240.91	227.92	119.18
2	199.63	38.60	245.29	1bii	141.44	273.92	53.43
3	139.78	33.35	316.35	1biii	244.67	173.89	37.92
4	107.72	28.36	8.77	2b	213.67	170.52	67.31
5	296.22	23.71	159.41	3b	129.53	225.45	63.00
6	274.13	17.06	181.94	4b	279.13	205.51	89.74
7	101.47	25.13	334.59	6b	206.62	172.11	60.25
8,11	234.22	46.11	251.8	7b	184.33	193.77	7.47
9	354.72	28.32	121.95	8b	97.10	148.83	-13.43
10	127.85	45.79	342.44	9b	197.28	175.98	-27.09
12	74.25	46.29	38.14	10b	76.16	212.28	15.96
13	224.41	33.05	265	11b	127.26	143.58	-67.44
				12b	225.98	208.69	72.82
				13b	191.52	230.56	34.70
				14b	196.86	197.18	17.64
				15b	169.84	222.24	17.36
				16b	240.12	173.72	33.62
				17b	169.84	222.24	17.36
				18b	223.05	212.64	77.64

Table 2.2: Crystal orientations of a.front side and b.back side of the sample No.1.

EBSD scanning, it is necessary to tackle the angular shift (± 3 deg) on some measuring points. If the initial peak position is already measured via XRD, time can be saved as the repositioning procedure of the grain/sample with respect to the X-ray beam is simplified.

2.3.3 Schmid factor

The Schmid factor SF of each grain in the sample 1 were calculated (Tab.2.3) using the Eq.1.7 mentioned in chapter 1 §1.2.3.2. In our case, an uniaxial force was applied on multicrystal samples in x-direction. This applied stress (σ) can be expressed in crystal coordinate system F (or $\sigma_{crystal}$) by multiplying a matrix of rotation in terms of Euler's angles. This matrix of rotation will be further presented in next chapter. For sample 1, for instance, the slip system was most likely to be activated in grain 9 (SF = 0.495) before grain 4 (SF = 0.398).

a. Front side			b. Back side		
Grain	Schmid factor	Number of activated slip system	Grain	Schmid factor	Number of activated slip system
1	0.4799	1	1bi	0.4357	1
2	0.4665	1	1bii	0.3318	1
3	0.4893	1	1biii	0.4990	1
4	0.3982	1	2b	0.4832	1
5	0.4969	1	3b	0.4802	1
6	0.4904	1	4b	0.4956	1
7	0.4893	1	6b	0.4811	1
8,11	0.4261	1	7b	0.4303	1
9	0.4952	1	8b	0.4520	1
10	0.3950	1	9b	0.4185	1
12	0.4335	1	10b	0.3785	1
13	0.4219	1	11b	0.4563	1
			12b	0.4427	1
			13b	0.4959	1
			14b	0.4404	1
			15b	0.4994	1
			16b	0.4992	1
			17b	0.4994	1
			18b	0.4170	1

Table 2.3: Schmid factor of each grain of a. front side and b. back side of sample No.1.

2.3.4 Initial microstructure for Sample No.2

Similarly, a second sample was prepared and its grain geometry (Fig.2.15-2.16), crystal orientations (Tab.2.4) and the SF values (Tab.2.5) on both sides of the sample were quantified.

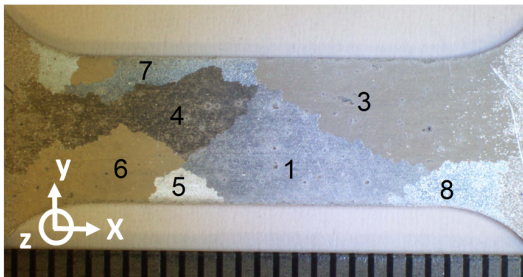


Figure 2.15: Front view of sample No.2 with its grains numbered.

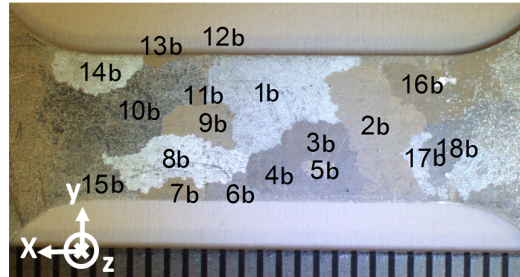


Figure 2.16: Back view of sample No.2 with its grains numbered.

a. Front side				b. Back side			
Grain	ϕ_1	Φ	ϕ_2	Grain	ϕ_1	Φ	ϕ_2
1	32.65	71.50	84.78	1b	141.14	291.72	102.95
3	12.31	54.52	88.75	2b	155.62	221.77	47.26
4	313.14	15.22	97.85	3b	180.01	235.89	91.88
5	103.46	41.60	25.07	4b	33.30	275.00	69.18
6	70.81	61.93	20.54	4b	122.75	248.39	85.70
7	124.85	106.59	92.30	6b	139.20	270.18	59.49
8	16.10	80.91	-1.08	7b	191.60	217.53	201.08
				8b	103.54	210.18	86.90
				9b	142.79	225.79	9.38
				10b	139.52	274.88	83.68
				11b	142.94	254.99	43.54
				12b	178.68	197.43	41.61
				13b	151.53	254.15	29.19
				14b	145.99	215.25	2.81
				15b	103.63	271.35	99.80
				16b	194.52	254.00	32.99
				17b	156.77	221.85	47.27
				18b	180.63	157.11	127.89

Table 2.4: Crystal orientations of both sides of sample No.2.

a. Front side			b. Back side		
Grain	Schmid factor	Number of activated slip system	Grain	Schmid factor	Number of activated slip system
1	0.4922	1	1b	0.4726	1
3	0.4640	1	2b	0.4683	1
4	0.4673	1	3b	0.4211	1
5	0.3266	1	4b	0.4687	1
6	0.4879	1	5b	0.4615	1
7	0.4648	1	6b	0.3897	1
8	0.4874	1	7b	0.4500	1
			8b	0.4677	1
			9b	0.3896	1
			10b	0.4564	1
			11b	0.3583	1
			12b	0.4247	1
			13b	0.3739	1
			14b	0.4513	1
			15b	0.4806	1
			16b	0.4798	1
			17b	0.4732	1
			18b	0.4561	1

Table 2.5: Schmid factor of each grain of both sides of sample No.2.

2.4 Conclusion

In summary, an aluminium alloy has been selected to prepare the samples used in this study. Its simple microstructure and mechanical properties (e.g. easy to obtain large grains via recrystallisation, small Young's modulus and slow relaxation) favour the local strain field measurement. Next, the sample shape with a maximized useful zone of $8 \times 18 \text{ mm}^2$ and thickness of 0.55 mm has been designed. Then, once the samples were machined, large grains on the sample were obtained via recrystallisation process. The samples were first submitted to an annealing at 450°C for two hours, then a critical work hardening at 4.7% strain and, finally, a recrystallisation annealing was performed at 540°C for two days to obtain grain sizes of about 5 mm. There are about 10-12 grains at each side and 2 grains in the thickness. After, the grain geometry of the two studied samples were captured by optical microscope and the crystal orientations were determined using XRD.

Elastic strain field measurement using X-ray diffraction

In this chapter, the methodologies to use X-ray diffraction (XRD) for intra-granular and inter-granular elastic strain ε^e measurement are discussed. First, the application of local ε^e measurement using XRD is presented. The experimental apparatus, X-ray diffractometer, is also introduced. Then, the ε^e measurement in a single crystal using XRD is given. Followed by, the methodologies developed to achieve local ε^e field measurement as well as the corresponding uncertainties quantification on a polycrystalline sample are described. Finally, this chapter is closed with discussion and conclusion sections.

3.1 Application of XRD in ε^e field measurement

X-ray diffraction (XRD) in crystals was first experimentally proved by Max von Laue in 1912 as the diffraction spots were captured once X-rays hit on the orderly arranged atoms within the crystal [Friedrich et al. (1912)]. These diffraction spots were then explained by William Lawrence Bragg using a governing rule linking crystal structure and wave nature, known as Bragg's Law [Bragg and Bragg (1913); Bragg (1915)]. Thanks to the direct interaction between X-rays and atoms in crystalline materials, XRD enables us to access the lattice spacing in crystal and consequently becomes a useful tool for elastic behaviour characterisation (refer to chapter 1 §1.2.2.1 for the relationship between elasticity and atomic distance of metallic materials).

In fact, the application of XRD in ε^e measurement has long been used in science and engineering. For example, the locked-in ε^e , also known as residual stress, in industrial products may speed up or prevent fatigue or cracking. Thus, XRD becomes a widespread tool to analyse materials failure as well as process development. The publication of Prév y (1996) reviews that XRD was first applied to quantify the plane-stress residual stress presented in hardened steels [Koistinen and Marburger (1959); Ogilvie (1952)]. In the following decades, XRD was largely applied in residual stress (ε^e) measurement to understand mechanical behaviour of metals in automotive and bearing [Hilley et al. (1971)], in aerospace and nuclear industries.

The theoretical basis of XRD has been further developed (e.g. methods proposed by Imura (1954); Macherauch and Muller (1961); Ortner (1986b); Zhou (1994), etc.) with certain limitations. Nowadays, many studies proved the feasibility of full ε^e tensor determination not only in polycrystalline texture but also in single crystal, such as nickel [Dupke and Reimers (1995); Eberl (2000); Morangais et al. (2015)],

titanium alloy [Shiro et al. (2008)], steels [Zhou (1994)], copper and zinc [Huang (2007)], etc. Although the experimental works shown in Zhou (1994)] and Huang (2007) use only one measurement to represent the local ε^e situation per grain, they give us a clue to make use of this technique on a pre-defined grid inside a grain and across the grains to achieve a full-field measurement of ε^e . In consequence, this method was considered and combined with in-situ tests to gain insight into the local mechanical behaviour of Aluminium alloy in our study.

3.2 Experimental apparatus: Diffractometer

All the X-ray diffraction measurements concerned in this study were performed on a Panalytical X'Pert Pro MRD 7-axis ($x, y, z, \psi, \phi, \omega$ and 2θ) goniometer (Fig.3.1). For a complete XRD path, starting from the cobalt X-ray tube ($\lambda_{K\alpha(Co)} = 0.17903\text{nm}$) operating at 45kV / 40mA, the beam first passes through an iron-filter to absorb the K_{β} component in the spectrum. A poly-capillary lens with a diameter of 8 mm is then needed to convert a highly divergent beam of X-rays into a quasi-parallel beam of low divergence (5°). The beam size is limited by a knob-adjustable crossed slit collimator before diffracting the sample positioned on the wafer holder. The diffracted beam goes through a vertical collimator and horizontal Soller slits with an opening angle of 0.27° (given by Panalytical) and 2.86° (which will be presented in §.3.5.2) respectively and is finally quantified by a Xenon filled gaseous proportional detector (see 61).

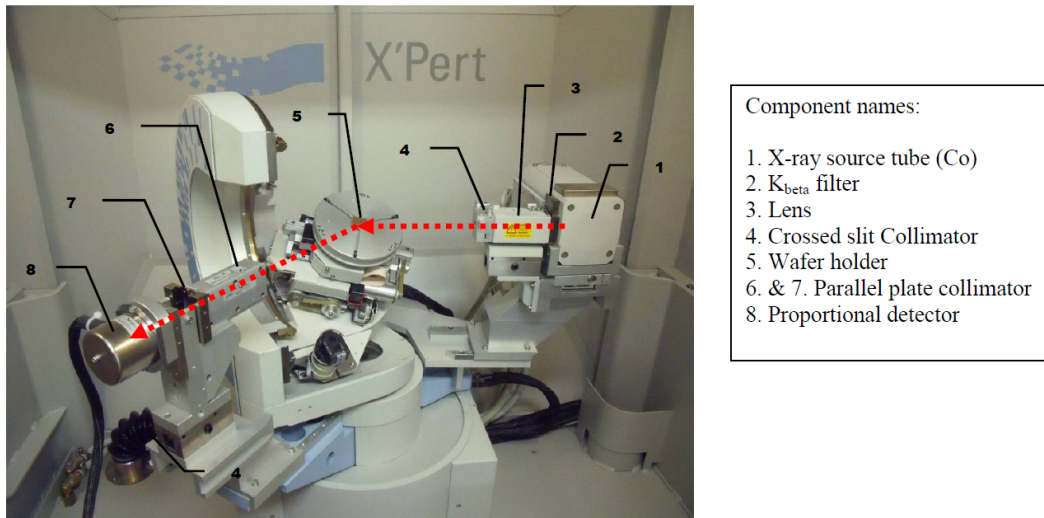


Figure 3.1: Panalytical X'Pert Pro MRD goniometer. The red arrows represent the full path of X-ray from being emitted up to being detected during the diffraction process.

3.3 General principle in ε^e full-field measurement

When a single crystal is mechanically loaded, the distance between atomic planes increases or decreases depending on the sign of the loading, some will be pulled away and others will get closer. If we want to apply the Bragg's law (see §.1.4.2) to calculate the change of one inter-reticular plane distance $\delta d_{(hkl)}$, XRD measurement should be conducted on the chosen atomic plane at both its initial and deformed states. The characterisation of lattice parameter a_0 using powder method by XRD gives a first idea of our Al-alloy at its initial state.

In our case, ε^e measurement is conducted in a FCC crystal structure and the first Ortner method [Ortner (1986b)] was applied referring to the works of Dupke and Reimers (1995); Zhou (1994); Eberl (2000); Huang (2007). If we want to determine its full ε^e tensor (i.e. ε_{ij}^e where $i=1,2,3$ and $j=1,2,3$), the contra-variant components of metric tensor $G^*_{n=i=1,2,\dots,6}$ at its initial and deformed states are required. Since there are 6 contra-variant components in G^* , at least 6 $\{hkl\}$ planes are needed to determine G^* . If more than 6 $\{hkl\}$ planes are taken into account, the measurement precision will be enhanced. Thus, XRD were conducted on more than 6 $\{hkl\}$ planes at two different states.

At the same time, a number of precautions should be taken during XRD measurement in single crystal. Although launching XRD on 6 well-chosen $\{hkl\}$ planes allows us to compose ε^e , more $\{hkl\}$ planes are suggested to reduce the measuring uncertainties. These $\{hkl\}$ planes in each grain were selected considering the accessibility of experimental device. The calculated ε^e using the combination of these planes should also achieve its minimum uncertainty [Ortner (1986a)].

In addition, unlike polycrystalline samples which always exhibit some planes well oriented to incident X-ray beam for XRD, the diffraction of each specific $\{hkl\}$ plane in a monocrystal occurs only when the crystal is correctly positioned (x, y, z) and oriented (ϕ , ψ , 2θ) with respect to X-ray beam. These (ϕ , ψ , 2θ) $_{\{hkl\}}$ can be calculated using its grain texture and the position/dimension of experimental apparatus.

Meanwhile, the frames of goniometer, sample and crystal are rarely identical, all their relationships should be clearly defined and linked with a matrix of rotation/transformation. This step facilitates the display of ε^e results. Also, the crystallographic structure will no more be cubic during deformation. For this, we made use of reciprocal space to simplify the ε^e calculation.

In order to define the final position of a peak, an iteration process was designed after understanding the relationship between each scanning axis and the shape of diffraction peak. Yet, in practice, further difficulties might be encountered during final peak position determination, such as broadening of peak in ψ -direction owing to beam divergence, existence of peak doublet due to the appearance of mosaicity because of the crystal orientation dispersion during plastic deformation and the nature of X-ray K_α line resulting in the presence of diffraction peak doublet. Thus, an experimental methodology was developed to obtain diffraction peak measurement as well as the determination of its final position. The uncertainty accompanying the calculated ε^e was also estimated.

Upon the completion of ε^e measurement inside a single crystal, the same procedure can be repeated on each measuring point (Zone of interest ZOI / pre-defined grid resolution) on the entire sample to yield a full-field ε^e data. The measurement procedure is synthesized in Fig.3.2.

3.4 ε^e measurement using XRD in single crystal

In this section, the theory and practice of ε^e measurement using XRD inside a crystal is presented in detail.

We first explain the reason of not considering the $\sin^2\psi$ method in our case. Then, a recall of the principle of X-ray Diffraction and the Bragg's law is given.

Meanwhile, the co-ordinate systems of goniometer, sample and crystal are rarely identical, all their relationships should be clearly defined and linked with a matrix of rotation/transformation. This step facilitates the display of ε^e results. Also, the crystallographic structure will no more be cubic during deformation. For this, we made use of reciprocal space to simplify the ε^e calculation.

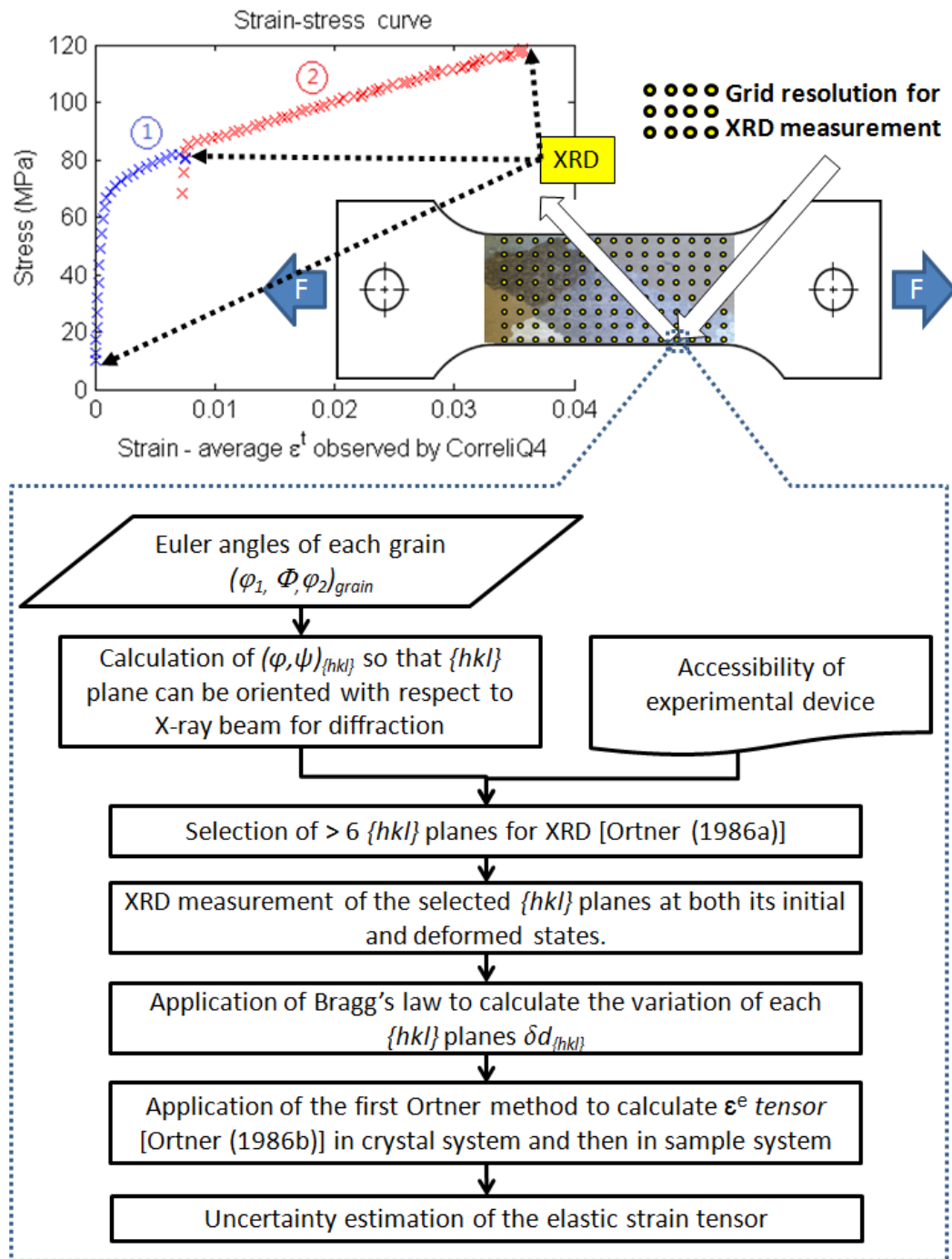
3.4.1 The $\sin^2\psi$ method and its limits

As mentioned in the publication of Ortner (2009), a traditional ε^e measuring method, known as $\sin^2\psi$ method [Macherauch and Muller (1961)], is designed for macroscopic elastic isotropic or quasi-isotropic specimens. This assumption is only valuable if the crystalline texture of a polycrystalline specimen or the elastic behaviour of each monocrystal is isotropic. In addition, the beam size of X-rays should be large enough to cover a sufficient number of small grains at a time, so that the diffracted area can be considered as an representative elementary volume [Welzel et al. (2005)]. However, it hardly meets our research objectives. As we want to obtain a rich experimental data-base with local ε^e values of a sample during mechanical loading, we chose to perform the measurement with a small beam size and large grain area (see 2.1.1 point.2-3). Thus, $\sin^2\psi$ method is not applicable in our case.

3.4.2 Recall of the principle of X-ray Diffraction and the Bragg's law

In chapter 1 §1.4.2, a general principle of XRD was presented. When incident X-rays are emitted and interact with electronic shells of atoms in the studied solid (al-alloy in our case), electrons absorb and re-radiate X-rays which can be detected. In a single crystal, crystal lattice (hkl) is used to describe the position of planes of atoms. At certain (hkl) spaced by distance $d_{(hkl)}$, a sharp peak in the intensity of diffracted X-ray radiation can be observed under the conditions described as follows (Fig. 3.3).

1. The incident X-rays are diffracted symmetrically and regularly along the normal of a (hkl) plane.

Figure 3.2: Schematic diagram of the general principle in ϵ^e full-field measurement.

- These three elements are always coplanar.
- The angle between the diffracted beam and the transmitted beam is always 2θ . Even though the diffraction angle is known as θ , 2θ is usually

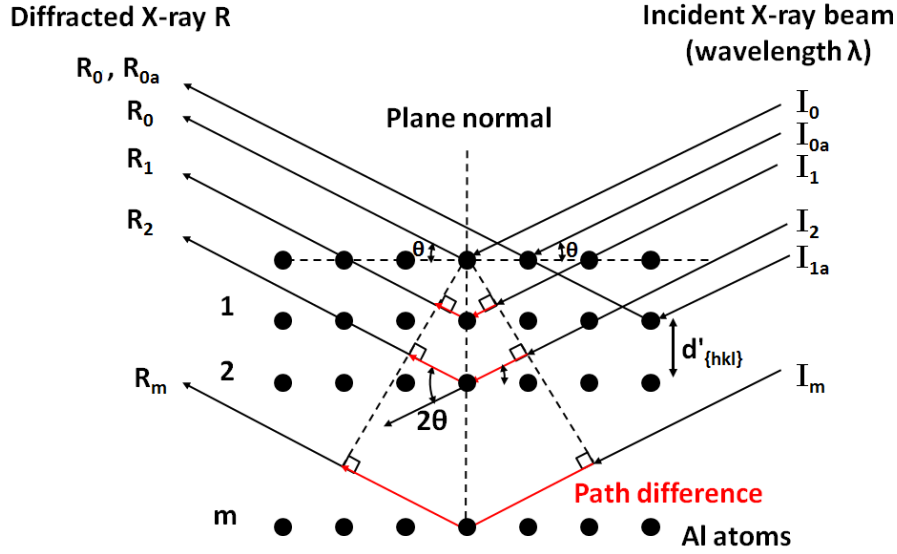


Figure 3.3: Diffraction of X-rays by a crystal [Cullity (1978)].

measured in practise.

2. The diffracted X-rays interfere constructively.
 - (a) The path difference of two in-phase X-rays (red line in Fig. 3.3) between two parallel (hkl) planes must be an integer multiple of the given wavelength (λ of the X-ray source). The monochromatic X-rays are assumed to be perfectly parallel.
 - (b) There is no path difference of X-rays on the same diffraction plane (e.g. I_0-R_0 and $I_{0a}-R_{0a}$, I_1-R_1 and $I_{1a}-R_{1a}$).
 - (c) For the path difference between X-rays (e.g. I_0-R_0 and I_1-R_1 or I_m-R_m), Bragg's law (Eq.3.1) [Bra13, Bra15] formulates the relationship between X-ray wavelength λ , inter-reticular distance $d_{(hkl)}$ (distance between atoms), diffraction angle θ and the order of the corresponding diffraction m (or order of interference):

$$2d_{hkl}\sin\theta_{(hkl)} = m\lambda \quad (3.1)$$

For the Bragg's law, since λ of monochromatic X-rays is constant, we can always imagine that higher-order diffractions (e.g. $m = 2, 3, \dots$) from (hkl) planes are the same as the first order diffraction ($m = 1$) from parallel $(mh \ mk \ ml)$ planes of spacing $d_{(mh \ mk \ ml)}/m$. From the formal point of view, this convention agrees with the definition of Miller indices because $(mh \ mk \ ml)$ planes are parallel to $(h \ k \ l)$ while $d_{(hkl)}$ is $1/m$ of $d_{(mh \ mk \ ml)}$. For instance, the second-order diffraction from (100) equals to the first-order diffraction from (200) . i.e. the Bragg's law can be simplified in the form as written in the chapter 1 Eq.(1.14):

$$2d_{hkl}\sin(\theta_{hkl}) = \lambda \quad (1.14)$$

If the crystal is under deformation, the distance between (hkl) planes changes (δd_{hkl}) and it can be calculated using the variation of diffraction angle ($\delta\theta_{hkl}$) measured in experiment, i.e. d_{hkl} can be used as a gauge for local elastic strain measurement. The elastic strain along (hkl) plane ε_{hkl} can be obtained by differentiating Eq. (1.14):

$$\begin{aligned} 2\delta d_{hkl}\sin\theta_{hkl} + 2d_{hkl}\cos\theta_{hkl}\delta\theta_{hkl} &= 0 \\ \frac{\delta d_{hkl}}{d_{hkl}} &= -\frac{\cos\theta_{hkl}}{\sin\theta_{hkl}}\delta\theta_{hkl} \\ \varepsilon_{hkl} &= -\cot\theta_{hkl} \cdot \delta\theta_{hkl} \end{aligned} \quad (3.2)$$

Remark that Bragg's law does not contain further information like intensities or width of the diffraction peak. Therefore, before making use of this equation to determine diffraction plane distance and its variation under deformation, an experimental methodology for diffraction peak measurement and then peak position determination was developed and it will be presented in section 3.5.

3.4.3 Difference between XRD measurement in an aggregate and a single crystal

As the X-ray beam size ($0.1 \times 0.1 \text{ mm}^2$) used is relatively small compared with the grain size (several mm^2) in our study, XRD measurement conducted on the oligo-crystalline samples was considered as in a monocrystal.

When talking about the difference between XRD measurement in an aggregate and a single crystal, this concept can be explained using pole figures. Each pole figure highlights the position as well as the presence of its corresponding family of $\{hkl\}$ planes in the zone of analysis by the X-ray beam within a single crystal or an aggregate.

A pole figure is a stereographic projection associated with the normal of a family of planes $\{hkl\}$ firstly projected on the sphere surface and then intersecting the equatorial plane of the sphere (Fig. 3.4). The position of the projected pattern in pole figure can be expressed using $(\phi, \psi)_{\{hkl\}}$.

Fig. 3.3 and Fig. 3.4 explain why diffraction in a single crystal takes place only in precise directions: the normal of the (hkl) plane has to be oriented with respect to the X-ray beam at $(\phi, \psi)_{(hkl)}$ and then positioned to form a diffracted angle $(\theta)_{(hkl)}$ for satisfying the Bragg's law. Following this line of reasoning, XRD measurement in an aggregate is relatively simple. An aggregate can be seen as a group of single crystals with sufficient small grain size with respect to X-ray beam size. No matter the sample texture is random or textured, once the sample normal is positioned at $(\theta)_{(hkl)}$, there are always some (hkl) planes having their normals in favour for diffraction. As it is not the case in single crystal, a method for correctly locating the diffraction planes is necessary in single crystal. It will be described in the following sections. Therefore, the method for correctly locating the $\{hkl\}$

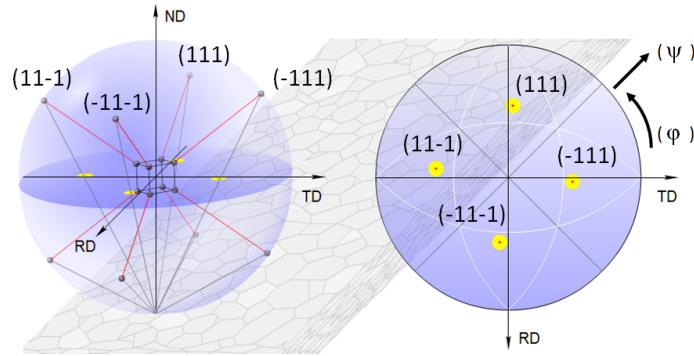


Figure 3.4: Schematic diagram of pole figure: stereographic projection of $\{111\}$ planes of a cubic structure [Source: <http://www.aluminium.matter.org.uk>].

planes for XRD to determine the elastic strain tensor calculation is described in the following sections.

3.4.4 Transformation between the sample and the crystal frames

We defined three orthogonal basis as reference system for the goniometer R_g , the sample R_s and the crystal R_c (Fig. 3.5).

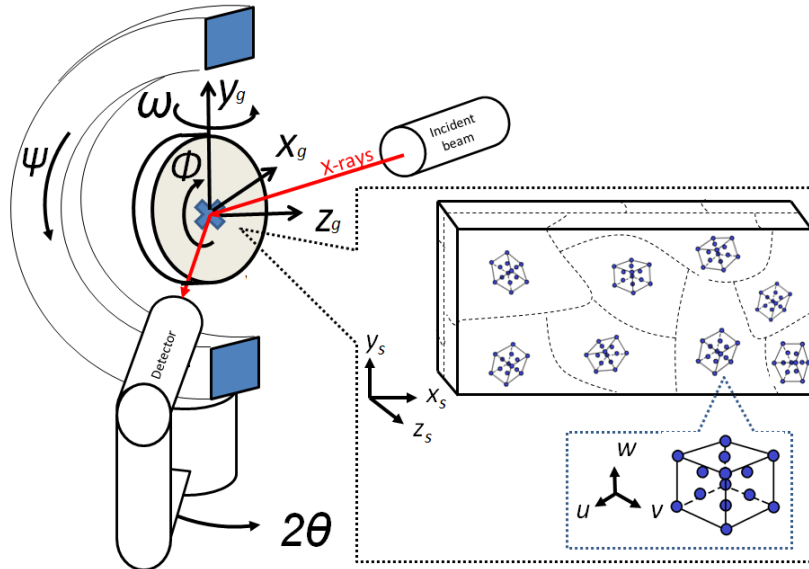


Figure 3.5: Scheme of frames $R_g (\vec{X}_g, \vec{Y}_g, \vec{Z}_g)^T$ given in the goniometer, $R_s (\vec{X}_s, \vec{Y}_s, \vec{Z}_s)^T$ in a sample and $R_c (\vec{u}, \vec{v}, \vec{w})^T$ in a crystal.

The sample is positioned in the goniometer, and the basis vectors of R_s are equal to the ones of R_g :

$$R_g = \begin{pmatrix} \vec{X}_g \\ \vec{Y}_g \\ \vec{Z}_g \end{pmatrix} = \begin{pmatrix} \vec{X}_s \\ \vec{Y}_s \\ \vec{Z}_s \end{pmatrix} = R_s \quad (3.3)$$

\vec{X}_s and \vec{Y}_s correspond to the longitudinal and transversal directions of the sample respectively. \vec{Z}_s is perpendicular to the sample surface. Also, the movement of ψ in the goniometer equals to the rotation of the sample around \vec{X}_s axis while ϕ corresponds to the rotation of the sample around \vec{Z}_s axis.

In every crystal, a reference system R_c is defined as:

$$R_c = \begin{pmatrix} \vec{u} \\ \vec{v} \\ \vec{w} \end{pmatrix} \quad (3.4)$$

where \vec{u} , \vec{v} and \vec{w} correspond to (100), (010) and (001) directions of the crystalline lattice.

In chapter 1, we presented how the Euler angles $(\varphi_1, \Phi, \varphi_2)$ pass from sample frame R_s to crystal frame R_c by rotating about axes $z_s-x_s'-z_s''$. With the given Euler angles of a crystal, this relationship can also be expressed using a matrix of rotation M_r :

$$\begin{aligned} M_r &= \begin{pmatrix} \cos\varphi_1 & \sin\varphi_1 & 0 \\ -\sin\varphi_1 & \cos\varphi_1 & 0 \\ 0 & 0 & 1 \end{pmatrix} \begin{pmatrix} 1 & 0 & 0 \\ 0 & \cos\Phi & \sin\Phi \\ 0 & \sin\Phi & \cos\Phi \end{pmatrix} \begin{pmatrix} \cos\varphi_2 & \sin\varphi_2 & 0 \\ \sin\varphi_2 & \cos\varphi_2 & 0 \\ 0 & 0 & 1 \end{pmatrix} \\ &= \begin{pmatrix} \cos\varphi_1\cos\varphi_2 - \sin\varphi_1\sin\varphi_2\cos\Phi & \sin\varphi_1\cos\varphi_2 + \cos\varphi_1\sin\varphi_2\cos\Phi & \sin\varphi_2\sin\Phi \\ -\cos\varphi_1\sin\varphi_2 - \sin\varphi_1\cos\varphi_2\cos\Phi & -\sin\varphi_1\sin\varphi_2 + \cos\varphi_1\cos\varphi_2\cos\Phi & \cos\varphi_2\sin\Phi \\ \sin\varphi_1\sin\Phi & -\cos\varphi_1\sin\Phi & \cos\Phi \end{pmatrix} \quad (3.5) \end{aligned}$$

Therefore, the transformation from sample to crystal frames can be achieved by

$$R_c = M_r R_s \quad (3.6)$$

In order to simplify the mathematical expression later, the elements of M_r will be written as $M_{r_{ij}}$.

3.4.5 Positioning of the normal of $\{hkl\}$ planes for XRD

Before adjusting the diffraction angle for XRD, the normal $\vec{N}_{(hkl)}$ to the analysed lattice (hkl) in a crystal is first positioned as coplanar $(\phi, \psi)_{(hkl)}$ as the path of X-ray diffraction. $\vec{N}_{(hkl)}$ can be calculated from $(\varphi_1, \Phi, \varphi_2)$ of the crystal.

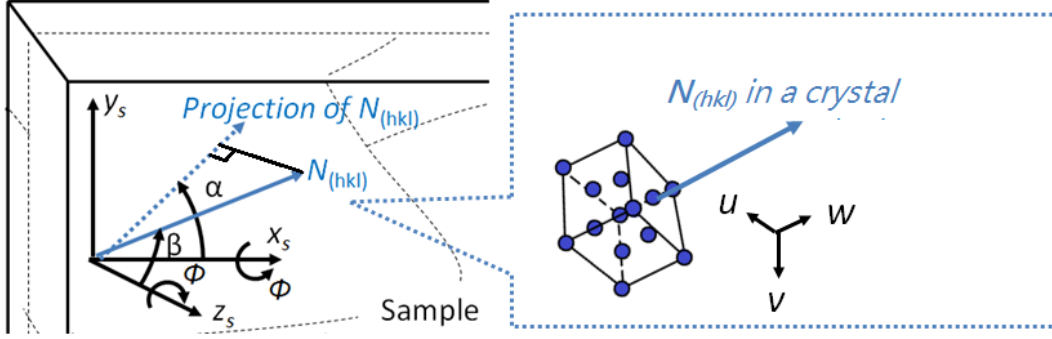


Figure 3.6: Scheme of positioning the normal of the analysed (hkl) plane $\vec{N}_{(hkl)}$ for XRD.

$\vec{N}_{(hkl)}$ can be expressed in both its original crystal (R_c) or sample frames (R_s). For the latter ones, $\vec{N}_{(hkl)}$ can be written using its projection on the surface X_s - Y_s forming an angle α from X_s axis coupled with an angle β between $\vec{N}_{(hkl)}$ and Z_s (Fig. 3.6), i.e.

$$\vec{N}_{(hkl)} = \|\vec{N}_{(hkl)}\| \begin{pmatrix} \sin\beta\cos\alpha & \sin\beta\sin\alpha & \cos\beta \end{pmatrix} R_s = \|\vec{N}_{(hkl)}\| \begin{pmatrix} 1 & 1 & 1 \\ h & k & l \end{pmatrix} R_c \quad (3.7)$$

and the frames can be linked using Eq. (3.6) so that

$$\|\vec{N}_{(hkl)}\| \begin{pmatrix} \sin\beta\cos\alpha & \sin\beta\sin\alpha & \cos\beta \end{pmatrix} R_s = \|\vec{N}_{(hkl)}\| \begin{pmatrix} 1 & 1 & 1 \\ h & k & l \end{pmatrix} M_r^{-1} R_s \quad (3.8)$$

The elements of the inverse matrix M_r^{-1} will be written as $M_{r_{-ij}}^{-1}$ where $i = 1, 2, 3$ and $j = 1, 2, 3$. Hence, the projection angle α and β can be calculated using

$$\begin{cases} \sin\beta\cos\alpha = \frac{1}{h}M_{r_{-11}}^{-1} + \frac{1}{k}M_{r_{-21}}^{-1} + \frac{1}{l}M_{r_{-31}}^{-1} \\ \sin\beta\sin\alpha = \frac{1}{h}M_{r_{-21}}^{-1} + \frac{1}{k}M_{r_{-22}}^{-1} + \frac{1}{l}M_{r_{-13}}^{-1} \\ \cos\beta = \frac{1}{h}M_{r_{-13}}^{-1} + \frac{1}{k}M_{r_{-23}}^{-1} + \frac{1}{l}M_{r_{-33}}^{-1} \end{cases} \quad (3.9)$$

As a result, :

$$\alpha = \begin{cases} \tan^{-1} \left(\frac{\frac{1}{h}M_{r-12}^{-1} + \frac{1}{k}M_{r-22}^{-1} + \frac{1}{l}M_{r-13}^{-1}}{\frac{1}{h}M_{r-11}^{-1} + \frac{1}{k}M_{r-21}^{-1} + \frac{1}{l}M_{r-31}^{-1}} \right) & \text{if denominator} > 0 \\ \tan^{-1} \left(\frac{\frac{1}{h}M_{r-12}^{-1} + \frac{1}{k}M_{r-22}^{-1} + \frac{1}{l}M_{r-13}^{-1}}{\frac{1}{h}M_{r-11}^{-1} + \frac{1}{k}M_{r-21}^{-1} + \frac{1}{l}M_{r-31}^{-1}} \right) + 180^\circ & \text{if denominator} < 0 \\ 0 & \text{if numerator} > 0 \text{ and denominator} = 0 \\ 90^\circ & \text{if numerator} < 0 \text{ and denominator} = 0 \\ \text{Rejected} & \text{if numerator} = \text{denominator} = 0 \end{cases} \quad (3.10)$$

$$\beta = \cos^{-1} \left(\frac{1}{h}M_{r-13}^{-1} + \frac{1}{k}M_{r-23}^{-1} + \frac{1}{l}M_{r-33}^{-1} \right) \quad (3.11)$$

Remarked that only the angle $\beta \in (0, 90^\circ]$ can be accessed in goniometer as $\psi \in [-90^\circ, 90^\circ]$. The ϕ and ψ of $\vec{N}_{(hkl)}$ in goniometer can thus be known:

$$\begin{cases} \phi = 90^\circ + \alpha \\ \psi = \beta \end{cases} \quad (3.12)$$

or, equivalently,

$$\begin{cases} \phi = -90^\circ + \alpha \\ \psi = -\beta \end{cases} \quad (3.13)$$

3.4.6 Definition of crystal frame in direct and reciprocal lattice and calculation of lattice parameter a_o of Al-alloy(5052)

3.4.6.1 Crystal frame in direct lattice

The unit cell in crystal lattice can be represented by its lattice parameters: three principal axes (\vec{u}_u , \vec{v}_u and \vec{w}_u) and the angles between axes (α , β and γ) (Fig. 3.7).

The reference system of the unit cell R_u is such that:

$$R_u = \begin{pmatrix} \vec{u}_u \\ \vec{v}_u \\ \vec{w}_u \end{pmatrix} \quad (3.14)$$

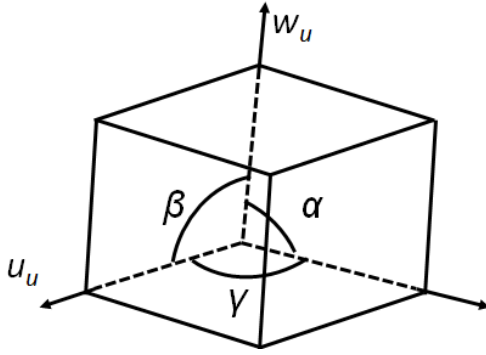


Figure 3.7: Lattice parameters of a unit cell in crystal structure.

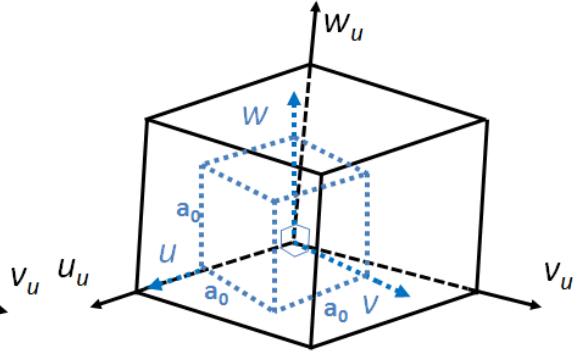


Figure 3.8: Schematic diagram of crystal frame with the non-orthogonal reference system of the unit cell R_u and the orthogonal reference system of crystal R_c .

A metric tensor G_u is introduced to define the relationship between the vectors of the reference system of the unit cell

$$\begin{aligned}
 G_u &= \begin{pmatrix} \vec{u}_u \cdot \vec{u}_u & \vec{u}_u \cdot \vec{v}_u & \vec{u}_u \cdot \vec{w}_u \\ \vec{v}_u \cdot \vec{u}_u & \vec{v}_u \cdot \vec{v}_u & \vec{v}_u \cdot \vec{w}_u \\ \vec{w}_u \cdot \vec{u}_u & \vec{w}_u \cdot \vec{v}_u & \vec{w}_u \cdot \vec{w}_u \end{pmatrix} \\
 &= \begin{pmatrix} u_u^2 & u_u v_u \cos \gamma & u_u w_u \cos \beta \\ u_u v_u \cos \gamma & v_u^2 & v_u w_u \cos \alpha \\ u_u w_u \cos \beta & v_u w_u \cos \alpha & w_u^2 \end{pmatrix} \quad (3.15) \\
 &= \begin{pmatrix} g_{u_{11}} & g_{u_{12}} & g_{u_{13}} \\ g_{u_{21}} & g_{u_{22}} & g_{u_{23}} \\ g_{u_{31}} & g_{u_{32}} & g_{u_{33}} \end{pmatrix}
 \end{aligned}$$

However, the non-orthogonal reference system R_u makes the calculation afterwards complicated. Therefore, an orthonormal crystal reference system R_c with principal axes perpendicular to each other can be defined (Fig. 3.8) with the covariant components written in Eq.(3.4):

$$R_c = \begin{pmatrix} \vec{u} \\ \vec{v} \\ \vec{w} \end{pmatrix} \quad (3.4)$$

so that

$$\begin{cases} \vec{u} = \frac{\vec{u}_u}{|\vec{u}_u|} \\ \vec{v} = \vec{w} \wedge \vec{u} \\ \vec{w} = \frac{\vec{u}_u \wedge \vec{v}_u}{|\vec{u}_u \wedge \vec{v}_u|} = \frac{\vec{w}_u^*}{|\vec{w}_u^*|} \end{cases}, \quad \vec{w}_u^* = \frac{\vec{u}_u \wedge \vec{v}_u}{\vec{w}_u \cdot (\vec{u}_u \wedge \vec{v}_u)} \quad (3.16)$$

where w_u^* is an intermediate vector, constructed from axis of reference system R_u .

w^* will be presented in the following subsections. For FCC, $u = v = w$ and they are named as lattice parameter a_0 . a_0 refers to the initial physical dimension of unit cells in the crystal lattice. i.e. $= a_0$ and the metric tensor of the orthonormal crystal frame G can be expressed as

$$G = a_0 I_{3 \times 3} \quad (3.17)$$

3.4.6.2 Crystal frame in reciprocal lattice

However, once the crystal deforms, the crystal frame will no more be orthogonal. Thus, the reciprocal reference system of unit cell R_u^* and crystal R_c^* is defined from direct lattice, using three principal axes in reciprocal lattice (\vec{u}_u^* , \vec{v}_u^* and \vec{w}_u^*) and (\vec{u}^* , \vec{v}^* and \vec{w}^*) respectively, to facilitate the ε^e calculation.

The definition of R_u^* and R_c^* with their contravariant components are:

$$R_u^* = \begin{pmatrix} \vec{u}_u^* \\ \vec{v}_u^* \\ \vec{w}_u^* \end{pmatrix} \quad (3.18)$$

and

$$R_c^* = \begin{pmatrix} \vec{u}^* \\ \vec{v}^* \\ \vec{w}^* \end{pmatrix} \quad (3.19)$$

where

$$\begin{cases} \vec{u}^* = \frac{\vec{v}_u^* \wedge \vec{w}_u^*}{|\vec{v}_u^* \wedge \vec{w}_u^*|} = \frac{\vec{u}_u}{|\vec{u}_u|} = \vec{u} \\ \vec{v}^* = \vec{w} \wedge \vec{u} = \vec{v} \\ \vec{w}^* = \frac{\vec{w}_u^*}{|\vec{w}_u^*|} = \vec{w} \end{cases} \quad (3.20)$$

In fact, R_c and R_c^* are identical. Similarly, the associated metric tensor G_u^* and G^* can be written as

$$\begin{aligned}
 G_u^* &= \begin{pmatrix} \vec{u}_u^* \cdot \vec{u}_u^* & \vec{u}_u^* \cdot \vec{v}_u^* & \vec{u}_u^* \cdot \vec{w}_u^* \\ \vec{v}_u^* \cdot \vec{u}_u^* & \vec{v}_u^* \cdot \vec{v}_u^* & \vec{v}_u^* \cdot \vec{w}_u^* \\ \vec{w}_u^* \cdot \vec{u}_u^* & \vec{w}_u^* \cdot \vec{v}_u^* & \vec{w}_u^* \cdot \vec{w}_u^* \end{pmatrix} \\
 &= \begin{pmatrix} u_u^{*2} & u_u v_u \cos \gamma^* & u_u^* w_u^* \cos \beta^* \\ u_u^* v_u^* \cos \gamma^* & v_u^{*2} & v_u w_u \cos \alpha^* \\ u_u^* w_u^* \cos \beta^* & v_u^* w_u^* \cos \alpha^* & w_u^{*2} \end{pmatrix} \\
 &= \begin{pmatrix} g_u^{11} & g_u^{12} & g_u^{13} \\ g_u^{21} & g_u^{22} & g_u^{23} \\ g_u^{31} & g_u^{32} & g_u^{33} \end{pmatrix} \\
 &= G_u^{-1}
 \end{aligned} \tag{3.21}$$

where \vec{u}_u^* , \vec{v}_u^* and \vec{w}_u^* represent the three principal axes of the crystal frame in reciprocal lattice, α^* , β^* and γ^* are the angles between each axis in the same frames.

$$G^* = a_0 I_{3 \times 3} \tag{3.22}$$

3.4.6.3 Lattice parameter a_0 of Al-alloy(5052)

The lattice parameter a_0 of our Al-alloy was characterised by XRD in its initial state without residual stress using the powder method. Two different sizes of powder were prepared by filing the material from different directions of the block. It is to ensure the powder contains a random orientation. During each powder sample preparation, a new brand file in steel is used. If not, the remaining particles during previous usage can pollute the prepared powders. The powder samples were scanned by XRD to obtain a 2θ spectrum summarized in Table 3.3.

Sample		{111}	{200}	{220}	{311}	{222}	{400}	{331}
T1	$2\theta_{\{hkl\}}(^{\circ})$	44.89	52.33	77.19	93.94	99.51	123.35	148.02
T2	$2\theta_{\{hkl\}}(^{\circ})$	44.87	52.28	77.16	94	99.54	123.91	148
Block	$2\theta_{\{hkl\}}(^{\circ})$	44.82	52.52	77.08	93.87	99.31	123.17	147.63

Table 3.1: $2\theta_{\{hkl\}}(^{\circ})$ measured on fine powder sample (T1), Coarse powder sample (T2) and block sample (yellow).

Recalling the Bragg's law equation (Eq.(1.14)), the relationship between $d_{\{hkl\}}$ and lattice parameter a_o can be written as:

$$d_{\{hkl\}} = \frac{a_o}{\sqrt{h^2 + k^2 + l^2}} \tag{3.23}$$

Sample	a_o (nm)
T1	0.406
T2	0.406
Block	0.407

Table 3.2: Lattice parameter a_o measured using fine powder sample (T1), Coarse powder sample (T2) and block sample (yellow).

The lattice parameter of Al-alloy(5052) is 0.406nm.

3.4.7 ε^e measuring method in monocrystal: First Ortner Method [Ortner (1986a,b)]

First Ortner method was applied when calculating ε^e of a deformed crystal. Thus, the strain tensor in crystal frame was defined. In order to enhance the precision of ε^e calculation, choice of $\{hkl\}$ planes and criteria associated were also specifically considered.

3.4.7.1 Determination of the strain tensor in crystal frame

The normal of (hkl) plane which is in diffraction position can be written in the orthonormal crystal frame in direct $\vec{N}_{(hkl)}$ or reciprocal lattice $\vec{N}_{(hkl)}^*$. i.e.

$$\vec{N}_{(hkl)} = \begin{pmatrix} 1 & 1 & 1 \\ h & k & l \end{pmatrix} \begin{pmatrix} \vec{u} \\ \vec{v} \\ \vec{w} \end{pmatrix} \quad (3.24)$$

and

$$\vec{N}_{(hkl)}^* = \begin{pmatrix} h & k & l \end{pmatrix} \begin{pmatrix} \vec{u}^* \\ \vec{v}^* \\ \vec{w}^* \end{pmatrix} \quad (3.25)$$

By making a dot product between projecting $\vec{N}_{(hkl)}$ along $\vec{N}_{(hkl)}^*$:

$$\left\| \vec{N}_{(hkl)} \cdot \vec{N}_{(hkl)}^* \right\| = 1 \quad (3.26)$$

which implies that

$$\left\| \vec{N}_{(hkl)}^* \right\| = \frac{1}{\left\| \vec{N}_{(hkl)} \right\|} \quad (3.27)$$

The $d_{(hkl)}^*$ can be seen as the norm of $\vec{N}_{(hkl)}^*$

$$\begin{aligned} \left\| \vec{N}_{(hkl)}^* \right\| &= \frac{1}{d_{(hkl)}} \\ &= d_{(hkl)}^* \end{aligned} \quad (3.28)$$

58 Chapter 3. Elastic strain field measurement using X-ray diffraction

The interreticular distance in reciprocal lattice $d_{(hkl)}^*$ or d^* can be calculated:

$$\|N_{(hkl)}^*\|^2 = \left((h \ k \ l) \begin{pmatrix} u^* \\ v^* \\ w^* \end{pmatrix} \right)^2 \quad (3.29)$$

$$(d^*)^2 = \begin{pmatrix} \vec{u}^* & \vec{v}^* & \vec{w}^* \end{pmatrix} \begin{pmatrix} h^2 & hk & hl \\ hk & k^2 & kl \\ hl & kl & l^2 \end{pmatrix} \begin{pmatrix} \vec{u}^* \\ \vec{v}^* \\ \vec{w}^* \end{pmatrix} \quad (3.30)$$

$$d^{-2} = h^2 \vec{u}^{*2} + k^2 \vec{v}^{*2} + l^2 \vec{w}^{*2} + 2kl \vec{v}^* \vec{w}^* + 2hl \vec{w}^* \vec{u}^* + 2hk \vec{u}^* \vec{v}^* \quad (3.31)$$

Eq. (3.31) can be written as

$$d^{*2} = \begin{pmatrix} h^2 & k^2 & w^2 & 2kl & 2hl & 2hk \end{pmatrix} \begin{pmatrix} \vec{u}^{*2} \\ \vec{v}^{*2} \\ \vec{w}^{*2} \\ \vec{v}^* \vec{w}^* \\ \vec{w}^* \vec{u}^* \\ \vec{u}^* \vec{v}^* \end{pmatrix} \quad (3.32)$$

$$= \begin{pmatrix} h^2 & k^2 & w^2 & 2kl & 2hl & 2hk \end{pmatrix} \begin{pmatrix} g^{11} \\ g^{22} \\ g^{33} \\ g^{31} \\ g^{23} \\ g^{12} \end{pmatrix}$$

One introduces $D^* = d^{*2}$ and it can be calculated using Bragg's law:

$$D^* = d^{-2} = \frac{4\sin^2\theta}{\lambda^2} \quad (3.33)$$

Recalling

$$d^* = \frac{1}{d}; D^* = d^{*2} = d^{-2} \quad (3.34)$$

Since there are 6 contravariant components in G^* , at least 6 $\{hkl\}$ planes are required to determine G^* . However, in order to enhance the measurement precision, more than 6 planes are desired. The relationship between the analysed $\{hkl\}$ plane distance (vector D^* in the reciprocal lattice) and reciprocal metric tensor G^* can be described with a matrix H , which is constructed using the frames of the diffraction vectors of these $\{hkl\}$ planes in the reciprocal lattice:

On the basis of Eq.3.30

$$\begin{pmatrix} D_1^* \\ D_2^* \\ D_3^* \\ \vdots \\ \vdots \\ D_n^* \end{pmatrix} = \begin{pmatrix} h_1^2 & k_1^2 & l_1^2 & 2k_1l_1 & 2h_1l_1 & 2h_1k_1 \\ \vdots & \vdots & \vdots & \vdots & \vdots & \vdots \\ \vdots & \vdots & \vdots & \vdots & \vdots & \vdots \\ h_n^2 & k_n^2 & l_n^2 & 2k_nl_n & 2h_nl_n & 2h_nk_n \end{pmatrix} \begin{pmatrix} G_1^* \\ G_2^* \\ G_3^* \\ G_4^* \\ G_5^* \\ G_6^* \end{pmatrix} \quad (3.35)$$

In Eq.3.35, $G_1^*=g^{11}$, $G_2^*=g^{22}$, $G_3^*=g^{33}$, $G_4^*=g^{23}$, $G_5^*=g^{31}$ and $G_6^*=g^{12}$. This equation can be rewritten as

$$D_{n \times 1}^* = H_{n \times 6} G_{6 \times 1}^* \quad (3.36)$$

The method of least squares has been proposed and used in the publication of Ortner (1986b) to determine G^* as follows,

$$G_{6 \times 1}^* = \left[(H^T \cdot H)^{-1} H^T \right]_{6 \times n} \cdot D_{n \times 1}^* \quad (3.37)$$

The elastic strain tensor ε^e is then determined by:

$$\varepsilon_{ij}^e = \varepsilon^{ij} = \frac{g^{ij} - g_0^{ij}}{2\sqrt{g_0^{ii}}\sqrt{g_0^{jj}}} \quad (3.38)$$

where g_0^{ij} et g^{ij} are the contra-variant coordinates of the initial and the deformed metric tensor G^* .

The calculated elastic strain tensor can be transformed from crystal coordinates ε_c^e to sample coordinates ε_s^e by using the matrix of rotation M_r (ref. Eq. 3.5).

$$\varepsilon_s^e = M_r^{-1} \varepsilon_c^e M_r \quad (3.39)$$

The advantage of using this method is its independence with respect to the 2θ rotation (i.e. $\delta\phi$ and $\delta\psi$ do not need to be considered).

3.4.7.2 Choice of $\{hkl\}$ planes and criteria associated

Besides the requirement to determine the six components of G^* , the measurement of additional $\{hkl\}$ planes will improve the precision of the calculation. Moreover, errors and existing limitations of the experimental apparatus should be taken into consideration. Crystal planes with a larger diffracting plane distance spacing (d-spacing) will have a smaller diffraction Bragg angle and, in consequence, a higher intensity can be obtained.

However, $\{hkl\}$ planes with large values of 2θ improve measurement precision (Tab. 3.3).

The choice of $\{hkl\}$ planes results in a compromise between peak intensity and precision of 2θ variation. Thus, for a sample of Al-alloy with FCC structure, only

$\{hkl\}$	$\{111\}$	$\{200\}$	$\{220\}$	$\{311\}$	$\{222\}$	$\{400\}$	$\{331\}$
2θ ($^\circ$)	44.87	52.29	77.11	93.99	99.51	123.42	148.14
$\delta 2\theta$ ($^\circ$)	-0.203	-0.241	-0.391	-0.527	-0.580	-0.912	-1.721

Table 3.3: Theoretical variation of 2θ corresponding to various $\{hkl\}$ planes of a crystal submitted to a strain of 4.29×10^{-3} (deformation corresponding to the elastic limit of Aluminium) in the $\langle 100 \rangle$ direction.

$\{220\}$, $\{311\}$ and $\{222\}$ planes are considered. According to the limits of the goniometer, 18 $\{hkl\}$ planes fulfil the above requirements. Yet, the grips of the micro-tensile machine restrict the accessible angles for X-ray beam diffracting towards the sample. Even so, a weak diffraction beam intensity is obtained once the cradle inclines more than 75° along the ψ -axis. In the remaining $\{hkl\}$ planes, planes forming a circle in the pole figure are preferred since this combination minimises the uncertainty [Ortner (1986a)]. As a result, after eliminating all the inaccessible $(\phi, \psi)_{hkl}$, 13 $\{hkl\}$ planes are left to be analysed at every XRD measuring point (Fig. 3.9).

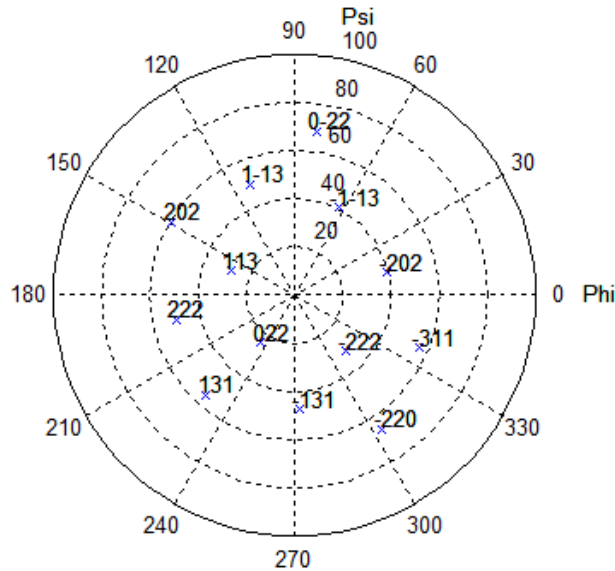


Figure 3.9: Location of the $\{hkl\}$ planes summarized for XRD measurement in grain 7. Only accessible $\{220\}$, $\{311\}$ and $\{222\}$ planes are plotted.

3.5 Development of an experimental methodology for diffraction peak measurement

As previously mentioned, a single crystal will produce diffraction signal only when its diffraction plane $\{hkl\}$ is inclined at $(\phi, \psi)_{\{hkl\}}$ to the incident beam at an angle

θ which fulfills the Bragg's law. Yet, once the crystal deforms, disorientation of crystal texture takes place and the diffraction plane distance $d_{\{hkl\}}$ changes. As a result, the new position $(\phi, \psi, 2\theta)_{\{hkl\}}$ of diffraction peak has to be searched.

Since the diffraction signal is very fine (width $< 1^\circ$), as for ε^e calculation with accuracy, each peak position should be cautiously measured at both its initial and deformed states. In addition, diffraction signal with high signal-to-noise ratio has to be achieved compromising between the beam size, scanning step size and acquisition time. As such, experimental methodologies are developed and presented in this section.

First, the shape of the diffraction peak along different scanning axes (ϕ , ψ and 2θ) is studied. Then, amendments were made in both experimental device and measuring configuration so as to enhance the intensity of diffraction signal. Afterwards, the approach to relocate the peak position and the adjustment on beam size to tackle the existence of mosaicity are presented. At the end, the peak simulation used for determining final 2θ position is introduced.

It is remarked that 2θ measurements were always conducted using θ - 2θ scanning.

3.5.1 Understanding the relationship between the diffraction signal and XRD scanning in ϕ , ψ and 2θ space

As it will be necessary to determine small $2\theta_{\{hkl\}}$ variations of the order of $0.4^\circ - 0.6^\circ$ during the mechanical loading (see Tab. 3.3), the diffraction peak $(\phi, \psi, 2\theta)_{\{hkl\}}$ at both its initial and deformed states should be measured with high accuracy. Before developing an experimental methodology for diffraction peak measurement, we should have a first idea of how the peak shape varies along different scanning axes in goniometer. Therefore, the shapes of $(\phi, \psi)_{\{hkl\}}$ peaks scanned consecutively in 2θ space are recorded. An example is made on the (-220) plane of grain 8 at X=-7, Y=0 on the sample 1 (Fig.3.10).

It is observed that there is a maximum intensity of the diffraction signal in ϕ , ψ and 2θ space where the $\{hkl\}$ planes are well-oriented with respect to the X-ray beam. In order to increase the accuracy of $d_{\{hkl\}}$ measurement, 2θ scanning is launched only when ϕ and ψ reach their maximum intensity. However, challenge might arise to define the final peak position due to the unfocused diffraction signal in ψ direction. This problem and its solution are sorted out in the next subsection.

3.5.2 Focusing the diffracted signal during (ϕ, ψ) measurement: prevent beam divergence using Soller's slits

Initially, the vertical parallel collimator in the goniometer narrows down the diffracted peak to a pointed ϕ signal but this peak remains broad in ψ direction (Fig.3.11a). It makes the determination of the final peak position for 2θ scanning difficult. In order to concentrate the diffracted signal per $(\phi, \psi)_{\{hkl\}}$ measurement (Fig.3.11b), a Soller slit (Fig.3.12) with vertical blades spaced 0.5mm is added in front of the punctual detector.

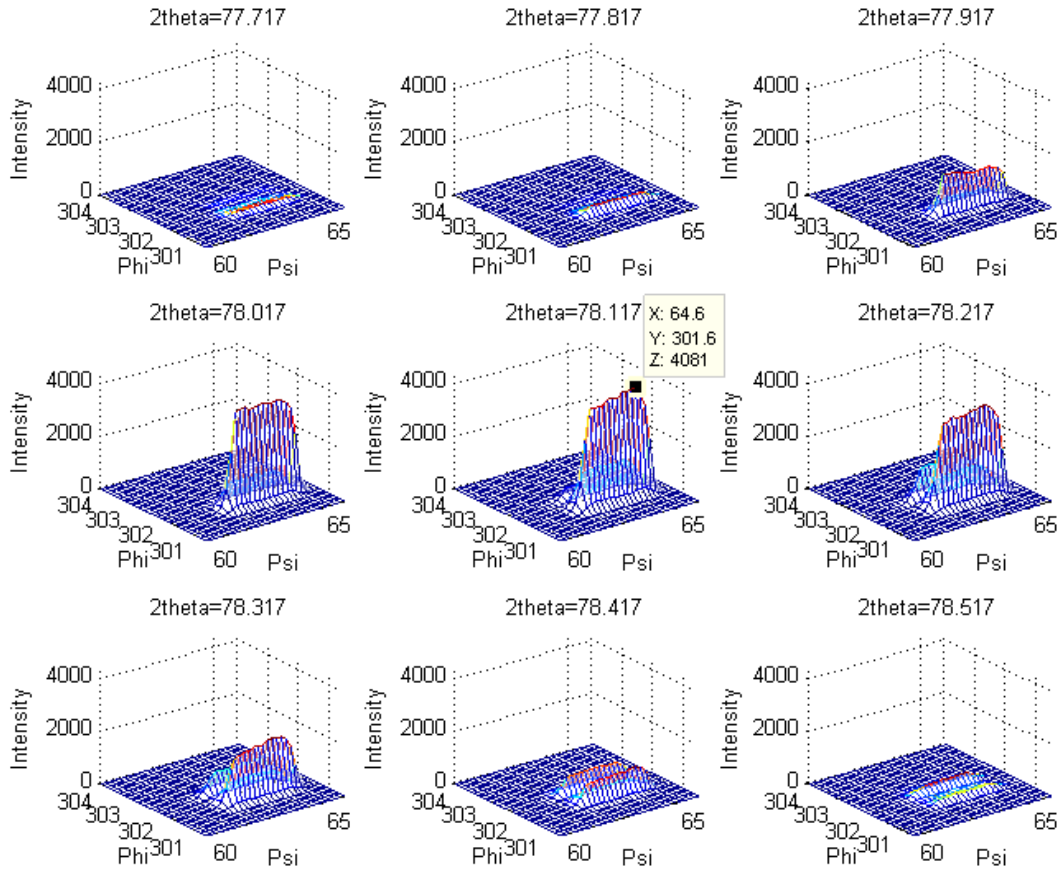


Figure 3.10: The $(\phi, \psi)_{(220)}$ peak shape of grain 8 at $X=-7, Y=0$ of sample 1 along the scanning axis of 2θ with every 0.1° shift. The maximum intensity takes place when $\phi=301.6^\circ$, $\psi=64.6^\circ$ and $2\theta=78.117^\circ$.

When the diffracted rays pass through the Soller slit/vertical parallel collimator, some of them may converge from the edges to the center of these components and then diverge. The maximum angle of the divergence (or the opening angle) β_1 is calculated with the length of Soller slit/vertical parallel collimator $L_{Collimator}$ and the spacing between the blades d_{Blades} (Fig.3.13).

$$\tan \frac{\beta_1}{2} = \frac{L_{Collimator}}{d_{Blades}} \quad (3.40)$$

Opening angle β_1 is $= 2 \tan^{-1}(0.5^\circ/20^\circ) = 2.86^\circ$.

3.5.3 Relocating peak position: iteration process

The positions of the diffraction peak/shapes change during deformation, we decided to consider only the peak positions with the highest intensity. Therefore, an iteration process was designed to search the position of a peak at both its initial

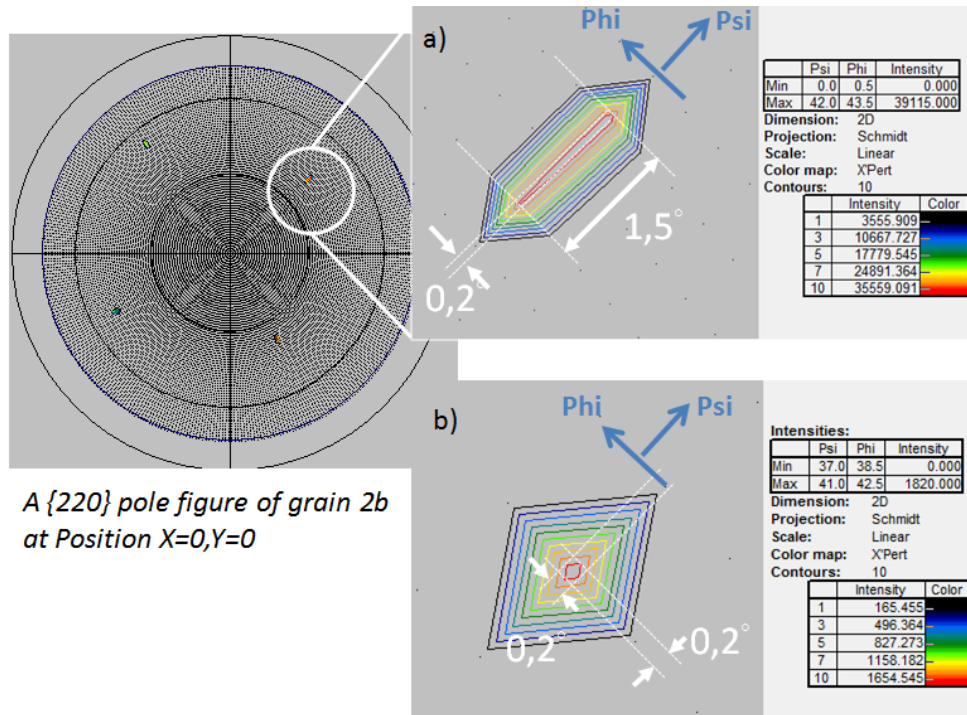


Figure 3.11: A $(\phi, \psi)_{(220)}$ peak of grain 2b of sample 1 scanned a) without and b) with Soller Slit. A more concentrated diffracted signal in both ψ and ϕ directions is achieved by adding a Soller slit in front of the punctual detector.

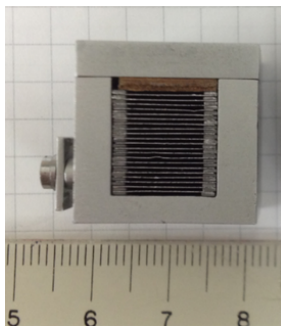


Figure 3.12: Soller Slit with vertical blades spaced d_{Blades} 0.5mm and length $L_{Collimator}$ 20mm.

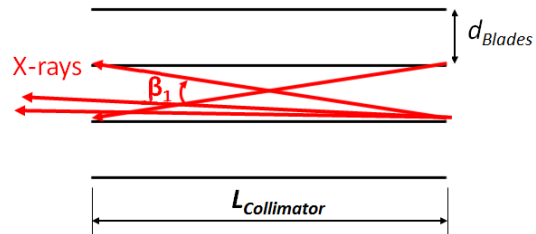


Figure 3.13: Scheme of opening angle β_1 in Soller slit/vertical parallel collimator.

and deformed state. Unlike the process proposed by Eberl (2000) searching along ω , 2θ and ψ , we relocated the peak position along ϕ , ψ and 2θ scanning successively around an initial position determined by the initial grain orientation. This optimisation procedure is repeated until convergence.

The stability of the optimisation process has been tested and validated in a crystal of an Al-alloy sample. Several sets of parameters (ϕ , ψ and 2θ) in the vicinity

of a given peak were considered as initial positions (Fig.3.14). The optimisation process was carried out from these various initial positions to determine the peak position along ϕ , ψ and 2θ . After 3 iterations, all processes converged to nearly the same 2θ value with a variation of 0.005° (Fig.3.15, Fig.3.16).

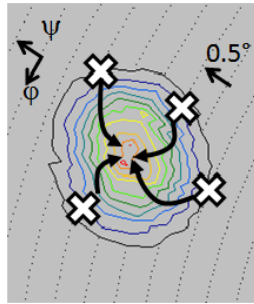


Figure 3.14: Method used for testing the stability of the optimisation process.

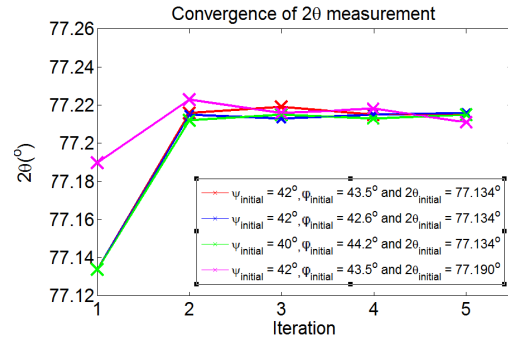


Figure 3.15: Changes in 2θ after several iterations of measurement starting from various initial positions. The dispersion of the final peak position $\Delta 2\theta$ is about 0.005° .

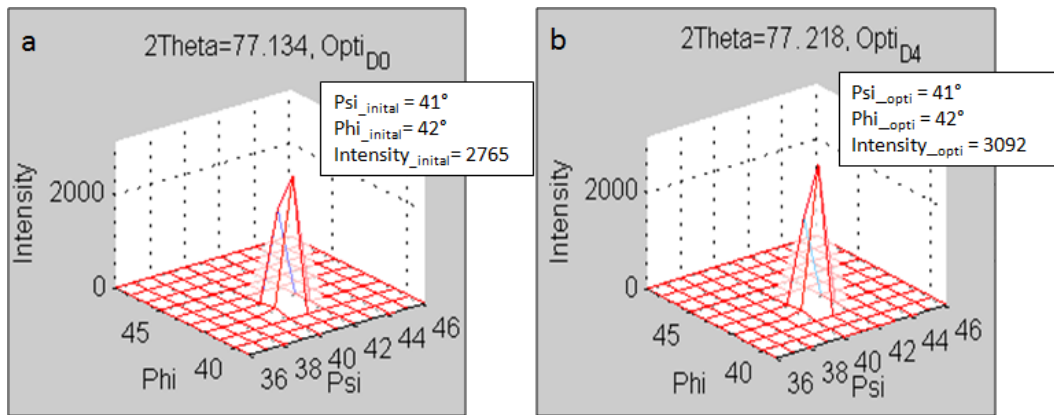


Figure 3.16: The intensity of a $2\theta_{(220)}$ peak (a) before and (b) after optimization

3.5.4 Handling of Mosaicity : Refinement of beam size, choice of scanning step size and acquisition time

Once the tensile test has started, the sample deforms elastically and plastically. The elastic deformation induces peak translation (Fig.1.21 in Chapter 1). After plastic deformation, orientation of a single crystal may change from one place to another one, which is called mosaicity. The mosaicity development as well as dislocation accumulation during plastic deformation cause XRD peak broadening and intensity

decrease (Fig.3.17). The grain disorientation and peak broadening are the evidence of heterogeneous deformation in materials [Crostack et al. (1989)]. The objective of the experimental procedure developed here is to measure peak translation without the interference due to plastic deformation. In some conditions, the plastic deformation may be so large that several distinct peaks may appear (Fig.3.17).

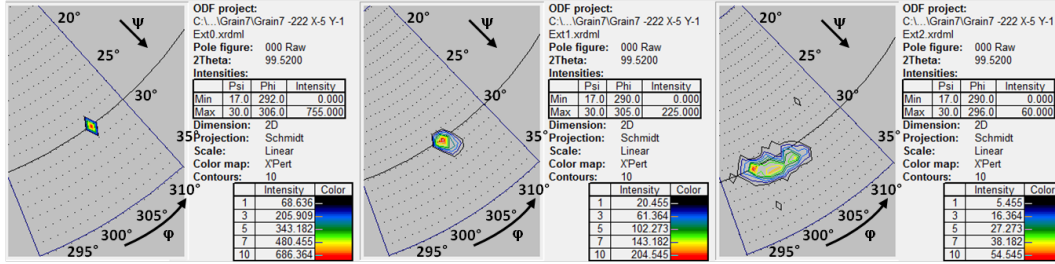


Figure 3.17: Evolution of a peak of $(-222)_{Grain7}$ of sample 1 from its initial state (left), to $\bar{\epsilon}_{xx}^t = 7.4 \times 10^{-3}$ (middle) and $\bar{\epsilon}_{xx}^t = 0.0356$ (right). Intensity drops as strain level increases due to the crystal orientation dispersion during plastic deformation.

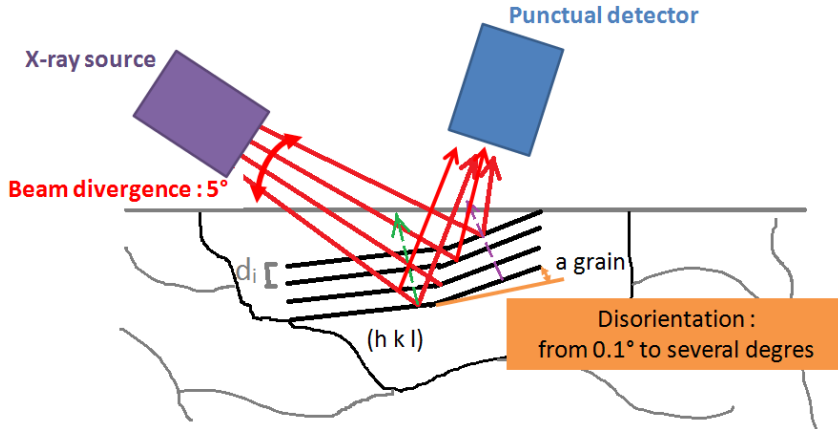


Figure 3.18: Condition for a X-ray beam is diffracted on the crystal lattice with disorientation - appearance of mosaicity

A minority of the incident beam has an inevitable divergenc of 5° (Fig.3.18). If disorientation exists inside a grain, a diffracted signal with more than one peak can be captured. It makes the analysis of the complete signal more complicated since the determination of the final peak position has to consider all the integrated signals. Moreover, error may appear during peak optimisation program in goniometer when two peaks with similar intensities appear. In order to minimize the measuring influence brought by mosaicity [Marty et al. (1997)] and to ensure a contentious XRD execution, the beam size has been refined to $0.1 \times 0.1 \text{ mm}^2$ (Fig.3.19).

At the same time, the parameters of XRD scanning were searched to better display the peak shape. For 2θ measurement, the scanning step size of 0.05° and the

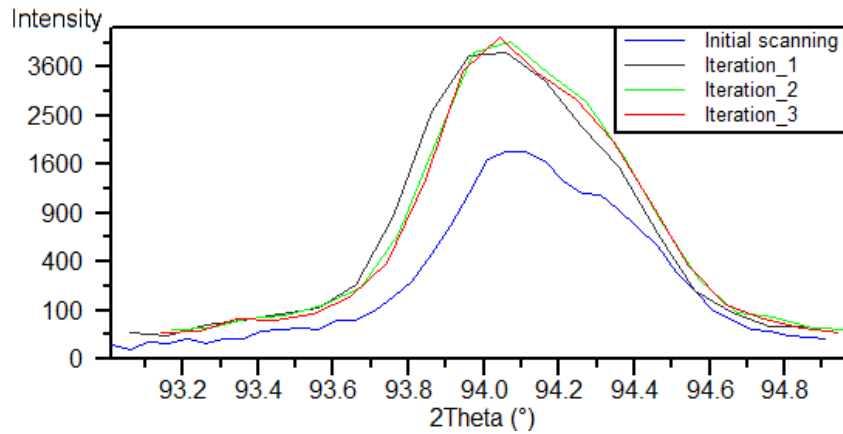


Figure 3.19: An iteration process conducted at a point with mosaicity using a beam size of $0.1 \times 0.1 \text{ mm}^2$.

acquisition time of 1 s were used (Fig.3.20) such that the diffraction signal contains less influence given by the background noise. The intensity is also sufficient for the peak measurement and optimisation, e.g. the signal to noise ratio always remains higher than 60.

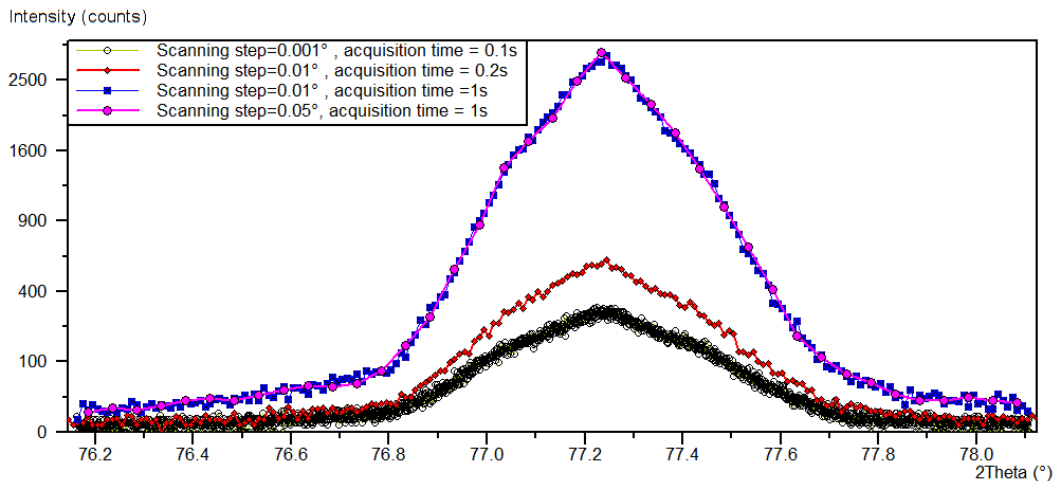


Figure 3.20: A 2θ scanning of a peak of $(220)_{Grain2b}$ of sample 1 with different scanning step sizes and acquisition times.

3.5.5 Determination of the final peak position: Peak simulation

The final 2θ peak position determination is presented. The X-ray K_α line is by far the strongest emitted X-ray spectral line. It contains 2 lines: $K_{\alpha 1}$ and $K_{\alpha 2}$ with wavelengths relatively close ($\lambda_{K_{\alpha 1}(Co)} = 0.178897 \text{ nm}$ and $\lambda_{K_{\alpha 2}(Co)} = 0.179285 \text{ nm}$).

3.5. Development of an experimental methodology for diffraction peak measurement 67

These components are not easily resolved. During 2θ measurement, both $K_{\alpha 1}$ and $K_{\alpha 2}$ interact with $\{hkl\}$ crystalline planes (Fig. 3.21) and, therefore, a diffraction peak doublet is obtained.

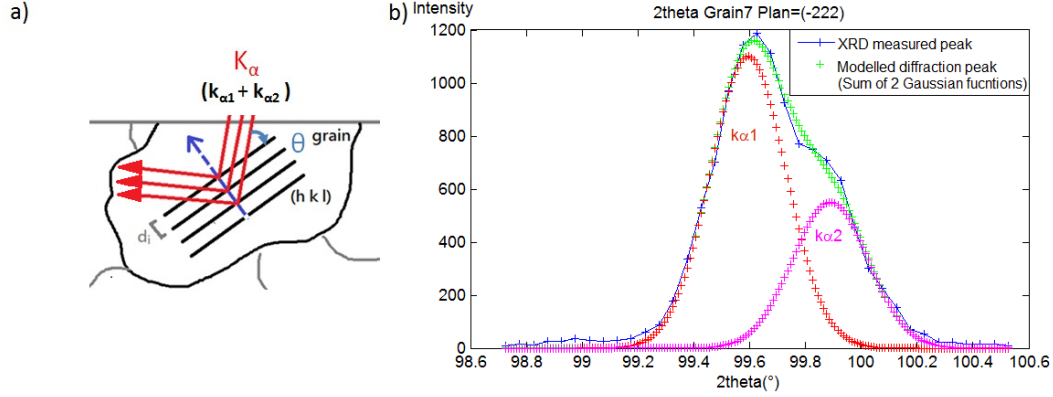


Figure 3.21: (a) Scheme of X-ray diffraction. (b) 2θ measured by XRD (solid line) contains peak doublets. Simulation of the peak (dashed line).

Owing to the complicated form of the peak, the 2θ position is difficult to be determined immediately. The peak position is sought through an inverse method by modelling the diffracted peak as the sum of two Gaussian functions \mathcal{G} (Eq.3.41).

Gaussian function \mathcal{G} for each spectral line is defined as

$$\mathcal{G}(A_p, h_p, 2\theta_p) = \frac{2A_p}{h_p} \sqrt{\frac{\ln 2}{\pi}} e^{-\frac{4(\ln 2)}{h_p^2} (2\theta_p - 2\theta)^2} \quad (3.41)$$

with the properties:

1. h_p is the full width at half maximum (FWHM)
2. Amplitude A_p of $K_{\alpha 1}$ is always twice as large as that of $K_{\alpha 2}$

$$A_{p_K\alpha 1} = 2A_{p_K\alpha 2} \quad (3.42)$$

3. $2\theta_p$ is the simulated final peak position. The Gaussian function \mathcal{G} is defined in the range $[2\theta_p - 2\theta, 2\theta_p + 2\theta]$. As d_{hkl} is the same for $K_{\alpha 1}$ and $K_{\alpha 2}$, Bragg's law (Eq.1.14) can be applied to describe the relationship of the peak position between $K_{\alpha 1}$ ($\theta_{K\alpha 1}$) and $K_{\alpha 2}$ ($\theta_{K\alpha 2}$).

$$\frac{\lambda_{K\alpha 1}}{\sin(\theta_{p_K\alpha 1})} = \frac{\lambda_{K\alpha 2}}{\sin(\theta_{p_K\alpha 2})} \quad (3.43)$$

Several peak forms were tested, Gaussian functions were the most appropriate to predict experimental diffraction peaks. After minimising the difference between ex-

perimental and simulated data, the optimised $2\theta_{p_{K\alpha 1}}$ was used to calculate elastic strain tensor.

3.5.6 Assumption of XRD in single crystal at deformed state

As the strain levels remain small ($\varepsilon^t < 5\%$) during the experiment presented, the displacement of the peaks was small enough to consider the position associated with the previous loading step as a starting point for searching for the peak position after deformation.

3.6 Uncertainty estimation of the elastic strain tensor σ_{ε^e}

The calculated ε^e using XRD signal includes also the errors coming from our experimental device or the numerical approach proposed to determine the final peak position. Thus, the associated uncertainties σ_{ε^e} should be quantified to ensure the obtained local elastic strain data is reliable.

It is first necessary to evaluate the uncertainty of peak position measurement σ_θ , and then, by knowing this value, σ_{ε^e} can be calculated. It is assumed that the error of the peak position σ_θ has two main sources: one is related to the peak repositioning by the diffractometer $\Delta 2\theta$, and another is linked to the discretization of the intensity curve in $\delta 2\theta$. So, a priori, both of these sources of error have to be quantified. Moreover, although the method chosen to estimate σ_{ε^e} is discretization-related (Eq.3.53), if the repositioning error shows a more significant value, it should be taken into account instead.

3.6.1 Uncertainty of peak position σ_θ

To evaluate σ_θ , two approaches were used. The first approach consisted in determining the position of a given peak from various initial positions, and comparing the final peak positions obtained. As mentioned in §.3.5.3, the error obtained is $\Delta 2\theta = \pm 0.0025^\circ$.

$$\Delta\theta \leq 0.00125^\circ \tag{3.44}$$

However, this approach took into account only one part of the measurement chain. It was also necessary to evaluate the accuracy of the method used to determine the peak position from the distribution of intensities around a peak. Inspired by the method for calculating displacement and total strain field uncertainties [Hild and Roux (2008)], an evaluation of the precision of peak position measurement with small shifts in θ was conducted as follows:

1. For existing XRD data measured with a scanning step size of 0.05° (blue line

with markers \times), a shift of $\delta\theta$ ($\leq 0.05^\circ$) was imposed, i.e. $2\theta' = 2\theta + \delta\theta$ (black markers $+$) (Fig. 3.22).

2. The discrete experimental points were projected on the shifted line by linear interpolation (green points with markers $*$).
3. The peak simulation process presented in §.3.5.5 was carried out to determine the peak positions for both the initial measurement $2\theta_{XRD}$ and shifted-projected measurement $2\theta_{shifted}$.
4. The change between the imposed $\delta\theta$ and the calculated $\delta\theta$ ($\delta\theta = 2\theta_{XRD}$ and $2\theta_{shifted}$) was calculated.

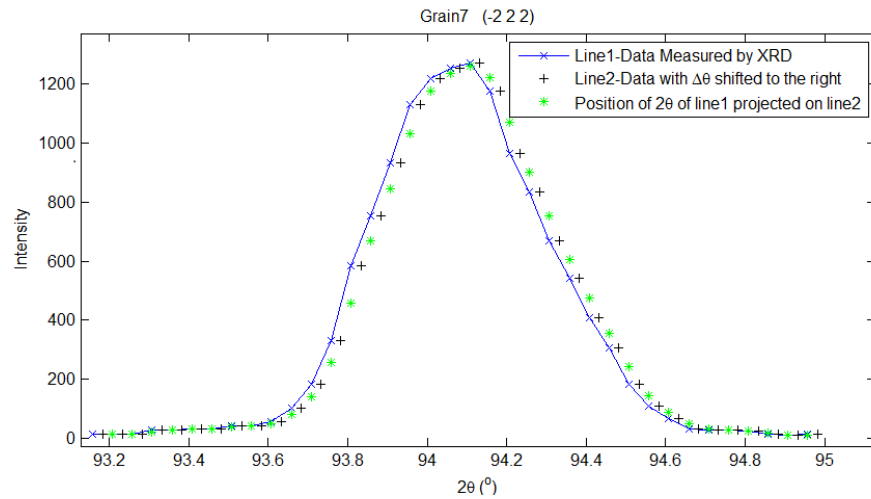


Figure 3.22: Method to evaluate the ability of detecting small peak displacements along θ .

A measuring point in Grain7 of sample 1 at position $X=-5$ $Y=-3$ was taken as an example in results of Tab. 3.4. Errors in $\delta\theta_{-202}$, $\delta\theta_{-131}$ and $\delta\theta_{-222}$ were observed for small peak displacements along θ (Tab. 3.4). The fractional changes between imposed and obtained $\delta\theta$ were calculated. This error was insignificant starting from $\delta\theta_{imposed} = 0.025^\circ$ — half of the scanning step size — until 0.0001° as the criterion of 5% of error was firstly reached using $\delta\theta_{-222}$. As a result, the smallest measurable shift is 0.0001° before reaching the arbitrary criterion.

The error in the measurement of θ is thus

$$\delta\theta \leq 0.0001^\circ \quad (3.45)$$

Since the error from peak repositioning $\Delta\theta$ ($\leq 0.00125^\circ$) is much larger than the one caused by the limitation of our peak simulation equation $\delta\theta$ ($\leq 0.0001^\circ$), $\Delta\theta$ is considered as the major contribution to the uncertainty of elastic strain tensor σ_{ε^e} . Assuming that $\Delta\theta$ follows normal distribution law and 99.7% of the values are

70 Chapter 3. Elastic strain field measurement using X-ray diffraction

$\delta\theta$ imposed($^\circ$)	$\delta\theta_{-202}$ ($^\circ$)	Error(%)	$\delta\theta_{-131}$ ($^\circ$)	Error(%)	$\delta\theta_{-222}$ ($^\circ$)	Error(%)
0.05	0.05	0	0.05	0	0.05	0
0.025	0.025	0	0.0249	0.4	0.0251	0.4
0.0125	0.0124	0.8	0.0124	0.8	0.0124	0.8
0.00625	0.0062	0.8	0.0062	0.8	0.0061	2.4
...
7.8×10^{-4}	7.7×10^{-4}	2.1	7.7×10^{-4}	1.9	7.6×10^{-4}	3.2
3.9×10^{-4}	3.8×10^{-4}	2.1	3.8×10^{-4}	1.9	3.8×10^{-4}	3.6
1.9×10^{-4}	1.9×10^{-4}	2.1	1.9×10^{-4}	1.7	1.9×10^{-4}	4.2
9.8×10^{-5}	9.6×10^{-5}	2.1	9.6×10^{-5}	1.3	9.3×10^{-5}	5.3

Table 3.4: Errors in $\delta\theta_{-202}$, $\delta\theta_{-131}$ and $\delta\theta_{-222}$ were observed for small peak displacement along θ in Grain7 of sample 1 at position X=-5 Y=-3. The changes between the imposed and obtained $\delta\theta$ were calculated as percentages. The lowest limit for the measurable shifting error was found to be 10^{-4} corresponding to 5%-change.

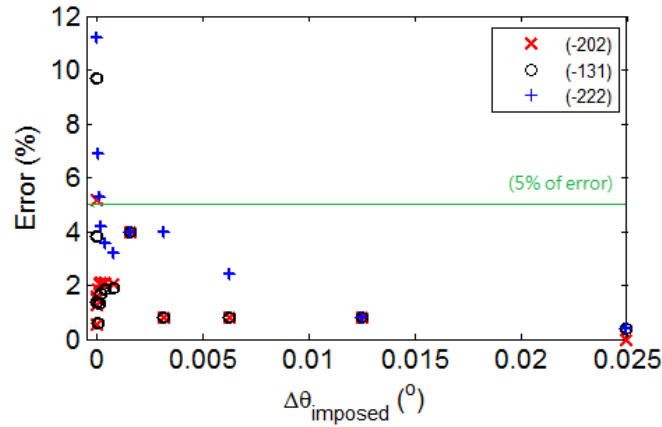


Figure 3.23: Error between $\delta\theta_{imposed}$ and $\delta\theta_{hkl}$ in Grain7 at a measuring point.

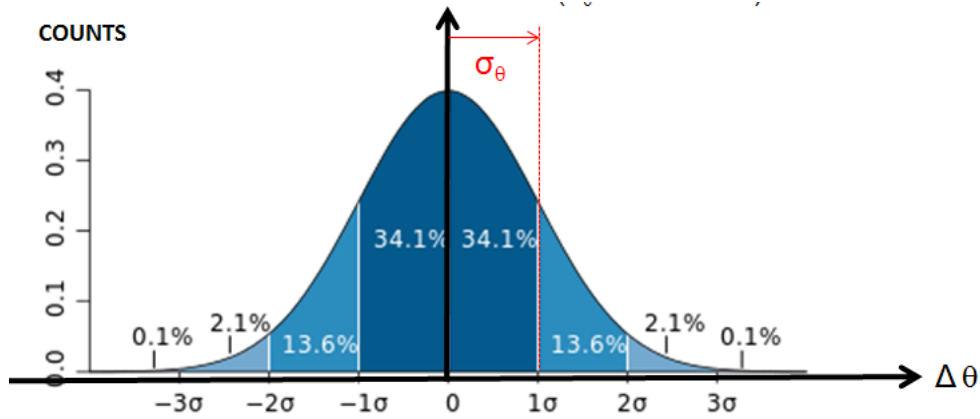


Figure 3.24: Since $\Delta 2\theta$ in peak repositioning = 0.005° , $\Delta\theta = \pm 0.00125$. Assume the uncertainty of θ is in normal distribution ($\sigma_\theta = 4.167e^{-4}$).

within 3 standard deviations of the mean (Fig.3.24), therefore its standard deviation σ_θ is one-third of $\Delta\theta$

$$\sigma_\theta = 0.00042^\circ \quad (3.46)$$

3.6.2 Uncertainty of the elastic strain tensor σ_{ε^e}

Given the uncertainty of the diffracting angles evaluated in Eq.3.46, the uncertainty for elastic strain tensor σ_{ε^e} can be quantified.

3.6.2.1 Range of uncertainty for elastic strain tensor σ_{ε^e}

Eq.(3.37) can be rewritten as

$$G_{6 \times 1}^* = B_{6 \times n} D_{n \times 1}^* \quad (3.47)$$

where $B = (H^T \cdot H)^{-1} H^T$ is known as the pseudoinverse of H .

$$\begin{pmatrix} G_1^* \\ G_2^* \\ \vdots \\ G_6^* \end{pmatrix} = \begin{pmatrix} B_{11} & B_{12} & B_{13} & \cdots & B_{1n} \\ B_{21} & B_{22} & B_{23} & \cdots & B_{2n} \\ \vdots & \vdots & \vdots & \ddots & \vdots \\ B_{61} & B_{62} & B_{63} & \cdots & B_{6n} \end{pmatrix} \begin{pmatrix} D_1^* \\ D_2^* \\ \vdots \\ D_n^* \end{pmatrix} \quad (3.48)$$

G_m^* is a linear function of D_n^* :

$$G_m^* = B_{m1} D_1^* + B_{m2} D_2^* + \cdots + B_{mn} D_n^* \quad , \quad m = 1, 2, \dots, 6 \quad (3.49)$$

$$G_m^* = \sum_{i=1}^n B_{mi} D_i^* \quad (3.50)$$

By expressing D_i^* as a function of θ using Eq.3.33, one obtains:

$$G_m^* = \frac{4}{\lambda^2} \sum_{i=1}^n B_{mi} \sin^2 \theta_i \quad (3.51)$$

72 Chapter 3. Elastic strain field measurement using X-ray diffraction

where θ_i is a diffraction angle measured during the experiment. Let $\theta_{i=1,\dots,n}$ and $\theta_{i=n+1,\dots,2n}$ be n diffraction angles measured (actual value) in the deformed and initial states respectively, so that θ_1 corresponds to the evolution of θ_{n+1} , θ_2 corresponds to the evolution of θ_{n+2} , etc. Now, ε^e in Eq.3.38 can be also expressed in terms of θ_i by

$$\varepsilon_{m=1,\dots,6}^e = \begin{pmatrix} \frac{\sum_{i=1}^n B_{1i}(\sin^2\theta_i - \sin^2\theta_{n+i})}{2 \sum_{i=1}^n B_{1i}\sin^2\theta_{n+i}} \\ \frac{\sum_{i=1}^n B_{2i}(\sin^2\theta_i - \sin^2\theta_{n+i})}{2 \sum_{i=1}^n B_{2i}\sin^2\theta_{n+i}} \\ \frac{\sum_{i=1}^n B_{3i}(\sin^2\theta_i - \sin^2\theta_{n+i})}{2 \sum_{i=1}^n B_{3i}\sin^2\theta_{n+i}} \\ \frac{\sum_{i=1}^n B_{4i}(\sin^2\theta_i - \sin^2\theta_{n+i})}{\sqrt{2 \sum_{i=1}^n B_{2i}\sin^2\theta_{n+i}} \sqrt{2 \sum_{i=1}^n B_{3i}\sin^2\theta_{n+i}}} \\ \frac{\sum_{i=1}^n B_{5i}(\sin^2\theta_i - \sin^2\theta_{n+i})}{\sqrt{2 \sum_{i=1}^n B_{1i}\sin^2\theta_{n+i}} \sqrt{2 \sum_{i=1}^n B_{3i}\sin^2\theta_{n+i}}} \\ \frac{\sum_{i=1}^n B_{6i}(\sin^2\theta_i - \sin^2\theta_{n+i})}{\sqrt{2 \sum_{i=1}^n B_{1i}\sin^2\theta_{n+i}} \sqrt{2 \sum_{i=1}^n B_{2i}\sin^2\theta_{n+i}}} \end{pmatrix} \quad (3.52)$$

where $\varepsilon_1^e = \varepsilon_{11}^e$, $\varepsilon_2^e = \varepsilon_{22}^e$, $\varepsilon_3^e = \varepsilon_{33}^e$, $\varepsilon_4^e = \varepsilon_{23}^e$, $\varepsilon_5^e = \varepsilon_{31}^e$ and $\varepsilon_6^e = \varepsilon_{12}^e$. When ε^e is represented by its first-order Taylor series expansion around the true values $\mu_1, \mu_2, \dots, \mu_{2n}$, it becomes:

$$\varepsilon_{m=1,\dots,6}^e \approx \varepsilon_m^e(\mu_1, \mu_2, \dots, \mu_{2n}) + \sum_{i=1}^{2n} \left[\frac{\partial \varepsilon_m}{\partial \theta_i}(\mu_1, \mu_2, \dots, \mu_{2n}) \right] [\theta_i - \mu_i] \quad (3.53)$$

Eq.(3.53) is of the form $\varepsilon_m^e \approx a_{m0} + \sum_{i=1}^{2n} a_{mi}(\theta_i - \mu_i)$ with

$$a_{m0} = \varepsilon_m^e(\mu_1, \mu_2, \dots, \mu_{2n}) \quad (3.54)$$

and

$$a_{mi} = \frac{\partial}{\partial \theta_i} B_m \varepsilon_m^e(\mu_1, \mu_2, \dots, \mu_{2n}) \quad (3.55)$$

The mean $\overline{\varepsilon_m^e}$ and the standard derivation $\sigma_{\varepsilon_m^e}^2$ can be calculated as follows:

$$\begin{aligned} \mu_{\varepsilon_m^e} &= E[\varepsilon_m^e] \\ &= E \left[a_{m0} + \sum_{i=1}^{2n} a_{mi}(\theta_i - \mu_i) \right] \\ &= E[a_{m0}] + \sum_{i=1}^{2n} (E[a_{mi}\theta_i] - E[a_{mi}\mu_i]) \\ &= a_{m0} + \sum_{i=1}^{2n} (a_{mi}E[\theta_i] - a_{mi}E[\mu_i]) \\ &= a_{m0} + \sum_{i=1}^{2n} (a_{mi}\mu_i - a_{mi}\mu_i) \\ &= a_{m0} \end{aligned} \quad (3.56)$$

$$\begin{aligned}
 \sigma_{\varepsilon_m^e}^2 &= E \left[(\varepsilon_m^e - \overline{\varepsilon_m^e})^2 \right] \\
 &= E \left[\left(\sum_{i=1}^{2n} a_{mi} (\theta_i - \mu_i) \right)^2 \right] \\
 &= E \left[\sum_{i=1}^{2n} a_{mi} (\theta_i - \mu_i) \sum_{j=1}^{2n} a_{mj} (\theta_j - \mu_j) \right] \\
 &= E \left[\sum_{i=1}^{2n} a_{mi}^2 (\theta_i - \mu_i)^2 + \sum_{i \neq j} \sum a_{mi} a_{mj} (\theta_i - \mu_i) (\theta_j - \mu_j) \right] \quad (3.57) \\
 &= \sum_{i=1}^{2n} a_{mi}^2 E \left[(\theta_i - \mu_i)^2 \right] + \sum_{i \neq j} \sum a_{mi} a_{mj} E \left[(\theta_i - \mu_i) (\theta_j - \mu_j) \right] \\
 &= \sum_{i=1}^{2n} a_{mi}^2 \sigma_{\theta_{-mi}}^2 + \sum_{i \neq j} \sum a_{mi} a_{mj} \sigma_{ij}
 \end{aligned}$$

Though $\theta_i(s)$ are dependent, the source of measuring error are independent ($\sigma_{\theta_{-mi}}^2 = \sigma_{\theta}^2$), the covariance σ_{ij} then disappears and the resulting approximated variance is

$$\sigma_{\varepsilon_m^e}^2 = \sum_{i=1}^n \left(\frac{\partial}{\partial \theta_i} \varepsilon_m^e \right)^2 \sigma_{\theta}^2 \quad (3.58)$$

For example, elastic strain tensor ε^e calculated with 13 diffraction planes in Grain7 of sample 1 at the same measuring point (position: X=-5 Y=-3) (Tab.3.5) is in sample co-ordinate system:

$$\varepsilon^e = \begin{pmatrix} 1.1 & 3 & 3 \\ 3 & -2 & 2 \\ 3 & 2 & 1 \end{pmatrix} \times 10^{-4} \quad (3.59)$$

The uncertainty σ_{ε^e} associated is:

$$\sigma_{\varepsilon^e} \leq \begin{pmatrix} 8.7 & 6.8 & 5.8 \\ 6.8 & 10.7 & 7.2 \\ 5.8 & 7.2 & 6.4 \end{pmatrix} \times 10^{-6} \quad (3.60)$$

3.6.2.2 Influence of the number of measuring planes on ε^e uncertainty

However, not every measuring point presents 13 diffraction planes since mosaicity increases during plastic deformation, as shown in Fig.3.17. In some regions of the specimens, the number of diffraction planes of a given point decreases during the test as plasticity and mosaicity increases. For example, the ε^e calculated with minimum 6 diffraction planes for Grain7 of sample 1 at the same measuring point (position: X=-5 Y=-3) in sample co-ordinate system is

h	k	l	$2\theta(^{\circ})$ ($\varepsilon_{xx}^t=0$)	$2\theta(^{\circ})$ ($\varepsilon_{xx}^t=0.0074$)
-2	0	2	77.1509	77.1755
-2	2	0	77.1746	77.1092
0	-2	2	77.1920	77.0938
0	2	2	77.1572	77.1310
2	0	2	77.1571	77.1439
-3	1	1	93.9495	93.9713
-1	-1	3	93.9894	93.9742
-1	3	1	94.0022	93.8989
1	-1	3	93.9911	93.9372
1	1	3	93.9695	93.9613
1	3	1	93.9867	93.9305
-2	2	2	99.5814	99.5601
2	2	2	99.5827	99.5495

Table 3.5: 2θ of 13 $\{hkl\}$ planes in Grain7 (X=-5,Y=-3) measured by XRD at its initial state and $\varepsilon_{xx}^t = 0.0074$.

$$\varepsilon^e = \begin{pmatrix} 1.7 & -7 & -3 \\ -7 & 0 & 3 \\ -03 & 3 & 1 \end{pmatrix} \times 10^{-4} \quad (3.61)$$

and its σ_{ε^e} range is

$$\sigma_{\varepsilon^e} \leq \begin{pmatrix} 3.9 & 5.7 & 6.1 \\ 5.7 & 5.1 & 4.2 \\ 6.1 & 4.0 & 1.8 \end{pmatrix} \times 10^{-5} \quad (3.62)$$

The uncertainty of ε^e calculated with 6 $\{hkl\}$ planes is much larger than those with 13 $\{hkl\}$ planes. Therefore, the number of $\{hkl\}$ planes used gives an influence towards ε^e accuracy. The more planes used for ε^e calculation, the more accurate the answer.

As the number of measuring planes depends on the point considered, the σ_{ε^e} range of each XRD measuring point was calculated according to the number of diffractable $\{hkl\}$ planes left over. It can be foreseen that the ε^e uncertainties σ_{ε^e} are always smaller than 10^{-5} . Considering a Gaussian distribution, it implies a total error range in ε^e smaller than $\pm 3 \times 10^{-5}$.

A confirmation of σ_{ε^e} calculated with 13 and 6 $\{hkl\}$ is made using a Monte Carlo Method (See Annex.5.3). Therefore, the analytical method presented in this section enables us to quantify the σ_{ε^e} during ε^e measurement.

3.7 Discussion

3.7.1 Penetration of X-ray beam during ε^e measurement - Why is it considered as a surface measurement in this experiment?

X-rays are partly transmitted and partly absorbed (or reflected) when they encounter any substance. X-ray absorption by material can be expressed in relation with the intensity of incident X-ray beam (I_0), intensity of transmitted beam after passing through a thickness x (I_x) perpendicularly, a linear absorption coefficient ($\mu/\rho=73.4\text{cm}^2/\text{g}$ for $\text{Co}_K\alpha$ X-ray and Aluminium as absorber) and material density (ρ) ($2.7\text{g}/\text{cm}^3$ for Aluminium) [Cullity (1978)].

$$I_x = I_0 e^{-(\mu/\rho)(\rho x)} \quad (3.63)$$

If half of the intensity is transmitted, the thickness of the material should be

$$\frac{I_x}{I_0} = e^{-209.358x} \quad (3.64)$$

$$x = 33\mu\text{m} \quad (3.65)$$

During XRD, X-ray beam is positioned with an inclination of θ to the sample surface, i.e. 77.134° for $\{220\}$. With less than half of the intensity is transmitted (or with at least half of the I_0 is diffracted), the depth of analysing zone of the tilted sample should be less than $33\mu\text{m} \times \sin(77.134^\circ/2) = 20.6\mu\text{m}$. Since the sample is 0.55mm thick, XRD only enables to obtain a surface information of a sample under mechanical test in our experiment.

3.7.2 Influence of the change of sample thickness towards the diffraction area during deformation.

The z-position of sample was regulated by determining where the sample cuts the X-ray beam in half when $2\theta = 0$. It is to ensure the sample was correctly positioned with respect to X-ray beam and the maximum intensity of diffraction signal was obtained. Otherwise, the diffracted signal at wrong position with non maximized intensity is meaningless.

As for understanding the impact of the change of sample thickness towards the diffraction area during deformation, the studied sample is assumed to be deformed up to $\varepsilon_{xx}^t = 4\%$ ($\varepsilon_{xx}^t = 3.56\%$ in the experiment of sample 1). The Poisson ratio is 0.3.

Then, the elastic strain in sample thickness ε_{zz}^e will be

$$\begin{aligned}
 \varepsilon_{zz}^e &= -0.3 \times (\varepsilon_{xx}^e) \\
 &= -0.3 \times (\varepsilon_{xx}^t - \varepsilon_{xx}^p) \\
 &= -0.3 \times (0.04 - \varepsilon_{xx}^p) \\
 &= -0.012 + 0.3 \times \varepsilon_{xx}^p
 \end{aligned} \tag{3.66}$$

i.e. the change of the thickness of the sample $\delta d_{sample\,thickness}$:

$$\begin{aligned}
 \delta d_{sample} &= \varepsilon_{zz}^e \times d_{sample} \\
 &= (-0.012 + 0.3 \times \varepsilon_{xx}^p) \times d_{sample} \\
 &= (-0.0066 + 0.165 \times \varepsilon_{xx}^p) mm
 \end{aligned} \tag{3.67}$$

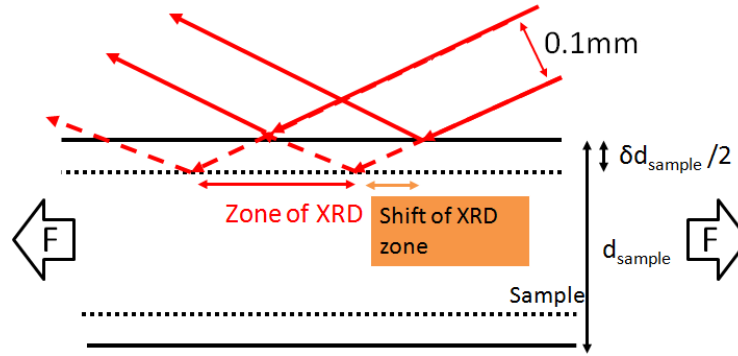


Figure 3.25: Scheme of the shift of XRD zone during deformation.

Since ε_{xx}^p is always smaller than ε_{xx}^t , $\delta d_{sample\,thickness}$ is between the value of -0.0066 mm and 0 mm. Thanks to the grip system at two ends of the sample, the deformation in thickness is symmetric. So, the maximum shift of the XRD zone for $2\theta_{220}$ (Fig.3.25):

$$\begin{aligned}
 \text{Maximum shift of the XRD zone} &= \frac{\frac{\delta d_{sample}}{2}}{\tan\left(\frac{2\theta_{min}}{2}\right)} \\
 &= \frac{0.0033}{\tan\left(\frac{77.134^\circ}{2}\right)} \\
 &= 4.2\mu m
 \end{aligned} \tag{3.68}$$

and the minimum shift of the XRD zone for $2\theta_{222}$

$$\begin{aligned}
 \text{Minimum shift of the XRD zone} &= \frac{\frac{\delta d_{sample}}{2}}{\tan\left(\frac{2\theta_{max}}{2}\right)} \\
 &= \frac{0.0033}{\tan\left(\frac{99.5^\circ}{2}\right)} \\
 &= 2.8\mu m
 \end{aligned} \tag{3.69}$$

As the beam size used during experiment is $0.1 \times 0.1\text{mm}^2$, the shift of the XRD zone during deformation is therefore negligible ($<6\%$).

3.8 Conclusion

In this chapter, the X-ray diffractometer used in experiment and its optical path during diffraction were presented. The experimental procedure designed for ε^e measurement using XRD was introduced in details.

A grid resolution of 1 cm x 1 cm for XRD was defined on the sample surface and each crystal contains about 10 points of measurement. A gradient of elastic strain can be thus given. It enriches the insight of local response of the sample during the deformation, rather than using only one measurement per crystal to represent local information. The technique of launching XRD in a single crystal was presented as well because diffraction signal can only be obtained under two conditions: the normal of the analysed $\{hkl\}$ planes is oriented correctly (ϕ , ψ and $2\theta\}_{hkl_{grain}}$ with respect to X-ray source and Bragg's law is satisfied. The position (ϕ , ψ) can be calculated using the grain orientation $(\varphi_1, \Phi, \varphi_2)_{grain}$.

For ε^e calculation, the First Ortner Method was applied. This method makes use of the relationship between evolution of diffraction planes δd_{hkl} and the lattice coordinates of at least 6 analysed $\{hkl\}$ planes to determine the local elastic strain. In order to improve the precision of ε^e calculation, the combinations of the chosen $\{hkl\}$ planes should give a minimum uncertainty and allow the accessibility of XRD under existing experimental circumstances. As a result, 13 $\{hkl\}$ planes per point of measurement were selected for XRD.

An experimental methodology for diffraction peak measurement was developed to enhance ε^e measurement using XRD. After understanding the impact brought to the shape of the diffraction peak by different scanning axes of ϕ , ψ and 2θ and the collimator, a Soller slit was first added to make the diffraction signal focused (to avoid the ambiguous situation in ψ direction with a broad maximum region). Then, an iteration process is designed to optimise ϕ , ψ and 2θ successively around the peak's initial position determined by the initial texture. During plastic loading, the evolution of mosaicity in crystal is inevitable and thus the beam size is narrowed down to $0.1 \times 0.1\text{mm}^2$ to cope with this situation. Finally, in order to accurately determine the final position of 2θ peak for ε^e calculation, the measured 2θ were simulated to by decomposing two $K_{\alpha 1}$ and $K_{\alpha 2}$ peaks after understanding the nature of X-ray source.

At the end of this chapter, an analytical algorithm was used to quantify the uncertainties of ε^e ($\pm 3 \times 10^{-5}$) measured by XRD. This method was also validated by a Monte Carlo method for its feasibility.

Development of an in situ method for measuring elastic and total strain fields.

This chapter presents the development of in situ ε^t and ε^e measurements. The application of digital image correlation for total strain measurement is first explained. Then, the development of the experimental setup combining X-ray diffraction and digital image correlation technique is shown. Finally, the experimental protocol and other concerns regarding the in-situ measurements are presented.

4.1 Total strain field measurement using digital image correlation (DIC)

4.1.1 Application of DIC

Digital image correlation (DIC) is widely used in many areas of science and engineering. It was firstly developed and applied for displacement field measurement in 2D [Lucas and Kanade (1981); Sutton et al. (1983); Chu et al. (1985)] since early 1980 and then in 3D [Kahn-Jetter and Chu (1990); Luo et al. (1994); Helm et al. (1996)] to study the behaviour of materials at the macroscopic scale. Thanks to its principles which are relatively independent of physical size of pixel of images, DIC has been also proved as a sufficiently robust technique to access the strain field with good precision at mesoscopic scale, e.g. image acquired through the optical microscope [Mazza et al. (1996); Mitchell et al. (1999)]. Strain field measurement using DIC can also take place at microscopic scale, e.g image acquired under SEM [Allais et al. (1994); Doumalin (2000); Tatschl and Kolednik (2003); Sutton et al. (2006, 2007a); Bourcier (2012); Guery (2014)] or through other photo-imaging technique (Camera) [Saai (2008); Tang et al. (2012)].

4.1.2 General principle

The 2D digital image correlation allows one to measure the displacement field on a sample surface from two images taken successively at two distinct moments during loading. These images are then compared to detect displacements of a matched spatial coordinate (or pixel) x_p from one image to another. Since it is almost impossible to find the matched point using a single pixel, the correlation algorithm is based on

the tracking of the grey value pattern of a reference $f(x_p)$ and a deformed $F(x_p)$ state in small local neighbourhood facets (called subset) between these images.

$$F(x_p) = f(x_p + U(x_p)) \quad (4.1)$$

where $U(x_p)$ is the unknown displacement field inside the subset. The reference images are assumed to be differentiable, a Taylor expansion to the first order is developed:

$$F(x_p) = f(x_p) + U(x_p) \cdot \nabla f(x_p) \quad (4.2)$$

In order to estimate $U(x_p)$ mathematically, an optimisation is made. Hild and Roux (2008) chose to work on the quadratic difference between right and left hand sides of Eq.4.1. This quadratic difference is then integrated over the studied domain J and then minimized. i.e.

$$\text{Min} \int_J [U(x_p) \cdot \nabla f(x_p) + f(x_p) - F(x_p)]^2 dx \quad (4.3)$$

From the displacement field, the total strain field ε^t in the subset can be sought:

$$\varepsilon^t = \frac{1}{2} (\nabla U + \nabla U^T) \quad (4.4)$$

The Software Correli_Q4 [Hild and Roux (2008)] developed by the laboratory of LMT-Cachan was used to determine the total strain field ε^t .

4.1.3 Speckle point

Since the deformed subset position is found by matching the area with the same grey level distribution before deformation (Fig. 4.1), a pattern feature on the analysed surface is required to allow the matching process. In our case, an artificial speckle painting was applied on the sample surface (Fig. 4.2).

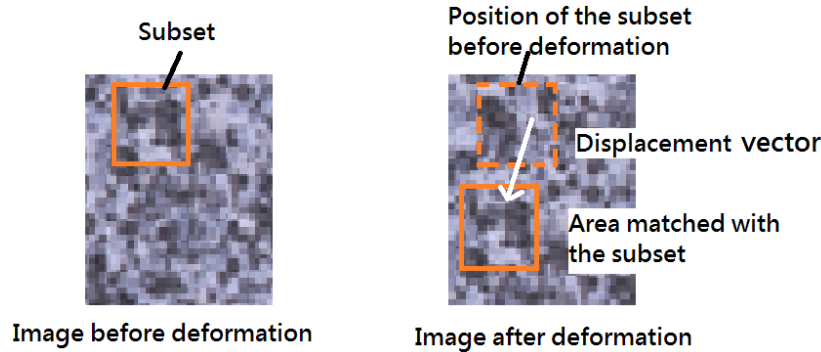


Figure 4.1: Subset before and after deformation.

The speckle was made of black and white spray painting. In order to fully cover the large grains, around 10 layers of black and white paintings are applied

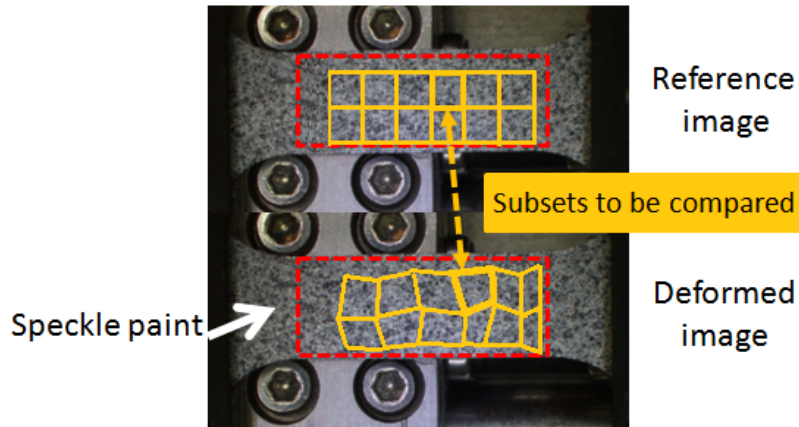


Figure 4.2: Speckle paint is applied on the sample for subset matching during displacement calculation.

alternatively on the sample surface and a thickness of about 0.01 mm is achieved. The thickness of the painting layer on representative samples was measured by a digital Dial indicator. Moreover, it was verified that the speckle spread out on the sample surface does not disturb the diffraction measurement (Fig. 4.3). All diffraction peaks of Al are still remarkable and no diffraction peak is added by the painting.

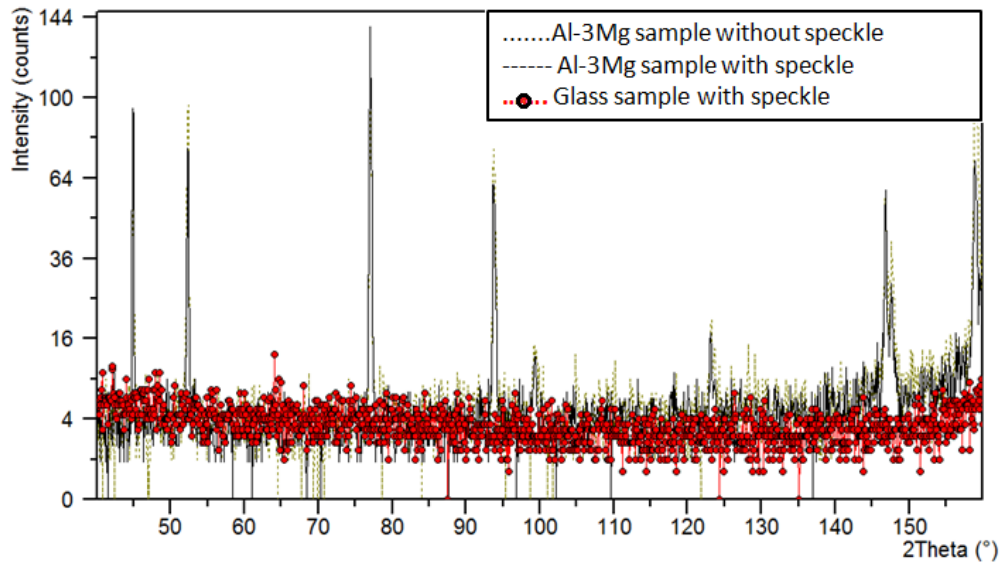


Figure 4.3: XRD measurements of aluminium and glass specimens covered by speckle painting.

4.1.4 Texture analysis of speckle painting and selection of DIC spatial resolution

4.1.4.1 Concept of DIC characterization

When using DIC to measure total strain fields, errors may come from the colour contrast on speckle pattern due to background lighting, optics of the camera/CCD (charge coupled detector), evolution of the texture of the grey levels during solicitation, size of subsets (or zone of interest ZOI), shape of subsets deformed during loading, etc. Therefore, several approaches were used to understand the source of errors and analyse these errors individually. First, the texture of the speckle painting applied on our sample was qualified. Then, the influence of DIC spatial resolution with various element sizes on ε^t calculation was studied. For the uncertainties related to the applied algorithm, they were quantified imposing a known displacement field (e.g. a constant field [Hild and Roux (2008)]) in a representative image. The image can be an image of the specimen (in our case) or artificial images made to push the software to its limits (see article on the comparison of different DIC softwares [Bornert et al. (2008)]). Finally, the choice of the size of subset was made after considering the effect of these uncertainties brought towards to the ε^t results as well as the spatial resolution applied during ε^t calculation.

4.1.4.2 Quality of speckle painting

During DIC analysis, the size of the compared subsets is defined regarding to the texture quality of the applied speckle paint. Sample 1 covered by speckle painting and a zone of 10.5 mm \times 5.1 mm was selected for speckle verification by Correli_Q4. The resolution captured by the camera is 10.2 $\mu\text{m}/\text{pixel}$ (Fig. 4.4). The high resolution of the image enables one to distinguish the black/white edges easily and avoids averaging blurred black-white area to a grey one.

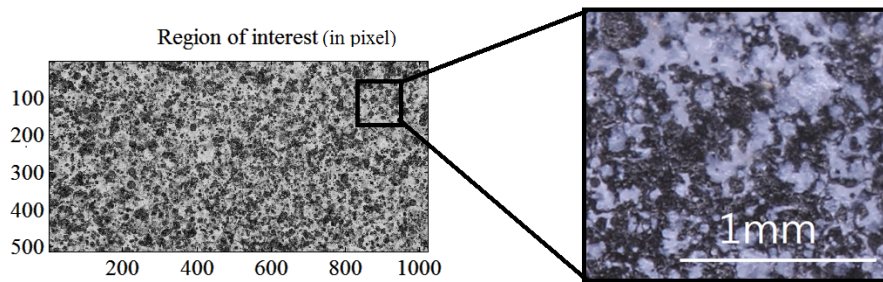


Figure 4.4: The speckle pattern is made of two colours: black and white. The edges of the painting is clear thanks to the high resolution of camera.

Images with speckle painting contain a large distribution of grey levels in the histogram (Fig. 4.5). The distribution of grey levels covers 69.3% of a 256-level grey scale ranging from 0 to 255 and it improves the accuracy of displacement field measurements.

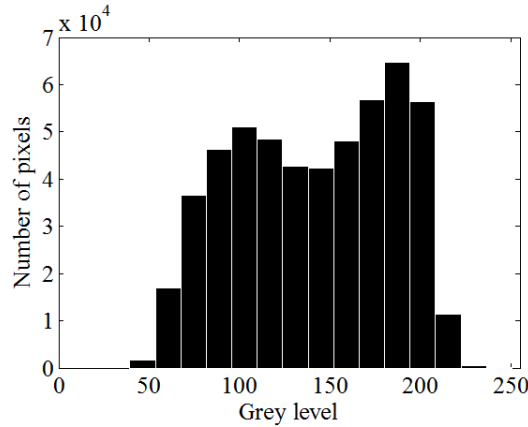


Figure 4.5: Grey level histogram of the speckle painting on representative samples.

4.1.4.3 Influence of DIC spatial resolution (different element sizes) on ε^t calculation

An example of ε^t calculated by various element sizes (called also zone of interest ZOI or subset) is given in Fig. 4.6. The map of ε_{xx}^t calculated with an element size of 16 pixels (Fig. 4.6a) is much noisier than those of 32 or 64 pixels. In fact, if the subset is too small to contain sufficient information for displacement interpretations, small local errors are induced and the cumulation of all these small errors results in a high uncertainty of calculated ε^t . Besides, we clearly see that with a coarser spatial resolution (Fig. 4.6c), there are some information not measured locally but "averaged" instead (refer to the regions pointed with white arrows in Fig. 4.6b and Fig. 4.6c).

In order to qualify every error, the uncertainties of ε^t calculated by Correli_Q4 were quantified using the images of the tested samples at their initial and deformed states.

1. Uncertainties of ε^t in the initial state - cumulative errors throughout the image acquisition process

An assumption of constant grey level (with respect to time) of the speckle painting is made during DIC calculation. However, in reality, the grey level of the painting changes due to the lighting system and the loading (roughness changes notably). In order to quantify DIC uncertainties caused by colour contrast while all other parameters being constant, 38 photos of the sample surface covered with speckled painting were taken in the same conditions of loading and lighting (initial state). Digital correlation was performed between any images taken in pairs (Fig. 4.7) using the element size 32 pixels (=362.4 μm). The total error of the strain field calculated using Correli_Q4 has a mean value of -5.1×10^{-6} with a standard deviation of 2.3×10^{-4} .

2. Uncertainties of ε^t after deformation - choice of the spatial resolution

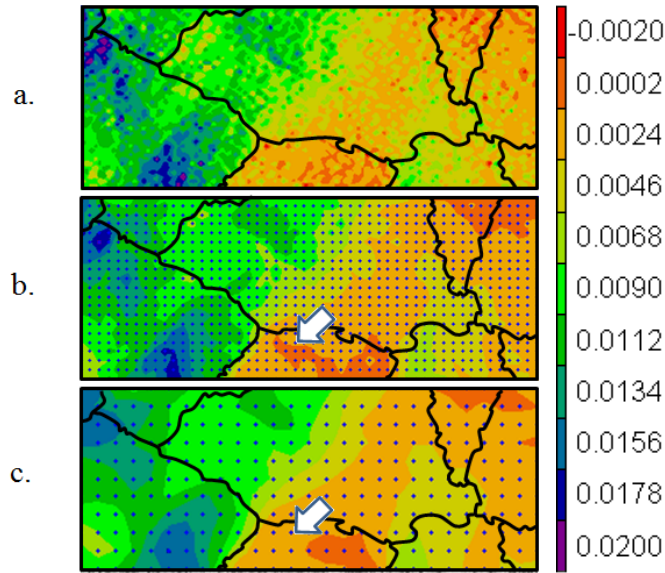


Figure 4.6: Map of ε^t_{xx} calculated using grid resolution of 16 pixels ($=181.2 \mu\text{m}$)(a), 32 pixels ($=362.4 \mu\text{m}$)(b) and 64 pixels ($=724.8 \mu\text{m}$)(c).

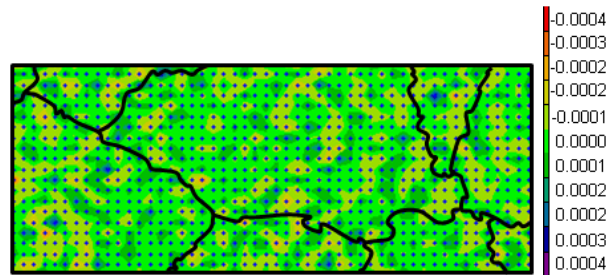


Figure 4.7: Error maps between 2 photos taken in the initial state under the same experimental conditions.

For the uncertainties related to the choice of algorithm parameters, analysis was made with 2 identical images of our specimen a constant displacement was imposed to one of them. This constant displacement was lower than one pixel, in order to evaluate if the image is sufficient enough for measuring relatively small displacements (sub-pixel). Then ε^t fields were calculated using Correli_Q4 with different element size ranging from 4 to 128 pixels. Two values are deduced from this calculations:

- (a) The displacement error, which is the difference between the applied displacement and the mean displacement calculated.
- (b) The displacement uncertainty, or the standard deviation of the error field.

As it can be seen in Fig. 4.8 and Fig. 4.9, displacement error and displacement

uncertainty decrease rapidly with larger ZOI sizes. For the element size 362.4 μm (=32 pixels), the average error is 3.1 nm ($= 2.75 \times 10^{-4}$ pixels) with a standard deviation of 17.8 nm ($= 1.57 \times 10^{-3}$ pixels).

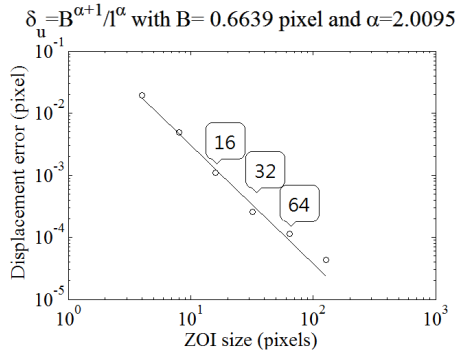


Figure 4.8: Displacement error with respect to the element size.

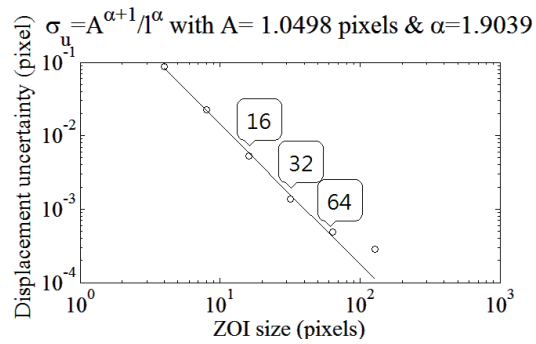


Figure 4.9: Standard deviation of displacement error with respect to the element size.

In our case, the element size 32 pixels is selected because it gives the best trade-off between the accuracy of ε^t results and the spatial resolution.

4.2 Implementation

In the objective of conducting in situ ε^t and ε^e measurements, the micro tensile machine and a single-lens reflex camera had to be installed inside the XRD apparatus. To integrate all the elements inside the diffractometer, the micro-machine was positioned on the cradle of the goniometer. The reflex camera faces the specimen vertically. A cable guide has been designed around the micro-machine for tidying up its power cable and preventing it crossing the beam during diffraction measurements (Fig. 4.10).

4.2.1 Micro-tensile test

4.2.1.1 Characteristics of the machine

The micro-machine used was designed by Deben for tensile testing in SEM. Two grips fix two ends of the sample and they move at the same rate during loading. This system maintains the sample centre position fixed and facilitates the positioning of the XRD zone on the sample after each deformation. The maximum tensile loading is 1kN. For this reason, the sample dimension and its material are carefully optimized (§.2.2). The maximum and minimum loading speed are 2 mm/min and 0.2 mm/min respectively. The control software supports synchronous data recording at sampling rate from $0.2s^{-1}$ to $5s^{-1}$. During the experiment, the sample was pulled at the minimum loading speed of 0.2 mm/min to ensure that more than 10 images

in the elastic part can be acquired. The data sampling rate is 0.1s during DIC measurement and 5s during XRD measurement.

4.2.1.2 Micro-machine fastening in the goniometer : machine mounting support and wire winding system

As for fixing the micro-machine on the cradle inside the diffractometer, two additional mounting plates were designed (See 65 and 66) and machined. Moreover, a cable guide around the micro-machine was designed and mounted on the cradle wafer to prevent it from crossing the beam during diffraction measurements (See 67). After considering the weight added on the wafer holder and the complexity of machining, it was fabricated using 3D printing in polymer. Moreover, a set of pulleys (Fig. 4.11) were integrated in the goniometer to ensure the power cable is fixed tight throughout the movement around ϕ, ψ and 2θ axis.

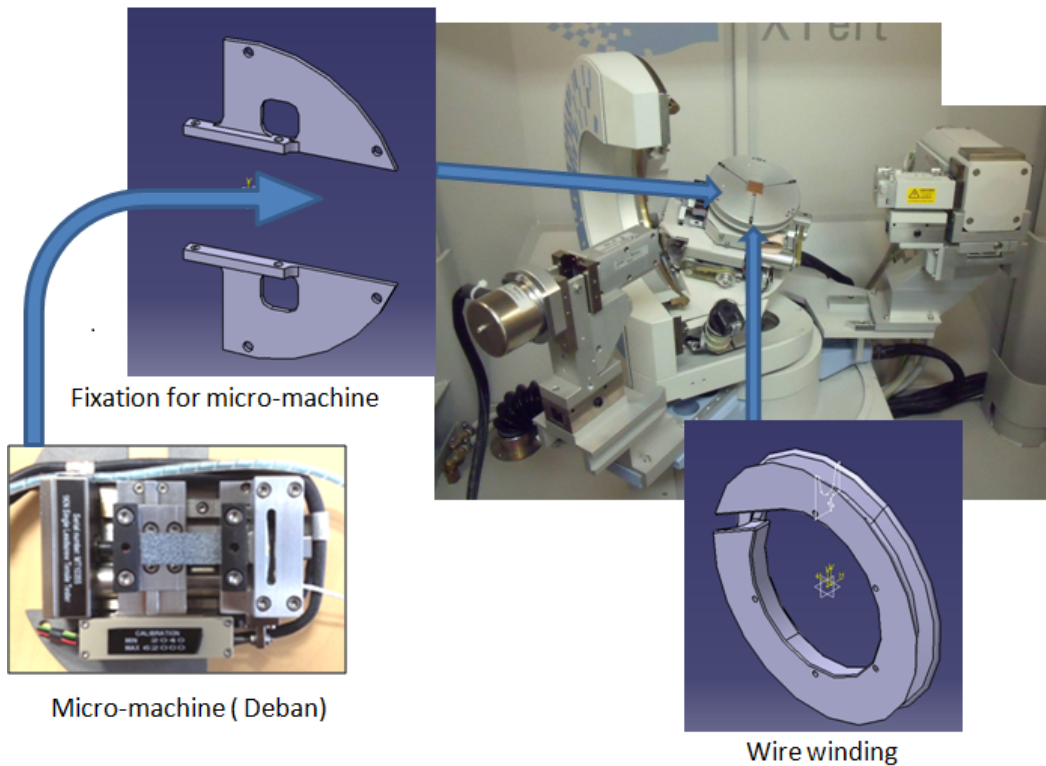


Figure 4.10: Scheme of installation of the micro-machine inside the goniometer.

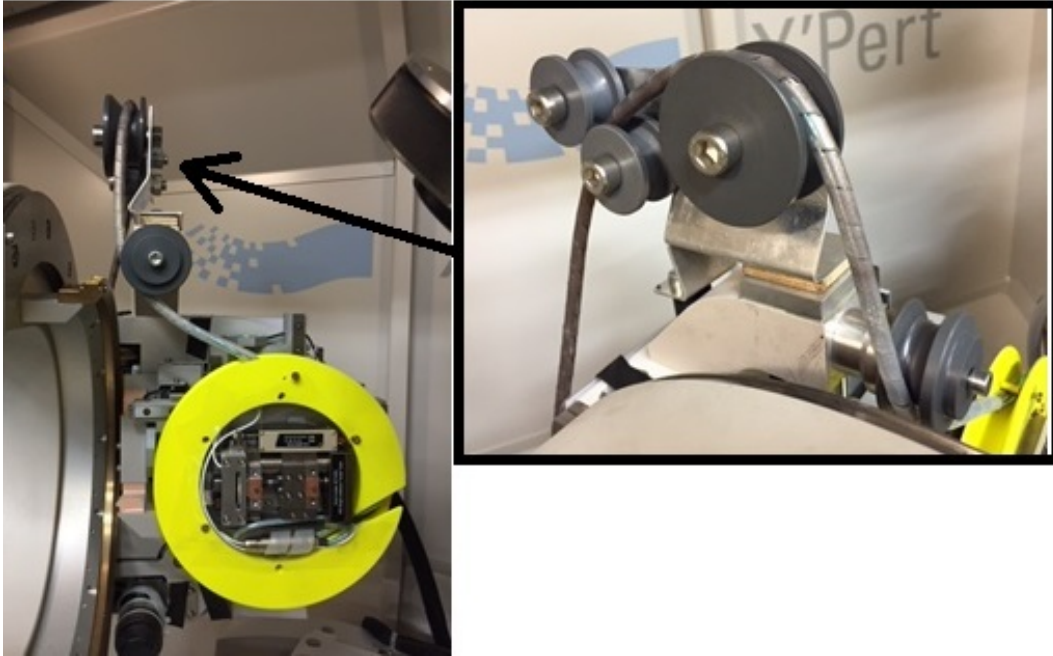


Figure 4.11: Wire winding system for the machine power cable.

4.2.2 Camera

In order to correctly calculate the total strain ε^t field using DIC, the pictures should be taken perpendicularly and in front of the sample surface. Moreover, the analysed images should neither be resized/transformed nor contain any distortion. The zone selected for analysis should be clearly focused. Therefore, a single-lens reflex camera was used.

4.2.2.1 Camera model and its performance parameters

In our experiments, a Canon EOS70D camera coupled with a lens Sigma 150 mm F2.8 EX DG OS HSM APO Macro was used. With an image taken by an objective with a magnification of 1:1.2 and a minimum distance of 180 mm from a sample surface, a maximized activated zone of $8 \times 19.5\text{mm}^2$ with no distortion can be captured. Compromising on the speckle pattern applied on the sample surface for DIC (§.4.1.4) and lighting system (§.4.2.2.3), the best average performance of the texture (e.g. grey level, resolution, uncertainties, etc.) is obtained with an exposure of f/8 at 1/30 s. Images can be automatically captured every five seconds.

4.2.2.2 Camera stand

A fixation (Fig. 4.12) was designed for mounting the camera inside the goniometer without disturbing XRD measurement. Therefore, the installation of every part of the camera stand should be positioned outside the path of X-ray beam (refer to Appendix 5.3) and all the necessary movement of x , y , ψ , ϕ and 2θ axis during

XRD. Also, this mounting system has to enable the lens of camera being positioned vertically and perpendicularly in front of the sample surface and avoid any distortion of the image during DIC measurement.

4.2.2.3 Lighting system

A lighting system is fixed concentrically with the camera lens (Fig. 4.13) in order to give a homogeneous brightness on the sample surface. The lighting system is made of a circle of LED. Photos taking under an even and constant lighting condition improves the quality of the strain field measured by DIC, as the average grey level of the speckle pattern among the images remains unchanged.



Figure 4.12: The camera stand inside the goniometer.



Figure 4.13: Ring of LED lighting around the objective.

4.2.3 Experimental set-up

Combining all the individual devices described above, an experimental set-up was developed (Fig. 4.14-4.15), which allows us to carry out a mechanical test, and measure elastic ε^t and total ε^t strain fields at similar loading levels in the diffractometer.

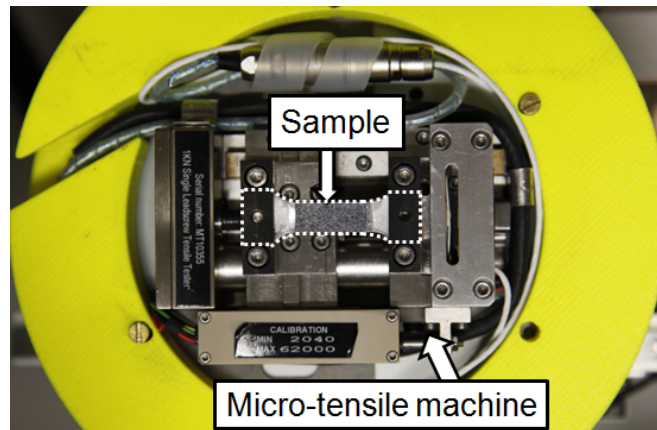


Figure 4.14: Sample inside the micro-machine, on the cradle of the diffractometer.

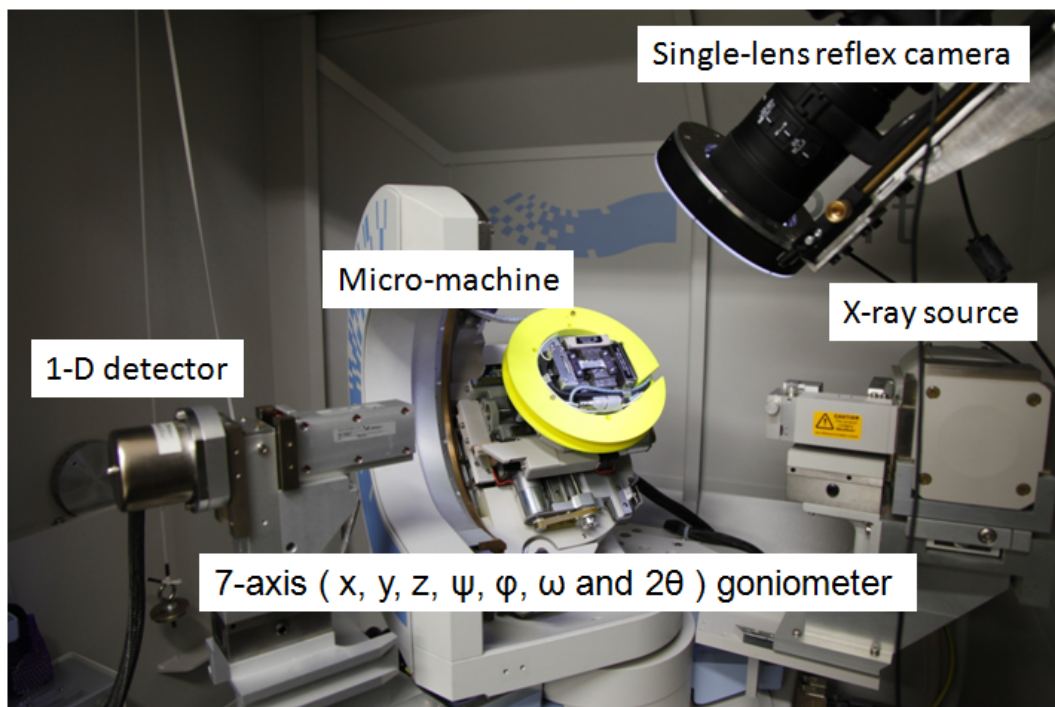


Figure 4.15: Experimental set-up.

4.3 Experimental protocol

In this section, a general principle of in situ full-field measurements is presented. Concerning the actual execution of each apparatus during in situ experiment, an experimental protocol was designed with procedure in detail, specific parameters of machine operation and the corresponding hypothesis.

4.3.1 Principle of in situ full-field measurements

Our research objective is to measure simultaneously both the elastic ε^e and total ε^t strain fields at each loading level imposed on our Al-alloy samples (refer to chapter 2) during tensile loading. The elastic strain field is measured by X-ray diffraction (XRD) (refer to chapter 3) while the total one is observed by digital image correlation (DIC). In Fig. 4.16, the methodology of both measured is given. The strain-stress curve was obtained using the ε^t observed by DIC and the truth stress calculated using a given initial cross-section of sample and the force detected by the loading cell.

4.3.2 Experimental procedure

Once an oligo-crystalline sample is prepared and the installation of all the experimental devices is ready, the in situ experiment can be executed. A detailed procedure was planned concerning the actual execution of each apparatus during in situ full-field measurements (Fig. 4.16).

1. Initial state: XRD scanning (Fig. 4.16 position O).

XRD scanning is first performed on the sample surface in its initial state. The signals obtained at this stage are used as reference for ε^e calculation. The experimental set-up provides an active zone of $15 \times 8 \text{ mm}^2$ on our sample surface for XRD measurement. The resolution of the grid measurement for XRD is $1 \times 1 \text{ mm}^2$. In fact, this fineness of the grid measurement is defined regarding to our grain size (about 5 mm) so that the gradient of elastic strain inside each crystal can be measured.

At each XRD measurement point, 13 $\{hkl\}$ planes should be measured in the shortest time. 13 $\{hkl\}$ planes are chosen in consideration of data accessibility and ≥ 6 planes are wanted to maximize the accuracy of elastic strain calculation. As there are 60 measuring points for sample 1 (Fig. 5.1) and 105 measuring points for sample 2 (5.38), an effective way of XRD measurement is required.

For measuring each $\{hkl\}$ plane in a monocrystal, its position with respect to the X-ray beam has to be correctly oriented $(\phi, \psi)_{\{hkl\}}$ for diffraction take place. These values are calculated based on the corresponding crystal texture. A peak optimisation of $(\phi, \psi)_{\{hkl\}}$ is carried out. Then, a 3-iterations process

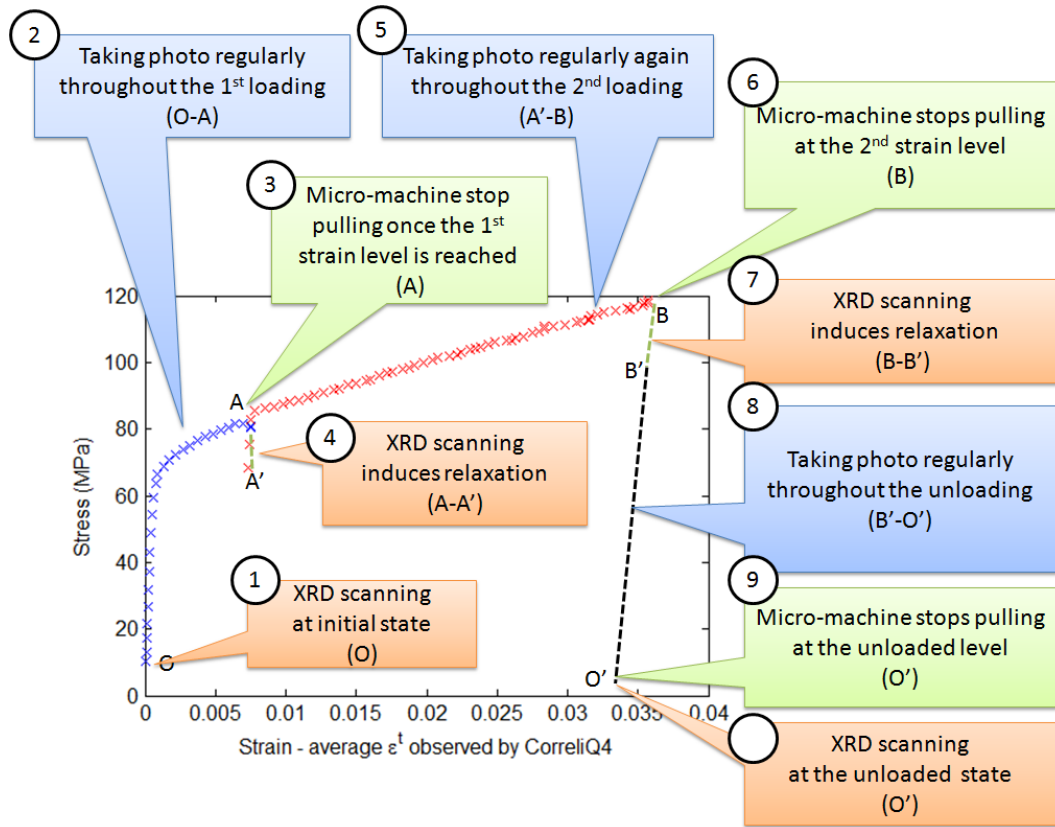


Figure 4.16: Methodology of XRD and DIC measurements on our sample during an in situ tensile loading.

of peak optimisation is conducted along $(\phi, \psi \text{ and } 2\theta)_{\{hkl\}}$. The maximum intensity of diffraction peak $(\phi, \psi \text{ and } 2\theta)_{\{hkl\}}$ implies that the $\{hkl\}$ plane is correctly oriented with respect to the X-ray beam, so the final peak position of $2\theta_{\{hkl\}}$ can be obtained.

The total measuring time to obtain an ε^e field is 3 days 22 hours for sample 1 and 6 days 21 hours for sample 2.

2. Taking photo regularly throughout the 1st loading (Fig. 4.16 position O-A).

Upon the termination of XRD measurement at initial state (O), the cradle moves to a orientation where the sample is perpendicular to and right in front of the camera lens. This position is used throughout all the photo-taking process so that the reference coordinates of every photo of the sample surface are the same for DIC calculations. The experimental set-up provides an observation area of $17 \times 8 \text{ mm}^2$ for DIC measurement. The resolution of photo is $10.2\mu\text{m}/\text{pixel}$ while the resolution of the grid measurement (subsets

or ZOI) for DIC is $362.4 \times 362.4 \mu\text{m}^2$ (32 pixels \times 32 pixels). A first photo of sample surface is taken at initial state (O) as reference image.

The sample is then pulled at a loading speed of 0.2 mm/min until the first strain level is reached ($\approx 1\%$) (in Fig. 4.16 position A). A slow loading speed is applied to ensure a sufficient number of photos (≥ 10) taken in the elastic part. Photos are taken regularly (5 s/photo) throughout the mechanical loading (O-A) using a focal length of f/8 with exposure time of 1/30s. The variation of the sample thickness is assumed to be too small to affect image focusing by camera during tensile loading. The force imposed by the machine is recorded at the same time with a sampling rate of 0.1 s. Therefore, the total strain of the sample on each photo and its corresponding applied load are known.

3. Micro-machine stops pulling once the 1st strain level is reached (A).

When the sample is pulled to the first strain level ($\approx 1\%$) (A), the distance between the grips is maintained constant. The evolution of force is recorded with a sampling rate of 5 s and the relaxation of sample can therefore be quantified.

4. XRD scanning during relaxation (A-A').

As XRD measurement takes several hours, a relaxation occurs. In other words, the XRD measurement on the deformed sample surface is performed during relaxation (A-A'). Relaxation has been quantified using a polycrystalline Al-alloy sample (5052) (See 4.4.2). Taking into account this phenomenon during the in situ experiment, XRD measurement is launched only after the major decrease in stress (after about 40 mins - 1 hour of waiting).

The sample is then reoriented to its position for XRD measurement. Assuming there is only small deformation in our experiment, the new position of diffraction peak of each $\{hkl\}$ plane should not be too far away from its previous one and it should be easily relocated from its initial position. Therefore, the final peak position obtained at previous strain level can be used as the initial position for searching the current position of the peak at the present stage for XRD measurement.

The variation of the distance between the grips during relaxation is also assumed too small ($\leq 1 \mu\text{m}$) to have an influence on XRD measurement.

5. Repeat steps 2-4 for each loading (A'-B') or unloading (B'-O') situation

For research interests, full-field measurements on a deformed sample surface at more than 2 strain levels give a richer local information.

Between, the same experimental protocol of XRD and DIC measurements can be applied during unloading situation. Although the strain field obtain during unloading by DIC is still total strain field, these results can be used to give a first idea of how heterogeneity varies during elasticity and plasticity of our material under the hypothesis of plastic strain being constant.

4.4 Discussion

During in situ measurements of elastic and total strain fields, all necessary precautions or usage limits shall be taken to minimise the uncertainty.

4.4.1 Size of X-ray beam spot on the specimen

Considering the beam size used during the experiment ($0.1 \times 0.1 \text{ mm}^2$), the limit of the movement of the wafer holder ($\phi \in [0, 360^\circ]$ and $\psi \in [0, 75^\circ]$) and $2\theta \in [77^\circ, 100^\circ]$, the maximum area spotted by X-ray beam during the diffraction is

$$\frac{0.1}{\sin\theta_{min}} \times \frac{0.1}{\cos\psi_{max}} = 0.16 \times 0.38 \text{ mm}^2 \quad (4.5)$$

and the minimum area is

$$\frac{0.1}{\sin\theta_{max}} \times \frac{0.1}{\cos\psi_{min}} = 0.13 \times 0.1 \text{ mm}^2 \quad (4.6)$$

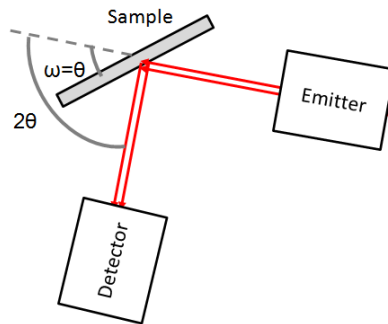


Figure 4.17: Scheme of X-ray beam spot on the specimen.

4.4.2 Movement of the grip system during a tensile test

The micro-machine is designed to pull the sample at two ends at the same rate so that the sample center remains unchanged. Yet, the movement of the grips is not perfectly symmetrical all the time. The grip movement with and without sample has been, therefore, verified using the DIC with a resolution of $10.2 \mu\text{m}/\text{pixel}$. It was observed that during the opening of grips, the left grip and right grip move alternatively apart to each other for every 0.1 mm . For the first 0.5 mm extension,

the sample center is shifted to the right of about $28\mu\text{m}$. Later, for an extension from 0.5 mm to 1 mm, the sample center keeps an offset of $15\mu\text{m}$ on the right from its initial position. For an extension >1 mm, the sample center has an offset of $5\mu\text{m}$ on the right. All rigid body movements caused by the grip system have to be excluded during ε^t calculation. The movement of material points can thus be tracked during the solicitation. However, it is negligible for programming diffractometer control file.

4.4.3 Relaxation

As X-Ray measurements take a very long time (3 days 22 hours for sample 1 and 6 days 21 hours for sample 2), a relaxation is unavoidable. A relaxation test was conducted on a representative polycrystalline Al-alloy sample (5052) (with around 3% of Mg) specimen (Fig. 4.18). Once the sample was pulled beyond the yield strength, the distance between the grips was maintained constant (31.05 mm) for 5 days. We observed that the force dropped 13.5% during the first 40 minutes then decreased another 6.87% slowly for the rest of time (Table 4.1). Taking into account this phenomenon during the in situ measurements, when the sample was pulled to a specific loading level, we needed to wait for 1 hour until the relaxation being stable before launching XRD measurement.

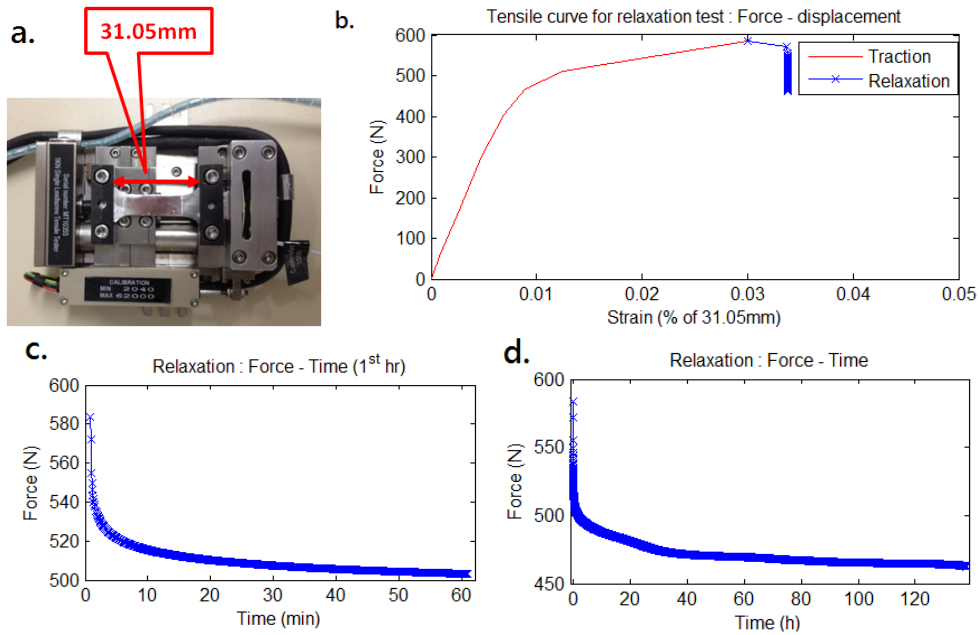


Figure 4.18: A relaxation test on a representative polycrystalline Al-alloy specimen. Once the sample was pulled beyond the yield strength, the distance between the grips was maintained constant (31.05 mm) for 5 days (a). The strain level was about 3.4% and the load 583.85N (b). The force dropped 13.5% during the first 40 minutes (c) then decreased another 6.87% slowly for the rest of time (d).

Duration	5 mins	40 mins	1 hr	1 day	5 days
% of force relaxation	10.66%	13.5%	13.81%	18.10%	20.37%

Table 4.1: % of force decrease with respect to relaxation time on a representative polycrystalline Al-alloy specimen under constant strain.

4.5 Conclusion

In conclusion, the analysing spatial resolution of 32 pixels ($362.4 \mu\text{m}$) for DIC is used regarding the quality of speckle pattern applied on sample surface. An experimental set-up Was developed in order to integrate the micro-tensile machine and camera inside a diffractometer for in situ measurements. Additional equipments, like wire winding, pulley system and lighting system, were attached to the set-up so as to facilitate the XRD measurement and to achieve better image quality. After considering the device's performance and the area of sample surface accessible by the apparatus, ZOI of $17 \times 8 \text{ mm}^2$ and $15 \times 8 \text{ mm}^2$ were defined for DIC and XRD measurement respectively. Combining the XRD measurement in previous chapter with DIC measurement, an experimental protocol was defined for in situ full-field measurements. XRD measurement is first conducted at sample's initial state. Then, images on the sample surface are taken regularly throughout the mechanical loading. Once the sample is pulled up to a assigned level, XRD is conducted on sample's surface again during relaxation. The maximum ($0.16 \times 0.38 \text{ mm}^2$) and minimum area ($0.13 \times 0.1 \text{ mm}^2$) spotted by XRD were also founded according to the limited movement of goniometer during the XRD measurement. The phenomenon of relaxation of our material was quantified and taken into account during the in situ measurements.

Experimental Results

In this chapter, the experimental results of tests carried out on samples 1 and 2 are presented and discussed.

Two samples with around twenty-five crystals were subjected to a simple tensile loading. ε^t and ε^e fields were measured on the upper surface of oligo-crystal specimens at each successive loading level. The method to perform DIC, XRD and tensile tests in-situ in the X-ray diffractometer was introduced in the previous chapter. Stress σ^e fields were then calculated from ε^e using the equation (Eq.(1.5)) presented in chapter 1.

Later, ε^t , ε^e and σ^e fields are displayed and the corresponding uncertainties during each measurement are also quantified. In order to better understand the experimental results, the evolution and distribution of local stress-strain at each successive loading/unloading level are plotted and discussed.

5.1 Experimental results of sample 1

In this section, the sample used and the zone of interest for DIC and XRD will be presented. The global stress-strain curve measured during the tensile test will be presented, as well as ε^t , ε^e and σ^e and their uncertainties fields acquired on the surface of the specimen. In the last section, ε^e field was determined through different methods, in order to have another way to validate it.

5.1.1 Zone of XRD and DIC measurement

The experimental setup provided an observation area of $17 \times 8.1 \text{ mm}^2$ for DIC measurement and we defined an area of $14 \times 3 \text{ mm}^2$ for XRD measurement (Fig.5.1).

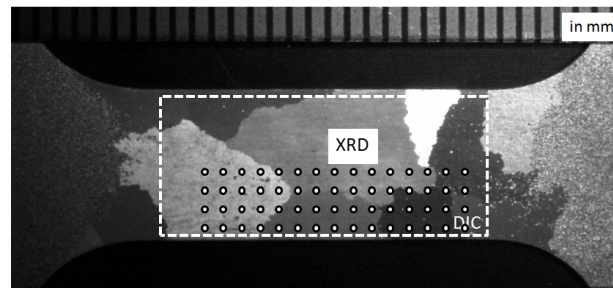


Figure 5.1: ZOI of XRD and DIC measurement of sample 1.

Since the XRD measurement is more time-consuming than DIC measurement, ε^e measurement were conducted on only one half of the entire active zone of the sample 1 in order to have a rapid validation of the methodology. Moreover, in order to facilitate the data analysis later, grain geometry (Fig.5.2-5.3) on both sides of the sample is recalled.

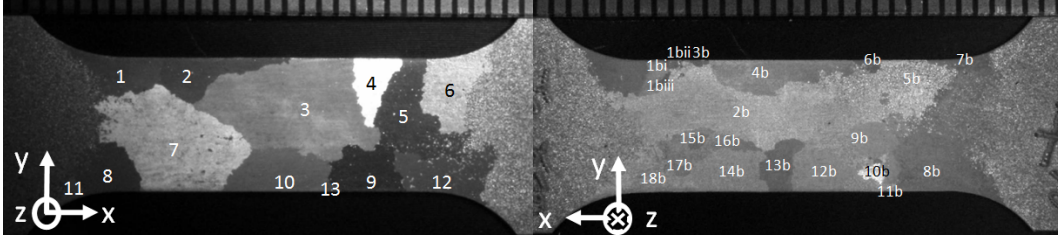


Figure 5.2: Front view of sample 1 with its grains numbered.

Figure 5.3: Back view of sample 1 with its grains numbered.

5.1.2 Tensile test

During the in-situ experiment, sample 1 was subjected to a symmetric tensile loading in the x-direction. The micro tensile machine was stopped twice for XRD measurements at increasing levels of strain, once was just after the yield stress at 81.1 MPa, ① $\varepsilon_{xx}^t = 0.0074$ and the second was at 118.6 MPa, ② $\varepsilon_{xx}^t = 0.0356$. Photos were taken throughout the entire tensile test and the total strain fields were calculated using Correli_Q4. The mean tensile stress measured during the test was plotted in Fig.5.4 versus the mean strain averaged over the useful part of the specimen.

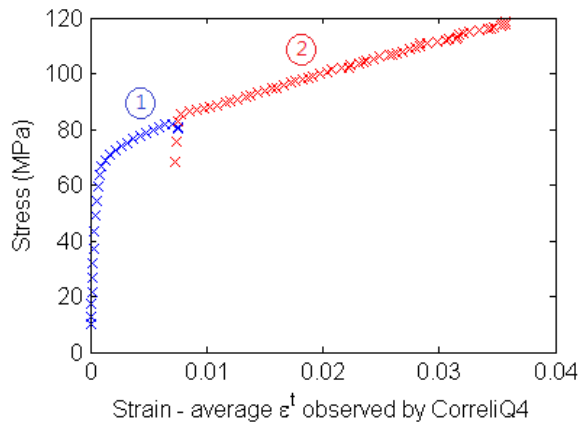


Figure 5.4: Stress-strain curve. The micro tensile machine was stopped once at ① $\varepsilon_{xx}^t = 0.0074$ and then at ② $\varepsilon_{xx}^t = 0.0356$.

5.1.3 Total strain field measurement ε^t

5.1.3.1 Map of ε^t

The area in sample 1 with validated data of total strain ε^t field is $15.99 \times 6.53 \text{ mm}^2$. The in-plane components ε_{xx}^t and ε_{yy}^t at two loading levels are plotted in Fig.5.5 - 5.8.

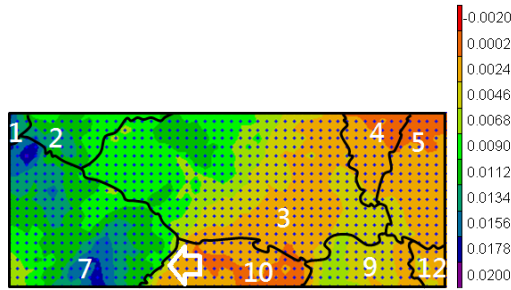


Figure 5.5: Map of ε_{xx}^t at level ①
($\overline{\varepsilon_{xx}^t} = 7.4 \times 10^{-3}$).

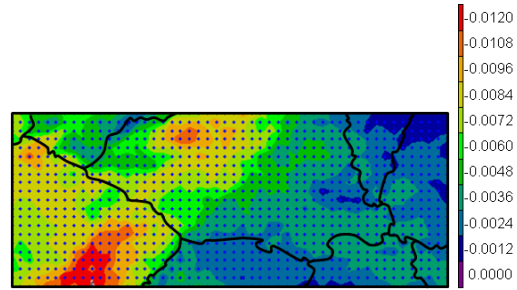


Figure 5.6: Map of ε_{yy}^t at level ①
($\overline{\varepsilon_{yy}^t} = -4.8 \times 10^{-3}$).

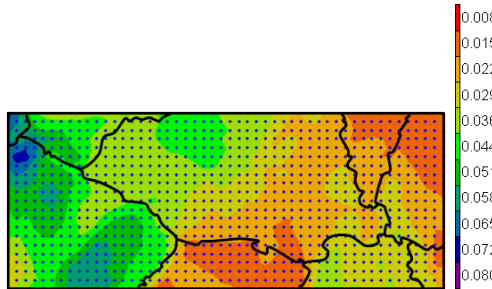


Figure 5.7: Map of ε_{xx}^t at level ②
($\overline{\varepsilon_{xx}^t} = 0.0356$).

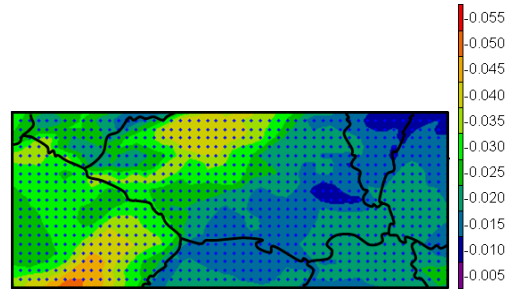


Figure 5.8: Map of ε_{yy}^t at level ②
($\overline{\varepsilon_{yy}^t} = -0.0221$).

It is important to recall that the element size of 32 pixels was used (refer to §4.1.4.3) so that the spatial resolution of ε^t calculated is $32 \text{ pixels} \times 10.2 \text{ } \mu\text{m}/\text{pixel} = 362.4 \text{ } \mu\text{m}$

As shown in Fig.5.5 and Fig.5.7, strain localised to a large extent grain by grain and the strain gradients are smooth. A more intense strain gradient can be seen at the grain boundary between grains 7 and 10 (indicated by the white arrow in Fig.5.5). This heterogeneity increases with the imposed loading. The magnitude of the axial strain is much higher on the left hand side of the sample than on the right hand side. This difference can be explained by the initial crystallographic orientation of grains on both the front and the back sides of the sample, since grains with favourable orientation to the loading direction and thus the highest Schmid Factor (SF) deform first. For example, grains 2, 3 and 7 on the left have a SF of about 0.5 (Table 5.1) while grains 4, 12 and 13 on the right have a SF of about 0.4. Although the SF of grains 5 and 9 on the right hand side are high, the grains right

behind (Fig.5.9) ,e.g. grain 1bi, 1bii and 14b, have low SFs, which explains why the strain is globally much lower on this side.

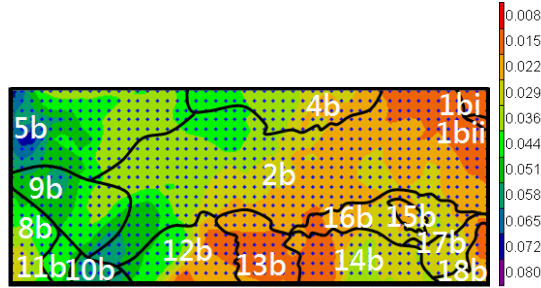


Figure 5.9: Map of ε^t_{xx} at level ② with grain boundaries of sample back side super-imposed ($\overline{\varepsilon^t_{xx}} = 0.0356$)

a. Front side			b. Back side		
Grain	Schmid factor	Number of activated slip system	Grain	Schmid factor	Number of activated slip system
1	0.4799	1	1bi	0.4357	1
2	0.4665	1	1bii	0.3318	1
3	0.4893	1	2b	0.4832	1
4	0.3982	1	4b	0.4956	1
5	0.4969	1	8b	0.4520	1
7	0.4893	1	9b	0.4185	1
9	0.4952	1	10b	0.3785	1
10	0.3950	1	11b	0.4563	1
12	0.4335	1	12b	0.4427	1
			13b	0.4959	1
			14b	0.4404	1
			15b	0.4994	1
			16b	0.4992	1
			17b	0.4994	1
			18b	0.4170	1

Table 5.1: Schmid factor of each grain of a. front side and b. back side of sample No.1.

5.1.3.2 Uncertainty of the total strain tensor σ_{ε^t}

In §4.1.4, uncertainties of ε^t were discussed and analysed in two aspects, errors cumulated throughout the image acquisition process (or namely colour contrast due to the lighting system) and algorithmic errors due to choice of the spatial resolution. The former one outweighed the second and represented the main error source of the total strain field σ_{ε^t} . Therefore, the algorithm error of ε^t that comes with the DIC software Correli_Q4 was not taken into account. In the experiment, σ_{ε^t} was considered only due to the image acquisition. Two pictures were taken under identical experimental conditions but at different times. The ε^t calculated

between these two pictures was considered as σ_{ε^t} . For sample 1, σ_{ε^t} has a mean value of -5.1×10^{-6} with a standard deviation of 2.3×10^{-4} (Fig. 5.10) at each measuring point.

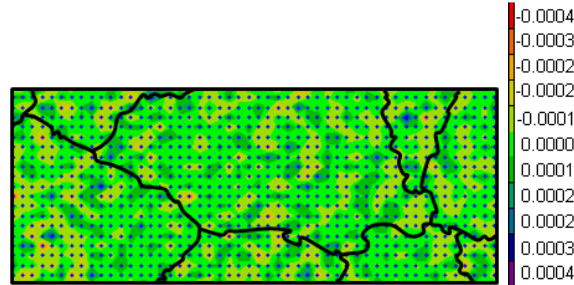


Figure 5.10: Error of total strain field σ_{ε^t} .

5.1.4 Elastic strain field measurement ε^e

5.1.4.1 Map of ε^e

Fields of components ε_{xx}^e and ε_{yy}^e obtained at levels ① and ② are shown in Fig.5.11-5.14. The mean values $\overline{\varepsilon^e}$ of elastic strain were listed in Tab.5.2. Similar to the ε^t results, zones with higher/lower elastic deformation were observed on the sample surface. Due to local grain disorientation during plastic deformation (mentioned in §3.5.4), the intensity of some $\{hkl\}$ peaks for some measuring points was too low to allow their measurement and thus elastic strain tensor calculation. This explains the absence of some strain field measurements in Fig.5.13-5.14.

Loading level	Mean value of ε^e ($\times 10^{-3}$)					
	$\overline{\varepsilon_{xx}^e}$	$\overline{\varepsilon_{yy}^e}$	$\overline{\varepsilon_{zz}^e}$	$\overline{\varepsilon_{yz}^e}$	$\overline{\varepsilon_{zx}^e}$	$\overline{\varepsilon_{xy}^e}$
①	1.2	-0.2	-0.3	-0.1	-0.1	-0.1
②	1.8	-0.3	-0.4	-0.1	-0.1	-0.1

Table 5.2: Mean value of ε^e of sample 1 at each successive loading level

5.1.4.2 Uncertainty estimation of the elastic strain tensor σ_{ε^e}

The uncertainty of the elastic strain tensor σ_{ε^e} at each strain level was estimated. The maps of σ_{ε^e} are shown in Fig.5.15-5.18. The mean values of σ_{ε^e} and its standard deviation value (Std) are listed in Tab.5.3-5.4. It can be seen that the ε^e uncertainties σ_{ε^e} are always smaller than 10^{-5} . Considering a Gaussian distribution, it implies a total error range in ε^e smaller than $\pm 3 \times 10^{-5}$.

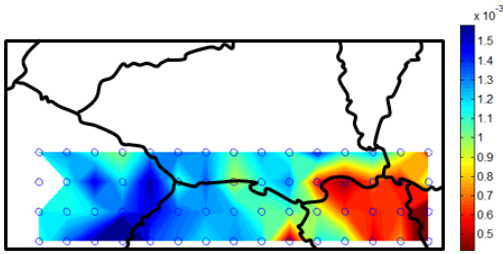


Figure 5.11: Map of ε_{xx}^e at level ①
 $(\overline{\varepsilon_{xx}^e} = 1.2 \times 10^{-3})$.

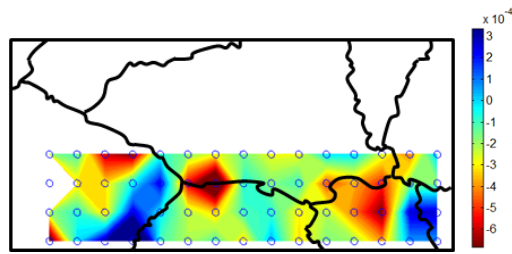


Figure 5.12: Map of ε_{yy}^e at level ①
 $(\overline{\varepsilon_{yy}^e} = -0.2 \times 10^{-3})$.

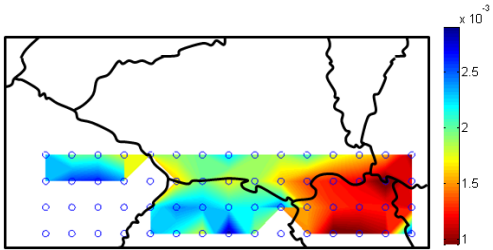


Figure 5.13: Map of ε_{xx}^e at level ②
 $(\overline{\varepsilon_{xx}^e} = 1.8 \times 10^{-3})$.

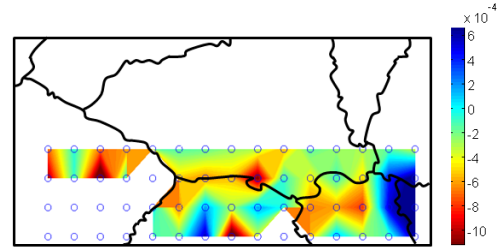


Figure 5.14: Map of ε_{yy}^e at level ②
 $(\overline{\varepsilon_{yy}^e} = -0.3 \times 10^{-3})$.

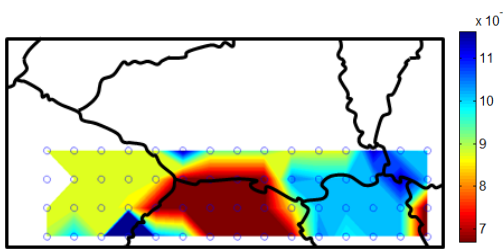


Figure 5.15: Map of $\sigma_{\varepsilon_{xx}^e}$ uncertainties at level ①

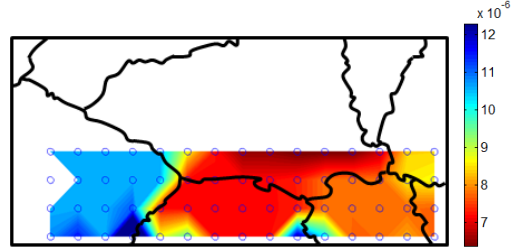


Figure 5.16: Map of $\sigma_{\varepsilon_{yy}^e}$ uncertainties at level ①

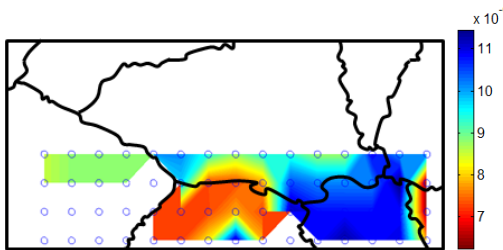


Figure 5.17: Map of $\sigma_{\varepsilon_{xx}^e}$ uncertainties at level ②

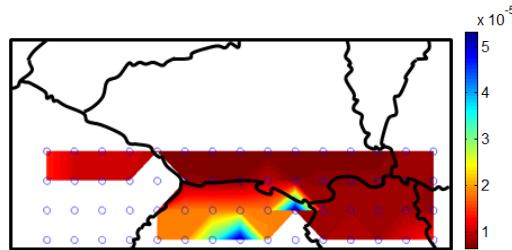


Figure 5.18: Map of $\sigma_{\varepsilon_{yy}^e}$ uncertainties at level ②

Loading level	Mean value of σ_{ε^e} ($\times 10^{-6}$)					
	$\overline{\sigma_{\varepsilon_{xx}^e}}$	$\overline{\sigma_{\varepsilon_{yy}^e}}$	$\overline{\sigma_{\varepsilon_{zz}^e}}$	$\overline{\sigma_{\varepsilon_{yz}^e}}$	$\overline{\sigma_{\varepsilon_{zx}^e}}$	$\overline{\sigma_{\varepsilon_{xy}^e}}$
①	8.7	9.2	8.2	6.4	8.7	6.7
②	13	9	10	7	11	8

Table 5.3: Mean value of σ_{ε^e} of sample 1 at each successive loading level

Loading level	Standard deviation of σ_{ε^e} ($\times 10^{-6}$)					
	$\text{Std}(\sigma_{\varepsilon_{xx}^e})$	$\text{Std}(\sigma_{\varepsilon_{yy}^e})$	$\text{Std}(\sigma_{\varepsilon_{zz}^e})$	$\text{Std}(\sigma_{\varepsilon_{yz}^e})$	$\text{Std}(\sigma_{\varepsilon_{zx}^e})$	$\text{Std}(\sigma_{\varepsilon_{xy}^e})$
①	1.8	3.2	3.2	1.8	2.3	2.3
②	9.8	5	6.2	1.8	4.8	4.6

Table 5.4: Standard deviation of σ_{ε^e} of sample 1 at each successive loading level

5.1.5 Stress field calculation σ^e

5.1.5.1 Map of σ^e

Recall the Eq.(1.5) presented in chapter 1, stress σ^e can be calculated using a 4th-order stiffness tensor C^e of aluminium and the strain tensors ε^e .

$$\begin{pmatrix} \sigma_{xx}^e \\ \sigma_{yy}^e \\ \sigma_{zz}^e \\ \sigma_{yz}^e \\ \sigma_{zx}^e \\ \sigma_{xy}^e \end{pmatrix} = \begin{pmatrix} C_{11}^e & C_{12}^e & C_{12}^e & 0 & 0 & 0 \\ C_{12}^e & C_{11}^e & C_{12}^e & 0 & 0 & 0 \\ C_{12}^e & C_{12}^e & C_{11}^e & 0 & 0 & 0 \\ 0 & 0 & 0 & C_{44}^e & 0 & 0 \\ 0 & 0 & 0 & 0 & C_{44}^e & 0 \\ 0 & 0 & 0 & 0 & 0 & C_{44}^e \end{pmatrix} \begin{pmatrix} \varepsilon_{xx}^e \\ \varepsilon_{yy}^e \\ \varepsilon_{zz}^e \\ \varepsilon_{yz}^e \\ \varepsilon_{zx}^e \\ \varepsilon_{xy}^e \end{pmatrix} \quad (1.5)$$

C_{ijkl}^e (in GPa) of aluminium in Eq.(1.5) could be calculated using Young's modulus $E = 70$ GPa and Poisson's ratio $\nu = 0.33$ [source: ASM Aerospace Specification Metals, Inc.]. C_{11}^e , C_{12}^e and C_{44}^e can be directly written as:

$$\begin{cases} C_{11}^e = \frac{E(1-\nu)}{(1+\nu)(1-2\nu)} = 103.7 \text{ GPa} \\ C_{12}^e = \frac{E\nu}{(1+\nu)(1-2\nu)} = 51.1 \text{ GPa} \\ C_{44}^e = \frac{E}{2(1+\nu)} = 26.3 \text{ GPa} \end{cases} \quad (5.1)$$

σ^e at each strain level are calculated in Tab.5.5 and the maps of σ^e are shown in Fig.5.19-5.22.

For our experimental situation, the out-of-plane components σ_{zz}^e in stress tensor should be zero. Yet, it is noted that non-negligible values were obtained here. In fact, the calculation of σ_{zz}^e depends on the value of ν applied in Eq.5.1. In our

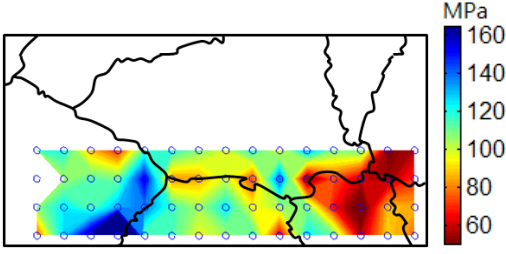


Figure 5.19: Map of σ_{xx}^e at level ①
($\bar{\sigma}_{xx}^e = 103.6$ MPa).

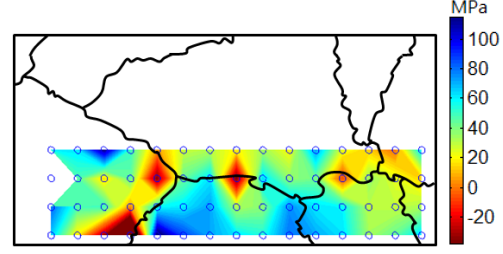


Figure 5.20: Map of σ_{yy}^e at level ①
($\bar{\sigma}_{yy}^e = 28.9$ MPa).

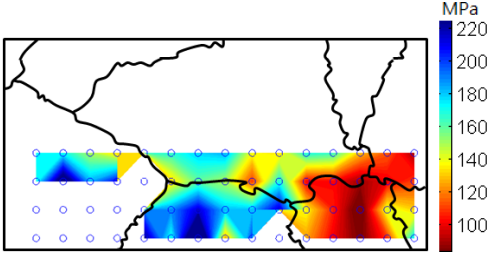


Figure 5.21: Map of σ_{xx}^e at level ②
($\bar{\sigma}_{xx}^e = 153.4$ MPa).

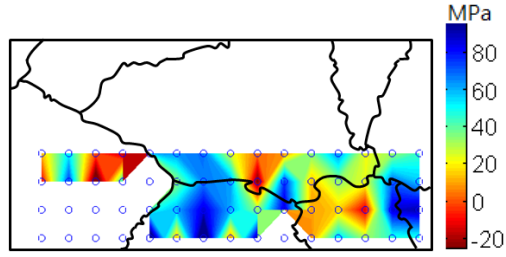


Figure 5.22: Map of σ_{yy}^e at level ②
($\bar{\sigma}_{yy}^e = 41.8$ MPa).

Loading level	Mean value of σ^e (MPa)					
	$\bar{\sigma}_{xx}^e$	$\bar{\sigma}_{yy}^e$	$\bar{\sigma}_{zz}^e$	$\bar{\sigma}_{yz}^e$	$\bar{\sigma}_{zx}^e$	$\bar{\sigma}_{xy}^e$
①	103.6	28.9	20.1	-2.7	-3.4	-3
②	153.4	41.8	35.2	-6.8	-6.2	-3

Table 5.5: Mean value of σ^e of sample 1 at each successive loading level

case, the literature value of $\nu = 0.33$ was used. If ν is calculated using the obtained $\varepsilon_{yy}^e/\varepsilon_{xx}^e$ or $\varepsilon_{yy}^e/\varepsilon_{xx}^e$ at loading level ① and ②, a mean value of $\nu = 0.25$ with a standard deviation of 0.19 was obtained. Although the σ^e of every XRD measured point can be recalculated using $\nu = 0.25$ in Eq.5.1 and then given negligible values in σ_{zz}^e (Tab.5.6), meanwhile, the calculated σ_{xx}^e values could not be consistent with the ones measured by load cell. This explains why the literature value of $\nu = 0.33$ was kept in Eq.5.1.

Loading level	Mean value of σ^e (MPa)					
	$\bar{\sigma}_{xx}^e$	$\bar{\sigma}_{yy}^e$	$\bar{\sigma}_{zz}^e$	$\bar{\sigma}_{yz}^e$	$\bar{\sigma}_{zx}^e$	$\bar{\sigma}_{xy}^e$
①	90.7	11.2	1.9	-2.9	-3.6	-3.2
②	133.7	14.9	8	-7.3	-6.6	-3.2

Table 5.6: Mean value of σ^e calculated using $\nu = 0.25$ at each successive loading level

At this moment, the question of out-of-plane components in our case still needs more investigation and the reason of this findings will be explored in the future.

5.1.5.2 Uncertainty estimation of the stress tensor σ_{σ^e}

The uncertainty of the stress field σ_{σ^e} at each strain level was calculated and the maps of σ_{σ^e} are shown in Fig.5.23-5.25. The mean value and the standard deviation (Std) of σ_{σ^e} are listed in Tab.5.7 and Tab.5.8. It can be seen that the σ_{σ^e} are always smaller than 4 MPa.

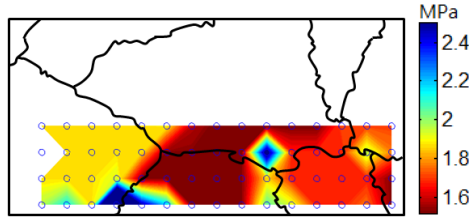


Figure 5.23: Map of ε_{xx}^e at level ①
($\overline{\sigma_{\sigma_{xx}^e}} = 1.8$ MPa).

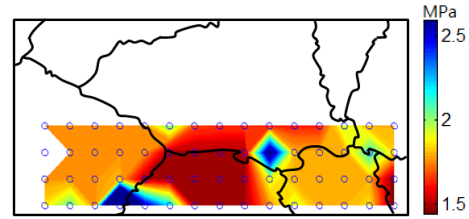


Figure 5.24: Map of ε_{yy}^e at level ①
($\overline{\sigma_{\sigma_{yy}^e}} = 1.8$ MPa).

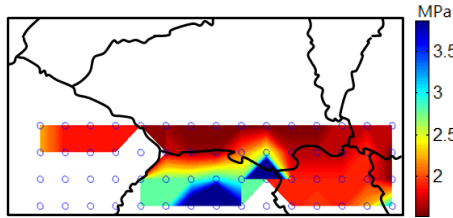


Figure 5.25: Map of ε_{xx}^e at level ②
($\overline{\sigma_{\sigma_{xx}^e}} = 1.8$ MPa).

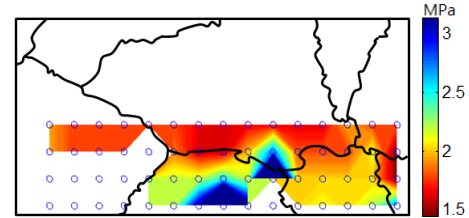


Figure 5.26: Map of ε_{yy}^e at level ②
($\overline{\sigma_{\sigma_{yy}^e}} = 2.3$ MPa).

Loading level	Mean value of σ_{σ^e} (MPa)					
	$\overline{\sigma_{\sigma_{xx}^e}}$	$\overline{\sigma_{\sigma_{yy}^e}}$	$\overline{\sigma_{\sigma_{zz}^e}}$	$\overline{\sigma_{\sigma_{yz}^e}}$	$\overline{\sigma_{\sigma_{zx}^e}}$	$\overline{\sigma_{\sigma_{xy}^e}}$
①	1.8	1.8	1.8	0.3	0.5	0.4
②	2.3	2.1	2.2	0.4	0.6	0.4

Table 5.7: Mean value of σ_{σ^e} of sample 1 at each successive loading level

Loading level	Standard deviation of σ_{σ^e} (MPa)					
	Std($\sigma_{\sigma_{xx}^e}$)	Std($\sigma_{\sigma_{yy}^e}$)	Std($\sigma_{\sigma_{zz}^e}$)	Std($\sigma_{\sigma_{yz}^e}$)	Std($\sigma_{\sigma_{zx}^e}$)	Std($\sigma_{\sigma_{xy}^e}$)
①	0.3	0.4	0.4	0.1	0.1	0.1
②	1.3	0.8	1.1	0.1	0.3	0.2

Table 5.8: Standard deviation of σ_{σ^e} of sample 1 at each successive loading level

5.1.6 Discussion

5.1.6.1 Evolution and scattering of local stress-strain at each loading level

In order to better understand the experimental results, the evolution and the distribution of local stress σ^e with the associated total strain ε^t at each point of XRD measurement (marked as ' \triangle ' and ' \square ' for the first and second loading levels respectively) are plotted in Fig.5.27. The mean tensile stress σ^e measured during the test versus the ε^t averaged over the useful part of the specimen is plotted (marked as 'x') in the same figure as reference. The σ^e - ε^t values among the 45 XRD measured points at each loading level were also averaged (i.e. $\overline{\sigma^e}$ - $\overline{\varepsilon^t}$) and plotted in Fig.5.27. ' \triangle ' and ' \square ' with thicker-edge correspond to the $\overline{\sigma^e}$ - $\overline{\varepsilon^t}$ value of the first and second loading level respectively.

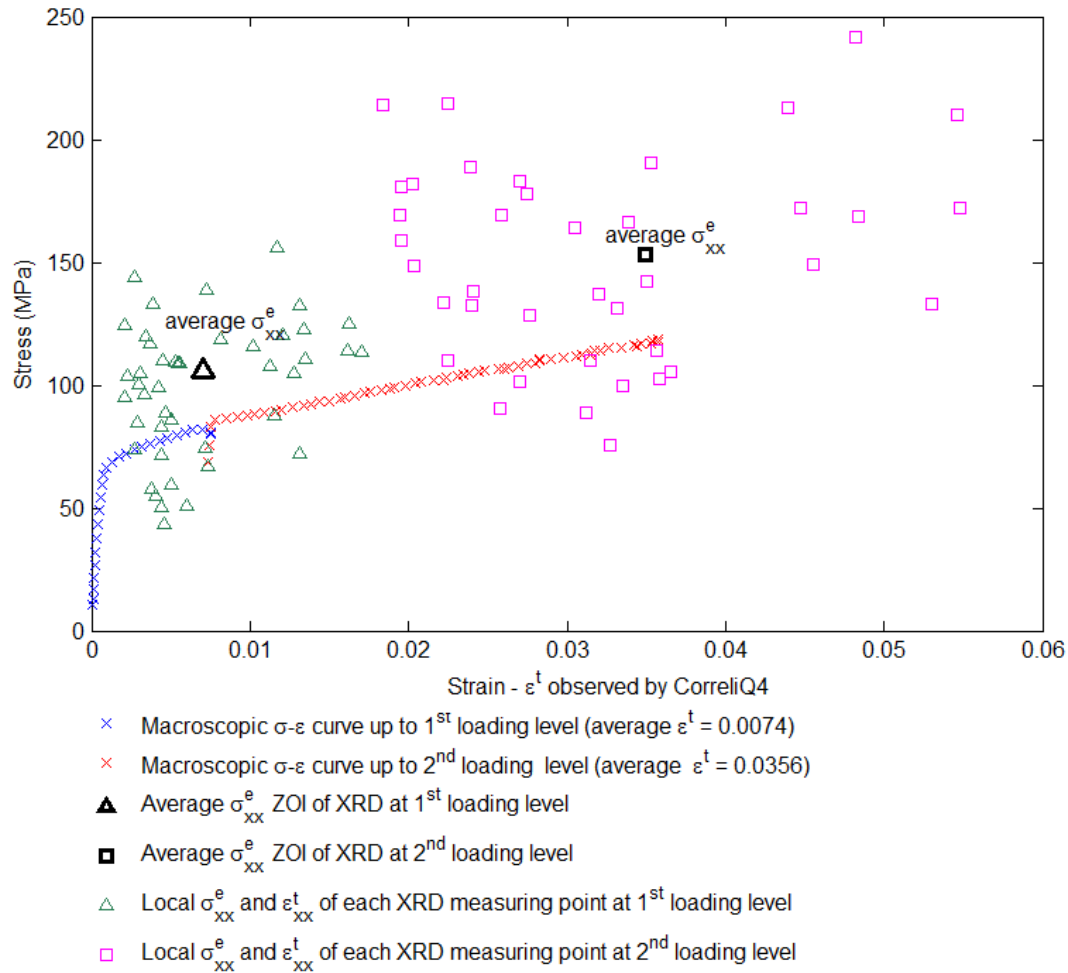


Figure 5.27: Distribution of the local σ^e - ε^t at each point of measurement of XRD on the sample 1 at loading level of $\overline{\varepsilon_{xx}^t} = 0.0074$ and 0.0356.

The two grids used to measure σ^e - ε^t are different. For this reason, it is not possible to associate directly a σ^e to a ε^t at the same localisation. We associate each σ^e value to the average of ε^t on the four closest DIC measured points. There are 45 measured points with σ^e - ε^t values in sample 1.

In Fig.5.27, both $\overline{\sigma_{xx}^e}$ calculated at level ① and ② were higher than the average stress captured by the load cell (Fig.5.27). In fact, $\overline{\sigma_{xx}^e}$ was calculated over the half of the specimen. The averaged stress value in this part could thus be twice as high as in the area not measured by XRD. It is also observed that the scattering of σ^e and ε^t increased during the loading. To better discuss the scattering of the local stress-strain at each loading level, the local σ^e - ε^t values of 10 measured points are plotted in Fig.5.28. The position of the selected points in sample 1 are indicated in Fig.5.29.

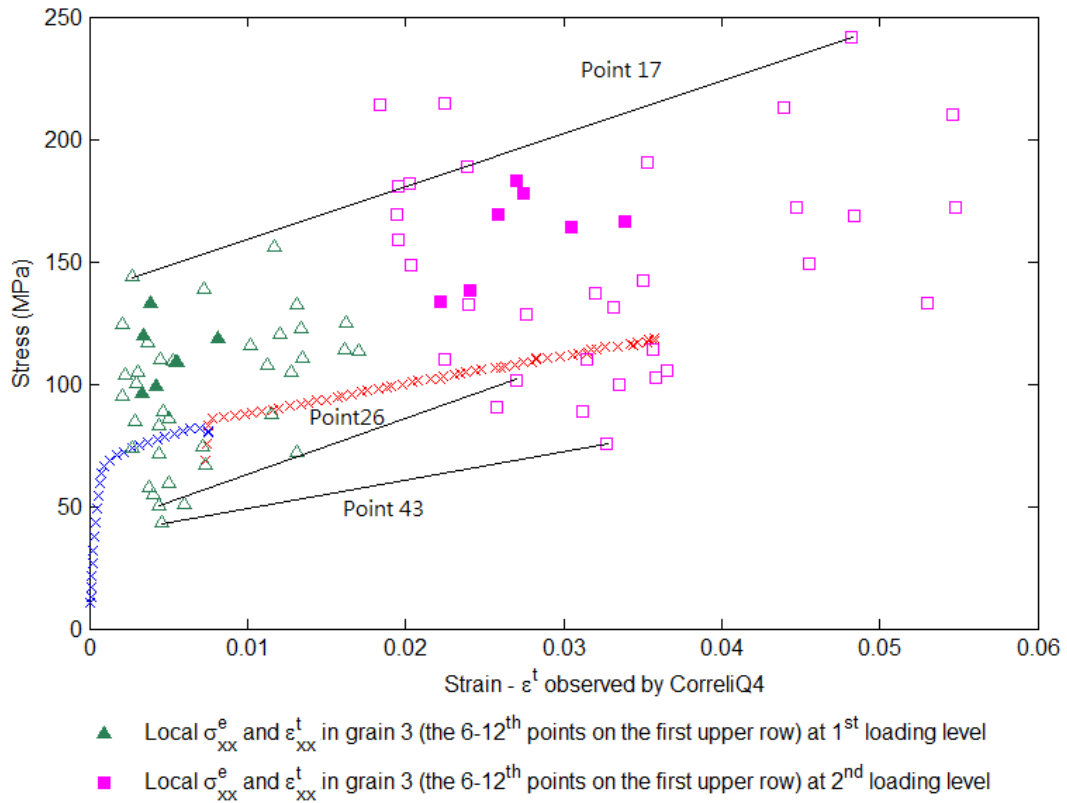


Figure 5.28: Distribution of the local σ^e - ε^t of a set of measuring point in grain 3 (the 6-12th points on the first upper row) and of points 17, 26 and 43 at loading level of $\overline{\varepsilon_{xx}^t} = 0.0074$ and 0.0356 .

Points 26 and 43 remain at very low σ^e value during the loading. On contrary, point 17 has a relatively high σ^e value among the other points throughout the tensile loading. Yet, for point 26, strain hardening begins between the first and the second loading levels. The corresponding ε^t values of these three points were lower than the others (below $\overline{\varepsilon_{xx}^t}$) at the beginning. At the second loading level, point

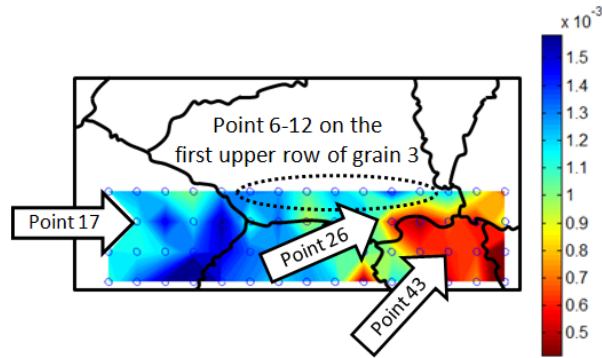


Figure 5.29: The XRD measuring points selected and traced in Fig. 5.28. (Maps of ε_{xx}^e at level ① ($\overline{\varepsilon_{xx}^e} = 1.2 \times 10^{-3}$))

17 was highly deformed (above $\overline{\varepsilon_{xx}^t}$) while it is not the case in point 26 and 43. At the same time, for the 8 selected points in grain 3 (including point 26 in grain 3), the scattering of both σ^e and ε^t values is large and increases during the loadings. It emphasises the research interest in full-field measurement of a material at grain scale as one measurement per crystal cannot represent the overall local mechanical response of a material [Zhou (1994); Huang (2007); Tran (2013)].

5.1.6.2 Analysis of the mechanical response of sample 1 under elastic and plastic loading and confirmation of the validity of the ε^e field measured by XRD

The zones with high/low level of strain in ε^t (Fig. 5.5 - 5.8) and ε^e (Fig. 5.11-5.14) fields are not comparable. For example, at loading level ②, compared to other parts of the sample, grain 10 showed a very low ε^t value (the region indicated with an arrow in Fig. 5.30) and a very high ε^e value (Fig. 5.31).

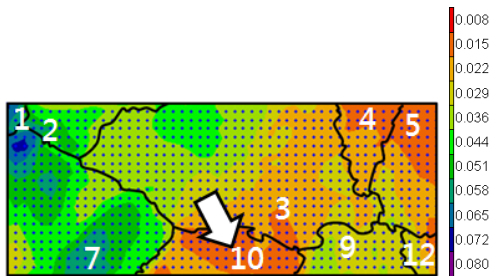


Figure 5.30: Recall the map of ε_{xx}^t at level ② ($\overline{\varepsilon_{xx}^t} = 0.0356$).

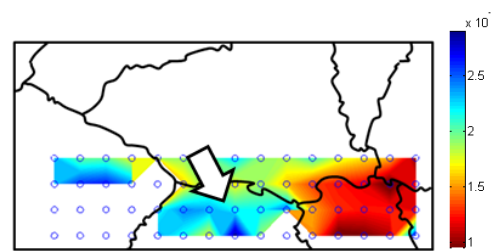


Figure 5.31: Recall the map of ε_{xx}^e at level ② ($\overline{\varepsilon_{xx}^e} = 1.8 \times 10^{-3}$).

In order to analyse the mechanical response of sample 1 under elastic and plastic loading, a third tensile test with loading ③ ($\overline{\varepsilon_{xx}^t} = 0.0378$) and unloading ③ ($\overline{\varepsilon_{xx}^t} = 0.0378$) was conducted on the same sample after the unloading which followed level

② (Fig. 5.32). It is assumed that the first part of the loading (between images 1 and 18) and the unloading part (between images 26 and 38) are purely elastic. The elastic strain deformation of these loading/unloading were characterised by DIC. Fig.5.34 shows the map of ε^t field calculated using images 1 and 18 while Fig.5.35 shows ε^t field calculated using image 38 and 26. During calculation, the size of subset was enlarged to 64 pixels (spatial resolution = 64 pixels \times 10.2 $\mu\text{m}/\text{pixels}$ = 652.8 μm) due to the sensibility of background noise. Besides, it is reminded that the calculation of ε^t value in ③ and ② were not using the same point of reference. In fact, for the image 1 used in ③, there was plastic deformation from the initial state to level ②.

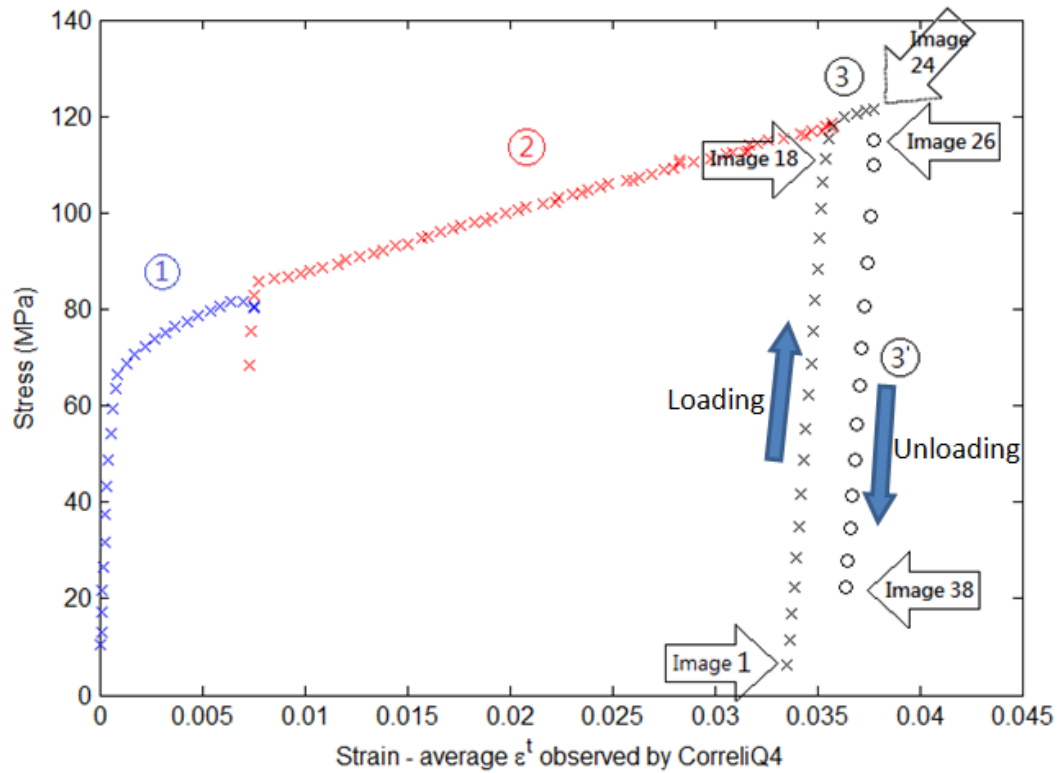


Figure 5.32: Stress-strain curve showing the third tensile test added.

For the strain field calculated between images 1 and 24 in ③ (Fig.5.33), the zones showing higher/lower ε^t value is similar to the one obtained in ② except in grains 9 and 10 (Fig. 5.30). The distribution of ε^t is still largely grouped by grain and the strain gradients inside are small. Grains 1, 2, 7 on the left of the zone of interest are still more deformed than grains 4, 5, 10, 12 on the right of the sample. A more intense strain gradient is observed at the grain boundary between grains 7 and 10 and the ε^t in grain 10 is still lower than that observed in the majority of the zone of interest. And here we can see that the right hand side of sample 1 does not undergo plastic deformation any more (grains 4,6,9 12 and a small part of grain 3). Grain 10 slightly plastified at ② but plastically deformed at ③. The left side

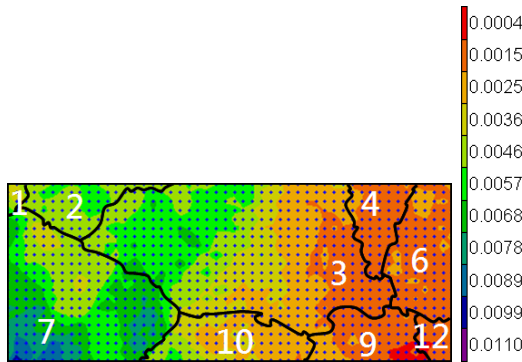


Figure 5.33: ε_{xx}^t calculated using image 1 and 24 during tensile loading at ③. Loading part: elastic and plastic deformation.

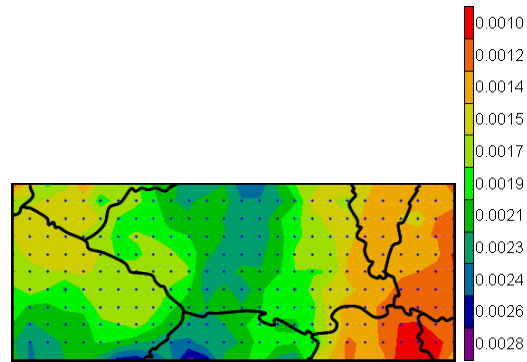


Figure 5.34: ε_{xx}^e calculated using image 1 and 18 during tensile loading at level ③ ($\overline{\varepsilon_{xx}^e} = 0.0018$). Loading part: elastic deformation.

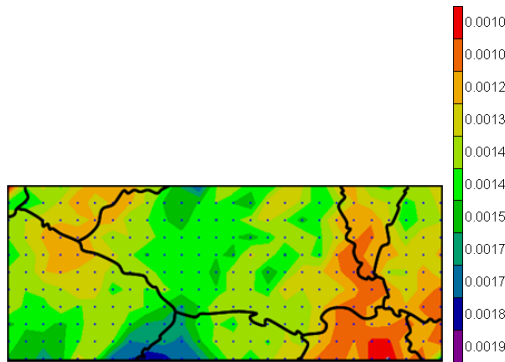


Figure 5.35: ε_{xx}^e calculated using image 38 and 26 during unloading at level ③ ($\overline{\varepsilon_{xx}^e} = 0.0014$). Loading part: elastic deformation.

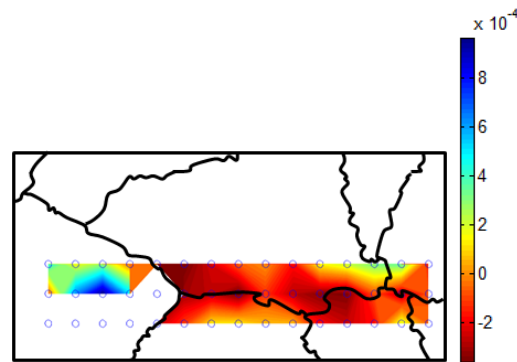


Figure 5.36: Difference between ε_{xx}^e at level ② (Fig.5.31) and ε_{xx}^e calculated during the elastic part of loading at level ③ (Fig.5.34).

of the specimen, which had already been largely deformed at level ②, is the zone that also has the most significant increment of strain to get to ③. Once the top left corner of the specimen was the most deformed zone at ②, and now the bottom left corner shows the most significant strain increment. Since the surface was not filmed during unloading after ②, it is not possible to add directly the increment of strain obtained at ③ to that measured at ②.

It can be observed that the total strain field measured during the elastic part of the loading/unloading (Fig.5.34-5.35) (images 1-18 and 38-26) is strongly different from the one measured during the elasto-plastic loading (Fig.5.33) (images 1-24). However, the strain field shown in Fig.5.34-5.35, i.e. measured during the elastic part of loading ③ and unloading ③, are very similar, in terms of distribution and

magnitude of strain value ($[1 \times 10^{-3}, 2.8 \times 10^{-3}]$), to the ε^e field obtained by XRD at loading level ② (Fig.5.31), e.g. grains 7 and 10 on the left of the zone of interest are more deformed than grains 5, 9, 12 on the right of the sample. In order to confirm the validity of the elastic strain field measured by XRD, the difference between ε_{xx}^e at level ② (Fig.5.31) and ε_{xx}^e calculated during the linear part of loading at level ③ (Fig.5.34) was made and plotted in Fig.5.36. The zone where these two strain fields are compared is quite limited, however, it is observed that a homogeneous distribution of the difference (-1.3×10^{-5}) can be observed to a large extent. This comparison allows to confirm the validity of the elastic strain field measured by XRD.

For further discussion, the difference ($\Delta\varepsilon_{xx}^e$) of the strain fields calculated in linear parts of loading / unloading is plotted in Fig.5.37. $\overline{\Delta\varepsilon_{xx}^e} = 4.46 \times 10^{-4}$ with a standard deviation of 1.26×10^{-4} was obtained. The distribution of the difference is not homogeneous. It is because the existence of plastification of the sample during loading / unloading is still unknown. However, referring to Fig.5.37, it can be seen that the region in the middle of the sample (Grains 3 and 10) slightly deform plastically. Thus, it is a hypothesis to be confirmed.

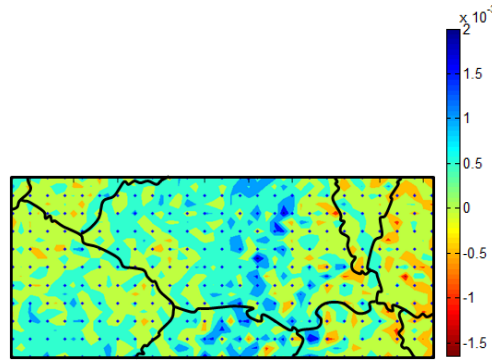


Figure 5.37: Difference of ε_{xx}^e calculated during the loading (Fig.5.34) and unloading (Fig.5.35).

The validation of the procedure in actual experimental conditions was made. A more complete in situ experiment could be conducted on a second specimen, with a larger measurement area, and regular discharges to access maximum information.

5.2 Experimental results of sample 2

Once the experimental protocol was validated using sample 1, a similar tensile test and ε^t - ε^e measurements were conducted in situ in the X-ray diffractometer on a second specimen, sample 2. On this sample, a tensile test was applied with 4 successive loadings and unloadings. Similar to previous section, sample 2 and the zone of interest for DIC and XRD will be presented. The global stress-strain curve measured during the tensile test will be shown, as well as ε^t , ε^e and σ^e and their uncertainties fields acquired on the surface of the specimen. Lastly, the evolution and distribution of local σ^e - ε^t will be discussed.

5.2.1 Zone of XRD and DIC measurement

For sample 2, a more complete zone of XRD were defined. The observation area of DIC and XRD is $17.1 \times 7.76 \text{ mm}^2$ and $14 \times 6 \text{ mm}^2$ respectively (Fig.5.38).

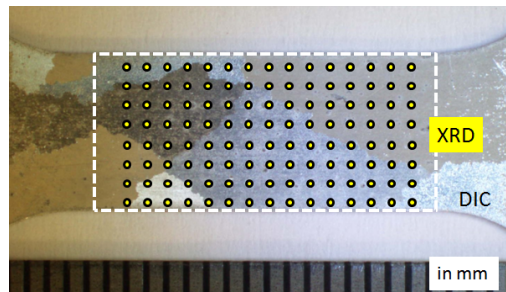


Figure 5.38: ZOI of sample 2.

The grain geometry of sample 2 is recalled in Fig.5.39-5.40) on both sides of the sample to facilitate the data analysis.

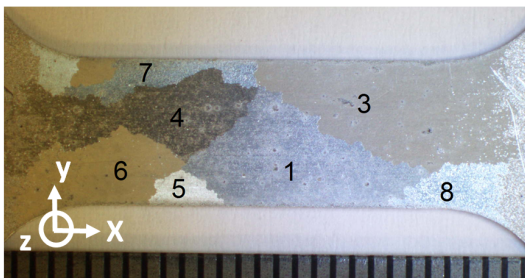


Figure 5.39: Front view of sample No.2 with its grains numbered.

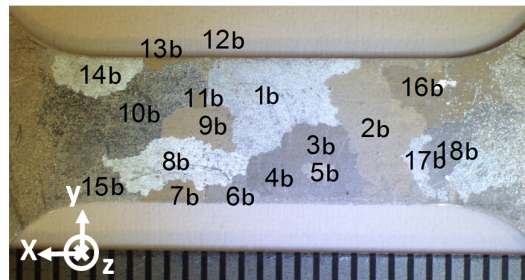


Figure 5.40: Back view of sample No.2 with its grains numbered.

5.2.2 Tensile tests

Similar to sample 1, sample 2 was also subjected to a symmetric loading in the x-direction. Four sets of loading (n) and unloading (n') were conducted at about every 1% of total strain. Photos were taken throughout the entire tensile test and ε^t was calculated using Correli_Q4. The mean strain ε^t was averaged over the useful part of the specimen. The mean tensile stress measured from the load cell during the test was plotted in Fig.5.41 versus the mean strain.

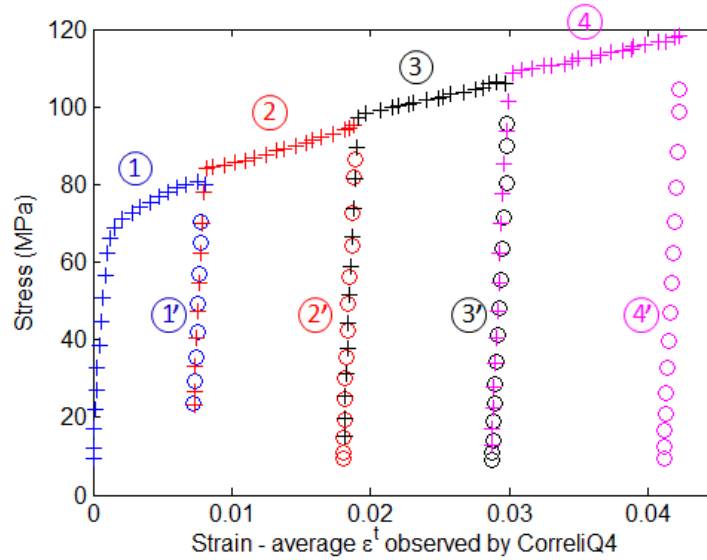


Figure 5.41: Stress-strain curve. The micro tensile machine was stopped once at ① $\varepsilon_{xx}^t = 0.0081$, ①' $\varepsilon_{xx}^t = 0.0072$, ② $\varepsilon_{xx}^t = 0.0188$, ②' $\varepsilon_{xx}^t = 0.0181$, ③ $\varepsilon_{xx}^t = 0.0297$, ③' $\varepsilon_{xx}^t = 0.0288$, ④ $\varepsilon_{xx}^t = 0.0423$ and ④' $\varepsilon_{xx}^t = 0.0412$.

5.2.3 Total strain field measurement ε^t

5.2.3.1 Map of ε^t

The validated area of total strain ε^t field of sample 1 is $15.99 \times 6.85 \text{ mm}^2$. The in-plane components ε_{xx}^t and ε_{yy}^t of loading ①, ②, ③ and ④ are plotted at the same scale in Fig.5.42.

Recalled that the element size of 32 pixels was used and the spatial resolution of ε^t calculated is $362.4 \mu\text{m}$.

As shown in Fig.5.42, ε_{yy}^t localised to a large extent grain by grain and the strain gradients are smooth. For ε_{xx}^t , the strain localised in grains 5 and 6. Intense strain gradients can be seen in grains 1, 3, 4 and 7 (indicated with black arrows in Fig.5.42) and the gradient increases with the imposed loading. The magnitude of the axial strain is much higher in the middle and on the right top corner of the sample than on the two ends. Although the grains have high SF values on both sides in the middle of the sample (e.g. grain 1 has a SF value of 0.49 and grains 1b

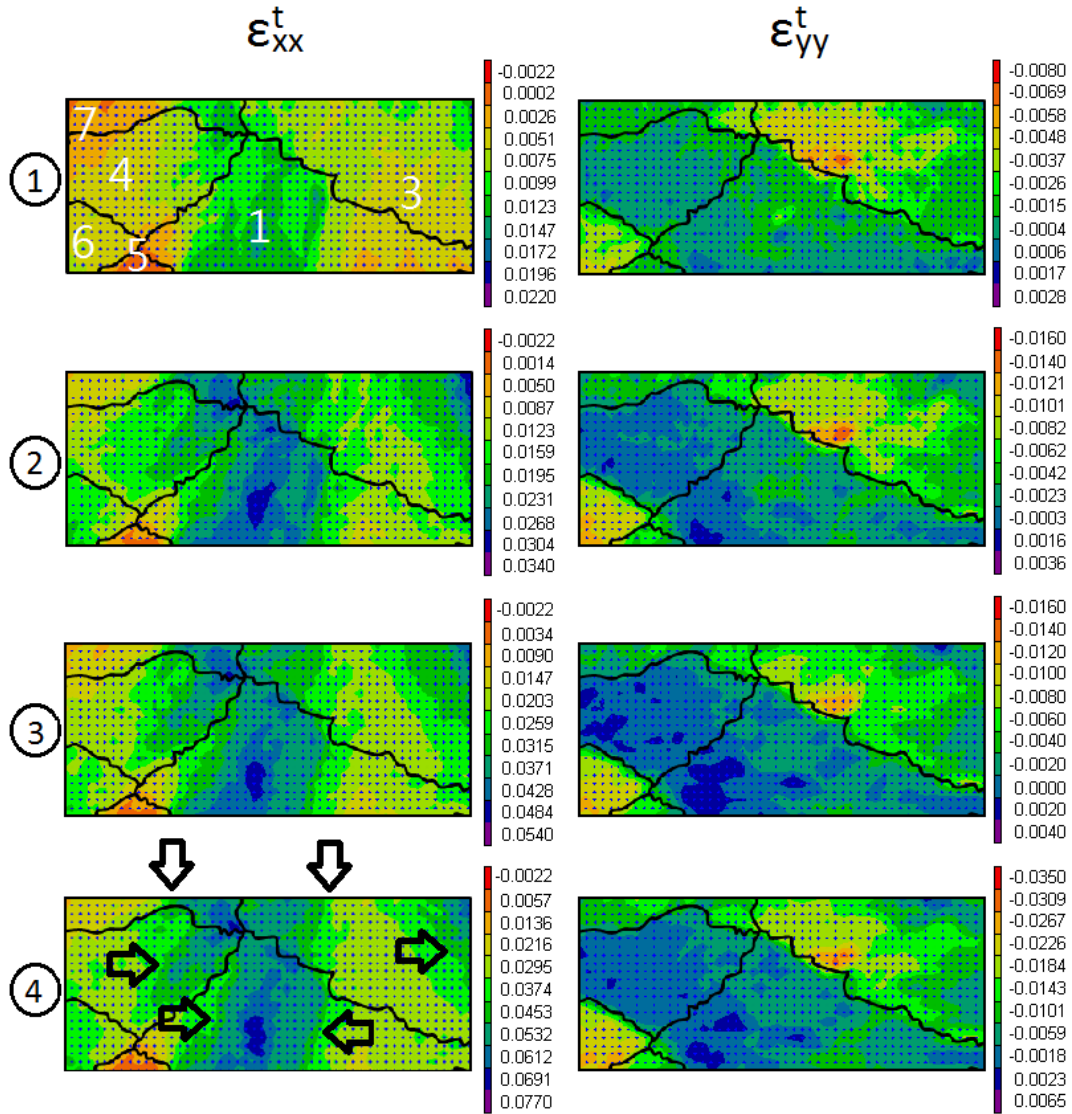


Figure 5.42: Map of ε_{xx}^t at level ① ($\varepsilon_{xx}^t = 0.0081$, $\varepsilon_{yy}^t = -0.0012$), ② ($\varepsilon_{xx}^t = 0.0188$, $\varepsilon_{yy}^t = -0.0031$), ③ ($\varepsilon_{xx}^t = 0.0297$, $\varepsilon_{yy}^t = -0.0047$) and ④ ($\varepsilon_{xx}^t = 0.0423$, $\varepsilon_{yy}^t = -0.0068$).

and 4b have SF value of 0.47 and 0.45 respectively), it is not sufficient to explain the localisation of strain. For example, the left hand side of the sample do not have strain localised but there are grains with SF values >0.46 (e.g. grains 4, 7, 2b, 16b and 4b). On the right hand back side of the sample, however, strain localised at the grain with weaker SF values (e.g. grain 14b). For these areas which cannot explained using SF values, it may be due to incompatibilities between grains of deformation. Even if they have close SF values, these grains probably did not have the same directions of slip planes, so if one deforms plastically along this plan, it leads to high stresses in the others. In order to further confirm this hypothesis, a finite element calculation and/or analysis of well-oriented slip system are proposed.

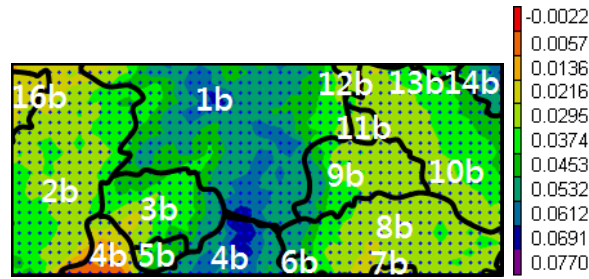


Figure 5.43: Map of ε_{xx}^t at level ④ with grain boundaries of sample back side superimposed ($\overline{\varepsilon_{xx}^t} = 0.0423$)

a. Front side			b. Back side		
Grain	Schmid factor	Number of activated slip system	Grain	Schmid factor	Number of activated slip system
1	0.4922	1	1b	0.4726	1
3	0.4640	1	2b	0.4683	1
4	0.4673	1	3b	0.4211	1
5	0.3266	1	4b	0.4687	1
6	0.4879	1	5b	0.4615	1
7	0.4648	1	6b	0.3897	1
			7b	0.4500	1
			8b	0.4677	1
			9b	0.3896	1
			10b	0.4564	1
			11b	0.3583	1
			12b	0.4247	1
			13b	0.3739	1
			14b	0.4513	1
			16b	0.4798	1

Table 5.9: Schmid factor of each grain of both sides of sample 2.

5.2.3.2 Uncertainty of the total strain tensor σ_{ε^t}

The error of the total strain field σ_{ε^t} is shown in Fig.5.44), it had a mean value of -4.9×10^{-6} with a standard deviation of 2.2×10^{-4} at each measuring point.

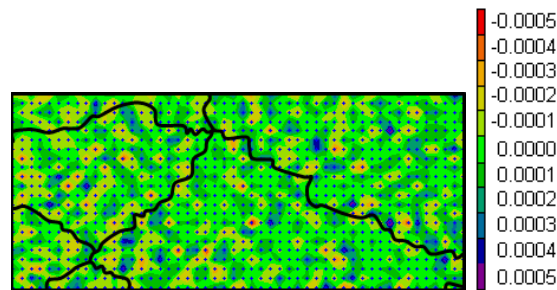


Figure 5.44: Error of total strain field σ_{ε^t} .

5.2.4 Elastic strain field measurement ε^e

5.2.4.1 Map of ε^e

Fields of components ε_{xx}^e and ε_{yy}^e obtained at levels ①, ②, ③ and ④ are shown in Fig.5.45. In order to analyse the evolution from one loading level to another, the ε^e fields are displayed with the same scale. The mean values $\overline{\varepsilon^e}$ of elastic strain were listed in Tab.5.10.

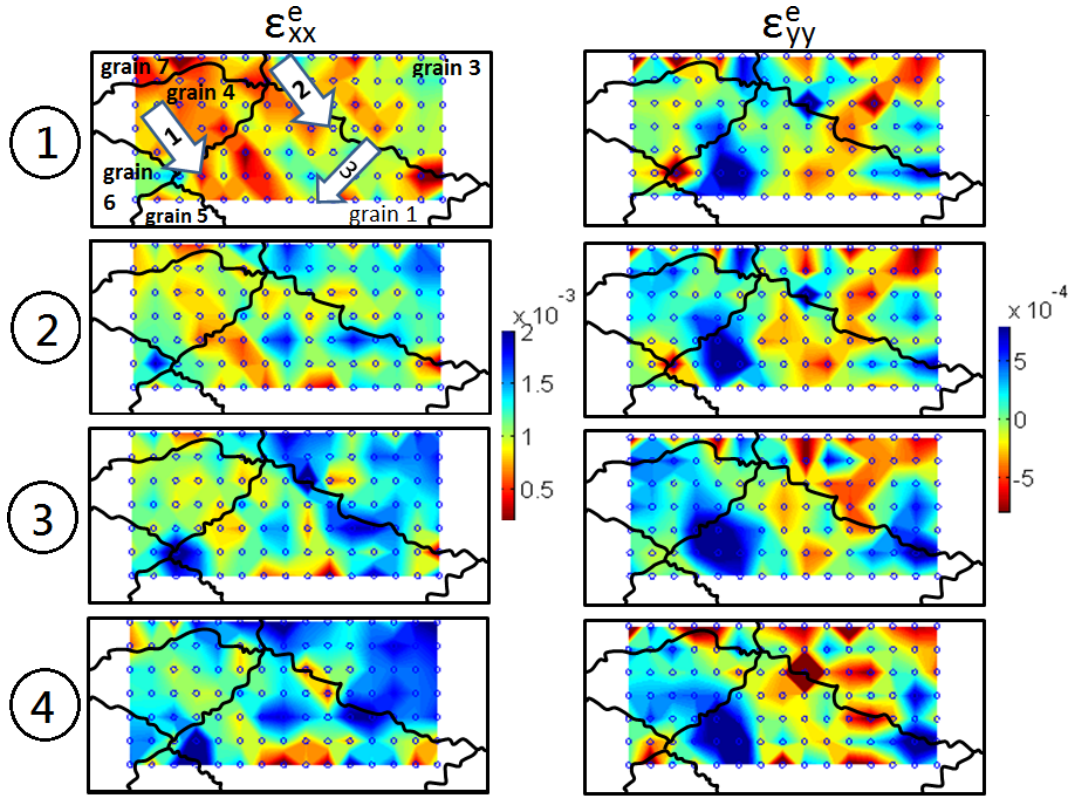


Figure 5.45: Maps of ε^e displayed with the same scale at loading level ① ($\overline{\varepsilon_{xx}^e} = 0.8 \times 10^{-3}$, $\overline{\varepsilon_{yy}^e} = -2 \times 10^{-5}$), ② ($\overline{\varepsilon_{xx}^e} = 1.1 \times 10^{-3}$, $\overline{\varepsilon_{yy}^e} = -3.5 \times 10^{-5}$), ③ ($\overline{\varepsilon_{xx}^e} = 1.2 \times 10^{-3}$, $\overline{\varepsilon_{yy}^e} = -4.8 \times 10^{-5}$) and ④ ($\overline{\varepsilon_{xx}^e} = 1.4 \times 10^{-3}$, $\overline{\varepsilon_{yy}^e} = -5 \times 10^{-5}$).

Loading level	Mean value of ε^e ($\times 10^{-3}$)					
	$\overline{\varepsilon_{xx}^e}$	$\overline{\varepsilon_{yy}^e}$	$\overline{\varepsilon_{zz}^e}$	$\overline{\varepsilon_{yz}^e}$	$\overline{\varepsilon_{zx}^e}$	$\overline{\varepsilon_{xy}^e}$
①	0.8	-0.	0.3	-0.1	0	-0.1
②	1.1	-0.	-0.4	-0.1	0	-0.1
③	1.3	-0.	-0.4	-0.1	0	-0.1
④	1.4	-0.1	-0.5	0	0	0

Table 5.10: Mean value of ε^e of sample 2 at each successive loading level

In Fig.5.45, similarly to ε^t results, zones with higher/lower elastic deformation

were observed on the sample surface. ε_{xx}^e is not homogeneous inside the grain. For example, higher strain values were found on the right of the sample and the intensity increases with the imposed loadings. In grain 3, intense strain gradients are seen and the localised strain in this area belongs to grain 10b and a small part of grains 1b and 9b (Fig.5.46). On the left hand side, lower strain values are found especially in grains 1, 4 and 7 and smooth strain gradients exist in the middle of these grains. If looking to the sample back side, the zone with lower strain values were localised in grains 2b, 3b, 4b and 6b. This heterogeneity increases with the imposed loading. Also, the evolution of strain hardening can be clearly observed inside crystals throughout the increase of loading, e.g. when the specimen macroscopically entered plastic deformation, the arrows (1) and (2) show the zones inside the same crystal with very low ε_{xx}^e values than other zones at ①. However, once the sample was pulled up to ②, strain hardening occurred at these two points and higher ε_{xx}^e values were found at ②, ③ and ④.

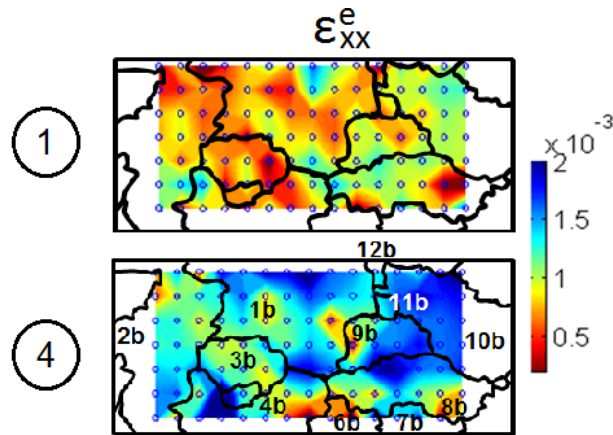


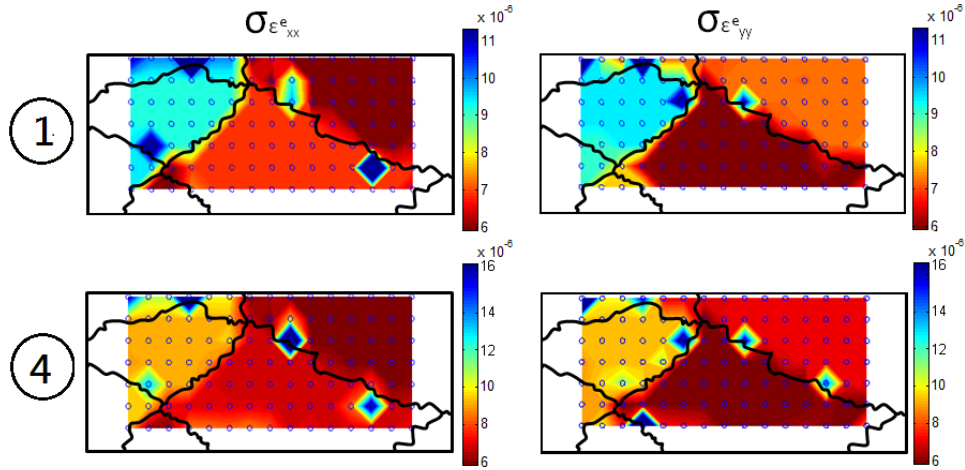
Figure 5.46: Map of ε_{xx}^e at level ① and ④ with grain boundaries of sample back side superimposed.

5.2.4.2 Uncertainty estimation of the elastic strain tensor σ_{ε^e}

The maps of σ_{ε^e} at strain level ① and ④ are shown in Fig.5.47. The mean values of σ_{ε^e} and its standard deviation value (Std) are listed in Tab.5.11-5.12.

ε^e uncertainties σ_{ε^e} are always smaller than 10^{-5} . The magnitudes of σ_{ε^e} are observed almost grouped by grain as the value of σ_{ε^e} is related to the selected diffraction planes (Chapter 3 §.3.6.2) while the chosen diffraction planes were different from one grain to another. Moreover, the point where uncertainty is locally high are mostly close to a grain boundary. Similar to sample 1, a total error range in σ_{ε^e} smaller than $\pm 3 \times 10^{-5}$ is implied considering a Gaussian distribution.

Comparing with σ_{ε^e} quantified in sample 1, the values are similar at ① but lower σ_{ε^e} value were obtained at ③. Actually, during XRD measurement for sample 2, the final peak position (ϕ , ψ and 2θ) converged at the previous loading was used as the initial positions of XRD scanning at the next loading. This modification

Figure 5.47: Map of σ_{ε^e} at level ① and ④.

Loading level	Mean value of σ_{ε^e} ($\times 10^{-6}$)					
	$\overline{\sigma_{\varepsilon^e_{xx}}}$	$\overline{\sigma_{\varepsilon^e_{yy}}}$	$\overline{\sigma_{\varepsilon^e_{zz}}}$	$\overline{\sigma_{\varepsilon^e_{yz}}}$	$\overline{\sigma_{\varepsilon^e_{zx}}}$	$\overline{\sigma_{\varepsilon^e_{xy}}}$
①	7.6	7.5	9.9	5.9	7.8	7.2
②	7.7	7.4	10	5.9	7.8	7.2
③	8.4	8.2	10.7	6.5	8.4	8
④	8	8	11	6	8	8

Table 5.11: Mean value of σ_{ε^e} of sample 2 at each successive loading level.

Loading level	Standard deviation of σ_{ε^e} ($\times 10^{-6}$)					
	$\text{Std}(\sigma_{\varepsilon^e_{xx}})$	$\text{Std}(\sigma_{\varepsilon^e_{yy}})$	$\text{Std}(\sigma_{\varepsilon^e_{zz}})$	$\text{Std}(\sigma_{\varepsilon^e_{yz}})$	$\text{Std}(\sigma_{\varepsilon^e_{zx}})$	$\text{Std}(\sigma_{\varepsilon^e_{xy}})$
①	2.2	1.3	3.8	1.2	2.5	1.8
②	2.2	1.4	3.8	1.3	2.5	1.9
③	3	2.9	4.5	2.4	4	2.6
④	3	3	4.5	2.5	4	2.7

Table 5.12: Standard deviation of σ_{ε^e} of sample 2 at each successive loading level.

allows ones to better relocate the new position of diffraction planes during plastic deformation so the number of diffraction planes is less reduced. As a result, σ_{ε^e} at ③ in sample 2 is lower than that of sample 1.

5.2.5 Stress field σ^e calculation

The maps of stress σ^e at each strain level are shown in Fig.5.48. Averaged values of σ^e at each strain level are calculated in Tab.5.13. The stress field is almost homogeneous at loading level ①, end of the elastic state. Since elasticity is isotropic in aluminium, there is no difference of stress distribution from a crystal to another.

Similarly, in sample 2, the out-of-plane components of stress tensor should be zero to verify the condition on free boundaries in the experimental situation. How-

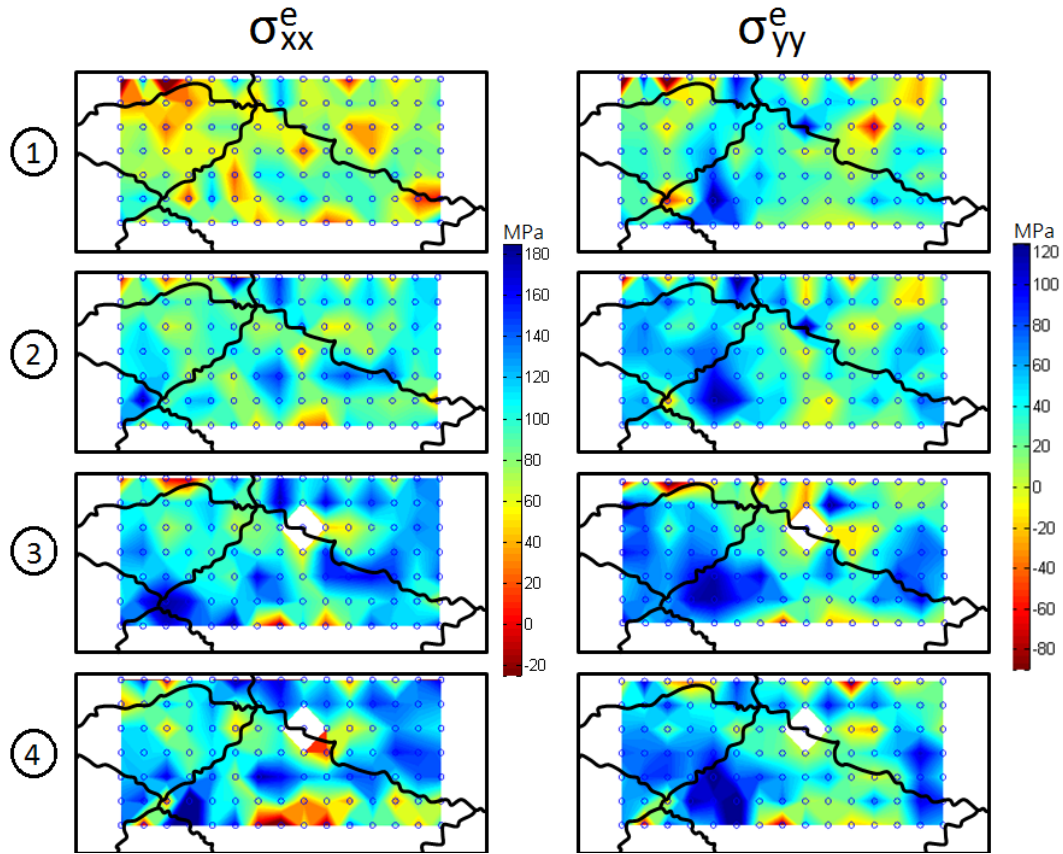


Figure 5.48: Maps of σ^e displayed with the same scale at loading level ① ($\bar{\sigma}_{xx}^e = 69.5$ MPa, $\bar{\sigma}_{yy}^e = 24.2$ MPa), ② ($\bar{\sigma}_{xx}^e = 94.9$ MPa, $\bar{\sigma}_{yy}^e = 38$ MPa), ③ ($\bar{\sigma}_{xx}^e = 108.3$ MPa, $\bar{\sigma}_{yy}^e = 39$ MPa) and ④ ($\bar{\sigma}_{xx}^e = 114.4$ MPa, $\bar{\sigma}_{yy}^e = 39.9$ MPa).

Loading level	Mean value of σ^e (MPa)					
	$\bar{\sigma}_{xx}^e$	$\bar{\sigma}_{yy}^e$	$\bar{\sigma}_{zz}^e$	$\bar{\sigma}_{yz}^e$	$\bar{\sigma}_{zx}^e$	$\bar{\sigma}_{xy}^e$
①	69.5	24.2	7.9	-3.5	1.0	-4.2
②	94.9	38	17.2	-3.3	0.3	-4.8
③	108.3	39	20	-2.8	-0.7	-3.8
④	114.4	39.9	17.6	-2.6	0.1	-2.3

Table 5.13: Mean value of σ^e of sample 2 at each successive loading level

ever, the non-negligible values were obtained. For sample 2, if ν is calculated using the obtained $\varepsilon_{yy}^e/\varepsilon_{xx}^e$ and $\varepsilon_{zz}^e/\varepsilon_{xx}^e$ at loading level ① and ②, a mean value of $\nu = 0.29$ with a standard deviation of 0.23 was obtained. Using $\nu = 0.29$ in Eq.5.1 gives negligible values in out-of-plane components of stress tensor, but the calculated σ_{xx}^e (in Tab.5.14) are still lower than the mean stress measured from the load cell during the test. Therefore, the literature value of $\nu = 0.33$ was kept in Eq.5.1. More investigation and discussion will be needed to answer the question of out-of-plane components in the future.

Loading level	Mean value of σ^e (MPa)					
	$\bar{\sigma}_{xx}^e$	$\bar{\sigma}_{yy}^e$	$\bar{\sigma}_{zz}^e$	$\bar{\sigma}_{yz}^e$	$\bar{\sigma}_{zx}^e$	$\bar{\sigma}_{xy}^e$
①	64.2	17.4	0.7	-3.6	1	-4.3
②	86.8	28.1	6.6	-3.4	0.3	-4.9
③	99.4	27.8	8.2	-2.9	-0.7	-3.9
④	105.2	28.4	5.4	-2.7	-0.1	-2.4

Table 5.14: Mean value of σ^e calculated using $\nu = 0.29$ at each successive loading level

5.2.5.1 Uncertainty estimation of the stress tensor σ_{σ^e}

The maps of uncertainty of the stress field σ_{σ^e} at strain level ① and ④ are shown in Fig.5.49. The mean value and the standard deviation (Std) of σ_{σ^e} are listed in Tab.5.15 and Tab.5.16. σ_{σ^e} are always smaller than 3.5 MPa.

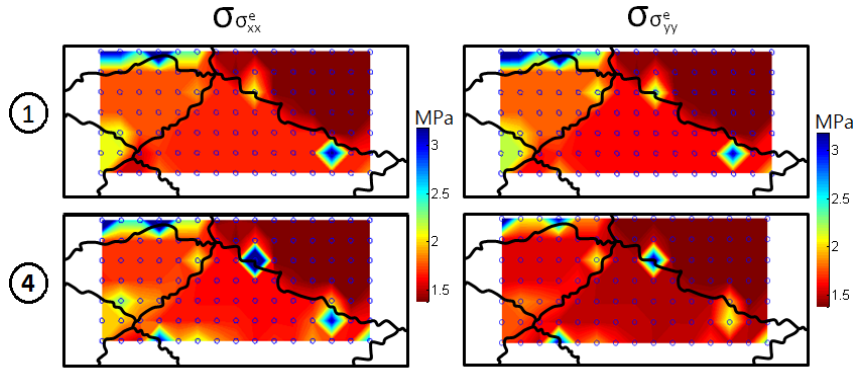


Figure 5.49: Map of σ_{σ^e} at levels ① and ④.

Loading level	Mean value of σ_{σ^e} (MPa)					
	$\sigma_{\sigma_{xx}^e}$	$\sigma_{\sigma_{yy}^e}$	$\sigma_{\sigma_{zz}^e}$	$\sigma_{\sigma_{yz}^e}$	$\sigma_{\sigma_{zx}^e}$	$\sigma_{\sigma_{xy}^e}$
① and ②	1.7	1.7	1.8	0.3	0.4	0.4
③ and ④	1.8	1.8	2	0.3	0.4	0.4

Table 5.15: Mean value of σ_{σ^e} of sample 2 at each successive loading level

Loading level	Standard deviation of σ_{σ^e} (MPa)					
	Std($\sigma_{\sigma_{xx}^e}$)	Std($\sigma_{\sigma_{yy}^e}$)	Std($\sigma_{\sigma_{zz}^e}$)	Std($\sigma_{\sigma_{yz}^e}$)	Std($\sigma_{\sigma_{zx}^e}$)	Std($\sigma_{\sigma_{xy}^e}$)
① and ②	1.7	1.7	1.8	0.3	0.4	0.4
③ and ④	0.5	0.5	0.6	0.1	0.2	0.1

Table 5.16: Standard deviation of σ_{σ^e} of sample 2 at each successive loading level

5.2.6 Discussion

5.2.6.1 Evolution and distribution of local σ^e - ε^t

Since a rich local mechanical response (4 loadings and 3 unloadings) were obtained for the second sample, which is much more than the previous one (2 loadings), in this part, the evolutions and the distributions of local stress σ^e with the associated total strain ε^t at each point of XRD measurement are plotted in two separated images — Fig.5.50 contains local σ^e - ε^t at loading level ① ($\overline{\varepsilon_{xx}^t} = 0.0081$) (marked as ‘ \triangle ’) and ③ ($\overline{\varepsilon_{xx}^t} = 0.0297$) (marked as ‘ \square ’) while Fig.5.51 contains the local results at loading level ② ($\overline{\varepsilon_{xx}^t} = 0.0297$) (marked as ‘+’) and ④ ($\overline{\varepsilon_{xx}^t} = 0.0288$) (marked as ‘ \circ ’). Filled symbols of ‘ \triangle ’, ‘ \square ’, ‘ \star ’ and ‘ \circ ’ correspond to the mean value $\overline{\sigma^e - \varepsilon^t}$ of loading level ①, ②, ③ and ④ respectively. The ε^t averaged over the useful part of the specimen against the mean tensile stress σ^e measured during the test is plotted (in straight line) in the same figure as reference.

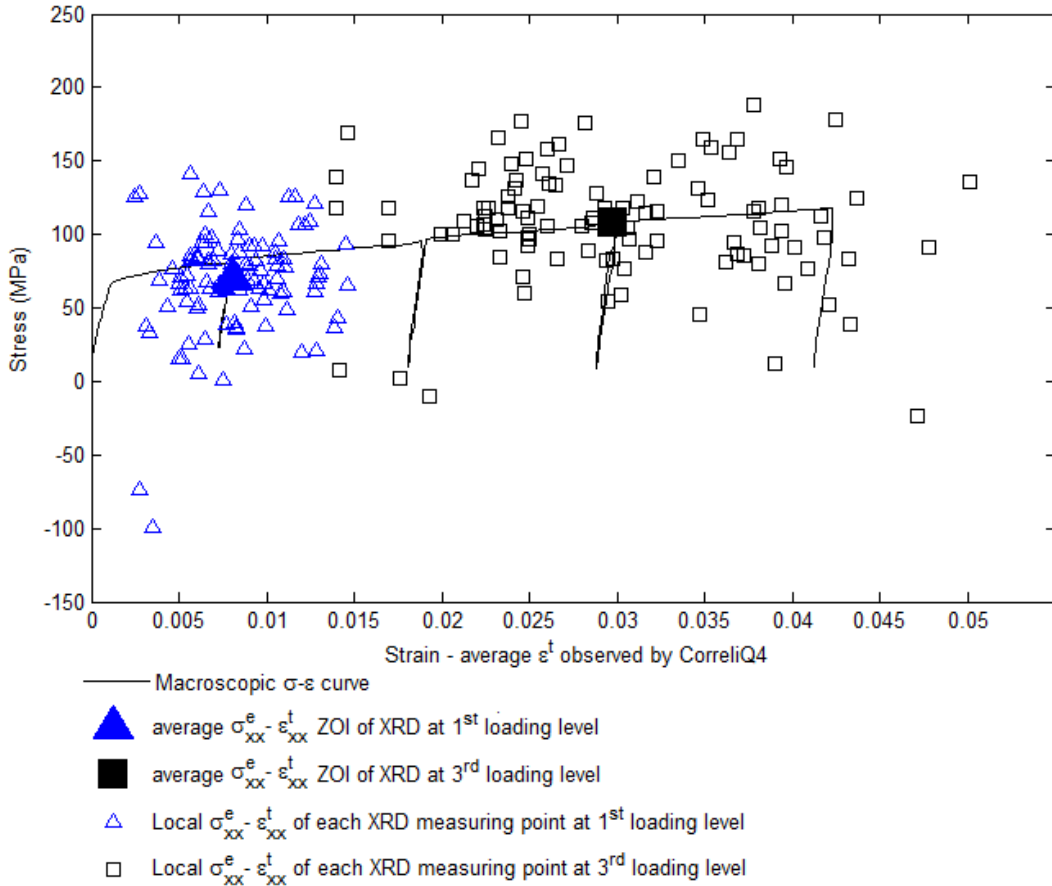


Figure 5.50: Distribution of the local σ^e - ε^t at each point of measurement of XRD on the sample 2 at loading level ① ($\overline{\varepsilon_{xx}^t} = 0.0081$) and ③ ($\overline{\varepsilon_{xx}^t} = 0.0297$).

In Fig.5.50-5.51, the averaged stress value in loading direction $\overline{\sigma_{xx}^e}$ at each loading level are close to the mean stress captured by the load cell. Thanks to a nearly full

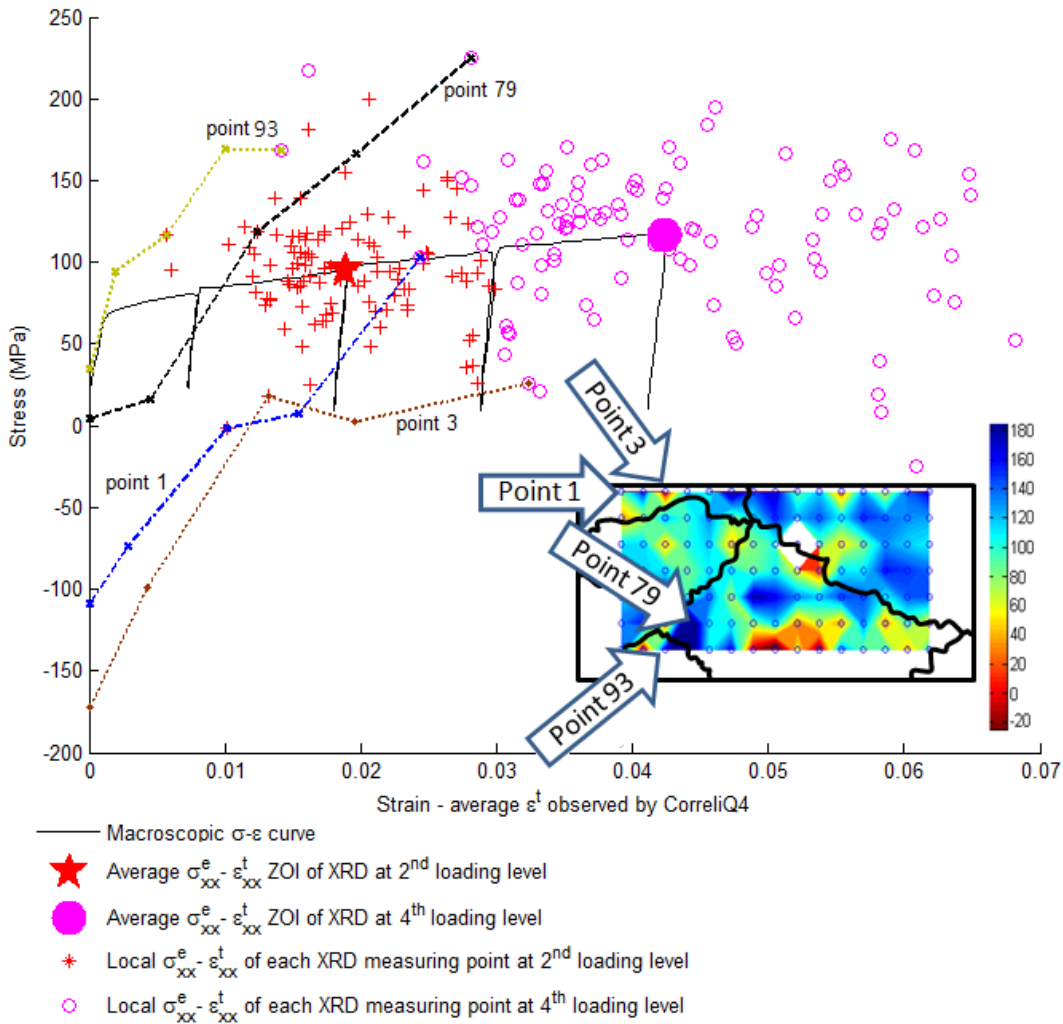


Figure 5.51: Distribution of the stress-strain at each point of measurement of XRD on the sample 2 at loading level ② ($\overline{\sigma_{xx}^t} = 0.0188$) and ④ ($\overline{\sigma_{xx}^t} = 0.0423$). The position of points 1, 3, 79 and 94 were indicated on the map of σ_{xx}^e at level ④ $\overline{\sigma_{xx}^e} = 114.4$ MPa.

sample surface (with 105 points of XRD measurement) characterized by XRD this time, the averaged stress value in this part can represent the global behaviour of sample 2. The scattering of local $\sigma^e - \varepsilon^t$ increases throughout the loadings. To better discuss the evolution of the local stress-strain at each loading level, the local $\sigma^e - \varepsilon^t$ values of 4 measured points are plotted in Fig.5.51. The position of the selected points are indicated in the same figure.

Points 1 and 3 remain at very low σ^e value from initial state to ③. At ④, σ^e of point 3 stays at low value while strain hardening begins for point 1 and its σ^e climbs to a value close to the mean σ^e of sample 2. Point 79 shows a very high σ^e value at ③ and ④. Before ③, its σ^e value is around the mean value at each loading

level. Point 94 has a relatively high σ^e value among the other points throughout the tensile loading.

The corresponding ε^t values of these four points were lower than the others throughout the tensile loading. Considering also the points with high ε^t values, five points of XRD measurement were picked from grain 1 and 3 (Fig. 5.52) and the corresponding local σ^e - ε^t curves were plotted (Fig.5.53 and Fig.5.54). The local σ^e - ε^t curves of the selected points also enable us to understand if the evolution of local σ^e - ε^t of each point of XRD measurement shares the same style as the average σ^e - ε^t performance does.

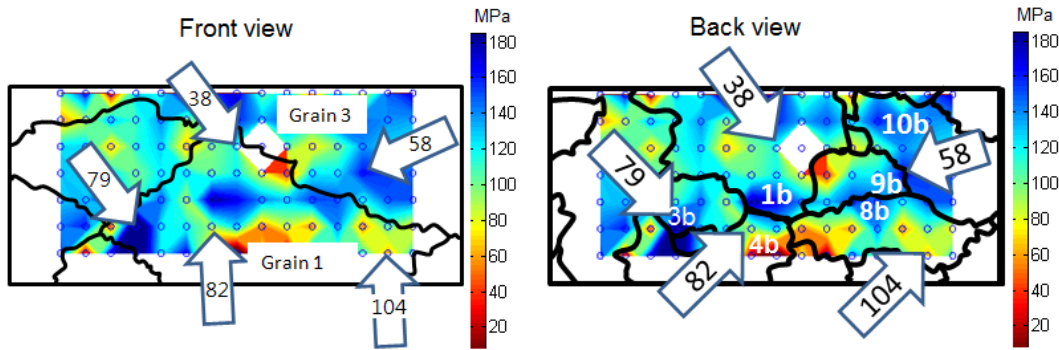


Figure 5.52: The position of 5 selected points of XRD measurement were indicated on the map of σ_{xx}^e at ④ ($\bar{\sigma}_{xx}^e = 114.4$ MPa) with grain boundaries of sample front and back side superimposed.

In Fig.5.53, the work hardening rate at point 79 is the highest among the points 38, 58 and 79. At ①, when the specimen macroscopically entered plastic deformation, the stress is very low at point 79 but high at point 38 and 58. However, once the sample was pulled up to the second loading level (② average $\varepsilon_{xx}^t = 0.0188$), a strain hardening occurred at point 79. Since then, point 79 showed a more significant strain hardening rate than point 38 — higher σ^e value was required for almost the same associated ε^t value. For the point 58 in grain 3 and the point 38 in grain 1, the shapes of σ^e - ε^t curves are similar to the average σ^e - ε^t behaviour. Meanwhile, point 38 is more likely to deform with lower applied stress comparing with point 58. In fact, SF value of the grains containing these two positions can be used as a clue of this observation. The point 58 belongs to grain 3 with SF = 0.464 at the front of the sample, grain 9b and grain 10b with SF = 0.3896 and 0.4564 respectively at the back of the sample while the point 38 belongs to grain 1 with SF = 0.4922 at the front of the sample, grain 1b with SF = 0.4726 at the back of the sample. As an overall performance, the SF values at the point 38 are all close to 0.5 which is more favourable to activate the slip system. Thus, a high ε^t value with low associated σ^e throughout the tensile loading for this point can be explained.

Being different from the σ^e - ε^t curves of previous discussed points or the averaged σ^e - ε^t curve, in Fig.5.54, points 82 and 104 in grain 1 are likely to deform with lower applied stress and a local ultimate tensile strength was observed at ③. Actually, the SF values of the grains around points 82 and 104 are very close to 0.5 (within

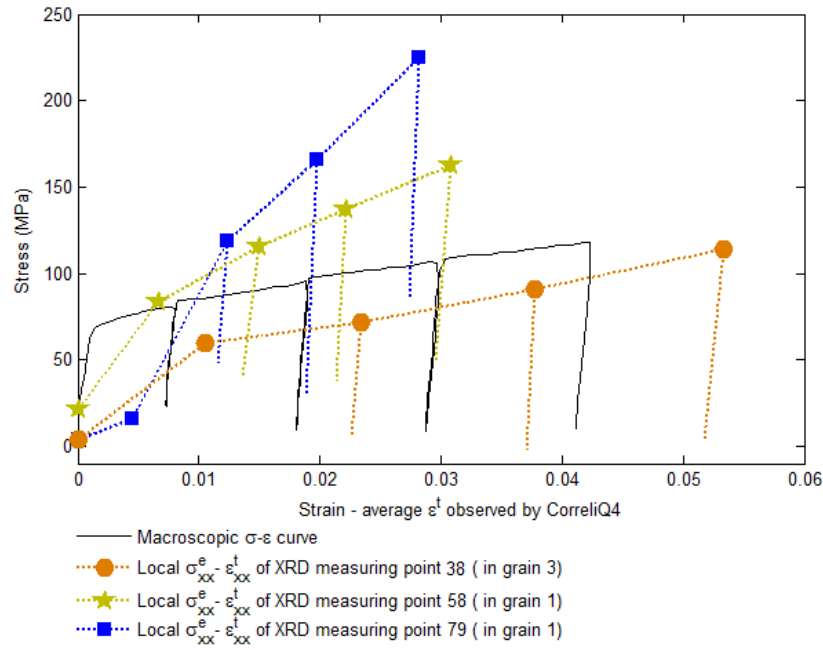


Figure 5.53: Evolution of local σ^e - ε^t of point 38 and 79 in grain 1 and 58 in grain 3 on the sample 2 during 4 loadings and 3 unloadings.

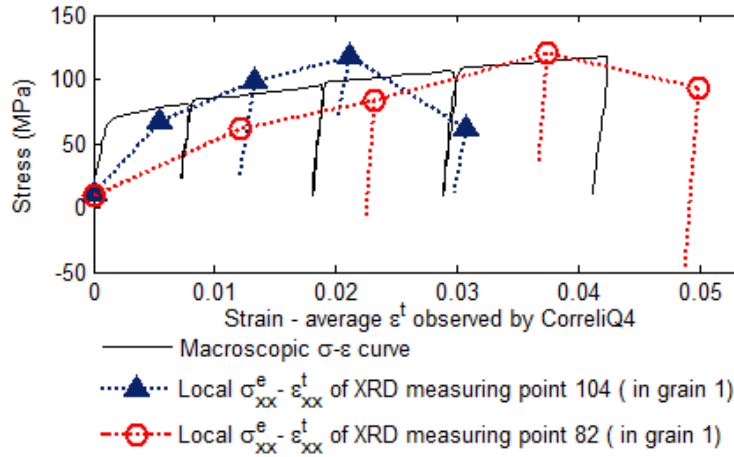


Figure 5.54: Evolution of local σ^e - ε^t of point 82 and 104 in grain 1 on the sample 2 during 4 loadings and 3 unloadings.

the range of 0.4687-0.4922), their slip system were likely to be activated during tensile loading and further plastified at ④.

5.2.6.2 Mechanical response of sample 2 during unloading

ε_{xx}^e fields calculated from XRD data at ②, ③ and ④ and ε_{xx}^t fields measured using DIC during the elastic part of the unloadings ②', ③' and ④' are shown with the

same scale in Fig.5.55. For further discussion, a map of ε_{xx}^e at ④ and a map of ε_{xx}^t at ④ with grain boundaries of sample back side superimposed were plotted in Fig.5.56. During ε_{xx}^t calculation, the size of subset was enlarged to 64 pixels (spatial resolution = 64 pixels \times 10.2 $\mu\text{m}/\text{pixels}$ = 652.8 μm) due to the sensibility of background noise.

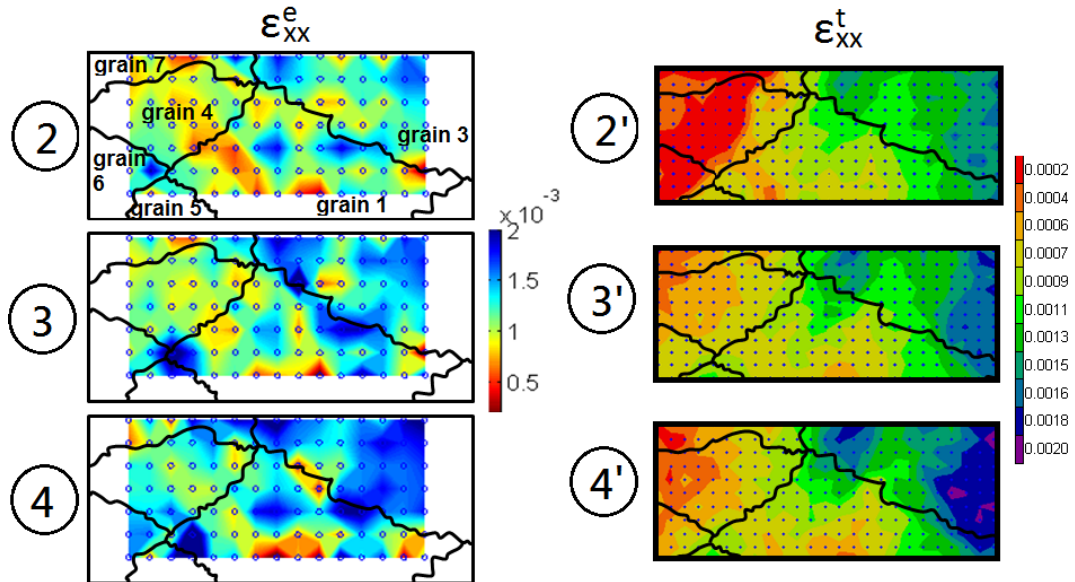


Figure 5.55: Map of ε_{xx}^e at ②, ③ and ④ and map of ε_{xx}^t measured during the elastic part of the unloadings ②', ③' and ④'.

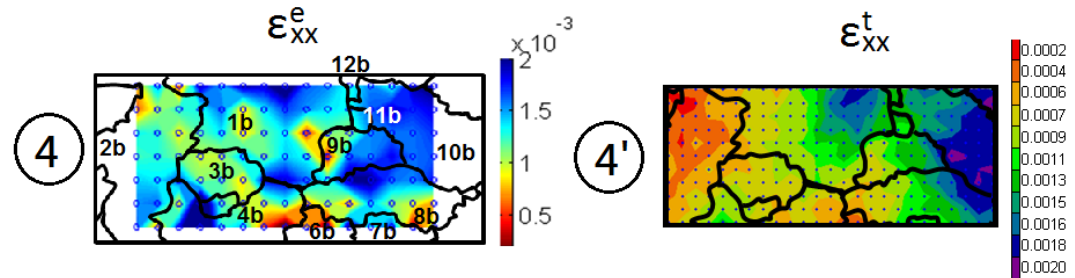


Figure 5.56: Map of ε_{xx}^e at ④ and map of ε_{xx}^t at ④ with grain boundaries of sample back side superimposed.

It is observed that these two strain fields present large similarities, in terms of distribution and magnitude of the axial strain ($[2 \times 10^{-4}, 2 \times 10^{-3}]$).

The distribution of local $\sigma^e - \varepsilon^t$ at ③ (marked as 'x') ($\overline{\varepsilon_{xx}^t} = 0.0297$) and ③ (marked as '○') ($\overline{\varepsilon_{xx}^t} = 0.0288$) are plotted in Fig.5.57. Filled symbols of '★' and '○' correspond to the mean value $\overline{\sigma^e - \varepsilon^t}$ of loading level ③ and ③ respectively. Dashed lines were put in the same figure to indicate the local behaviour of the same measured points.

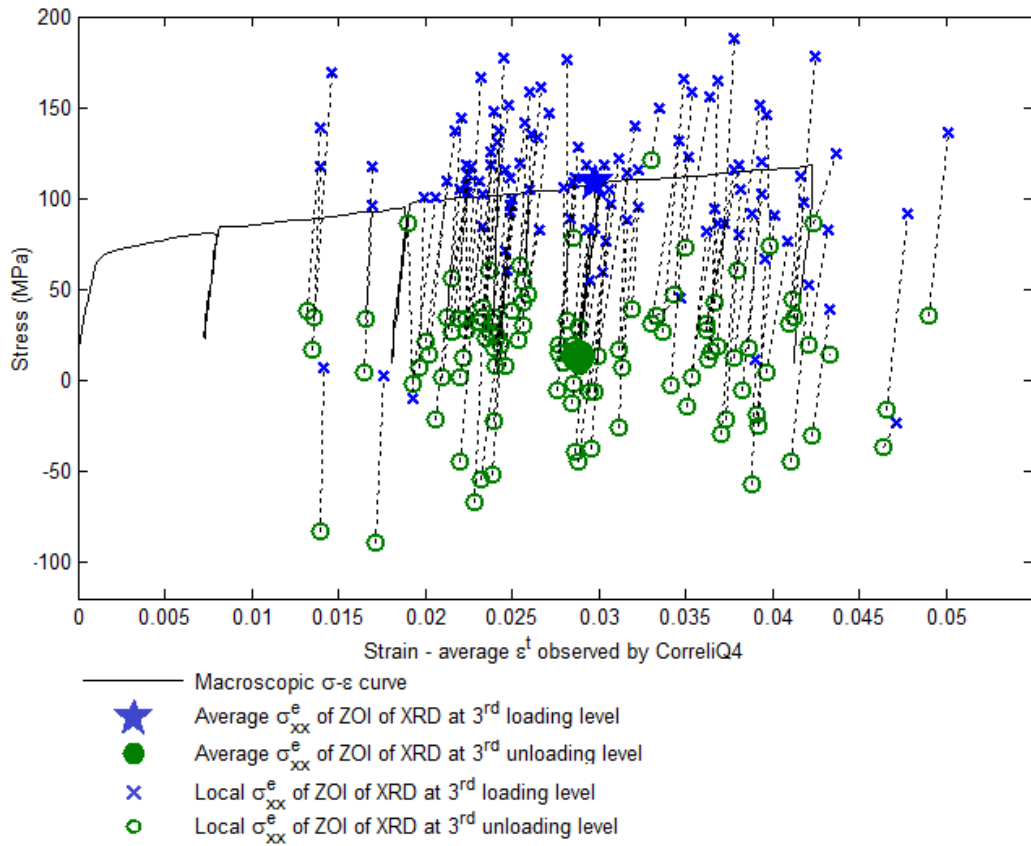


Figure 5.57: Distribution of the local σ^e - ε^t at ③ ($\overline{\sigma_{xx}^t} = 0.0297$) and ③ ($\overline{\sigma_{xx}^t} = 0.0288$).

The scattering of the local σ^e - ε^t at ③ and ③ remains almost unchanged. The averaged stress value in loading direction $\overline{\sigma_{xx}^e}$ at ③ and ③ are close to the mean stress captured by the load cell. At ③, a significant variability of local stresses is observed, reflecting the fact that macro stress is almost zero. We can see that all the points do not have an unloading to the same extent. Variability exists among $\Delta\sigma_{xx}^e$ reached during the unloading ③ → ③. The variation $\Delta\sigma_{xx}^e$ is imposed by the local mechanical condition around the point observed.

Regarding the slope of the unloading curves (dashed lines), it is obvious that the Young's modulus of aluminium cannot be found as the relative uncertainty in σ^e and ε^t measurement is too high in the tests. However, if we exclude the measured points for which the slopes are clearly unrealistic, the average value of the unloading slope is 103 GPa. This result is quite reasonable by taking the measurement uncertainties into account.

5.3 Conclusion

We have presented and discussed in this chapter the experimental results of tests carried out on samples 1 and 2.

Both the oligo-crystalline samples were subjected to simple tensile loadings up to ε^t about 0.4%. There were two loading levels for sample 1 ($\overline{\varepsilon_{xx}^t} = 7.4 \times 10^{-3}$ and 0.0356) and four loading levels ($\varepsilon_{xx}^t = 0.0081, 0.0188, 0.0297$ and 0.0423) and three unloading levels ($\varepsilon_{xx}^t = 0.0181, 0.0288$ and 0.0412.) for sample 2.

At each successive loading level, ε^t - ε^e fields on sample surface were measured in situ in the X-ray diffractometer. For sample 1, the area with validated data of ε^t and ε^e field is $15.99 \times 6.53 \text{ mm}^2$ and $14 \times 3 \text{ mm}^2$ respectively. For sample 2, the area with validated data of ε^t and ε^e field is $15.99 \times 6.85 \text{ mm}^2$ and $14 \times 3 \text{ mm}^2$ respectively. σ^e fields were calculated from ε^e using the theoretical value of aluminium mechanical properties, i.e. Young's modulus $E = 70 \text{ GPa}$ and Poisson's ratio $\nu = 0.33$.

Maps of ε^t , ε^e and σ^e fields were displayed with the initial grain geometry superimposed. Localisation of strain or stress were observed and this heterogeneity increases with the imposed loading. Moreover, the work hardening inside crystals was observed. The corresponding uncertainties during each measurement were also quantified. The general uncertainty in ε^t and in ε^e were $\pm 4 \times 10^{-4}$ and $\pm 3 \times 10^{-5}$ respectively. The uncertainties in σ^e were smaller than 3MPa.

In order to better understand the experimental results, for both sample 1 and 2, the evolution and the distribution of local stress σ^e with the associated total strain ε^t at each point of XRD measurement were plotted and discussed. For sample 1, the average stress $\overline{\sigma_{xx}^e}$ calculated using ε^e value at loadings were greater than the average stress captured by the loading cell. It is because ε^e measurement were conducted on only one half of the entire active zone of the sample 1 in order to have a rapid validation of the methodology. $\overline{\sigma_{xx}^e}$ in this part could thus be twice as high as in the area not measured by XRD. For sample 2, $\overline{\sigma_{xx}^e}$ were close to the average stress captured by the loading cell as nearly full of the sample was characterised by XRD. For both the samples, the scattering of local stress σ^e - ε^t was large and it increases during the loadings. The observation emphasises the research interest in full-field measurement of a material at grain scale as one measurement per crystal cannot represent the overall local mechanical response of a material. In addition, ε^e was also compared with ε^t measured during the elastic part of the loading/unloading and the validity of the elastic strain field measured by XRD was confirmed.

General Conclusion and Perspective

In this chapter, a general conclusion is given and several perspectives are suggested afterwards to close this manuscript.

General Conclusion

This thesis aims at measuring stress-strain ($\sigma - \varepsilon$) relationship at the grain scale in a polycrystalline sample. Therefore, an experimental method was developed and its corresponding protocol was also validated to obtain two distinct mechanical measurements simultaneously during a tensile test.

From literature review, a solid background about our research concerns was depicted. The mechanical quantities, total ε^t and elastic strain ε^e fields of a material under loading, were ultimately short-listed as local information thanks to their simplicity as well as accessibility during measurement. Digital image correlation (DIC) and X-ray diffraction (XRD) were selected respectively for ε^t and ε^e measurements. It is because DIC method is sufficiently sensitive (up to $\pm 4 \times 10^{-4}$) to small total strain. Also, the auxiliary speckle is easy and practical to deposit on studied samples. The required apparatus is also simple — only a camera installed perpendicularly in front of the sample surface is needed to be integrated with ε^e measurement. Meanwhile, XRD is a direct, non-destructive and effective method to measure the evolution of inter-reticular plane distance d_{hkl} as local elastic strain of a crystal under loading. Also, XRD still enables the measurement under the rotation of grain when sample is deformed plastically.

During material selection and sample preparation, samples in aluminium alloy (5052) with a maximized useful zone of $8 \times 18 \text{ mm}^2$ and thickness of 0.55 mm have been used. We chose aluminium as the studied material because of its simple microstructure and mechanical properties (e.g. easy to obtain large grains via recrystallisation, small Young's modulus and slow relaxation) favouring the local strain field measurement. In order to achieve strain measurement at the grain scale, the samples were submitted to a specific recrystallisation procedure to obtain grain sizes of about 5mm. For each sample, there are about 10-12 grains at each side and 2 grains in the thickness. The grain geometry of the two studied samples were captured by optical microscope and the crystal orientations were determined using XRD.

For XRD measurement, the X-ray diffractometer used in experiment and its optical path during diffraction were presented. The experimental procedure designed for ε^e measurement using XRD was introduced in details. A grid resolution of 1 cm x 1 cm for XRD was defined on the sample surface. Each crystal was ensured

to contain about 10 points of measurement so that a gradient of elastic strain can be measured. The arrangement of the grid resolution also enriches the insight of local response of the sample during the deformation, rather than using only one measurement per crystal to represent local information. The technique of launching XRD in a single crystal was presented as well because diffraction signal can only be obtained under two conditions: the normal of the analysed $\{hkl\}$ planes is oriented correctly $(\phi, \psi$ and $2\theta)_{hkl_grain}$ with respect to X-ray source and Bragg's law is satisfied. The position (ϕ, ψ) can be calculated using the grain orientation $(\varphi_1, \Phi, \varphi_2)_{grain}$.

For ε^e calculation, the First Ortner Method was applied. This method makes use of the relationship between evolution of diffraction planes δd_{hkl} and the lattice coordinates of at least 6 analysed $\{hkl\}$ planes to determine the local elastic strain. In order to improve the precision of ε^e calculation, the combinations of the chosen $\{hkl\}$ planes should give a minimum uncertainty and allow the accessibility of XRD under existing experimental circumstances. As a result, 13 $\{hkl\}$ planes per point of measurement were selected for XRD.

An experimental methodology for diffraction peak measurement was developed to enhance ε^e measurement using XRD. After understanding the impact brought to the shape of the diffraction peak by different scanning axes of ϕ , ψ and 2θ and the collimator, a Soller slit was first added to make the diffraction signal focused (to avoid the ambiguous situation in ψ direction with a broad maximum region). Then, an iteration process was designed to optimise ϕ , ψ and 2θ successively around the peak's initial position determined by the initial texture. During plastic loading, the evolution of mosaicity in crystal is inevitable and thus the beam size was narrowed down to $0.1 \times 0.1 \text{ mm}^2$ to cope with this situation. Finally, in order to accurately determine the final position of 2θ peak for ε^e calculation, the measured 2θ were simulated by decomposing two $K_{\alpha 1}$ and $K_{\alpha 2}$ peaks after understanding the nature of X-ray source. An analytical algorithm was introduced to quantify the uncertainties of ε^e ($\pm 3 \times 10^{-5}$) measured by XRD. This method was validated by a Monte Carlo method for its feasibility.

For DIC measurement, the analysing spatial resolution of 32 pixels ($362.4 \mu\text{m}$) was set regarding to the quality of speckle pattern applied on sample surface.

An experimental apparatus was developed in order to integrate the micro-tensile machine and camera inside a diffractometer for in situ measurements. Additional equipments, like wire winding, pulley system and lighting system, were attached to the set-up so as to facilitate the XRD measurement and to achieve better image quality. After considering the device's performance and the area of sample surface accessible by the apparatus, ZOI of $17 \times 8 \text{ mm}^2$ and $15 \times 8 \text{ mm}^2$ were defined for DIC and XRD measurement respectively. Combining the XRD measurement in previous chapter with DIC measurement, an experimental protocol was defined for in situ full-field measurements. XRD measurement was first conducted at sample's initial state. Then, images on the sample surface were taken regularly throughout the mechanical loading. Once the sample was pulled up to an assigned level, XRD was conducted on sample's surface again during relaxation. The maximum ($0.16 \times 0.38 \text{ mm}^2$) and minimum area ($0.13 \times 0.1 \text{ mm}^2$) spotted by XRD were also

determined according to the limited movement of goniometer during the XRD measurement. The phenomenon of relaxation of the material tested was quantified and taken into account during the in situ measurements.

Two samples with around twenty-five grains were subjected to simple tensile loadings up to ε^t about 0.4%. They were deformed every 0.1% and, then, total ε^t and elastic strain ε^e fields were measured by digital image correlation technique and X-ray diffraction respectively at successive loadings. σ^e fields were calculated from ε^e using Young's modulus $E = 70$ GPa and Poisson's ratio $\nu = 0.33$. Maps of ε^t , ε^e and σ^e fields were displayed with the initial grain geometry superimposed. Localisation of strain or stress were observed and this heterogeneity increases with the imposed loading. Moreover, visualisation of the work hardening inside crystals was made. The corresponding uncertainties during each measurement were also quantified. The general uncertainty in ε^t and in ε^e were $\pm 4 \times 10^{-4}$ and $\pm 3 \times 10^{-5}$ respectively. The uncertainties in σ^e were smaller than 3MPa. In order to better understand the experimental results, the evolution and the distribution of local stress σ^e with the associated total strain ε^t at each point of XRD measurement were plotted and discussed. For both the samples, the scattering of local stress σ^e - ε^t was large and it increased during the loadings. The findings underlines the importance in full-field measurement of a material at grain scale since one local measurement per crystal cannot represent the overall local mechanical response of a material. Besides, ε^e was also compared with ε^t measured during the elastic part of the loading/unloading and the validity of the elastic strain field measured by XRD was confirmed.

The validated experimental methodologies and results provide a basis for future development of a crystal plasticity model that better accounts for microstructural effects.

Perspective

Several perspectives can be considered towards our developed experimental method.

The first aspect is about the improvement of the measuring method and its acquisition speed. During the experiments, a majority of the measuring time was dedicated to X-ray measurement due to the fact that the corresponding signal detection only relied on the 1-D punctual detector in our goniometer. Once elastic strain deformation takes place, the diffraction plane distance changes and thus time has to be spent plane by plane for searching the new position of the diffraction peak. Therefore, improvement in experimental apparatus or X-ray method can be sought so as to shorten the measuring time of elastic strain field. For example, the feasibility of using a 2-D detector together with the punctual one should be studied. In this way, after each deformation, the new diffraction peak position of 13 $\{hkl\}$ planes per point of XRD measurement can be first approximately located by the 2-D detector at the same time. Then, the precise position of each diffraction peak can be precisely sought by the punctual detector.

And now, once the goal of collecting local mechanical response was achieved, the

second step of the work, as presented in chapter 1, should be to consider the way of effectively applying the super rich database for crystal plasticity models identification. The results can help validating the hypothesis used during the construction of the constitutive equations. Since the local information collecting methods during the tensile loading was validated, improvements of test machine and specimen can be searched to cater for other behaviour observations, e.g. for fatigue investigation, the evolutions of the local magnitudes (total strain, plastic strain, elastic strain and stress) should be quantified during the cycling loadings.

Last but not least, application of this method can be further developed for understanding specific mechanical behaviour of other materials or to solve the coupled multi-physics problems. For instance, for shape memory alloy (SMA) [Hirsinger et al. (2004); Fall et al. (2016)], the accessibility of local $\sigma - \varepsilon$ during stress-induced martensitic phase transformation enables us to conclude a more accurate mechanical condition for local phase transformation. Other examples are magnetic materials [Daniel et al. (2015)] or piezoelectric materials [Airoldi et al. (1991)], if we want to accessing local $\sigma - \varepsilon$ during electrical resistance measurements (as a function of temperature) for better understanding the coupled magneto-elastic behaviour or having local $\sigma - \varepsilon$ together with strain-induced magnetic field for a further insight in the coupled electrical-mechanical behaviour, the challenge of related apparatus installation in the goniometer without disturbing both XRD and magnetic/electrical current measurements has to be overcome in the first place.

Bibliography

- A. Abdul-Latif, J.Ph. Dingli, and K. Saanouni. Modeling of complex cyclic inelasticity in heterogeneous polycrystalline microstructure. *Mechanics of Materials*, 30(4):287 – 305, 1998. (Cited on page 12.)
- G. Airoldi, T. Ranucci, and G. Riva. Mechanical and electrical properties of a niti shape memory alloy. *Le Journal de Physique IV*, 1(C4):C4-439, 1991. (Cited on page 132.)
- L. Allais, M. Bornert, T. Bretheau, and D. Caldemaison. Experimental characterization of the local strain field in a heterogeneous elastoplastic material. *Acta Metallurgica et Materialia*, 42(11):3865 – 3880, 1994. (Cited on pages 13 and 79.)
- A. Andrade-Campos, S. Thuillier, P. Pilvin, and F. Teixeira-Dias. On the determination of material parameters for internal variable thermoelastic–viscoplastic constitutive models. *International Journal of Plasticity*, 23(8):1349 – 1379, 2007. (Cited on page 26.)
- S. Andrieux, A. Ben Abda, and H. D. Bui. Sur l’identification de fissures planes via le concept d’écart à la réciprocité en élasticité. *C.R. Acad. Sci. Paris (série II)*, 324:1431–1438, 1997. URL <https://hal.archives-ouvertes.fr/hal-00111565>. (Cited on page 26.)
- V. Aubin, P. Quaegebeur, and S. Degallaix. Cyclic plasticity of a duplex stainless steel under non-proportional loading. *Material Sciences and Engineering*, 346(1-2):208–215, 2003. (Cited on page 1.)
- S. Avril, M. Bonnet, A-S. Bretelle, M. Grédiac, F. Hild, P. Ienny, F. Latourte, D. Lemosse, S. Pagano, E. Pagnacco, and F. Pierron. Overview of identification methods of mechanical parameters based on full-field measurements. *Experimental Mechanics*, 48(4):381–402, August 2008a. (Cited on pages v and 24.)
- S. Avril, F. Pierron, Y. Pannier, and R. Rotinat. Stress reconstruction and constitutive parameter identification in plane-stress elasto-plastic problems using surface measurements of deformation fields. *Experimental Mechanics*, 48(4):403–419, 2007. (Cited on page 25.)
- S. Avril, F. Pierron, M.A. Sutton, and J. Yan. Identification of viscoplastic parameters and characterization of Lüders behaviour using digital image correlation and the virtual fields method. *Mechanics of Materials*, 40(9):729–742, September 2008b. (Cited on pages 25 and 26.)
- C. Badulescu, M. Grédiac, H. Haddadi, J.-D. Mathias, X. Balandraud, and H.-S. Tran. Applying the grid method and infrared thermography to investigate plastic deformation in aluminium multicrystal. *Mechanics of Materials*, 43(1):36 – 53, 2011. (Cited on pages v and 11.)

- A. Baldi. Residual stress measurement using hole drilling and integrated digital image correlation techniques. *Experimental Mechanics*, 54(3):379–391, 2014. (Cited on pages 15 and 20.)
- F. Barbe, L. Decker, D. Jeulin, and G. Cailletaud. Intergranular and intragranular behavior of polycrystalline aggregates. part 1: Finite element model. *International Journal of Plasticity*, 17(4):513 – 536, 2001a. (Cited on page 12.)
- F. Barbe, S. Forest, and G. Cailletaud. Intergranular and intragranular behavior of polycrystalline aggregates. part 2: Results. *International Journal of Plasticity*, 17(4):537 – 563, 2001b. (Cited on page 12.)
- J. Bauch, J. Brechbühl, H.-J. Ullrich, G. Meinl, H. Lin, and W. Kebede. Innovative analysis of X-ray microdiffraction images on selected applications of the Kossel technique. *Crystal Research and Technology*, 34:71–88, 1999. (Cited on page 19.)
- A. Ben Abda, H. Ben Ameer, and M. Jaoua. Identification of 2D cracks by elastic boundary measurements. *Inverse Problems*, 15(1):67, 1999. URL <http://stacks.iop.org/0266-5611/15/i=1/a=011>. (Cited on page 26.)
- L. Bodelot. *Coupled study of kinematic and thermal fields at the microstructure scale of metallic materials*. Theses, Université des Sciences et Technologie de Lille - Lille I, November 2008. (Cited on page 21.)
- M. Bornert, F. Brémand, P. Doumalin, J.-C. Dupré, M. Fazzini, M. Grédiac, F. Hild, S. Mistou, J. Molimard, J.-J. Orteu, L. Robert, Y. Surrel, P. Vacher, and B. Watrisse. Assessment of digital image correlation measurement errors: Methodology and results. *Experimental Mechanics*, 49(3):353–370, 2008. (Cited on page 82.)
- M. Bourcier. *Multiscale study of ductile deformation mechanisms of synthetic polycrystalline sodium chloride*. Phd thesis, Ecole Polytechnique, November 2012. (Cited on pages 13 and 79.)
- D. Bouscaud, S. Berveiller, R. Pesci, E. Patoor, and A. Morawiec. Local stress analysis in an SMA during stress-induced martensitic transformation by kossel microdiffraction. *Residual Stresses IX Advanced Materials Research*, 996:45–51, Aug 2014a. (Cited on page 19.)
- D. Bouscaud, A. Morawiec, R. Pesci, S. Berveiller, and E. Patoor. Strain resolution of scanning electron microscopy based Kossel microdiffraction. *Journal of Applied Crystallography*, 47(5):1699–1707, Oct 2014b. (Cited on pages 15, 18 and 19.)
- W. H. Bragg. Bakerian lecture: X-rays and crystal structure. *Philosophical Transactions of the Royal Society of London A: Mathematical, Physical and Engineering Sciences*, 215(523-537):253–274, 1915. (Cited on page 43.)
- W. H. Bragg and W. L. Bragg. The reflection of x-rays by crystals. *Proceedings of the Royal Society of London A: Mathematical, Physical and Engineering Sciences*, 88(605):428–438, 1913. (Cited on page 43.)

- A. Brahme, M.H. Alvi, D. Saylor, J. Fridy, and A.D. Rollett. 3D reconstruction of microstructure in a commercial purity aluminium. *Scripta Materialia*, 55(1):75 – 80, 2006. (Cited on page 12.)
- H.D. Bui, A. Constantinescu, and H. Maigre. Numerical identification of planar cracks in elastodynamics using the instantaneous reciprocity gap. *Inverse Problems*, 20:993–1001, 2004. (Cited on page 26.)
- S. Calloch. *Essais triaxiaux non-proportionnels et ingénierie des modèles de plasticité cyclique*. PhD thesis, Ecole Normale Supérieure de Cachan, France, 1997. (Cited on page 1.)
- S. Calloch, D. Dureisseix, F. Hild, et al. Identification de modèles de comportement de matériaux solides: utilisation d’essais et de calculs. *Technologies et Formations*, 100:36–41, 2002. (Cited on page 25.)
- D. Cédât, O. Fandeur, C. Rey, and D. Raabe. Polycrystal model of the mechanical behavior of a Mo-TiC30vol.% metal-ceramic composite using a 3D microstructure map obtained by a dual beam FIB-SEM. *Acta Materialia*, 60:1623–1632, 2012. (Cited on pages 12 and 29.)
- A. Chrysochoos. *Dissipation et blocage d’énergie lors d’un écrouissage en traction simple*. PhD thesis, Université de Montpellier II, 1987. (Cited on page 21.)
- A. Chrysochoos and H. Louche. An infrared image processing to analyse the calorific effects accompanying strain localisation. *International Journal of Engineering Science*, 38(16):1759 – 1788, 2000. (Cited on page 21.)
- Andre Chrysochoos, B Berthel, F Latourte, A Galtier, Stéphane Pagano, and Bertrand Wattrisse. Local energy analysis of high-cycle fatigue using digital image correlation and infrared thermography. *The Journal of Strain Analysis for Engineering Design*, 43(6):411–422, 2008. (Cited on pages 21 and 25.)
- T.C. Chu, W.F. Ranson, and M.A. Sutton. Applications of digital-image-correlation techniques to experimental mechanics. *Experimental mechanics*, 25(3):232–244, 1985. (Cited on pages 13 and 79.)
- D. Claire, F. Hild, and S. Roux. A finite element formulation to identify damage fields: the equilibrium gap method. *International Journal for Numerical Methods in Engineering*, 61(2):189–208, 2004. (Cited on page 26.)
- Damien Claire, François Hild, and Stéphane Roux. Identification of damage fields using kinematic measurements. *Comptes Rendus Mécanique*, 330:729–734, 2002. (Cited on page 26.)
- Andrei Constantinescu. On the identification of elastic moduli from displacement-force boundary measurements. *Inverse Problems in Engineering*, 1(4):293–313, 1995. (Cited on page 25.)

- H.-A. Crostack, W. Reimers, and G. Eckold. Analysis of the plastic deformation in single grains of polycrystalline materials. In G. Beck, S. Denis, and A. Simon, editors, *International Conference on Residual Stresses*, page 190. Springer Netherlands, 1989. ISBN 978-94-010-7007-2. (Cited on page 65.)
- B.D. Cullity. *Elements of X-ray diffraction*. Addison-Wesley, 1978. (Cited on pages 48 and 76.)
- J. Dally and W. Riley. *Experimental Stress Analysis*. McGraw-Hill, 1978. (Cited on page 14.)
- Laurent Daniel, Olivier Hubert, and Mahmoud Reikik. A simplified 3-d constitutive law for magnetomechanical behavior. *IEEE Transactions on Magnetics*, 51(3): 1–4, 2015. (Cited on page 132.)
- J. De Jaeger, D. Solas, T. Baudin, O. Fandeur, J.-H. Schmitt, and C. Rey. Inconel 718 single and multipass modelling of hot forging. *Superalloys 2012*, 2012. (Cited on pages v, 10, 11 and 167.)
- B Devindre and M Condat. Model validation of a 3D simulation of dislocation dynamics: discretization and line tension effects. *Acta metallurgica et materialia*, 40(10):2629–2637, 1992. (Cited on page 2.)
- P. Doumalin. *Local Microextensometry by digital image correlation. Application to micromechanical studies by scanning electron microscopy*. Phd thesis, Ecole Polytechnique, June 2000. (Cited on pages 13 and 79.)
- R Dupke and W Reimers. X-ray diffraction investigations on individual grains in the polycrystalline ni-base superalloy in 939 during cyclic loading ii: residual stresses. *Zeitschrift für Metallkunde*, 86(10):665–670, 1995. (Cited on pages 43 and 45.)
- R. Dürr. Displacement field analysis: calculation of distortion measures from displacement maps. *Ultramicroscopy*, 38(2):135 – 141, 1991. (Cited on page 14.)
- F. Eberl. *Second order heterogeneities in a multicrystal: Experimental developments using X-ray diffraction and comparison with finite element model*. PhD thesis, ENSAM, France, 2000. (Cited on pages v, 15, 30, 43, 45 and 63.)
- J. D. Eshelby. The determination of the elastic field of an ellipsoidal inclusion, and related problems. *Proceedings of the Royal Society of London A: Mathematical, Physical and Engineering Sciences*, 241(1226):376–396, 1957. (Cited on page 12.)
- P. Evrard, I. Alvarez-Armas, V. Aubin, and S. Degallaix. Polycrystalline modeling of the cyclic hardening/softening behavior of an austenitic-ferritic stainless steel. *Mechanics of Materials*, 42(4):395 – 404, 2010a. (Cited on pages v, 12 and 26.)

- P. Evrard, V. Aubin, Ph. Pilvin, S. Degallaix, and D. Kondo. Implementation and validation of a polycrystalline model for a bi-phased steel under non-proportional loading paths. *Mechanics Research Communications*, 35(5):336 – 343, 2008. (Cited on pages 12 and 26.)
- P. Evrard, A. El Bartali, V. Aubin, C. Rey, S. Degallaix, and D. Kondo. Influence of boundary conditions on bi-phased polycrystal microstructure calculation. *International Journal of Solids and Structures*, 47(16):1979 – 1986, 2010b. (Cited on pages v, 11 and 26.)
- Mame Daro Fall, Olivier Hubert, Frederic Mazaleyrat, Karine Lavernhe-Taillard, and Alexandre Pasko. A multiscale modeling of magnetic shape memory alloys: Application to nimnga single crystal. *IEEE Transactions on Magnetics*, 52(5):1–4, 2016. (Cited on page 132.)
- R. Forestier, E. Massoni, and Y. Chastel. Estimation of constitutive parameters using an inverse method coupled to a 3D finite element software. *Journal of Materials Processing Technology*, 125–126:594 – 601, 2002. (Cited on page 24.)
- P. Franciosi. *Etude théorique et expérimentale du comportement élastoplastique des monocristaux métalliques se déformant par glissement: modélisation pour un chargement complexe quasi statique*. PhD thesis, Paris 13, 1984. (Cited on page 10.)
- P. Franciosi and A. Zaoui. Multislip in F.C.C. crystals: a theoretical approach compared with experimental data. *Acta Metallurgica*, 30(8):1627 – 1637, 1982. (Cited on page 1.)
- J. Friedel, editor. *Dislocations*. International Series of Monographs on Solid State Physics. Pergamon, 1964. (Cited on page 5.)
- W. Friedrich, P. Knipping, and M. von Laue. *Interferenz-Erscheinungen bei Röntgenstrahlen*. Mathematisch-Physikalische Klasse: Sitzungsberichte. Verlag der Kgl. Bayer. Akad. der Wiss., 1912. (Cited on page 43.)
- K. Genovese, L. Lamberti, and C. Pappalettere. Identification of mechanical properties of bovine bones by combining PS-ESPI and global optimization. In *Speckle06: Speckles, From Grains to Flowers*, pages 634108.1–634108.7. International Society for Optics and Photonics, 2006. (Cited on page 24.)
- G. Geymonat, F. Hild, and S. Pagano. Identification de paramètres mécaniques par mesure de champ de déplacement. *Comptes rendus-Mecanique*, 6(330):403–408, 2002. (Cited on page 25.)
- G. Geymonat and S. Pagano. Identification of mechanical properties by displacement field measurement: a variational approach. *Meccanica*, 38(5):535–545, 2003. (Cited on page 25.)

- M. Giton, Caro A. S. Bretelle, and P. Ienny. Hyperelastic behaviour identification by a forward problem resolution: application to a tear test of a silicone-rubber. *Strain*, 42(4):291–297, 2006. (Cited on page 24.)
- A. Glacet. Estimation de contraintes résiduelles à l'échelle de la microstructure. Research internship report , master of science, ENS Cachan, 2015. (Cited on page 21.)
- H.T Goldrein, S.J.P Palmer, and J.M Huntley. Automated fine grid technique for measurement of large-strain deformation maps. *Optics and Lasers in Engineering*, 23(5):305 – 318, 1995. Interferogram Analysis. (Cited on page 14.)
- M. Grédiac and F. Hild. *Full-Field Measurements and Identification in Solid Mechanics*. John Wiley Sons, Inc., 2013. (Cited on pages v and 24.)
- M. Grédiac and F. Pierron. Applying the virtual fields method to the identification of elasto-plastic constitutive parameters. *International Journal of Plasticity*, 22(4):602–627, 2006. (Cited on pages 25 and 26.)
- M. Grédiac, E. Toussaint, and F. Pierron. Special virtual fields for the direct determination of material parameters with the virtual fields method. 2—application to in-plane properties. *International Journal of Solids and Structures*, 39(10):2707–2730, 2002. (Cited on page 25.)
- Michel Grédiac. Principe des travaux virtuels et identification. *Comptes rendus de l'Académie des sciences. Série 2, Mécanique, Physique, Chimie, Sciences de l'univers, Sciences de la Terre*, 309(1):1–5, 1989. (Cited on page 25.)
- A. Guery. *Développement d'une méthode de corrélation d'images numériques adaptée aux mesures cinématiques dans les polycristaux: application à l'identification de paramètres de lois de plasticité cristalline*. PhD thesis, Ecole normale supérieure de Cachan, 2014. (Cited on pages 13, 24, 26 and 79.)
- Y. Guilhem, S. Basseville, F. Curtit, J.-M. Stéphan, and G. Cailletaud. Numerical investigations of the free surface effect in three-dimensional polycrystalline aggregates. *Computational Materials Science*, 70(0):150 – 162, 2013. (Cited on pages v and 12.)
- S. Gungor. Formation of Moiré fringes by superimposing two line patterns which vary in line spacing and rotation. <http://materials.open.ac.uk/staff/Gungor/image005.gif>, n.d. October 2015. (Cited on page 15.)
- J.D. Helm, S.R. McNeill, and M.A. Sutton. Improved threedimensional image correlation for surface displacement measurement. *Optical Engineering*, 35(7):1911–1920, 1996. (Cited on pages 13 and 79.)
- M. Hendricks. *Identification of the mechanical properties of solid materials*. PhD thesis, Eindhoven University of Technology, 1991. (Cited on page 24.)

- Eva Hériprié. *Méthode de couplage multi-échelles entre simulations numériques polycristallines et mesures de champs pour l'identification des paramètres de lois de comportement et de fissuration des matériaux métalliques. Application à l'étude des alliages TiAl*. PhD thesis, Ecole Polytechnique, 2006. (Cited on page 23.)
- F. Hild and S. Roux. Correliq4: a software for "finite-element" displacement field measurements by digital image correlation. Internal report 269, ENS Cachan, 2008. (Cited on pages v, 68, 80 and 82.)
- ME Hilley et al. Residual stress by x-ray diffraction-sae j784a. *Society of Automotive Engineers, Inc., Warrendale, PA*, 1971. (Cited on page 43.)
- Laurent Hirsinger, Nicolas Creton, and Christian Lexcellent. Stress-induced phase transformations in ni–mn–ga alloys: experiments and modelling. *Materials Science and Engineering: A*, 378(1):365–369, 2004. (Cited on page 132.)
- T Hoc, J Crépin, L Gélébart, and A Zaoui. A procedure for identifying the plastic behavior of single crystals from the local response of polycrystals. *Acta Materialia*, 51(18):5477–5488, 2003. (Cited on page 24.)
- W. Huang. *Contribution à l'analyse par diffractométrie X des déformations et des contraintes à l'échelle des grains*. PhD thesis, ENSAM, Paris, France, 2007. (Cited on pages v, 30, 44, 45 and 108.)
- D. Hull and D.J. Bacon, editors. *Introduction to Dislocations (Fourth Edition)*. Butterworth-Heinemann, Oxford, 2001. (Cited on page 5.)
- H.B. Huntington. *The elastic constants of crystals*. Solid state reprints. Academic Press, 1958. (Cited on pages 4 and 169.)
- Toru Imura. The study of deformation of single crystals by the divergent x-ray beams. *Bulletin of University of Osaka Prefecture, Japan*, 1954. (Cited on page 43.)
- B. Jaoul. *Étude de la plasticité et application aux métaux*. Dunod, 1965. (Cited on page 5.)
- Z. L. Kahn-Jetter and T. C. Chu. Three-dimensional displacement measurements using digital image correlation and photogrammic analysis. *Experimental Mechanics*, 30(1):10–16, 1990. (Cited on pages 13 and 79.)
- J. Kajberg and G. Lindkvist. Characterisation of materials subjected to large strains by inverse modelling based on in-plane displacement fields. *International Journal of Solids and Structures*, 41(13):3439 – 3459, 2004. (Cited on page 24.)
- J. Kajberg and B. Wikman. Viscoplastic parameter estimation by high strain-rate experiments and inverse modelling – speckle measurements and high-speed photography. *International Journal of Solids and Structures*, 44(1):145 – 164, 2007. (Cited on page 24.)

- T. Kanit, S. Forest, I. Galliet, V. Mounoury, and D. Jeulin. Determination of the size of the representative volume element for random composites: statistical and numerical approach. *International Journal of Solids and Structures*, 40(13–14): 3647 – 3679, 2003. (Cited on page 12.)
- DP Koistinen and RE Marburger. A simplified procedure for calculating peak position in x-ray residual stress measurements on hardened steel. *Trans. ASM*, 51:537–550, 1959. (Cited on page 43.)
- E. Kroner. Berechnung der elastischen Konstanten des Vielkristalls aus den Konstanten des Einkristalls. *Zeitschrift für Physik*, 151(4):504–518, 1958. (Cited on page 12.)
- L.P. Kubin and B. Devincre. From dislocation mechanisms to dislocation microstructures and strain hardening. In J.B. Bilde Soerensen et al., editor, *Deformation-Induced microstructures: Analysis and Relation to Properties (20th Risoe Symposium)*, pages 61–83. Risoe natl. Lab., Roskilde, Denmark, 1999. (Cited on page 9.)
- P. Ladeveze and D. Leguillon. Error estimate procedure in the finite element method and applications. *SIAM Journal on Numerical Analysis*, 20(3):485–509, 1983. (Cited on page 25.)
- F. Latourte. *Identification des paramètres d’une loi élastoplastique de Prager et calcul de champs de contrainte dans des matériaux hétérogènes*. PhD thesis, University of Montpellier 2, 2007. (Cited on pages 25 and 26.)
- Felix Latourte, Andre Chrysochoos, Stéphane Pagano, and Bertrand Wattrisse. Elastoplastic behavior identification for heterogeneous loadings and materials. *Experimental Mechanics*, 48(4):435–449, 2008. (Cited on page 25.)
- R.A. Lebensohn and G.R. Canova. A self-consistent approach for modelling texture development of two-phase polycrystals: Application to titanium alloys. *Acta Materialia*, 45(9):3687 – 3694, 1997. (Cited on page 12.)
- Y. Li, P. Bompard, C. Rey, and V. Aubin. Polycrystalline numerical simulation of variable amplitude loading effects on cyclic plasticity and microcrack initiation in austenitic steel 304L. *International Journal of Fatigue*, 42:71–81, 2012. (Cited on pages v, 11 and 167.)
- M. Libert. *Etudes expérimentale et numérique de l’effet des mécanismes de plasticité sur la rupture fragile par clivage dans les aciers faiblement alliés (in French)*. PhD thesis, Ecole Centrale de Paris, 2007. (Cited on page 29.)
- M. Libert, C. Rey, L. Vincent, and B. Marini. Temperature dependent polycrystal model application to bainitic steel behavior under tri-axial loading in the ductile–brittle transition. *International Journal of Solids and Structures*, 48(14–15): 2196 – 2208, 2011. (Cited on page 29.)

- B. D. Lucas and T. Kanade. An iterative image registration technique with an application to stereo vision. *IJCAI*, 81:674–679, 1981. (Cited on pages 13 and 79.)
- W. Ludwig, A. King, P. Reischig, M. Herbig, E.M. Lauridsen, S. Schmidt, H. Proudhon, S. Forest, P. Cloetens, and S.R. Du Roscoat. New opportunities for 3D materials science of polycrystalline materials at the micrometre lengthscale by combined use of X-ray diffraction and X-ray imaging. *Materials Science and Engineering: A*, 524(1):69–76, 2009. (Cited on page 12.)
- P.-F. Luo, Y.J. Chao, and M.A. Sutton. Application of stereo vision to three-dimensional deformation analyses in fracture experiments. *Optical Engineering*, 33(3):981–990, 1994. (Cited on pages 13 and 79.)
- E. Macherauch and P. Muller. Das $\sin^2\psi$ -verfahren in der rontgenographischen spannungsmessung. *Z.A. Physik*, 13:305–312, 1961. (Cited on pages 43 and 46.)
- G. Martin, C.W. Sinclair, and J.-H. Schmitt. Plastic strain heterogeneities in an Mg-1Zn-0.5Nd alloy. *Scripta Materialia*, 68:695–698, 2013. (Cited on page 30.)
- B. Marty, P. Moretto, P. Gergaud, J.L. Lebrun, K. Ostolaza, and V. Ji. X-ray study on single crystal superalloy SRR99: Mismatch γ/γ' , mosaicity and internal stress. *Acta Materialia*, 45(2):791 – 800, 1997. (Cited on page 65.)
- E. Mazza, G. Danuser, and J. Dual. Light optical deformation measurements in microbars with nanometer resolution. *Microsystem Technologies*, 2(2):83–91, 1996. (Cited on pages 13 and 79.)
- M.H.H. Meuwissen, C.W.J. Oomens, F.P.T. Baaijens, R. Petterson, and J.D. Janssen. Determination of the elasto-plastic properties of aluminium using a mixed numerical–experimental method. *Journal of Materials Processing Technology*, 75(1–3):204 – 211, 1998. (Cited on page 24.)
- H. L. Mitchell, H. T. Kniest, and Oh Won-Jin. Digital photogrammetry and microscope photographs. *The Photogrammetric Record*, 16(94):695–704, 1999. (Cited on pages 13 and 79.)
- J. Molimard, R. Le Riche, A. Vautrin, and J.R. Lee. Identification of the four orthotropic plate stiffnesses using a single open-hole tensile test. *Experimental Mechanics*, 45(5):404–411, 2005. (Cited on page 24.)
- A. Molinari, S. Ahzi, and R. Kouddane. On the self-consistent modeling of elastic-plastic behavior of polycrystals. *Mechanics of Materials*, 26(1):43 – 62, 1997. (Cited on page 12.)
- A Morançais, Mathieu Fèvre, M François, Nicolas Guel, Serge Kruch, P Kanouté, and A Longuet. Residual stress determination in a shot-peened nickel-based single-crystal superalloy using x-ray diffraction. *Journal of Applied Crystallography*, 48(6), 2015. (Cited on page 43.)

- A. Morawiec. A profile-based method of determining intragranular strains using Kossel diffraction patterns. *Advanced Materials Research*, 996:52–57, 2014. (Cited on page 19.)
- P. Mu. *Etude de l'amorçage en fatigue plastique d'un acier inoxydable austénitique*. PhD thesis, Ecole Centrale de Lille, 2011. (Cited on pages 10 and 26.)
- H. Mughrabi. The cyclic hardening and saturation behaviour of copper single crystals. *Materials Science and Engineering*, 33(2):207 – 223, 1978. (Cited on page 1.)
- R.E. Ogilvie. *Stress Measurement with the X-ray Spectrometer*. Massachusetts Institute of Technology, 1952. (Cited on page 43.)
- C.W.J. Oomens, M.R.v. Ratingen, J.D. Janssen, J.J. Kok, and M.A.N. Hendriks. A numerical-experimental method for a mechanical characterization of biological materials. *Journal of Biomechanics*, 26(4–5):617 – 621, 1993. (Cited on page 24.)
- E. Orowan. Zur Kristallplastizität iii. *Z. Phys.*, 89:634–659, 1934. (Cited on page 5.)
- B. Ortner. The choice of lattice planes in X-ray strain measurements of single crystals. *Adv. in X-ray Analysis*, 29:113–118, 1986a. (Cited on pages ii, 45, 57, 60 and 167.)
- B. Ortner. Simultaneous determination of the lattice constant and elastic strain in cubic single crystal. *Adv. in X-ray Analysis*, 29:387–394, 1986b. (Cited on pages ii, 43, 45, 57, 59 and 167.)
- B. Ortner. Why we should give up the $\sin^2\psi$ method. *Powder Diffraction*, 24:16–21, 6 2009. (Cited on page 46.)
- Y. Pannier, S. Avril, R. Rotinat, and F. Pierron. Identification of elasto-plastic constitutive parameters from statically undetermined tests using the virtual fields method. *Experimental Mechanics*, 46(6):735–755, 2006. (Cited on pages 25 and 26.)
- D. Peirce, R.J. Asaro, and A. Needleman. Material rate dependence and localized deformation in crystalline solids. *Acta metallurgica*, 31(12):1951–1976, 1983. (Cited on page 10.)
- J. Petit, M. Bornert, F. Hofmann, O. Robach, J.S. Micha, O. Ulrich, C. Le Bourlot, D. Faurie, A.M. Korsunsky, and O. Castelnau. Combining Laue microdiffraction and digital image correlation for improved measurements of the elastic strain field with micrometer spatial resolution. *Procedia {IUTAM}*, 4(0):133 – 143, 2012. (Cited on pages 15 and 20.)
- J. Philibert, A. Vignes, Y. Bréchet, and P. Combrade. *Métallurgie, du minerai au matériau*. Masson, 1998. ISBN 2-225-82978-0. (Cited on page 34.)

- F. Pierron, S. Avril, and V. The Tran. Extension of the virtual fields method to elasto-plastic material identification with cyclic loads and kinematic hardening. *International Journal of Solids and Structures*, 47(22–23):2993 – 3010, 2010. (Cited on pages 25, 26 and 27.)
- M. Polanyi. Über eine Art Gitterstörung, die einen Kristall plastisch machen könnte. *Z. Phys.*, 89:660–664, 1934. (Cited on page 5.)
- L. Portier. *Contribution numérique à l'étude de la déformation progressive des structures Etude expérimentale et étude comparative de lois de comportement*. PhD thesis, Ecole Normale Supérieure de Cachan, France, 1999. (Cited on page 1.)
- D. Post. New optical methods of Moiré fringe multiplication. *Experimental Mechanics*, 8(2):63–68, 1968. (Cited on page 14.)
- P.S. Prevéy. Current applications of x-ray diffraction residual stress measurement. *Developments in Materials Characterization Technologies*, pages 103–110, 1996. (Cited on page 43.)
- N.J. Rendler and I. Vigness. Hole-drilling strain-gage method of measuring residual stresses. *Experimental Mechanics*, 6(12):577–586, 1966. (Cited on page 20.)
- O. Robach, J.-S. Micha, O. Ulrich, and P. Gergaud. Full local elastic strain tensor from Laue microdiffraction: simultaneous Laue pattern and spot energy measurement. *Journal of Applied Crystallography*, 44(4):688–696, Aug 2011. (Cited on pages 15, 19 and 20.)
- A. Saai. *Physical model of the plasticity of a metal crystal CFC subjected to alternating loads: Contribution to the definition of multiscale modeling of shaping metal*. PhD thesis, University of Savoie, France, 2008. (Cited on pages v, 11, 13, 21, 22, 30, 34 and 79.)
- A. Saai, H. Louche, L. Tabourot, and H. J. Chang. Experimental and numerical study of the thermo-mechanical behavior of Al bi-crystal in tension using full field measurements and micromechanical modeling. *Mechanics of Materials*, 42: 275–292, 2010. (Cited on pages v, 11, 14 and 167.)
- E. Schmid and W. Boas. *Plasticity of Crystals*, volume 4. Springer-Verlag, Jul 1951. (Cited on page 30.)
- B.M. Schroeter and D.L. McDowell. Measurement of deformation fields in polycrystalline OFHC copper. *International Journal of Plasticity*, 19:1355–1376, 2003. (Cited on page 15.)
- J. Schwartz, O. Fandeur, and C. Rey. Fatigue crack initiation modelling of 316LN steel based on non local plasticity theory. *Procedia Engineering*, 2(1):1353–1362, 2010. (Cited on pages 2, 10, 11, 26, 27 and 167.)

- Julien Schwartz. *Approche non locale en plasticité cristalline: application à l'étude du comportement mécanique de l'acier AISI 316LN en fatigue oligocyclique*. PhD thesis, Ecole centrale de Paris, 2011. (Cited on pages v and 2.)
- A. Shiro, M. Nishida, and T. Jing. Residual stress estimation of ti casting alloy by xray single crystal measurement method. *AIP Conference Proceedings*, 989(1):96–100, 2008. (Cited on page 44.)
- F. Sidoroff. Incremental constitutive equation for large strain elasto plasticity. *International Journal of Engineering Science*, 20(1):19 – 26, 1982. (Cited on page 1.)
- L. St-Pierre, E. Héripré, M. Dexet, J. Crépin, G. Bertolino, and N. Bilger. 3D simulations of microstructure and comparison with experimental microstructure coming from O.I.M analysis. *International Journal of Plasticity*, 24(9):1516 – 1532, 2008. (Cited on page 12.)
- M.A. Sutton, N. Li, D. Garcia, N. Cornille, J.J. Orteu, S.R. McNeill, H.W. Schreier, and X. Li. Metrology in a scanning electron microscope: theoretical developments and experimental validation. *Measurement Science and Technology*, 17(10):2613, 2006. (Cited on pages 13 and 79.)
- M.A. Sutton, N. Li, D. Garcia, N. Cornille, J.J. Orteu, S.R. McNeill, H.W. Schreier, X. Li, and A.P. Reynolds. Scanning electron microscopy for quantitative small and large deformation measurements part II: experimental validation for magnifications from 200 to 10,000. *Experimental Mechanics*, 47(6):789–804, 2007a. (Cited on pages 13 and 79.)
- M.A. Sutton, S.R. McNeill, J.D. Helm, and Y.J. Chao. Advances in two-dimensional and three-dimensional computer vision. In: *Rastogi, P.K. (ed.) Photomechanics*, page 323–372, 2000. (Cited on page 13.)
- M.A. Sutton, W.J. Wolters, W.H. Peters, W.F. Ranson, and S.R. McNeill. Determination of displacements using an improved digital correlation method. *Image and Vision Computing*, 1(3):133 – 139, 1983. (Cited on pages 13 and 79.)
- M.A. Sutton, J. Yan, X. Deng, C.-S. Cheng, and P. Zavattieri. Three-dimensional digital image correlation to quantify deformation and crack-opening displacement in ductile aluminum under mixed-mode I/III loading. *Optical Engineering*, 46(5):051003–051003–17, 2007b. (Cited on page 14.)
- L. Tabourot. *Loi de comportement élastoviscoplastique du monocristal en grandes transformations*. PhD thesis, Institut National Polytechnique de Grenoble, 1992. (Cited on page 10.)
- M. Tang, H. Xie, J. Zhu, X. Li, and Y. Li. Study of Moiré grating fabrication on metal samples using nanoimprint lithography. *Optical Express*, 20:2942–2955, 2012. (Cited on pages 14, 15 and 79.)

- A. Tatchl and O. Kolednik. On the experimental characterization of crystal plasticity in polycrystals. *Materials Science and Engineering: A*, 356(1):447–463, 2003. (Cited on pages 13 and 79.)
- G.I. Taylor. The mechanism of plastic deformation of crystals. part I. theoretical. *Proceedings of the Royal Society of London*, 145(855):362–387, 1934. (Cited on page 5.)
- C. Teodosiu, J.-L. Raphanel, and L. Tabourot. Finite element simulation of the large elastoplastic deformation of multicrystals. In *5th MECAMAT International seminar on Large Plastic Deformations: Fundamental Aspe.* C. Teodosiu, J.L. Raphanel, F. Sidoroff, 1992. (Cited on page 10.)
- H.-S. Tran. *Identification of a crystal plasticity model by resetting finite element on kinematic fields measurements from a tensile test on pure aluminium multicrystals developed by critical hardening.* PhD thesis, University of Paris 13, 2013. (Cited on pages 26, 30, 34 and 108.)
- M. Van Ratingen. *Mechanical identification of inhomogeneous solids: a mixed numerical experimental approach.* PhD thesis, Eindhoven University of Technology, 1994. (Cited on page 24.)
- U. Welzel, J. Ligot, P. Lamparter, A. C. Vermeulen, and E. J. Mittemeijer. Stress analysis of polycrystalline thin films and surface regions by X-ray diffraction. *Journal of Applied Crystallography*, 38(1):1–29, Feb 2005. (Cited on page 46.)
- A. Zeghadi, F. N’guyen, S. Forest, A.-F. Gourgues, and O. Bouaziz. Ensemble averaging stress–strain fields in polycrystalline aggregates with a constrained surface microstructure—part 1: anisotropic elastic behaviour. *Philosophical Magazine*, 87(8-9):1401–1424, 2007. (Cited on page 32.)
- F. Zerilli. Dislocation mechanics-based constitutive equations. *Metallurgical and Materials Transactions A*, 35(9):2547–2555, 2004. (Cited on page 1.)
- Z. Zhou. *Determination des deformations et des contraintes dans les matériaux monocristallins par la diffraction des rayons x.* PhD thesis, Ecole d’Arts et Métiers, Paris, 1994. (Cited on pages v, 43, 44, 45, 108 and 167.)

Drawing of the micro-tensile machine

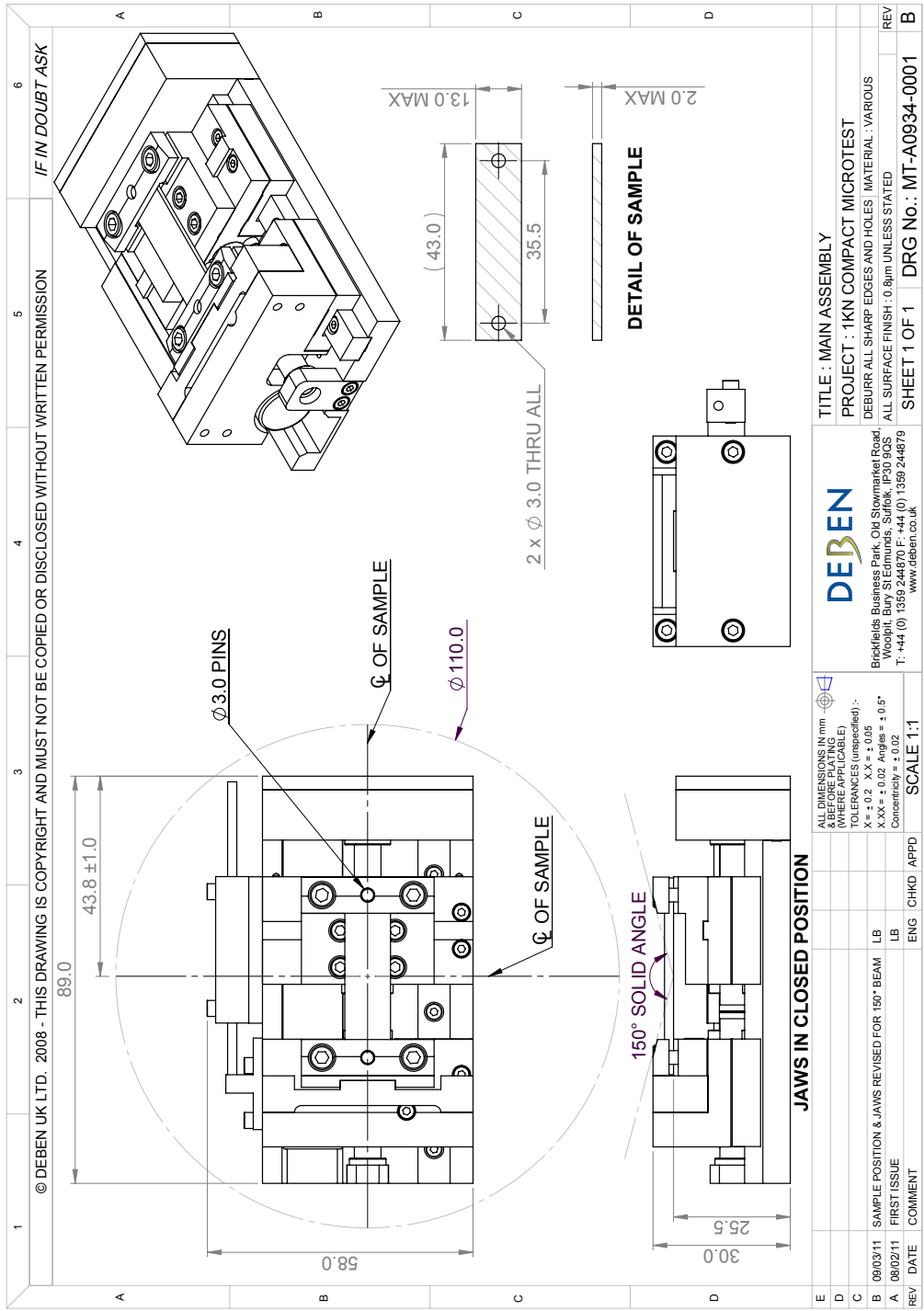


Figure 58: Drawing of the micro-tensile machine operating in X-ray diffractometer.

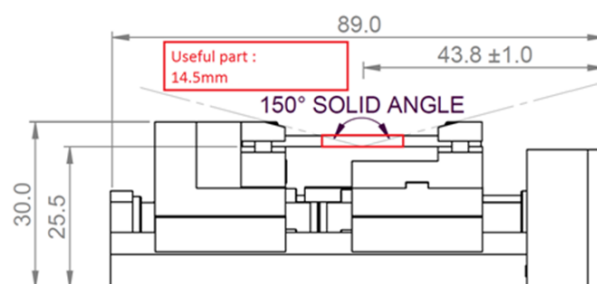


Figure 59: Maximum active zone of sample surface during XRD measurement.

Drawing of the sample

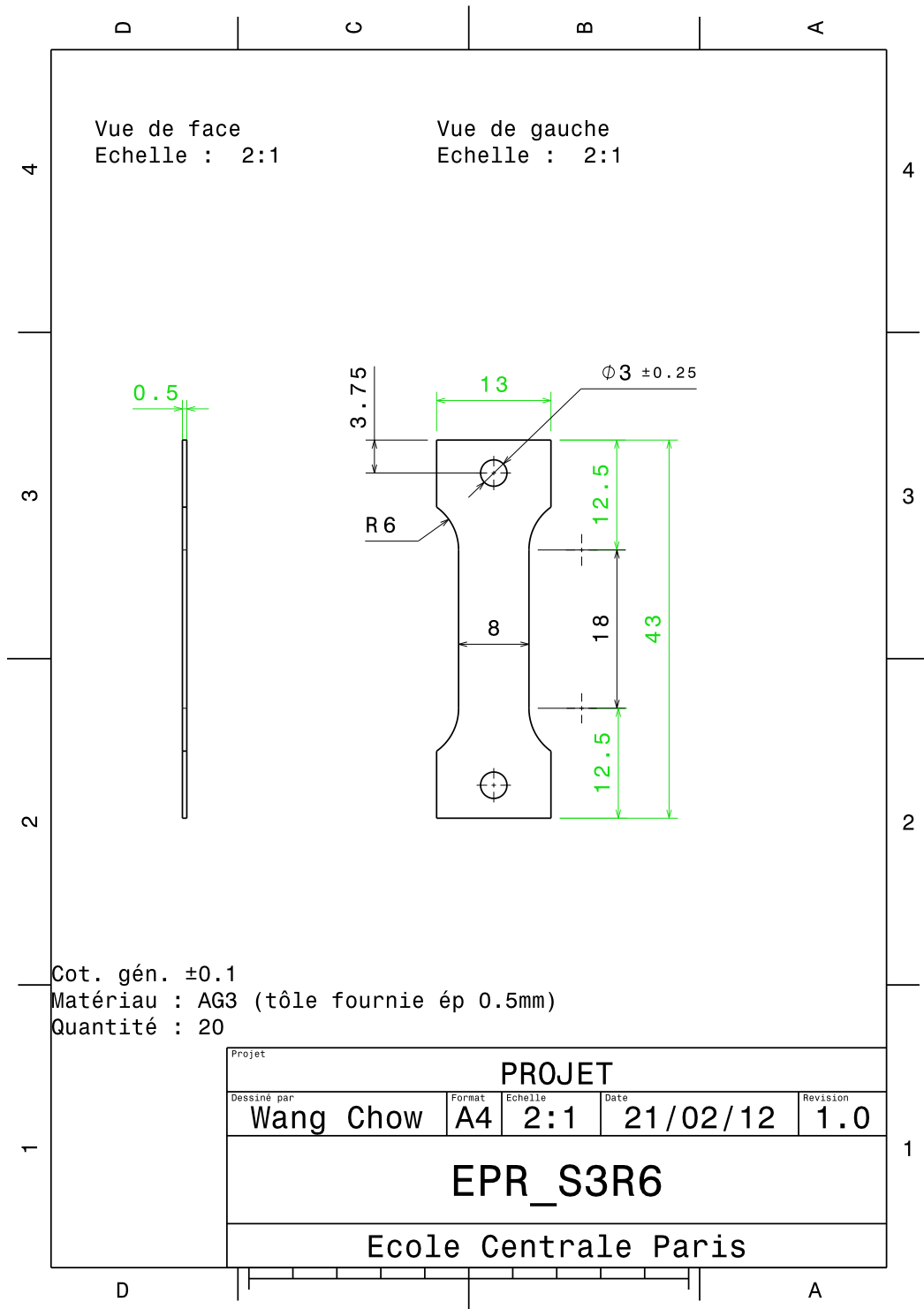


Figure 60: Drawing of the sample.

Full path of X-ray diffraction



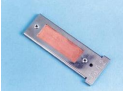



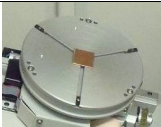

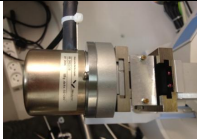
No.	Components	Reference		Image	Description
	X-ray Diffractometer	PW3040/60	X'Pert Pro MRD		
1	Source tube	PW3376/00	Ceramic tube Co LFF (LFF- Long and fine focus)		<ul style="list-style-type: none"> • 1.8kW for X'Pert system • Supporting 2 types of focus: <ul style="list-style-type: none"> a. linear focus b. punctual focus • Change of focus by simple rotation • Auto-recognition of focus and anodes • 2 windows • Maximum tension (kV) = 40 • Maximum current (mA) = 45 • Normal powder diffraction work on specimens with large amounts of Fe. Optimum resolution and high intensity.
2	Beam attenuators		Cu 0,1mm Cu 0,2mm		<ul style="list-style-type: none"> • For mirror with Cu radiation. Enables large dynamic range.
	Beta filter kits	PW3151/00	Beta filter in Iron		<ul style="list-style-type: none"> • Beta filter for Co radiation.
3	Lens	PW3146/60	Poly-capillary lens 8 mm		<ul style="list-style-type: none"> • Part of PW3146/00 or PW3146/60. • Incident beam. • Poly-capillary lens with diameter of 8 mm. • For stress, texture and parallel beam phase analysis. • For Cu, Co, Fe and Cr radiation.
4	Crossed slit	PW3084/62	Crossed slit Collimator (knob adjustable)		<ul style="list-style-type: none"> • Support horizontal and vertical adjustment • Incident beam. Acts like a divergence slit combined with a mask. Continuously adjustable between 0 mm and 10 mm. • Precision up to 0.02mm
5	Wafer holder	PW3061/22	4inch wafer holder		<ul style="list-style-type: none"> • Stage accessory for the MRD Cradle.
6 & 7	Collimator	PW3098/27	Parallel plate collimator (0,27°)		<ul style="list-style-type: none"> • Diffracted beam. • With Soller slit holder. • For low resolution phase analysis on thin film samples and samples with rough surfaces and reflectivity analysis.
8	Detector	PW3011/20	Xe proportional detector (Miniprop. Large Window)		<ul style="list-style-type: none"> • Proportional detector (Xe gas, window: 20x24 mm). • For all applications except with Mo, W and Ag radiation.

Figure 61: A list of the components of X-ray diffractometer. Throughout the entire XRD process (from XR being emitted up to being detected during the diffraction process), each component which is passed by the beam is characterized and recorded in order.

Uncertainty estimation of the elastic strain tensor σ_{ε^e} - Monte Carlo Method

The σ_{ε^e} calculated by the analytical method was also compared using Monte Carlo Method. A number (N) of random errors is drawn within the range of $\Delta\theta(\pm 0.0025^\circ)$ in normal distribution for each diffraction angles used in ε^e calculation. ε^{e-N} are calculated using Eq.(3.52).

h	k	l	$2\theta(^\circ) (\varepsilon_{xx}^t=0)$	$2\theta(^\circ) (\varepsilon_{xx}^t=0.0074)$
-2	0	2	$77.1755+\Delta\theta_{14}^N$	$77.1509+\Delta\theta_1^N$
-2	2	0	$77.1092+\Delta\theta_{15}^N$	$77.1746+\Delta\theta_2^N$
0	-2	2	$77.0938+\Delta\theta_{16}^N$	$77.1920+\Delta\theta_3^N$
0	2	2	$77.1310+\Delta\theta_{17}^N$	$77.1572+\Delta\theta_4^N$
2	0	2	$77.1439+\Delta\theta_{18}^N$	$77.1571+\Delta\theta_5^N$
-3	1	1	$93.9713+\Delta\theta_{19}^N$	$93.9495+\Delta\theta_6^N$
-1	-1	3	$93.9742+\Delta\theta_{20}^N$	$93.9894+\Delta\theta_7^N$
-1	3	1	$93.8989+\Delta\theta_{21}^N$	$94.0022+\Delta\theta_8^N$
1	-1	3	$93.9372+\Delta\theta_{22}^N$	$93.9911+\Delta\theta_9^N$
1	1	3	$93.9613+\Delta\theta_{23}^N$	$93.9695+\Delta\theta_{10}^N$
1	3	1	$93.9305+\Delta\theta_{24}^N$	$93.9867+\Delta\theta_{11}^N$
-2	2	2	$99.5601+\Delta\theta_{25}^N$	$99.5814+\Delta\theta_{12}^N$
2	2	2	$99.5495+\Delta\theta_{26}^N$	$99.5827+\Delta\theta_{13}^N$

Table 17: $\Delta\theta_{n=1,\dots,26}^N$ are generated for 13 measured planes. Then, they are imposed for each measured diffraction angles for calculating ε^{e-N} .

Recall Eq.(3.52):

$$\varepsilon_{m=1,\dots,6}^e = \begin{pmatrix} \frac{\sum_{i=1}^n B_{1i}(\sin^2\theta_i - \sin^2\theta_{n+i})}{2 \sum_{i=1}^n B_{1i} \sin^2\theta_{n+i}} \\ \frac{\sum_{i=1}^n B_{2i}(\sin^2\theta_i - \sin^2\theta_{n+i})}{2 \sum_{i=1}^n B_{2i} \sin^2\theta_{n+i}} \\ \frac{\sum_{i=1}^n B_{3i}(\sin^2\theta_i - \sin^2\theta_{n+i})}{2 \sum_{i=1}^n B_{3i} \sin^2\theta_{n+i}} \\ \frac{\sum_{i=1}^n B_{4i}(\sin^2\theta_i - \sin^2\theta_{n+i})}{\sqrt{2 \sum_{i=1}^n B_{2i} \sin^2\theta_{n+i}} \sqrt{2 \sum_{i=1}^n B_{3i} \sin^2\theta_{n+i}}} \\ \frac{\sum_{i=1}^n B_{5i}(\sin^2\theta_i - \sin^2\theta_{n+i})}{\sqrt{2 \sum_{i=1}^n B_{1i} \sin^2\theta_{n+i}} \sqrt{2 \sum_{i=1}^n B_{3i} \sin^2\theta_{n+i}}} \\ \frac{\sum_{i=1}^n B_{6i}(\sin^2\theta_i - \sin^2\theta_{n+i})}{\sqrt{2 \sum_{i=1}^n B_{1i} \sin^2\theta_{n+i}} \sqrt{2 \sum_{i=1}^n B_{2i} \sin^2\theta_{n+i}}} \end{pmatrix} \quad (3.52)$$

Regarding to the stability of the calculating system (Fig.62), N=100000.

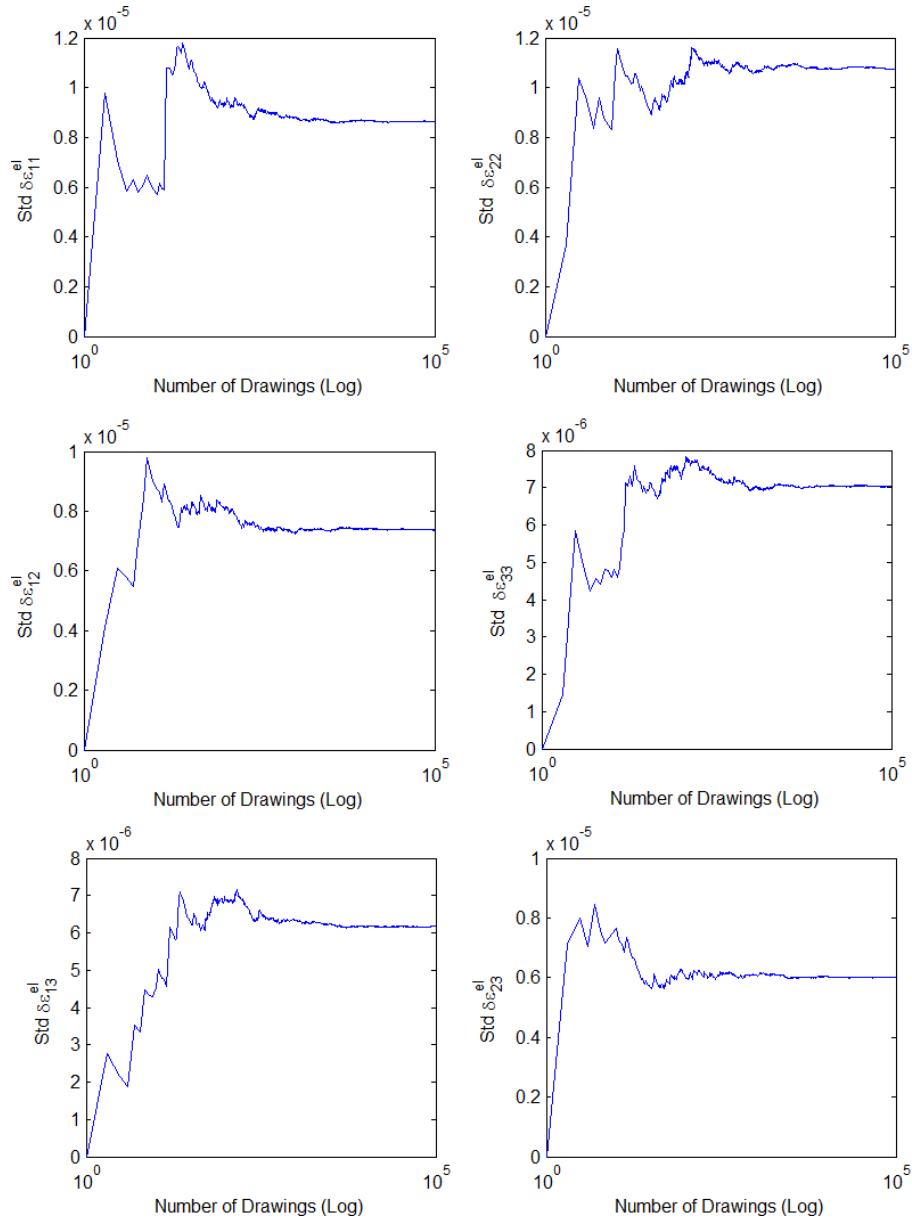


Figure 62: Stability of the calculating system $= \sigma(\varepsilon^e - \varepsilon^e)/N$.

The calculation is first made for both 13 and 6 measured planes. The uncertainty σ_{ε^e} calculated for 13 and 6 measured planes using the analytical method (Eq.3.60 and 3.62 respectively) are accurate to 10^{-6} to those calculated by Monte Carlo method. Therefore, the analytical method presented can be used to quantify the σ_{ε^e} during ε^e measurement.

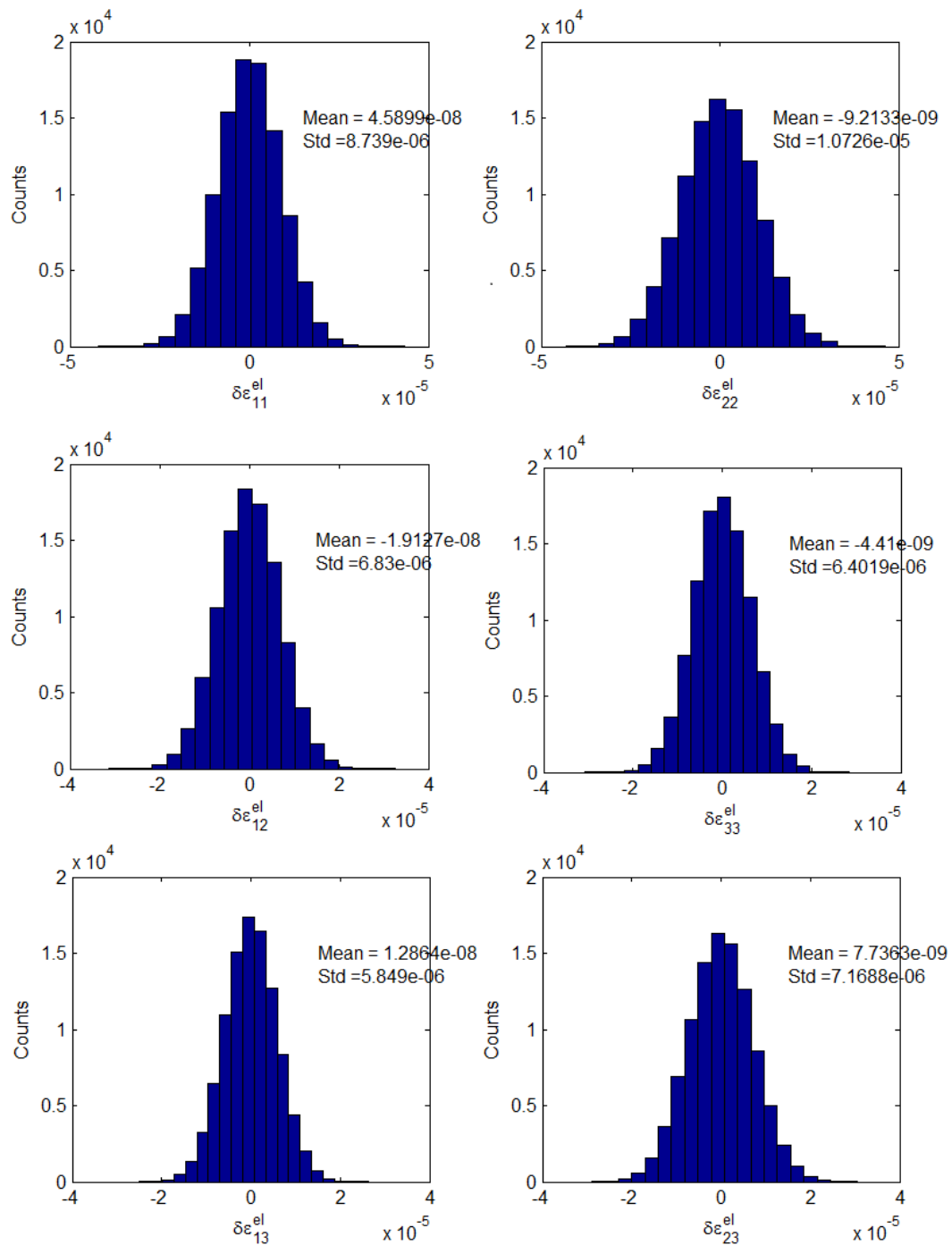


Figure 63: $\Sigma \epsilon^e$ calculated for 13 measured planes by Monte Carlo Method.

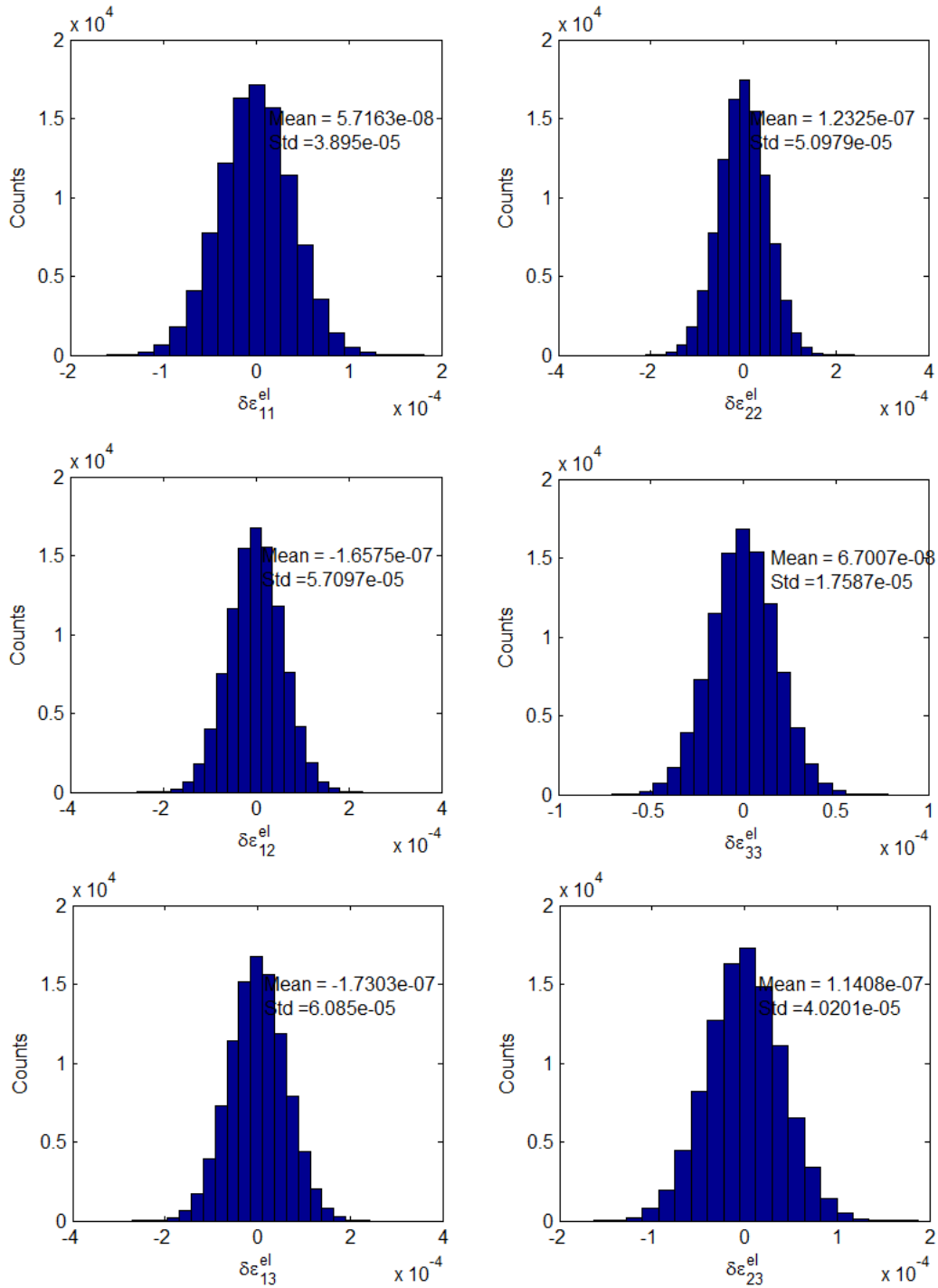


Figure 64: $\Sigma\varepsilon^e$ calculated for 6 measured planes by Monte Carlo Method.

Drawing of the supplementary
elements for experimental setup
assembly

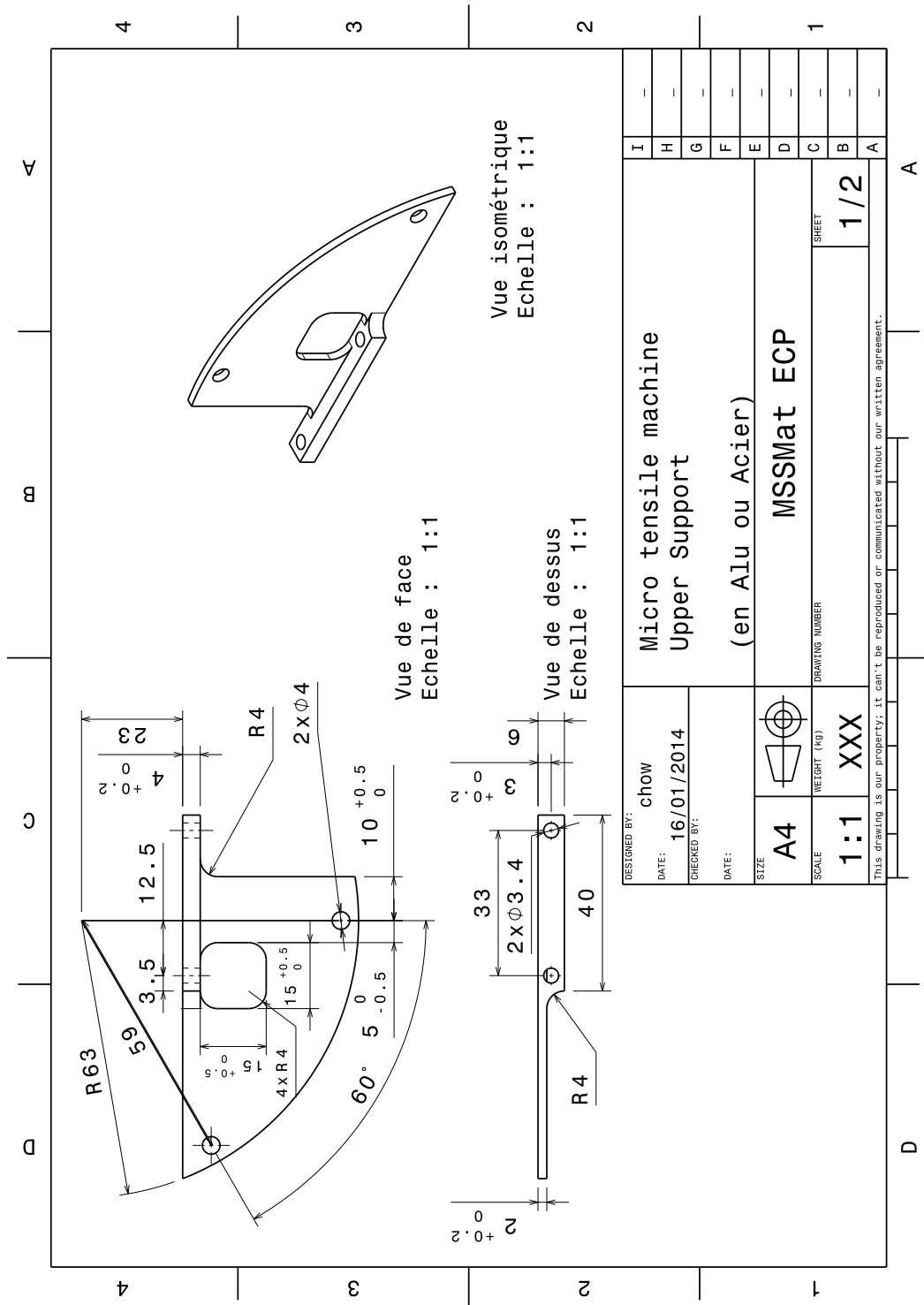


Figure 65: Mounting system of the micromachine on the wafer holder in goniometer - upper support.

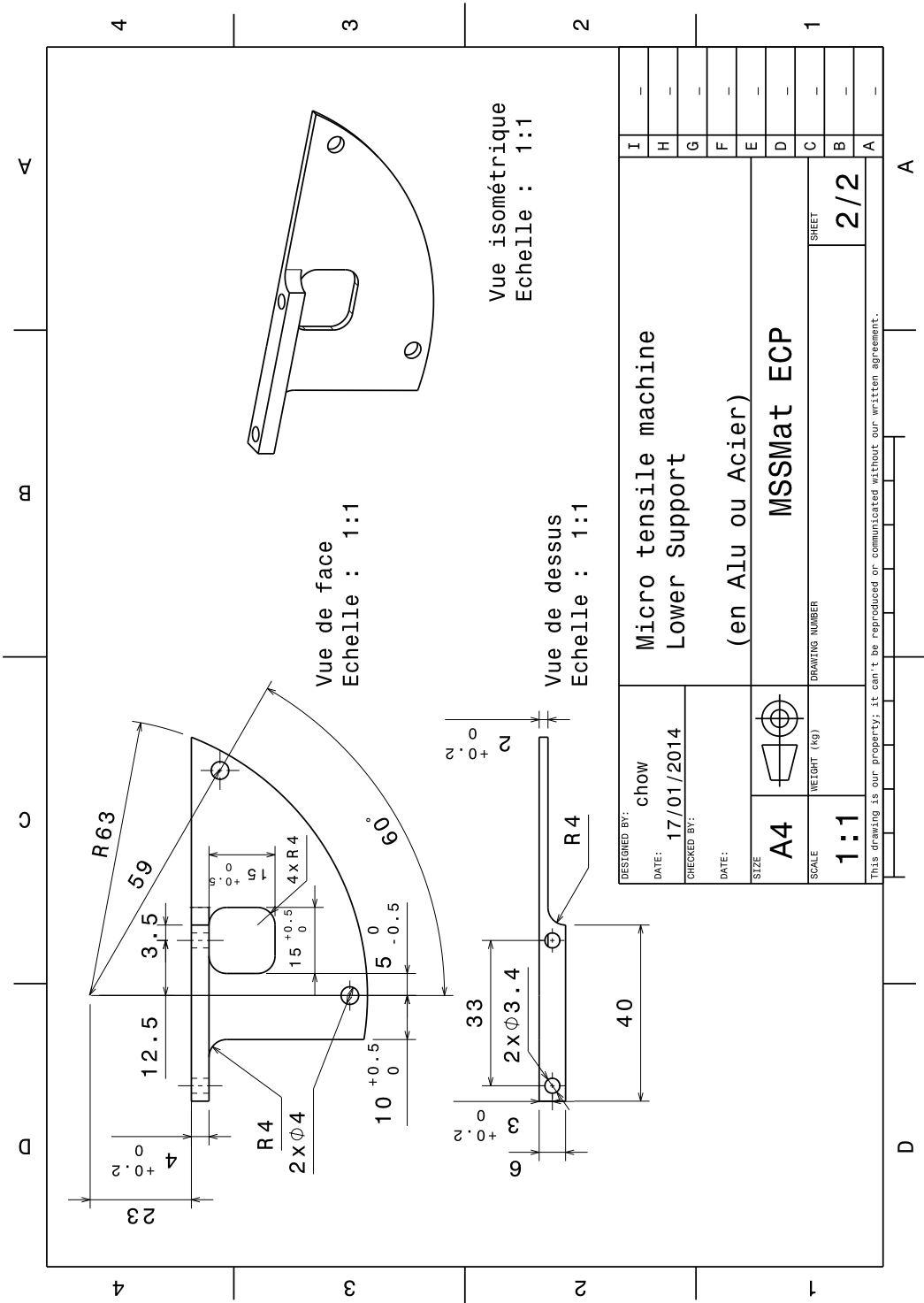


Figure 66: Mounting system of the micromachine on the wafer holder in goniometer - lower support.

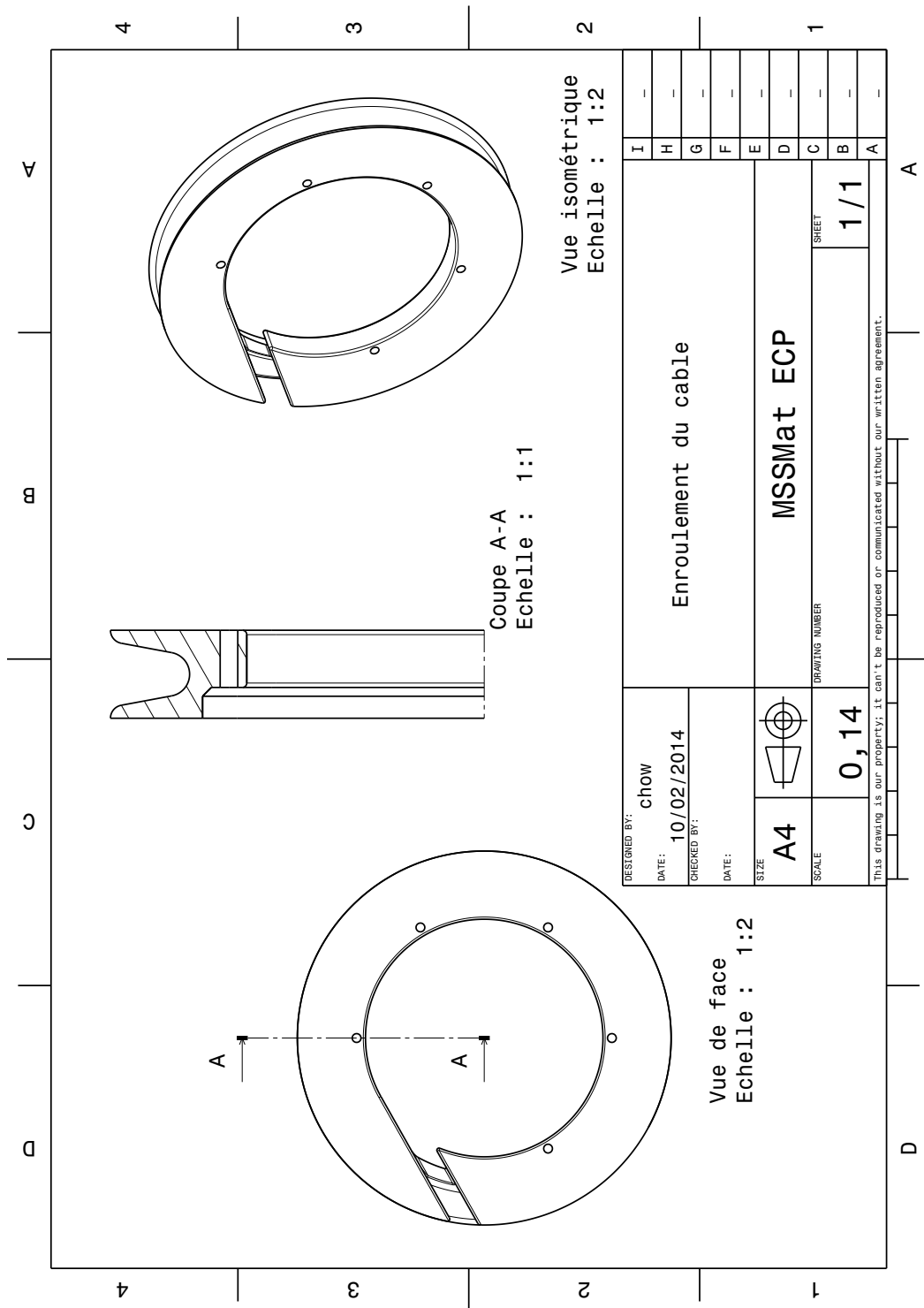


Figure 67: Wire winding to tide up the connecting cable (3D printing in polymer).

Experimental Potocol - complementary information

.1 Position of the sample center in goniometer

In order to correctly perform XRD measurement on the specified analysing points on the sample surface, the position of the sample center with respect to the X-ray beam in the goniometer is taken as reference (Fig.68). The reference position (Tab.19) is used for programming diffractometer control file.

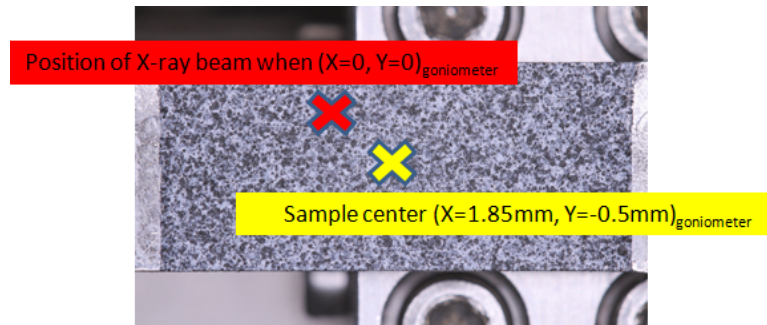


Figure 68: Position of the sample inside the micro-machine with respect to the X-ray beam in the goniometer.

$X_{\text{goniometer}}$	$Y_{\text{goniometer}}$	$Z_{\text{goniometer}}$
1.85mm	-0.5mm	0.35mm

Table 18: The position of sample center in goniometer.

.2 Position of the sample on the goniometer during DIC

During ε^t measurement, the specimen surface has to be first positioned perpendicularly to and in front of the digital camera in the goniometer (Tab.19).

$X_{goniometer}$	$Y_{goniometer}$	Ψ	Φ	2θ	Offset
-0.5mm	-35mm	11.16°	45°	70°	43°

Table 19: The position and the orientation of the sample in the goniometer during DIC.

.3 Restriction of the movement of goniometer during in-situ measurement

The description of the X-ray diffraction apparatus and XRD measurement are given in §.3.2. During XRD, the diffraction path should not be blocked by any component of the experimental setup. Meanwhile, the movement of every axis of the goniometer is also restricted to prevent collisions between machine components and the camera in the working area.

Axis	$X_{goniometer}$	$Y_{goniometer}$	$Z_{goniometer}$	Ψ	Φ	2θ
Min	-8mm	-5mm	0.35mm	0°	0°	70°
Max	8mm	-5mm	0.35mm	75°	360°	110°

Table 20: Restriction of the movement of goniometer during in-situ measurement.

.4 In-situ measuring procedure of XRD and DIC

Once the oligo-crystalline samples are ready and their initial microstructure are known, the in-situ measurement under loading can be executed.

1. According the zone of analysis/interest (ZOI) of the samples for DIC and XRD measurement, the grains to be diffracted are listed and the position of 13 diffraction planes $(\phi, \psi)_{\{hkl\}_{grain}}$ are calculated.
2. The value of the loading cell is initialized before fixing the sample inside the micro-machine. After the fixation, the extension value is initialized. The extension is set to zero and the synchronous data recording (file streaming) is started at sampling rate of 5s.
3. Take the first photo as reference is taken.
 - format: .CR2 and .tiff
 - Exposure time: 1/30s
 - focal length/entrance pupil diameter: f/8)
 - resolution: 10.2 μ m/pixel

- distance to the sample surface: 180mm
4. Regarding to the location of ZOI on the grain, the goniometer control file is programmed in format of .xml. The XRD measurement is first conducted at sample's initial state. For each XRD measurement:
 - (a) Starting with the initial $\phi_{(hkl)}$, $\psi_{(hkl)}$ and $2\theta_{(hkl)}$
 - (b) Optimisation of orientation - peak position of $(\phi, \psi)_{(hkl)}$
 - Range of scanning : Texture scanning ($\phi \pm 7.5, \psi \pm 7.5$)
 - Step size = 1°)
 - Acquisition time = 0.2s)
 - Total scanning time = 3min2s)
 - (c) Optimisation of $\phi_{(hkl)}$
 - Range of scanning : $\phi \pm 5^\circ$)
 - Step size = 0.1°)
 - Acquisition time = 0.2s)
 - Total scanning time = 22s)
 - (d) Optimisation of $\psi_{(hkl)}$
 - Range of scanning : $\psi \pm 5^\circ$)
 - Step size = 0.1°)
 - Acquisition time = 0.2s)
 - Total scanning time = 22s)
 - (e) Optimisation of $2\theta_{(hkl)}$
 - Range of scanning : $2\theta \pm 5^\circ$)
 - Step size = 0.05°)
 - Acquisition time = 1s)
 - Total scanning time = 40s)
 - (f) Repeating steps (b)-(e) 3 times.
 5. Stop the file streaming and orient the sample perpendicularly in front of the camera.
 6. The sample is then pulled/compressed until a specified extension at a loading speed of 0.2 mm/min and data are recorded at the sampling rate of 0.1 s. Photos are taken for every 5 s automatically.

7. Stop the file streaming. Keep the grip system unchanged and restart the file streaming at the sampling rate of 5 s.
8. Reorient the sample back to the position for XRD measurement. The goniometer control file is reprogrammed regarding to optimised $\phi_{(hkl)}$, $\psi_{(hkl)}$ and $2\theta_{(hkl)}$ position. The XRD measurement is using the scanning parameter listed in step (4) relaunched after 40mins of relaxation of the material.
9. Repeat the step (4)-(8) until the end of the experiment.

Résumé substantiel en français

Au cours des dernières deux décennies, la modélisation micromécanique a été largement développée afin de relier directement la microstructure réelle d'un matériau à ses propriétés macroscopiques (mécanique, thermique, électrique, etc.). Les lois de plasticité cristalline visent à prédire les comportements locaux et macroscopiques et/ou les changements de la microstructure lors d'un chargement thermomécanique [Saai et al. (2010); Schwartz et al. (2010); De Jaeger et al. (2012); Li et al. (2012)]. Cependant, étant donné l'échelle des mécanismes que ces modèles décrivent, les mesures sont difficiles à réaliser et l'identification des paramètres devient délicate. Il est également nécessaire d'utiliser des données expérimentales à l'échelle du grain. L'objectif de l'étude présentée ici est de développer une procédure robuste pour obtenir au moins deux réponses mécaniques locales distinctes d'un matériau à l'échelle du grain.

Étant donné l'adaptabilité des méthodes expérimentales et l'axe de recherche de l'étude, les champs de déformation élastique ε^e et totale ε^t ont été choisis comme variables à mesurer. Ces deux champs ont été mesurés en même temps à chaque niveau de chargement successif lors d'essais de traction avec décharges. Le champ total ε^t a été déterminé par Corrélation d'Images Numériques (CIN) proposé dans le travail d'Hild et Roux (2008) (Correli_Q4) et le champ élastique ε^e a été calculé à partir de la mesure de Diffraction des Rayons X (DRX) suivant la méthode mentionnée dans Ortner (1986a,b); Zhou (1994) (Première méthode d'Ortner).

Un alliage d'aluminium (5052) a été sélectionné pour la préparation des échantillons utilisés dans cette étude. Afin d'effectuer ces mesures à l'échelle du cristal, deux échantillons de forme et de dimensions spécifiques ont été préparés. Chaque échantillon est composé de 12 grains de chaque côté et deux grains dans l'épaisseur pour faciliter les mesures de déformations à l'intérieur des grains.

Une méthode de mesure du pic de diffraction a été développée et validée afin d'obtenir une mesure locale du champ ε^e dans les échantillons oligo-cristallins. Une technique spécifique de DRX a été utilisée pour quantifier précisément les changements élastiques dans les monocristaux. L'analyse des données expérimentales a été réalisée avec la première méthode d'Ortner. La combinaison et le nombre de plans $\{hkl\}$ pour chaque point de mesure DRX ont été déterminés afin d'améliorer la précision du calcul de ε^e . Les incertitudes sur ε^e ont été précisément quantifiées. Pour la mesure de CIN, une couche de peinture (mouchetis) est nécessaire sur la surface de l'échantillon. La résolution spatiale de CIN a été définie par rapport à la qualité du mouchetis appliqué.

Ce manuscrit présente ensuite le dispositif développé pour expérimental développé pour effectuer simultanément la CIN, la DRX et l'essai de traction *in-situ* dans un diffractomètre à rayons X. La résolution spatiale de chaque mesure sur la surface de l'échantillon a été définie pour atteindre ses meilleures performances. Le

protocole expérimental *in-situ* a également été développé et validé.

Les champs ε^t et ε^e des deux échantillons ont été obtenus lors d'essais de traction in situ. En plus des résultats et des analyses, les incertitudes ont également été quantifiées.

List of Tables

1.1	Elastic constants and anisotropy coefficients of several common FCC metals [Huntington (1958)]	4
1.2	12 slip-systems in a FCC structure: 4 close-packed $\{111\}$ planes and 3 close-packed directions of the form $\langle 110 \rangle$ within each plane.	7
2.1	Chemical composition (in Wt%) of the aluminium alloy used (5052)	32
2.2	Crystal orientations of a.front side and b.back side of the sample No.1.	39
2.3	Schmid factor of each grain of a. front side and b. back side of sample No.1.	40
2.4	Crystal orientations of both sides of sample No.2.	41
2.5	Schmid factor of each grain of both sides of sample No.2.	41
3.1	$2\theta_{\{hkl\}}(^{\circ})$ measured on fine powder sample (T1), Coarse powder sample (T2) and block sample (yellow).	56
3.2	Lattice parameter a_o measured using fine powder sample (T1), Coarse powder sample (T2) and block sample (yellow).	57
3.3	Theoretical variation of 2θ corresponding to various $\{hkl\}$ planes of a crystal submitted to a strain of 4.29×10^{-3} (deformation corresponding to the elastic limit of Aluminium) in the $\langle 100 \rangle$ direction. .	60
3.4	Errors in $\delta\theta_{-202}$, $\delta\theta_{-131}$ and $\delta\theta_{-222}$ were observed for small peak displacement along θ in Grain7 of sample 1 at position X=-5 Y=-3. The changes between the imposed and obtained $\delta\theta$ were calculated as percentages. The lowest limit for the measurable shifting error was found to be $10^{-4^{\circ}}$ corresponding to 5%-change.	70
3.5	2θ of 13 $\{hkl\}$ planes in Grain7 (X=-5,Y=-3) measured by XRD at its initial state and $\varepsilon_{xx}^t = 0.0074$	75
4.1	% of force decrease with respect to relaxation time on a representative polycrystalline Al-alloy specimen under constant strain.	95
5.1	Schmid factor of each grain of a. front side and b. back side of sample No.1.	100
5.2	Mean value of ε^e of sample 1 at each successive loading level	101
5.3	Mean value of σ_{ε^e} of sample 1 at each successive loading level . . .	103
5.4	Standard deviation of σ_{ε^e} of sample 1 at each successive loading level	103
5.5	Mean value of σ^e of sample 1 at each successive loading level	104
5.6	Mean value of σ^e calculated using $\nu = 0.25$ at each successive loading level	104
5.7	Mean value of σ_{σ^e} of sample 1 at each successive loading level . . .	105
5.8	Standard deviation of σ_{σ^e} of sample 1 at each successive loading level	105
5.9	Schmid factor of each grain of both sides of sample 2.	115
5.10	Mean value of ε^e of sample 2 at each successive loading level	116

5.11	Mean value of σ_{ε^e} of sample 2 at each successive loading level. . . .	118
5.12	Standard deviation of σ_{ε^e} of sample 2 at each successive loading level.	118
5.13	Mean value of σ^e of sample 2 at each successive loading level	119
5.14	Mean value of σ^e calculated using $\nu = 0.29$ at each successive loading level	120
5.15	Mean value of σ_{σ^e} of sample 2 at each successive loading level . . .	120
5.16	Standard deviation of σ_{σ^e} of sample 2 at each successive loading level	120
17	$\Delta\theta_{n=1,\dots,26}^N$ are generated for 13 measured planes. Then, they are imposed for each measured diffraction angles for calculating ε^{e-N} . .	155
18	The position of sample center in goniometer.	163
19	The position and the orientation of the sample in the goniometer during DIC.	164
20	Restriction of the movement of goniometer during in-situ measurement.	164

Titre : Développement d'une méthode in situ pour mesurer les champs de déformation élastique et totale à l'échelle du grain

Mots clés : Diffraction des Rayons X, Corrélation d'image numérique, Aluminium

Résumé : Au cours des dernières deux décennies, la modélisation micromécanique a été largement développée afin de relier directement la microstructure réelle d'un matériau à ses propriétés macroscopiques (mécanique, thermique, électrique, etc.). Les lois de plasticité cristalline visent à prédire les comportements locaux et macroscopiques et/ou les changements de la microstructure lors d'un chargement thermomécanique. Cependant, étant donné l'échelle des mécanismes que ces modèles décrivent, les mesures sont difficiles à réaliser et l'identification des paramètres devient délicate. Il est également nécessaire d'utiliser des données expérimentales à l'échelle du grain. L'objectif de l'étude présentée ici est de développer une procédure robuste pour obtenir au moins deux réponses mécaniques locales distinctes d'un matériau à l'échelle du grain.

Les champs total et élastique ont été sélectionnés et ensuite mesurés en même temps à chaque niveau de chargement successif lors d'essais de traction avec décharges. Le champ total a été déterminé par Corrélation d'Images Numériques (CIN) et le champ élastique a été calculé à partir de la mesure de Diffraction des Rayons X (DRX). Deux échantillons oligo-cristallins en alliage d'aluminium (5052) ont été utilisés dans cette étude. Le dispositif et méthode expérimental a été développé pour effectuer simultanément la CIN, la DRX et l'essai de traction in-situ dans un diffractomètre à rayons X. En plus des résultats et des analyses, les incertitudes ont également été quantifiées.

Title : Development of an in situ method for measuring elastic and total strain fields at the grain scale

Keywords : X-ray diffraction, Digital image correlation, Aluminum

Abstract: Micromechanical modelling was widely developed during the past 20 years as they enable ones to make direct links between the actual microstructure of a material and its macroscopic properties such as mechanical, thermal, electrical, etc. Crystal plasticity models aim at predicting local and macroscopic behaviours and/or changes of the microstructure during thermomechanical loading. However, the parameters of these models are difficult to identify, because the mechanisms they describe are at a small scale and are thus complicated to measure. For this reason, the crystalline model identification requires the use of experimental data at the grain scale. The objective of the study presented here is to develop a robust procedure to obtain at least two distinct local mechanical responses of a material at the grain scale.

The total and elastic strain fields have been chosen to be characterised referring to the research interest and the adaptability of experimental methodologies. When samples were subjected to simple tensile loadings and unloadings, strain fields were measured on the sample surface simultaneously at each successive level. Total strain fields were determined by the Digital Image Correlation technique (DIC) while elastic strain fields were calculated from the X-ray diffraction (XRD) measurements. Two oligo-crystalline samples of an aluminium alloy (5052) has been prepared and used in this study. The experimental device and methodology was designed and developed to perform DIC, XRD and tensile tests in-situ in an X-ray diffractometer. The total and elastic strain fields of two samples through in situ tension experiments were obtained. Besides results and analysis, the corresponding uncertainties during each measurement were quantified as well.

